

The Pennsylvania State University
The Graduate School
Department of Engineering Science and Mechanics

IN SITU STRENGTH EVOLUTION IN THE SINTERING OF
BRONZE POWDER METAL COMPACTS AND
APPLICATION TO THERMAL CYCLE DESIGN

A Thesis in
Engineering Science and Mechanics

by
Gregory A. Shoales

Submitted in Partial Fulfillment

of the Requirements

for the Degree of

Doctor of Philosophy

May 1998

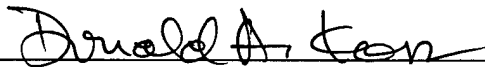
We approve the thesis of Gregory A. Shoales.

Date of Signature



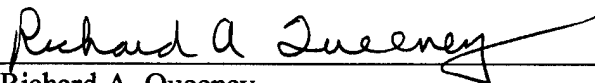
Randall M. German
Brush Chair Professor in Materials
Thesis Advisor
Chair of Committee

23 Mar 98



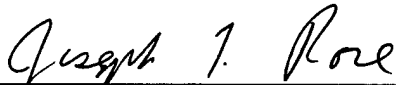
Donald A. Koss
Professor of Materials Science and Engineering

3/3/98



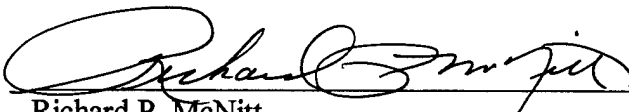
Richard A. Queeney
Professor of Engineering Mechanics

3/3/98



Joseph L. Rose
Paul Morrow Professor in Design and Manufacturing

3/3/98



Richard P. McNitt
Professor of Engineering Science and Mechanics
Head of Department of Engineering Science and Mechanics

3/23/98

Abstract

Powder metallurgy allows fabrication of complex net-shape components. Accurate design specification of these components requires precise prediction of their response to sintering process parameters. Nonuniform sintering responses, such as strain gradients, can result in process failures such as distortion and cracking. To avoid these types of process failures without costly trial and error design, the most important response to understand is the compact's strength as it evolves during the sintering process.

A unique device and method have been developed to measure the *in situ* strength as a function of sintering process parameters. The specific strength parameter investigated and modeled in this work was transverse rupture. This strength was precisely determined for 90Cu-10wt.%Cu prealloyed powder bronze compacts in response to sintering time, temperature and heating rate. At a sintering temperature of approximately 350°C the green strength of 10 MPa decreased 50% due to the annealing of the cold worked strength afforded during compaction. At higher temperatures, a dramatic increase in strength (dependent also on time and heating rate) due to sintering was observed. As the compact was processed beyond approximately 600°C, thermal softening dominated sintering strengthening to cause an overall degradation in strength with respect to temperature. This first ever data made possible a model to predict the *in situ* evolution of strength during sintering. The consequence of this work is to identify the thermal cycles that maximize strength, thereby minimizing distortion and otherwise improving dimensional tolerances.

Table of Contents

	<u>page</u>
List of Figures	vii
List of Tables	xiii
Acknowledgments	xv
Chapter 1. Introduction	1
Chapter 2. Background	3
2.1 Physical Response to Sintering	5
2.2 Dimensional Variation	5
2.2.1 Dilatometry	7
2.2.2 Video Imaging	10
2.3 Sintering Stress	15
2.4 Development of Properties	21
2.5 Modeling Concept	23
2.5.1 Green Strength	23
2.5.2 Annealing	25
2.5.3 Sinter Strengthening	26
2.5.4 Thermal Softening	29
2.6 Statement of Hypothesis	29
Chapter 3. Experimental Procedures	31
3.1 <i>In situ</i> Strength Measurement	31
3.1.1 Selection of Strength Property	32
3.1.2 Powder Selection	33
3.1.3 Powder Characterization	34
3.1.4 Test Apparatus Development	41
3.1.4.1 Configuration	41
3.1.4.2 Operating Parameters	47
3.1.4.3 Calibration	47
3.1.5 Compaction and Test Specimen Fabrication	49
3.1.6 Test Procedures	50
3.2 Strength Due to Sintering	53
3.3 Thermal Softening	54
3.4 Dilatometric Analysis	56
3.5 Differential Thermal Analysis	59

3.6 Quenching	61
3.7 Metallography	61
3.8 Microstructural Analysis: Grain Size Measurement	63
3.9 Microstructural Analysis: X-Ray Diffraction	65
3.10 Hardness Measurements	66
Chapter 4. Experimental Results	68
4.1 <i>In situ</i> Strength Evolution	68
4.1.1 Constant Heating Rate Sintering	69
4.1.2 Isothermal Sintering	69
4.1.3 Thermal Softening Behavior	72
4.2 Compact Sintered Strength	75
4.2.1 Constant Heating Rate Sintering	75
4.2.2 Sintering with Isothermal Holds	79
4.3 Additional Sintering Outcomes	84
4.3.1 Densification	85
4.3.2 Grain Growth	88
4.3.3 Neck Growth	88
4.4 Bulk Material Characteristics	98
4.4.1 Melting	98
4.4.2 Phase Evaluation	99
4.4.3 Thermal Softening	106
4.4.4 Hardness	106
Chapter 5. Modeling	110
5.1 Model Development	110
5.1.1 Green Strength	110
5.1.2 Annealing	111
5.1.3 Sinter Strength	115
5.1.3.1 Contributions of Sintering Outcomes	116
5.1.3.2 Master Sintering Curve	119
5.1.4 Thermal Softening	122
5.2 Model Implementation	125
5.2.1 Process Profile Sheet	125
5.2.2 Annealing Sheet	126
5.2.3 MSC Parameter Sheet	127
5.2.4 <i>In situ</i> Transverse Rupture Strength Sheet	128
Chapter 6. Discussion	130
6.1 <i>In situ</i> Strength Evolution of Bronze	131

6.1.1	Annealing of Green Strength	131
6.1.2	Sinter Strengthening	135
6.1.2.1	MSC Equivalent Energy	137
6.1.2.2	MSC - Sinter Strength Correlation	143
6.1.3	Thermal Softening	147
6.2	Additional Sintering Outcomes	158
6.2.1	Phase Evaluation	158
6.2.2	Melt Characteristics	159
6.3	Model Application	161
6.3.1	Other Powder Compacts	161
6.3.1.1	Strength Evolution in B-406 Grade Bronze	162
6.3.1.2	Strength Evolution in W-Cu-Co	163
6.3.2	Thermal Cycle Design	166
Chapter 7.	Conclusions	174
References	178
Appendix A.	Raw FTT Data of B-409 Grade Bronze	187
Appendix B.	Sinter Strength of B-409 Grade Bronze	190
Appendix C.	Thermal Softening of Dense B-409 Grade Bronze	192
Appendix D.	<i>In situ</i> Transverse Rupture Strength Model - Program Description ...	193
Appendix E.	Raw FTT Data from Additional Powders	198

List of Figures

	<u>page</u>
Figure 2.1: A copper split bolt, a titanium trigger guard and a stainless steel microelectronics package which were warped during sintering.	6
Figure 2.2: Schematic of SyncroVision [®] model 2SCOX11 diagnostic video camera system as installed on CM horizontal tube furnace.	13
Figure 2.3: Captured video images obtained using the SyncroVision [®] video imaging system showing bronze transverse rupture bar at various temperatures.	14
Figure 2.4: Plot comparing axial shrinkage for prealloyed 90Cu-10wt.%Sn bronze powder compact as measured by conventional contact dilatometry and noncontact SyncroVision [®] video imaging system.	16
Figure 2.5: The curvature at any point on a curve surface described by two principal radii given as R_1 and R_2	17
Figure 2.6: Sintering of two spheres showing the development of the interparticle bond starting with a) initial point contact and progressing from b) early stage neck growth to c) late stage neck growth.	18
Figure 2.7: Schematic of stress applied to a porous sintered material illustrating decrease of cross section, crack propagation along pores and stress concentrations at the pores.	27
Figure 3.1: A scanning electron microscope image of the loose B-409 bronze powder.	42
Figure 3.2: Kimberly Comstock and the author operating FTT with its PC based data acquisition system (photo courtesy of J. Thomas).	44
Figure 3.3: Section view of the FTT test region with close up of transverse rupture strength test 2-point supports and mid-span load ram.	45
Figure 3.4: Time versus temperature of the FTT test section when operated at maximum heating rate.	48
Figure 3.5: Photograph of FTT test chamber interior with retort cap removed.	55

Figure 3.6: Schematic illustration of the Anter Laboratories Unitherm™ Model 1161 vertical dilatometer.	57
Figure 3.7: TA Instruments SDT 2960 used for differential thermal analysis.	60
Figure 3.8: Schematic illustration of a CM vertical tube furnace used for quenching.	62
Figure 4.1: <i>In situ</i> transverse rupture strength versus test temperature for prealloyed 90Cu-10wt.%Sn bronze compacts sintered at 10°C/min in hydrogen.	70
Figure 4.2: <i>In situ</i> transverse rupture strength versus test temperature for prealloyed 90Cu-10wt.%Sn bronze compacts sintered at 5°C/min in hydrogen.	71
Figure 4.3: <i>In situ</i> transverse rupture strength versus test temperature for prealloyed 90Cu-10wt.%Sn bronze compacts sintered at 10°C/min in hydrogen with isothermal holds at the test temperature of either 10 or 20 min.	73
Figure 4.4: <i>In situ</i> transverse rupture strength versus test temperature for prealloyed 90Cu-10wt.%Sn bronze compacts sintered at 10°C/min in hydrogen with an isothermal hold at 400°C for 20 min.	74
Figure 4.5: <i>In situ</i> transverse rupture strength versus test temperature for prealloyed 90Cu-10wt.%Sn bronze compacts sintered in hydrogen at 10°C/min to the peak temperature, indicated by series legend, followed by cool to the test temperature.	76
Figure 4.6: <i>In situ</i> transverse rupture strength normalized to room temperature strength versus test temperatures for prealloyed 90Cu-10wt.%Sn bronze compacts sintered in hydrogen at 10°C/min to the peak temperature, indicated by series legend, followed by cool to the test temperature.	77
Figure 4.7: Room temperature transverse rupture strength versus maximum sinter temperature for prealloyed 90Cu-10wt.%Sn bronze compacts sintered in hydrogen at constant heating rates of 5, 10, or 20°C/min.	78
Figure 4.8: Room temperature transverse rupture strength versus maximum sinter temperature for prealloyed 90Cu-10wt.%Sn bronze compacts sintered at 10°C/min with isothermal holds of either 10 or 20 min at the maximum temperature.	80
Figure 4.9: Room temperature transverse rupture strength versus maximum sinter temperature for prealloyed 90Cu-10wt.%Sn bronze compacts sintered at 5°C/min with an isothermal hold of 60 min at the maximum temperature.	81

Figure 4.10: Room temperature transverse rupture strength versus maximum sinter temperature for prealloyed 90Cu-10wt.%Sn bronze compacts sintered at 20°C/min with an isothermal hold of 60 min at the maximum temperature.	82
Figure 4.11: Room temperature transverse rupture strength versus maximum sinter temperature for prealloyed 90Cu-10wt.%Sn bronze compacts sintered at either 5°C/min or 10°C/min with isothermal holds of 20 or 60 minutes at 400°C.	83
Figure 4.12: Dilatometric plot of shrinkage and shrinkage rate in transverse and press directions versus temperature for prealloyed 90Cu-10wt.%Sn bronze compact sintered at 10°C/min in hydrogen.	86
Figure 4.13: Dilatometric plot fractional density versus temperature for prealloyed 90Cu-10wt.%Sn bronze compact sintered at 10°C/min in hydrogen.	87
Figure 4.14: Optical micrograph of prealloyed 90Cu-10wt.%Sn bronze compact sintered to 400°C at 10°C/min in hydrogen and water quenched to room temperature at approximately 10 ³ °C/s.	89
Figure 4.15: Optical micrograph of prealloyed 90Cu-10wt.%Sn bronze compact sintered to 500°C at 10°C/min in hydrogen and water quenched to room temperature at approximately 10 ³ °C/s.	90
Figure 4.16: Optical micrograph of prealloyed 90Cu-10wt.%Sn bronze compact sintered to 600°C at 10°C/min in hydrogen and water quenched to room temperature at approximately 10 ³ °C/s.	91
Figure 4.17: Characteristic grain size versus temperature for prealloyed 90Cu-10wt.%Sn bronze compact sintered at 10°C/min in hydrogen.	92
Figure 4.18: Fracture surface scanning electron microscope image of transverse rupture bar fabricated from prealloyed 90Cu-10wt.%Sn bronze powder and tested at room temperature after sintering at 10°C/min in hydrogen to 400°C.	93
Figure 4.19: Fracture surface scanning electron microscope image of transverse rupture bar fabricated from prealloyed 90Cu-10wt.%Sn bronze powder and tested at room temperature after sintering at 10°C/min in hydrogen to 500°C.	94
Figure 4.20: Fracture surface scanning electron microscope image of transverse rupture bar fabricated from prealloyed 90Cu-10wt.%Sn bronze powder and tested at room temperature after sintering at 10°C/min in hydrogen to 600°C.	95

Figure 4.21: Fracture surface scanning electron microscope image of transverse rupture bar fabricated from prealloyed 90Cu-10wt.%Sn bronze powder and tested at room temperature after sintering at 10°C/min in hydrogen to 700°C.	96
Figure 4.22: Fracture surface scanning electron microscope image of transverse rupture bar fabricated from prealloyed 90Cu-10wt.%Sn bronze powder and tested at room temperature after sintering at 10°C/min in hydrogen to 800°C.	97
Figure 4.23: Differential thermal analysis (DTA) plot of temperature difference versus temperature showing two continuous cycles for prealloyed 90Cu-10wt.%Sn bronze.	100
Figure 4.24: X-ray diffraction pattern of as-received prealloyed 90Cu-10wt.%Sn powder.	102
Figure 4.25: X-ray diffraction pattern of prealloyed 90Cu-10wt.%Sn compact water quenched from 400°C after sintering at 10°C/min in hydrogen.	103
Figure 4.26: X-ray diffraction pattern of prealloyed 90Cu-10wt.%Sn compact water quenched from 500°C after sintering at 10°C/min in hydrogen.	104
Figure 4.27: X-ray diffraction pattern of prealloyed 90Cu-10wt.%Sn compact water quenched from 600°C after sintering at 10°C/min in hydrogen.	105
Figure 4.28: Transverse rupture strength normalized to room temperature strength versus test temperature for high density prealloyed 90Cu-10wt.%Sn compacts.	107
Figure 4.29: Microhardness versus temperature of as-received prealloyed 90Cu-10wt.%Sn bronze powder compacts water quenched after sintering at 10°C/min in hydrogen to 400°C, 500°C and 600°C.	108
Figure 6.1: Evaluation of time step (Δt) for annealing model.	136
Figure 6.2: Natural log of MSC parameter ($\ln \theta$) versus measured room temperature transverse rupture strength for $Q_s = 10$ kJ/mol.	138
Figure 6.3: Natural log of MSC parameter ($\ln \theta$) versus measured room temperature transverse rupture strength for $Q_s = 1000$ kJ/mol.	139
Figure 6.4: Linear correlation coefficient versus equivalent activation energy (Q_s) for correlation of MSC parameter (θ), as calculated by Equation 6.2, with all room temperature strength measurements specified in Appendix B.	141

Figure 6.5: Correlation coefficient and standard error versus equivalent activation energy (Q_s) for correlation of MSC parameter (θ), as calculated by Equation 6.2, with all room temperature strength measurements specified in Appendix B.	142
Figure 6.6: Natural log of MSC parameter ($\ln \theta$) versus measured room temperature transverse rupture strength for $Q_s = 130$ kJ/mol.	145
Figure 6.7: Effect of time step (Δt) on sintering strength model.	146
Figure 6.8: Room temperature transverse rupture strength, as determined by the sinter strengthening model, for constant rate sintering versus heating rate and temperature.	148
Figure 6.9: Room temperature transverse rupture strength, as determined by the sinter strengthening model, for isothermal sintering versus time and temperature. ...	149
Figure 6.10: Prediction of <i>in situ</i> strength evolution using FTT cooling data to derive thermal softening.	152
Figure 6.11: Prediction of <i>in situ</i> strength evolution using thermal softening data from dense 90Cu-10wt.%Sn bronze compacts to derive thermal softening portion of the model.	155
Figure 6.12: Comparison between <i>in situ</i> strength evolution model and data plotted by transverse rupture strength versus test temperature. Data for B-409 grade bronze derived from constant 10°C/min to test temperatures up through 600°C followed by subsequent cooling to lower test temperatures.	156
Figure 6.13: Comparison between <i>in situ</i> strength evolution model and data plotted by transverse rupture strength versus test temperature. Data for B-409 grade bronze derived from constant 10°C/min to test temperatures up through 700°C followed by subsequent cooling to lower test temperatures.	157
Figure 6.14: Comparison of <i>in situ</i> strength evolution model prediction and data for United States Bronze Powders, Inc. grade B-406 prealloyed 90Cu-10wt.%Sn bronze compacts.	164
Figure 6.15: Comparison of <i>in situ</i> strength evolution model prediction and data for W-Cu-Co compacts.	167
Figure 6.16: Predicted transverse rupture strength versus time for 50°C/min to 400°C followed by a 6 min hold and continued heating at 10°C/min.	169

Figure 6.17: Predicted transverse rupture strength versus time for 10°C/min to 400°C followed by a 20 min hold and continued heating at 10°C/min to 600°C. Also shown for comparison are the FTT data from Appendix A which match this sinter profile.	171
Figure 6.18: A contour map of <i>in situ</i> strength evolution versus time and temperature for instantaneous heating.	173
Figure D-1: <i>In situ</i> strength evolution model flow chart.	193
Figure D-2: Sample process profile sheet for the <i>in situ</i> strength evolution model. ..	194
Figure D-3: Sample annealing sheet for the <i>in situ</i> strength evolution model.	195
Figure D-4: Sample MSC parameter sheet for the <i>in situ</i> strength evolution model.	196
Figure D-5: Sample <i>in situ</i> transverse rupture strength sheet for the <i>in situ</i> strength evolution model.	197

List of Tables

	<u>page</u>
Table 3.1: Summary of Horiba LA-910 repeatability and calibration measurements.	35
Table 3.2: Particle characterization summary for United States Bronze Powders B-409 grade prealloyed powder.	43
Table 5.1: Strength of compacted particles as a function of compaction parameters.	112
Table 6.1: Summary of <i>in situ</i> strength evolution model parameters.	134
Table A-1: Raw FTT data presented in Section 4.1.1. <i>In situ</i> transverse rupture strength measurements from prealloyed 90Cu-10wt.%Sn bronze compacts sintered at constant heating rate to test temperature in hydrogen.	187
Table A-2: Raw FTT data presented in Section 4.1.2. <i>In situ</i> transverse rupture strength measurements from prealloyed 90Cu-10wt.%Sn bronze compacts sintered in hydrogen. Sintering profiles included an isothermal hold at or below the test temperature with constant heating rate thermal transitions.	188
Table A-3: Raw FTT data presented in Section 4.1.3. <i>In situ</i> transverse rupture strength measurements from prealloyed 90Cu-10wt.%Sn bronze compacts sintered in hydrogen. Sintering profiles included constant rate heating to a peak temperature followed by subsequent cooling to lower test temperature.	189
Table B-1: Raw data presented in Section 4.2.1. Room temperature transverse rupture strength measurements from prealloyed 90Cu-10wt.%Sn bronze compacts sintered in hydrogen. Sintering profiles included constant heating to a peak sintering temperature followed by cooling to room temperature.	190
Table B-2: Raw data presented in Section 4.2.2. Room temperature transverse rupture strength measurements from prealloyed 90Cu-10wt.%Sn bronze compacts sintered in hydrogen. Sintering profiles included an isothermal hold at or below the peak temperature followed by cooling to room temperature with constant heating rate thermal transitions.	191
Table C-1: Raw data presented in Section 4.4.3. Transverse rupture strength measurements performed at various temperatures on prealloyed 90Cu-10wt.%Sn bronze compacts that had been sintered 0.96 density fraction.	192

Table E-1: Raw data for FTT measurements of bronze compacts sintered in hydrogen.	198
Table E-2: Raw data for FTT measurements of W-10wt.%Cu (with 0.35wt.% admixed Co) compacts sintered in hydrogen.	199
Table E-3: Raw data for FTT measurements of W compacts sintered in hydrogen. ..	200
Table E-4: Raw data for FTT measurements of Ni_3Al (with 0.04wt.% admixed B) compacts sintered in a 90% argon - 10% hydrogen mix.	201
Table E-5: Raw data for FTT measurements of FC0208 (with Cu155) compacts sintered in a 80% nitrogen - 20% hydrogen mix.	202
Table E-6: Raw data for FTT measurements of FC0208 (with Cu278) compacts sintered in a 80% nitrogen - 20% hydrogen mix.	203

Acknowledgments

I would like to extend the utmost gratitude to my advisor, Professor Randall M. German, for his inspiration and guidance during my past three years of research in the P/M Lab. His leadership was immeasurable help to my early identification of an industrially significant area of research. Additionally, Professor German's demand for excellence has significantly contributed to the overall quality of my thesis in the field of powder metallurgy. Particular praise goes to the true inspiration of my life, Carmella and my son Matthew, for their support during these past years.

I would like to acknowledge the United States Air Force (USAF) and in particular the Department of Engineering Mechanics at the USAF Academy for permitting me the opportunity to achieve this goal. I also extend my thanks to Harvey Brush for his endowment of the Brush Chair Professorship in Materials as this was the major funding source for my research. I am indebted to Tom Pelletiers of United States Bronze Powders, Inc. for the donation of the bronze powder. Much appreciation also goes to Kim Comstock for her assistance in gathering and managing the data. I'd also like to recognize the time dedicated by Ann Kelly and Sherri Bingert at Los Alamos National Labs in the metallographic preparation of the bronze samples as well as Tracy Potter and Julian Thomas for their assistance in translating my design to a working test device.

Lastly, I thank the many friends and colleagues with whom I have shared time in the P/M Lab. Of these I'd like to particularly recognize Sundar, Tony, Shiva, Anish, Anand, Karthik, Chris, Tim, Ken, Gretchen, Mark, Kate, Steve, Neal, Anita, Ron, Robin, Judy, Helen, Lou and Bethala.

Chapter 1

Introduction

Powder metallurgy (P/M) processes are unique among all other manufacturing techniques. P/M manufacturing is an efficient means to produce highly accurate net-shape components that frequently possess properties unavailable by any other process. The efficiency stems from the fact that the engineering material starts as a powder. The fluid-like character of the powder makes possible the filling of dies and molds to obtain designed component shape. The powder is then consolidated to achieve desired properties by thermally processing through sintering. Since the microstructure starts at the scale of the powder, which is uniformly distributed in the shaping step, materials in finished P/M components are characteristically finer grained and more homogeneous than their wrought or cast counterparts.

It is the thermal parameters of sintering that create the greatest potential for failure in P/M manufacturing. Process gradients during sintering cause nonuniform responses, such as strain gradients, to the thermal environment. Such gradients result in stresses, which, if in excess of the allowable strength, lead to warping and cracks. Therefore, effective engineering design of high tolerance net shape components dictates a thorough understanding of not only the sintering environment, but also the component's response to that environment. Much progress has been made to address the issue of heat transport mechanisms and the development of sintering stress. What had been previously unknown

is how the strength of P/M components evolve from the relatively weak green state to the fully sintered final state. This work answers that question. The successful development of a model which predicts *in situ* strength evolution of sintering P/M components was made possible by *in situ* measurement of that property. As the first step of this research, making these first ever measurements required the design and development of a unique test device. This device (informally known as the flaming tensile tester or FTT) performed a transverse rupture strength test during the sintering cycle at any desired temperature or atmosphere, thus providing the key data to not only develop but also to validate the model. In this research the FTT was used to precisely determine the strength evolution of bronze compacts and other P/M systems. The model, derived from the bronze measurements, is demonstrated by application to design of thermal cycles which maximize *in situ* strength and thus the resistance to environmental stresses associated with sintering. Using this model to create strength evolution sintering maps, a new opportunity exists to balance such sintering stresses with the development of strength and thus enhance dimensional precision.

Chapter 2

Background

Powder metallurgy (P/M) describes both a technology and a manufacturing process to produce engineering components from particulate materials or powders. Unique among all other metalworking processes, P/M offers unparalleled advantages in economically making high performance, highly detailed and near net-shape components to precise design tolerances [1,2]. Unlike machining components from cast or wrought forms, P/M processes powder such that the engineering material and the component are formed concurrently. P/M manufacturing is also economical because the processes are easily automated and generally depend on a relatively low technology, well established, manufacturing infrastructure. Typical P/M manufacturing equipment includes; particulate mixers and mills, mechanical and hydraulic compaction presses, injection molders, and a variety of furnaces [1,3]. By starting with powders, components can be manufactured with unique high performance properties due to microstructural control. The most obvious factor for such control is that the small scale of the powder particles set the initial size of the microstructure in the final components. Specialty alloy materials, impossible by conventional methods such as casting, are made possible by combinations of the right elemental powders. The two primary elements of all P/M manufacturing are shaping and sintering. Shaping is simply a process step to form the desired component geometry from loose powder with enough handling strength to reach the next processing step. Sintering

is a thermally activated process that creates bonds between the loose powder particles to achieve the desired component properties.

Shaping is accomplished through a variety of techniques that take advantage of the fluid like character of powder to fill some type of mold that will give the component its designed shape. The powder injection molding (PIM) technique mixes the powder with a binder. This mixture is then injected into a mold [4]. In PIM it is desirable that the powder-binder mixture has a high enough particle content such that there is particle to particle contact after the mold is filled. The binder provides handling strength for the shaped component and is subsequently removed via a thermal, solvent or catalytic process. Following this debinding step, the second primary element of P/M, sintering, is used to achieve densification and desired component design properties. The other major forming practice is cold consolidation pressing. This technique relies upon the application of an external force or stress to mechanically bond the powder. Again, the fluid character of the powder permits the filling of a component shaped mold. The external stress deforms the powder particles against one another and therefore creates particle to particle interlocks and cold welded bonds [5-8]. In this technique, it is these cold bonds that provide the handling strength. The external stress provides a high degree of densification from the initial loose powder. Improved properties and possible further densification occurs during the subsequent sintering step.

As mentioned previously, sintering is a thermally activated process. Typical sintering temperatures are well in excess of one half the absolute melting temperatures [2]. Many powder systems are sintered at nearly 80% of the absolute melting temperature and

often involve formation of a liquid phase [2,9]. It is the thermal nature of sintering that presents one of the potential limitations of P/M. Processing at such high temperatures can cause parts to permanently deform or warp out of tolerance or, in the worse case, cause complete component failure through cracks [2,10-23]. Figure 2.1 shows just such process failures in a copper split bolt, a titanium trigger guard and a stainless steel microelectronics package which were warped during sintering. Also shown in this figure is a successfully sintered (flat) microelectronics package for comparison.

2.1 Physical Response to Sintering

Preventing these types of component defects often requires an iterative redesign to either the “green” component, or more often the sintering thermal cycle. To save the time and cost associated with this sort of trial and error design, many efforts have focused on better understanding the physical responses to the thermal process of sintering. Responses include dimensional variations, the generation of internal stress, and the development of macroscopic material properties.

2.2 Dimensional Variation

Dimensional variation of P/M components is the most commonly used monitor of sintering [2]. Depending on the powder and the specific P/M process, dimensions can decrease (shrink) or increase (swell). It is customary to express dimensional variation as a percent shrinkage or swelling where the change (ΔL) is divided by the original length (L_0). Also based on the powder and process, $\Delta L/L_0$ ranges between less than 0.1% for pressed

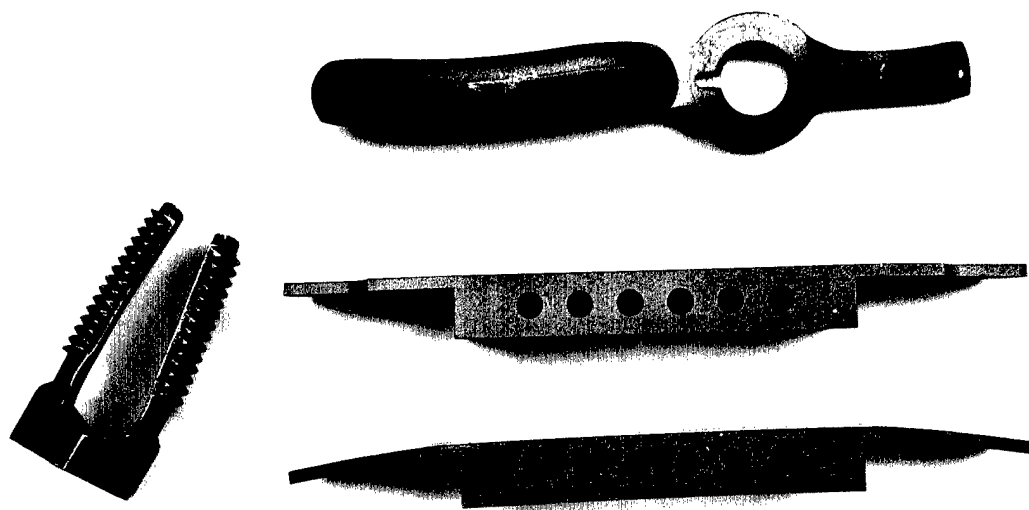


Figure 2.1: A copper split bolt, a titanium trigger guard and a stainless steel microelectronics package which were warped during sintering. Also shown in this figure is a successfully sintered (flat) microelectronics package for comparison (photo courtesy of J. Thomas).

parts to nearly 30% for PIM [4]. For obvious reasons, design of precision P/M components requires an awareness of all dimensional changes in response to sintering. Shrinkage also provides an effective means to monitor the progress of bulk transport sintering mechanisms, which tend to move particles closer together, without having to microscopically measure individual particles. In production P/M process design it is often sufficient to measure shrinkage or swelling (negative shrinkage) directly by comparing the dimensions before and after the part is sintered. On the other hand, research and development requires precise *in situ* dimensional response during the sintering cycle. These *in situ* measurements can be obtained using dilatometry or most recently using high temperature video imaging techniques. The later of these two techniques is particularly useful to simultaneously determine shrinkage in two dimensions. As a process control, shrinkage information must be obtained in all critical component dimensions to determine the degree of isotropy. Components that have undergone anisotropic shrinkage are said to have experienced distortion.

2.2.1 Dilatometry

Direct *in situ* shrinkage ($\Delta L/L_0$) and shrinkage rate determinations in one direction are accomplished using a dilatometer during the sintering cycle. Configuration, calibration and operation of this device is fully detailed in Section 3.3 and shown in Figure 3.6. These measurements are often the first step of P/M research and manufacturing development. The reason is simply that shrinkage (or lack there of) is frequently the key property to monitor the success of a sintering process [1, 24-25]. Vollertsen and Geiger [24]

concluded linear shrinkage during the sintering cycle, as determined by dilatometry, is the primary source of nominal component dimensional deviation during the entire P/M process. Bocchini [25] used dilatometry to demonstrate the dominance of compacting pressure on dimensional control during sintering of pressed unalloyed ferrous components. These data were also used to support the conclusion that alloying elements cause a further loss of precision in the sintered components.

Dowson [26] used published dilatometric results to demonstrate the sintering shrinkage difference between sintering prealloyed 90Cu-10wt.%Sn bronze powder versus the same percentage mix of elemental copper and tin powders. According to these data, prealloyed powder exhibited little dimensional change until approximately 740°C where it begins to shrink. Shrinkage at this point was from sinter densification due to bulk diffusion events. The elemental mix however exhibited a steady swelling starting at 500°C with a relatively large increase in swelling rate slightly below 800°C. These swelling data were due to the formation of a tin-rich liquid which rapidly diffuses into the copper particles.

Another application of dilatometry was by German [27] to verify the supersolidus liquid phase sintering (SLPS) model of Liu, Tandon and German [28,29]. This type of sintering uses prealloyed powders heated to between the liquidus and solidus. The liquid forms inside the particles resulting in particle disintegration and a capillary force acting on the mushy particle-liquid mixture. The capillary force acting on the mushy particle mixture results in very rapid densification. Such a technique is also known to produce a high density fine grain sintered structure [2, 30]. German used dilatometer measurements

of bronze, nickel and stainless steel alloys to verify the densification predictions of his model. These data demonstrated excellent correlation with the SLPS model for a wide range of materials and as a consequence proved the value of the model predictions.

Breitkreutz and Haedecke [31, 32] used dilatometry to determine the activation energy in a silver as well as a bronze-copper powder. Measurements were taken from cyclic heating and cooling going to progressively higher (25°C each cycle) temperatures. Although the presentation of their work was not mathematically rigorous enough to verify the result, they claim the procedure permits the identification of two separate activation energies for these powders. Grain boundary and volume diffusion activation energies for the silver powder were shown to be in good agreement with diffusion test results. For the copper-bronze powder mixture, an activation energy was identified for the swelling event of tin migration and the higher temperature shrinkage event of copper transport. Again both agreed well with literature values obtained from diffusion tests. The potential consequence of the work is it provides an alternative approach to activation energy determinations for sintering models.

Measurements of sintering shrinkage such as those just discussed involve the use of the traditional dilatometer. The drawback of this device is that, however well designed, it is a direct contact form of measurement that can potentially impact the sintering kinetics and therefore the measurement itself. Indeed, in one study by Cai, Messing, and Green [33] the force of the dilatometer probe was cyclically varied as a means of measuring the mechanical response of a powder compact. An alternative is the noncontact technique of ultrasonic measurements made possible by laser pulse excitation and interferometric

reception. Dawson *et al.* [34] employed such a technique to monitor the densification of iron compacts. They claimed laser ultrasonics is more sensitive and provides information about actual particle bonding as opposed to just direct shrinkage information. Their results showed good agreement with dilatometry results for the same powder. They report repeatability difficulties however, which they attribute to increased sensitivity to process variables. Such a method does require significantly more data reduction and assumptions to deduce actual material properties. Ultrasonic measurements are based on sonic velocity through media which in turn is dependent on the media density and stiffness properties [35]. Therefore, the most obvious assumption that needs to be made before the data can be reconciled into meaningful properties is the evolving relation between the density and stiffness of the sintering media. Until these relationships are better understood, a minimum step is usually to correlate the ultrasonic data with that of the same P/M system from the more conventional dilatometer source.

2.2.2 Video Imaging

As stated previously, simultaneous *in situ* shrinkage measurements in more than one direction are invaluable to determine the isotropy of the sintering process. Several techniques using enhanced charged couple device (CCD) camera systems have successfully measured two dimensional shrinkage and warping during various P/M thermal processes. As with the use of laser ultrasonics, these techniques are completely noncontact and therefore cannot impact the sintering kinetics or the shrinkage measurement.

Yoel, Miller and Olson [17-19] used a far field microscope mounted to a CCD camera in an attempt to image vacuum debinding and sintering of 17-4PH stainless steel powder injection molded (PIM) parts. The sample was illuminated with what was described as a "high intensity source". At debinding temperatures up through 220°C they reported 5 μm resolution and sufficient image quality to qualitatively observe the surface morphology during binder removal. Poor image resolution at higher temperatures due to insufficient illumination made microscopic observations at sinter temperatures impractical. However, using an unmagnified CCD camera with various combinations of infrared filters and high intensity illuminators, they were able to macroscopically gauge typical P/M parts during sintering. Although image quality again deteriorated at higher temperatures and image analysis required considerable practice, quantitative shrinkage measurements were possible. On 17-4PH parts sintered to 1200°C at a heating rate of 5°C/min, their observations indicated the greatest shrinkage occurred early in the heating ramp and during post-sinter cooling rather than during the isothermal sinter soak.

Mizuno, Kawasaki and Watanabe [20-23] used a similar combination of high illumination (xenon lamp) and optical (blue) filters. However, they added a computer work station based video image enhancement and analysis system. In published results thus far, the total system has achieved resolutions of better than 30 μm through maximum sintering temperatures of 1300°C. They have successfully applied the system to several P/M processes. Measurements have been made of several test specimens as well as actual P/M components made by injection molding 304L stainless steel (SS304) [21-22]. These data showed the highest shrinkage takes place early in the sintering cycle due to poor

thermal conductivity caused by high porosity. The technology was further applied to other P/M problems such as compaction gradients in carbonyl nickel [20] and functional material gradients in compacted layers of SS304 and partially stabilized zirconia (PZT) [23]. For measurements in both of these studies they expanded the capability of the image analyzer to include a digital correlation system. This system precisely maps the distribution of shrinkage anisotropy (distortion) in compacts sintered up to 1300°C. Their overall results also indicated that most deformation occurred *during* the ramp to maximum temperature.

A further enhancement of CCD camera technology is the application of the Syncro Vision® video imaging system to P/M sintering. This system, schematically depicted in Figure 2.2, uses electronic as well as optical filters to mask all source light. This eliminates any difficulty in trying to record a high resolution image through excessive high temperature infrared emissions. The sintering part is then illuminated from a focused xenon strobe whose flash is synchronized with the shuttering of the CCD camera. The operation of the system is further described by Lal, Shoales and German [12] in published work on the thermal characterization of prealloyed 90Cu-10wt.%Sn bronze powder compacts. Recorded measurements of rectangular and cylindrical compacts provided detailed histories of distortion evolution during 5°C/min heating ramps from room temperature to 975°C. Captured video images of bronze transverse rupture bars, fabricated as described in Section 3.1.5, for selected temperatures are shown in Figure 2.3. They also found excellent correlation between video shrinkage measurement in one direction and measurements from the dilatometer described in Section 3.3. This

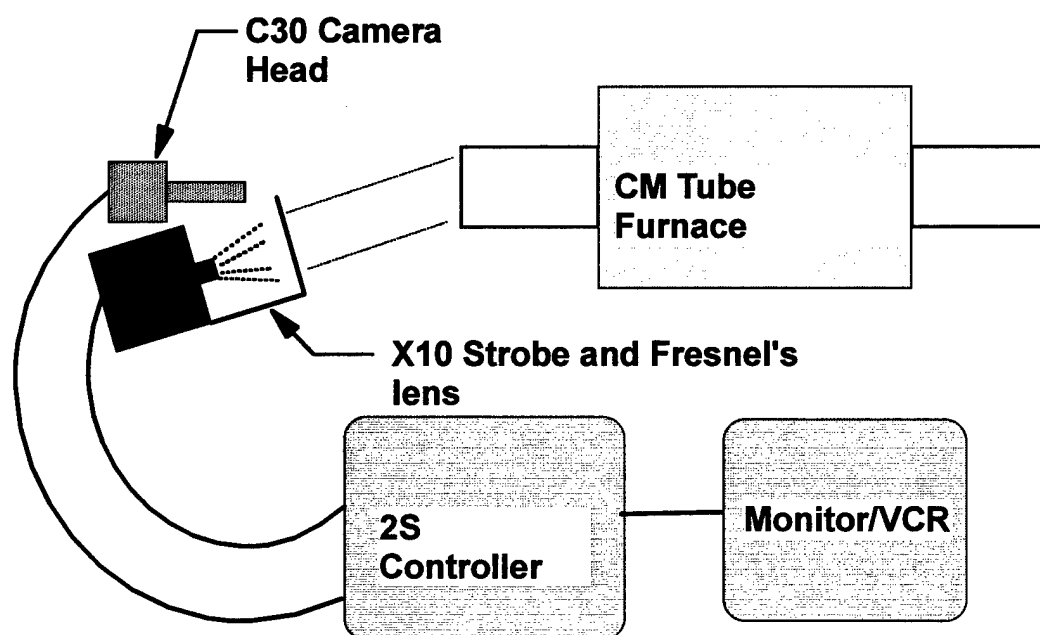


Figure 2.2: Schematic of SyncroVision[®] model 2SCOX11 diagnostic video camera system as installed on CM horizontal tube furnace.

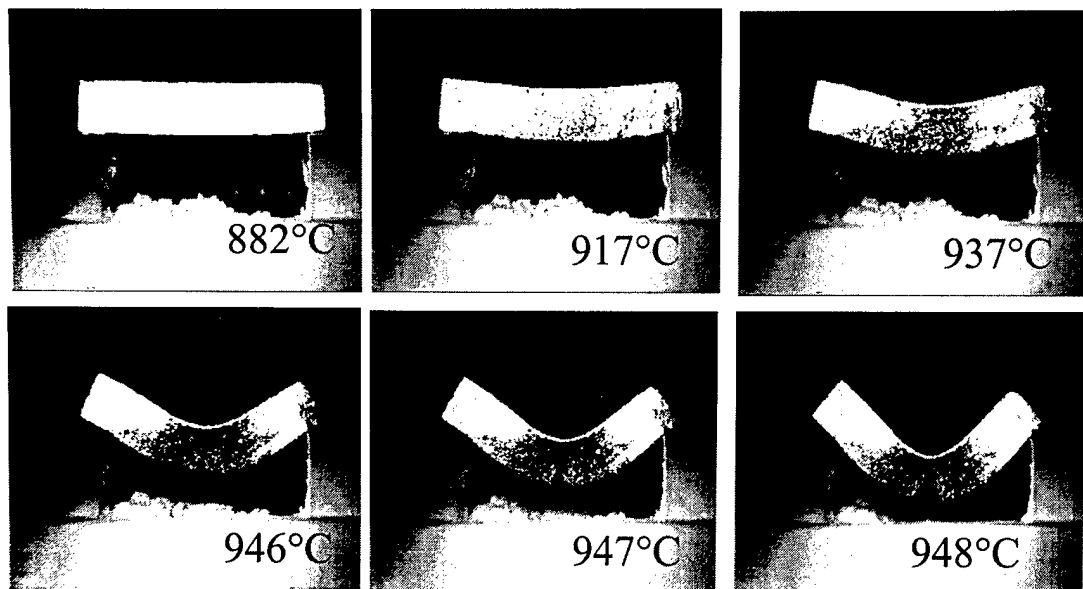


Figure 2.3: Captured video images obtained using the SyncroVision[®] video imaging system showing bronze transverse rupture bar at various temperatures. The bar was supported at two ends with a span of 25 mm. Heating rate was 5°C/min in an argon atmosphere in a CM horizontal tube furnace [12].

comparison between the contact dilatometric and the noncontact video measurements is shown in Figure 2.4. These measurements agreed with the earlier result of Dowson that significant shrinkage begins somewhat below 800°C.

2.3 Sintering Stress

The creation of bonds between particles requires the growth of the “necks” at the points of contact. Such growth requires transport of mass from the particle surface or particle interior to the neck region. It is the sintering stress that provides the driving force for mass transport. As outlined by German [1,2], the Laplace equation expresses the stress of a curved surface. Considering a curved surface described by two principal radii (R_1 and R_2 in units of m) as depicted in Figure 2.5, the Laplace equation for stress in Pa (σ) is shown by Equation 2.1;

$$\sigma = \gamma \left(\frac{1}{R_1} + \frac{1}{R_2} \right) \quad (2.1)$$

where γ is known as the surface energy in units of J/m². Considering the simplistic example of the initial stage sintering of spherical particles. The point of contact between spheres, as depicted in Figure 2.6a, represents a highly curved surface as compared to the spherical surface away from the neck. This causes a stress gradient that is responsible for the flow of mass to the neck region. The growth of the neck, as depicted in Figures 2.6b and 2.6c, corresponds to a reduction of surface curvature at the neck. This reduction therefore relaxes the driving force and the process slows. In later stages, it is the same

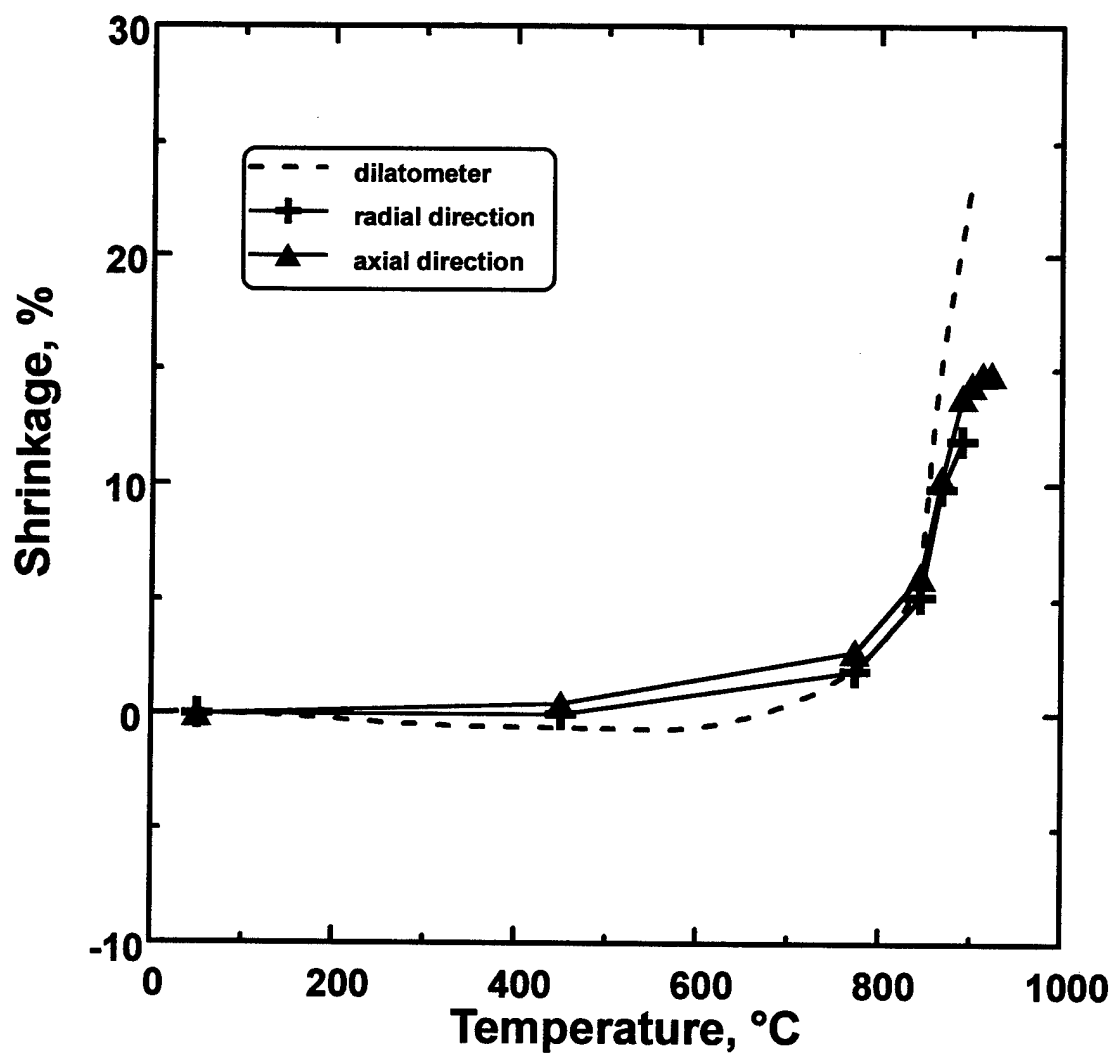


Figure 2.4: Plot comparing axial shrinkage for prealloyed 90Cu-10wt.%Sn bronze powder compact as measured by conventional contact dilatometry and noncontact SyncroVision® video imaging system. Both measurements for samples heated at 5°C/min in an argon atmosphere [12].

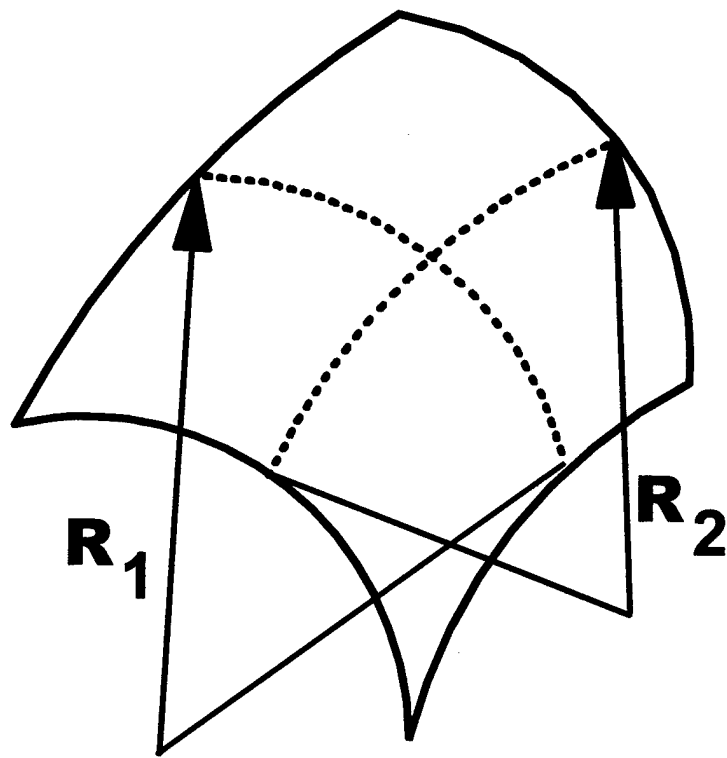


Figure 2.5: The curvature at any point on a curve surface described by two principal radii given as R_1 and R_2 .

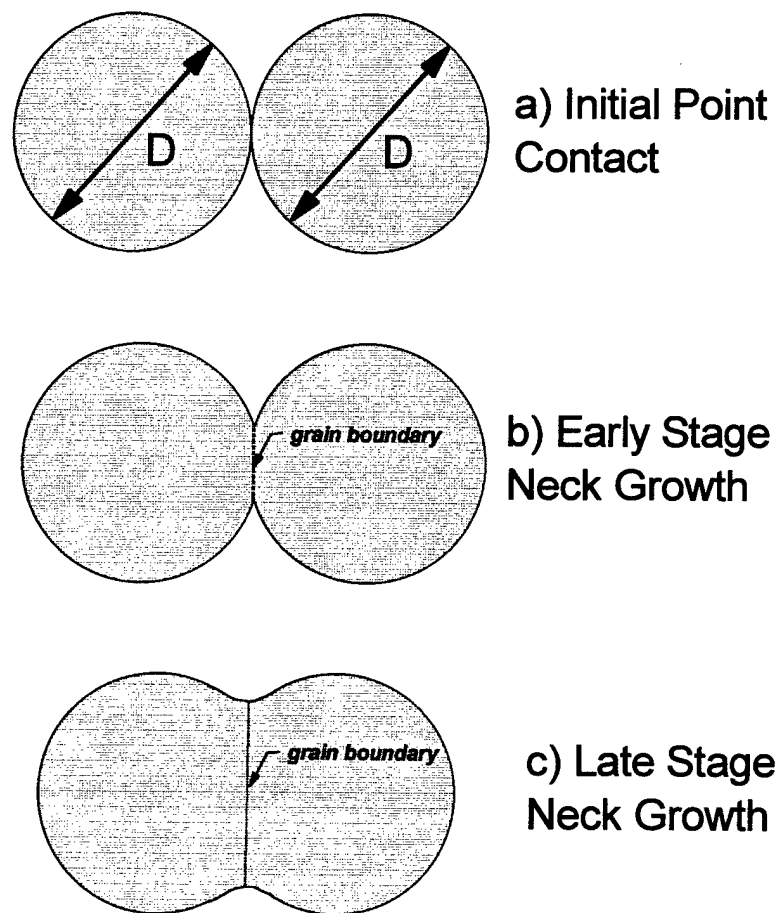


Figure 2.6: Sintering of two spheres showing the development of the interparticle bond starting with a) initial point contact and progressing from b) early stage neck growth to c) late stage neck growth.

pore curvature driven Laplacean sintering stress which can lead to the removal or coalescence of those pores. Overall a reduction of surface energy is the driving force of nature behind sintering.

Many sintering models use just such a driving force or sintering stress between two particles extended to a whole system of particles. Several attempts to measure and model this sintering stress have been published. Aigeltinger [36] developed a model that precisely described measurements of sintering stress taken earlier by Gregg and Rhines [37]. Their experiments applied a tensile stress to sintering 12, 30 and 48 μm copper powder compacts through temperatures up to 1050°C. Stress was increased at each temperature until the shrinkage rate was reduced to zero. The model and experiments both concluded this sintering stress increases dramatically after the initial sintering stage of interparticle neck growth is complete. The maximum measured value was 200 kPa for the 12 μm powder.

Several studies have concluded that inhomogeneities in the powder mixture will locally alter the stress field. Tseng and Funkenbusch [38] investigated the effect of inclusions by mixing manufactured hard agglomerated particles into an otherwise homogeneous zinc oxide powder. Experimental measurements and subsequent modeling indicated what they referred to as a “back stress” in the local area of the hard agglomerates. This back stress was sufficient to overcome the sintering stress at earlier stages of densification than otherwise experienced by the pure homogeneous powder. They also concluded that agglomerate size did not play a significant role compared to the

volume percent of inclusions present. Increasing the volume percent from 5 to 20% decreased overall compact densification by over 10%.

German [39] investigated another type of inhomogeneity and its apparent influence on sintering stress when he modeled the sintered density of bimodal powder mixtures. Bimodal powder mixture were thought attractive due to higher packing and therefore green densities. German's model discovered however, that although smaller diameter particles have higher curvature and therefore higher sintering stress, there is a stress interaction between the large and small particles that decreases the overall density of the sintered mixture. His model, verified by comparison to existing experimental results, predicts a decreased sinter density with decreased mixture homogeneity.

Investigations by Lenel *et al.* [40-42] postulated, and later verified by experiment, the presence of other sintering stress besides those explained by surface tension. They conducted their experiments on loose and compacted copper powder specimens. Powder shapes included both irregularly shaped electrolytic and flake. Prior to their work, shrinkage in powder compacts had been attributed to the flattening of pores to disc shapes oriented transverse to the pressing direction. These discs would then provide higher driving force at the edges than the center and therefore provide for greater shrinkage in the transverse than the axial direction. When green specimens were cut in both radial and transverse directions, there was no visible pattern of orientation to the disc shape pores. Further experiments applied an increasing external stress and used dilatometry measurements at each stress level to detect the temperature of shrinkage onset. When repeating these measurements for samples compacted at different pressures, they found

more stress was needed to achieve similar onset temperature for specimens compacted at higher pressures. Since specimens pressed at higher pressures would have higher residual stresses, they concluded residual stress and externally applied stress cause shrinkage in the low-temperature range (up to 400°C). This effect was independent of whether the measurements were made in the radial or axial direction. In addition to residual stress, they concluded gravity is an important contribution to sintering stress. Loose powder samples of irregular shaped powder were vibration settled in a cylindrical graphite mold and sintered for one hour at 930°C in pure hydrogen. First samples were sintered with the axial direction oriented vertically and then samples were covered and sintered on their sides (axial direction oriented horizontally). In both cases shrinkage in the direction oriented with gravity was 15% greater than the other direction. It was further discovered that gravity is an important stress in later stage sintering of compacted parts. Compacts of the irregularly shaped powder were sintered at 925°C for one hour in pure hydrogen using various support configurations. Results showed more than 4% radial dimension variation between the top and bottom of 50 mm high specimens. This sort of anisotropic shrinkage of course represents distortion in the sintered part as discussed in the previous section.

2.4 Development of Properties

Work cited in Section 2.2 has made great progress describing the *in situ* shrinkage and distortion. Citations of Section 2.3 present some of the possible sources of stress that could lead to such dimensional variations. However, these categories of research say little

of what this response means in terms of sintered component failure. Accepted theories in the study of strength of materials provide convenient definitions of failure [43,44].

Permanent deformation is said to occur when the applied stress exceeds the material's yield strength. A macroscopic material separation or crack occurs when the applied stress exceeds the material's ultimate strength. In general the sum of all sources of stress in a mechanical system must not exceed the allowable strength. The stiffness (modulus) describes the proportionality of normalized deformation (strain) to the applied stress.

Much progress has also been made in modeling sintering kinetics and heat transport during sintering [2]. But we are still unable to predict the process conditions that result in warpage or cracking. Applying the above failure definitions to P/M component sintering, if the *in situ* distortion in response to a sintering stress exceeds the yield strength of the component, then the distortion will exist in the final sintered part. Alternatively, if the sintering stress exceeds the ultimate strength of the component, then a crack will exist the final sintered part. Thus, adequate modeling of the *in situ* response must also include the evolution of the compact's mechanical properties. Of the mechanical properties that evolve during sintering, strength and stiffness are most important to resist component failures

Evolution of elastic modulus was indirectly investigated by Martin and Rosen [45]. In this work they used ultrasonic velocity as a means of measuring surface area reduction in sintering zinc oxide. Their work showed a significant increase in ultrasonic velocity prior to any change in density during the ramp to sintering temperature. Since ultrasonic velocity is proportional to elastic modulus and density [35], this result infers the evolution

of the modulus during sintering. When it comes to strength, the literature is full of examples of strength as a result of sintering at various temperatures. However, prior to this research, there was no published work with regard to strength evolution *during* sintering. The present work investigates the *in situ* strength evolution of a sintering powder compact. Such knowledge is fundamental to determining sintering cycles that minimize distortion and defects. Given a complete understanding of the physical response of a sintering compact, intelligent choices can be made for P/M thermal cycles.

2.5 Modeling Concept

The final goal of this research will be to develop a constitutive model for the strength evolution of a P/M compact as it sinters. Many mechanisms are at work leading to the final sintered strength of P/M components. The research will require the measurement of *in situ* strength during sintering to help identify the dominate mechanisms. The following sections review the expected sources of *in situ* strength during sintering.

2.5.1 Green Strength

The purpose of the compaction step, as discussed previously in this chapter, is to provide shaping, initial densification, and handling strength for the green part prior to the sintering step [46]. Green strength can therefore be considered the input strength to the whole process of strength evolution. This strength depends on the bulk material properties, the powder shape, and the compaction pressure. During compaction there is both elastic and plastic (permanent) deformation. The materials with the greatest elastic

springback, usually exhibit the lowest strength [5]. Springback is also responsible for creating additional void space, thereby lowering compact density, and possibly creating crack initiation sites. Additionally, very hard powder materials are more resistant to plastic deformation.

Overall, it is the size and quality of contact areas between powder particles and the green fractional density that determines the compact's strength [5,6,11,46]. The quality of these particle contact areas arises from particle shape, bulk material properties, and if necessary, the addition of a binder phase. Spherical particles must be deformed sufficiently to increase the area beyond the simple point contacts found in ideal spherical packing. On the other hand, a compacted irregularly shaped powder is further strengthened by interlocks of particle irregularities. If the material is very hard it will be resistant to plastic deformation. If spherical particles are also hard, plastic deformation from compaction will not produce sufficient green strength. In this case, one option is to increase the green strength by the addition of a removable binder phase. The binder phase is the normal source of green strength in the PIM process discussed previously in this chapter. As discussed there, it is added to the powder prior to shaping and removed during or prior to sintering. Binder removal can be a thermal, catalytic, or chemical process. In the absence of binder, high green strength requires soft irregular particles. Addition of binder makes P/M components from hard spherical powders practical.

Several attempts to model the compact's green strength versus the various inputs to the compaction process. German [5] has cataloged many these models that relate apparent density, compacted density and compaction parameters to the green strength.

This strength is usually determined via direct measurement since its value is ultimately one of the key measures of success for the compaction step.

2.5.2 Annealing

As the temperature increases during the sintering cycle, some of the green strength is lost due to the annealing of the interparticle cold welds as well as the bulk material cold working. Transformation to the fully annealed condition is both time and temperature dependent. Reed-Hill and Abbaschian [47] suggest the time constant of annealing follows an Arrhenius type law. This form is easily implemented in the model for the simple case of constant heating rate. Such implementation would only require a temperature dependent exponential decay of the annealed portion of green strength. Parameters for this model would be determined from strength measurements at temperature where the green compact undergoes recrystallization. Measurements would be made for the applicable heating rate to determine the degree of transformation as well as recrystallization onset and completion temperatures. Measurements of pure copper and various copper alloys cited by Cahn [48] suggested recrystallization for bronze at typical heating rates would be complete by at most 500°C. Belk *et al.* [49] investigated annealing of cold worked tungsten-copper composites. They found the copper phase fully recrystallized after one hour in air at 400°C. Their results also showed minimal influence of degree of cold work upon the onset and completion temperatures.

Time and temperature effects are required by the more sophisticated model to replicate true sintering cycles which include a variety of heating rates as well as isothermal

holds. Therefore a kinetic model of annealing is expected for the present work. The Johnson-Mehl-Avrami (JMA) kinetic equation was successfully used by Nath *et al.* [50] to model nonisothermal annealing in low carbon steels. Wang *et al.* [51] used the JMA equation to model transformation rates during the annealing of nickel. Shercliff and Ashby [52] used an empirically derived model (what they referred to as process modeling) with an experimentally determined equivalent activation energy to predict the strength of annealed aluminum alloys. The implications of annealing is that, depending on the onset of sintering (also time and temperature dependent), the P/M component could actually get weaker than the green state before it sinter strengthens.

2.5.3 Sinter Strengthening

The strengthening of a powder compact is fundamentally dependent on interparticle bonding via diffusion events. Sintering parameters include densification, surface area reduction, neck formation and growth, and decrease in porosity. At the first level, the increase in strength can be related to a decrease in porosity. The most obvious impact of porosity on sintered strength, as illustrated in Figure 2.7, is the corresponding decrease in cross section available for the distribution of applied loads and eased crack propagation path. Also illustrated in Figure 2.7, are stress concentrations as a result of the porosity voids in the bulk material. Haynes [53] has cataloged many proposed relationships between density or porosity and sintered strength. He also went on to relate sintered strength, specifically transverse rupture strength, to the square of the neck size

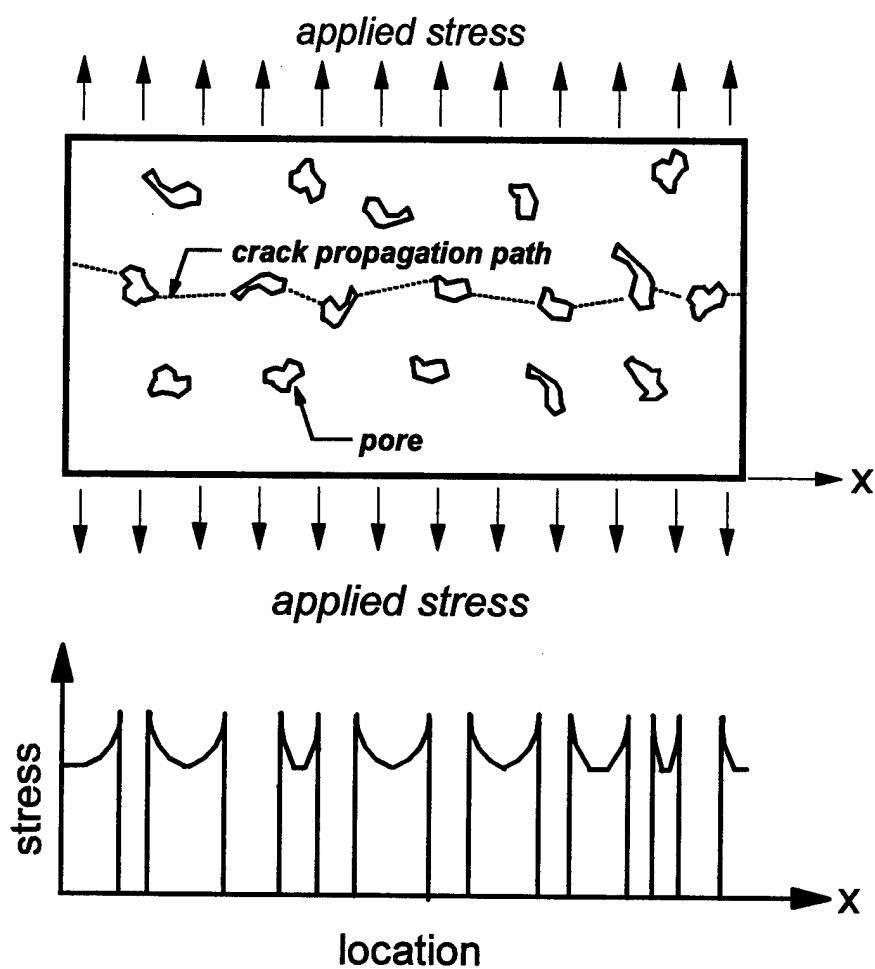


Figure 2.7: Schematic of stress applied to a porous sintered material illustrating decrease of cross section, crack propagation along pores and stress concentrations at the pores.

ratio. Nyce and Schaffer [54] demonstrated the key parameter is the area of the interparticle bond.

In the later stages of sintering, the bulk material can experience a strength loss due to grain growth. This relationship between grain size and yield stress was determined by Hall [55] and Petch [56] and is given by Equation 2.2;

$$\sigma \sim \frac{1}{\sqrt{G}} \quad (2.2)$$

where σ is the yield stress and G is the grain size. Later investigations by Armstrong *et al.* [57] on copper, brass and other polycrystalline metals concluded this relation applies to strengths beyond the yield point. The same conclusion was made by Hansen and Ralph [58] while investigating the behavior of copper.

Modeling of all these contributions to sinter strengthening could be treated individually or strength could be considered one of the possible response outcomes to the sintering process. In this case, such a response could be modeled phenomenologically as suggested by Su and Johnson [59,60]. Their Master Sintering Curve (MSC) approach lumps all sources of a particular thermally activated, time dependent process into a single master parameter. Experimentally determined response data are used to empirically determine an “equivalent activation energy” which is the only adjustable parameter in the model. This modeling technique is very similar to that used by Shercliff and Ashby [52] as discussed in Section 2.5.2.

2.5.4 Thermal Softening

The most significant detriment to strength during sintering is thermal softening of the bulk material. There are extensive data cataloged for material properties as a function of service temperature [61,62]. These temperature dependent data are determined by tests of wrought forms and typically for temperatures far below normal sintering values. Most of the models for thermal softening depend on strain rate effects. Dieter [63] gives a simplified model that applies to constant strain and strain rate that, as discussed for annealing in Section 2.5.2, follows an Arrhenius type law. The thermal softening character of the strength of sintered material could also be empirically modeled. Data for such a model would be available using the same device and technique required to investigate the *in situ* property of the current research.

2.6 Statement of Hypothesis

P/M process design requires knowledge relating compact sintering stress to the mechanisms of sintering to be balanced with a like knowledge of compact strength development. The proposed work will define a minimum series of tests that will in turn define the key parameters of a new *in situ* strength evolution model. By defining the path a compact takes from green to fully sintered strength, this phenomenological model will predict dangerous combinations of temperature, heating rate, and time that could lead to component failure. Manufacturing savings will be realized by avoiding the current practice of trial and error sintering process design. The minimum set of tests will include the effects of green strength, annealing, sintering, and thermal softening. As a major

consequence of the current work, this new model will become part of a larger finite element model to provide total P/M process design. This total package will include; die or mold shape, green part specifications, and optimum debinding and/or sintering process requirements.

Chapter 3

Experimental Methods

This chapter outlines the methods used to obtain the experimental data required for the modeling concept outlined Section 2.5. The sections of this chapter are divided into categories according to the type of measurement made and the equipment used. Each section or subsection includes a description of the equipment and, where appropriate, its operating principles. Details of the calibration procedures as well as an assessment of measurement uncertainty are also provided. Finally, the specific procedure or test protocols used in this research are listed for each measurement.

3.1 *In situ* Strength Measurement

The primary measurement required by this research was *in situ* strength as it evolved during the sintering thermal cycle. This required a comparative measure of strength to be precisely determined for a powder compact at any instant during the sintering cycle. The primary limitation on this determination was that the test measurement itself could not alter the sintering trajectory of the compact and therefore the test outcome. Additional requirements, to account for the variation of sintering thermal cycles, was that the strength property must be measurable under different temperatures, heating rates, and atmospheres. The atmosphere requirement implied the specimen must be constrained to a test region within a sealed chamber prior to the test.

3.1.1 Selection of Strength Property

Several strength test configurations were considered. The tensile test is the most fundamental form of mechanical test [63]. Strength is easily characterized by the tensile test due to a well established, standardized test protocol and a uniform stress field in the test specimen [64]. The primary limitation for the present work was the requirement to continuously grip the sintering powder compacts prior to and during the test. The force applied by the grips to the delicate green parts introduces the possibility of pretest damage which could act as an artificial failure initiation site. In addition, the constraint translates into an externally applied force which would certainly alter the sintering of the compact. Finally, this test is sensitive to load eccentricities which would drive an additional level of complication into test device design and the interpretation of the results.

A ring strength test requires a ring shaped specimen to be loaded on its outer circumference between two flat surfaces [1,64,65]. This requirement to constrain a round specimen to the test area would be difficult while additionally meeting the requirement to leave the specimen undisturbed (so as not to alter the sintering trajectory) prior to testing. The test does have the advantage that failure occurs in the gage section relatively far from the load application surfaces, thus limiting their possible influence in the measurement.

The standard test for transverse rupture strength (TRS) [66] is the most widely used test to characterize the strength of green compacts. Since all P/M parts start off green, this seemed a logical test to evaluate comparative strength evolution. This test was also an ideal choice because it requires flat sided specimens to rest well supported and undisturbed prior to test. A possible disadvantage of this test was the claim by Thomas

and Rosen [67] of edge effects due to the close proximity of the supports to the mid-span load application. Direct comparisons of ring and TRS tests for WC-Co by Vandeput and Mastrantonis [68] and for alumina by Rolf and Weyand [69], however, found no appreciable difference in the quality of results between TRS and ring tests. Phadke [70] determined the linear relationship between hardness and TRS for Fe-Cu (Cu wt.% from 2 to 8). Talmage [71], Lindskog and Bocchini [72], and Dixon and Clayton [73] determined a similar relationship between hardness and tensile strength for over 25 types of sintered steels and superalloys. Comparing the quality of their results from the standpoint of dispersion and repeatability, there was no significant difference between tests of TRS or tensile strength.

3.1.2 Powder Selection

The alloy chosen for this study was a gas atomized prealloyed 90Cu-10wt.%Sn bronze. It was procured from the manufacturer, United States Bronze Powders, Inc., in a size increment designated B-409. This grade is a spherical powder and is sieved to -325 mesh (-45 μm) by the manufacturer. The choice was based on the alloy's relatively low sintering temperature and simple chemistry, and the powder's near spherical shape. Sintering practice for this powder calls for maximum temperatures between 790°C and 850°C [25,26]. Therefore the upper bound for *in situ* measurements will be 850°C.

3.1.3 Powder Characterization

Size analysis was accomplished with a Horiba LA-910 which uses the Fraunhofer and Mie principles of angular light scattering in an aqueous environment to measure particle size [1]. A suspension was made using 1 to 3 g of powder in approximately 60 ml of distilled water with 10% sodium metaphosphate. Each run produced a distribution of particle size based on equivalent spherical volumes. Increased bias would be introduced in measurements of powders with increasingly lower degrees of sphericity. The repeatability of the device was monitored via five monthly tests of a suspension made from a single lot of carbonyl iron. Additional repeatability measurements as well as a relative measure of accuracy was made using a standardized powder. Specifically, this was a -230/+325 (-63 μm /+45 μm) mesh gas atomized stainless steel. These repeatability and accuracy checks are reported by the D_{10} , D_{50} , and D_{90} sizes and their standard deviations. These data are presented in Table 3.1 for the month of the bronze measurements of this research (Jan 97) as well as the averages for the twelve preceding months. Multiple runs were performed on bronze powder suspensions until the standard deviation for the median size was under 5%.

An Arnold meter was used to determine apparent density according to the method described in ASTM Standard B703 [74] and MPIF Standard 48 [66]. This device consisted of a 2.54 ± 0.025 cm thick steel plate and a hollow brass cylindrical container. The steel plate has a 3.1664 ± 0.025 cm diameter hole which forms a 20 cm^3 cylindrical volume. The brass container was filled with powder and slid across the hole in the plate twice. The amount of powder that fell into the hole was weighed using a Denver

Table 3.1: Summary of Horiba LA-910 repeatability and calibration measurements.

Powder	Stainless Steel			Carbonyl Iron		
Cumulative Distribution Points	D ₁₀	D ₅₀	D ₉₀	D ₁₀	D ₅₀	D ₉₀
12 month average, μm	58	65	75	2	4	8
12 month SD, %	0.8	0.5	0.7	4	4	5
Jan 97 particle size, μm	60	67	76	2	4	8
Jan 97 SD, %	0.2	0.7	1.1	5	7	8

Instruments A-200DS precision electronic balance (calibrated accuracy of ± 0.0004 g) and the apparent density, ρ in g/cm^3 , was calculated using Equation 3.1;

$$\rho = \frac{M}{V} \quad (3.1)$$

where M was the mass of the powder in g and V was the 20 cm^3 volume. Total percent bias uncertainty for this measurement was calculated by considering the accumulation of bias uncertainties in both the manufacturing tolerance of the volume, as required by the Standards, and the bias uncertainty of the mass measurement. Individual absolute system uncertainties were accumulated by root mean squares weighted with their respective partial derivatives from the governing function using Equation 3.2 [75,76];

$$\frac{u_y}{y} = 100 \sqrt{\left(m_1 \frac{u_1}{x_1}\right)^2 + \left(m_2 \frac{u_2}{x_2}\right)^2 + \dots + \left(m_n \frac{u_n}{x_n}\right)^2} \quad (3.2)$$

where u_y/y is the accumulated percent uncertainty, x_1, x_2, \dots, x_n are the measured variables, m_1, m_2, \dots, m_n are the powers of these variables in the governing function, and u_1, u_2, \dots, u_n are the corresponding uncertainties. Expanding Equation 3.1 to include all the measured variables resulted in Equation 3.3;

$$\rho = \frac{4 M}{\pi L D^2} \quad (3.3)$$

where L is the thickness of the steel plate in cm, D is the diameter of its hole in cm, and M is the afore mentioned mass measurement in g. Using these dimensions and applying Equation 3.2 to Equation 3.3, the percent bias uncertainty in apparent density (B_ρ/ρ) was shown in Equation 3.4;

$$\frac{B_\rho}{\rho} = 100 \sqrt{\left(\frac{u_M}{M}\right)^2 + \left(2 \frac{u_D}{D}\right)^2 + \left(\frac{u_L}{L}\right)^2} \quad (3.4)$$

where u_M , u_D , and u_L are the bias uncertainties for M , D , and L as previously specified.

The resulting percent bias uncertainty for the apparent density measurement is 0.02%.

The measurement was repeated for 6 samplings of the bronze powder. Due to the invariant volume, the mean and standard deviation of the five mass measurements formed the basis of the entire precision uncertainty. The percent precision uncertainty (P_x/X) at a confidence level of $c\%$ was calculated using Equation 3.5 [76];

$$\frac{P_x}{X} = \frac{100}{X} t_{\alpha/2, \nu} \frac{S_x}{\sqrt{n}} \quad (c\%) \quad (3.5)$$

where X was the measurement, α was 0.10 for 90% confidence level (from $1-c/100$), n was 6 (the number of samples), ν was 5 (the degree of freedom from $n-1$), and S_x was the sample standard deviation. Values of t were found from tabulated values of the Student's t -distribution [76]. The six repeats yielded sample mean and standard deviation of 98.3 and 0.5 g, respectively, for a precision uncertainty of 0.5%. Finally, the bias (B_ρ/ρ) and

precision ($P\rho/\rho$) percent uncertainty were combined to find the total apparent density uncertainty ($U\rho/\rho$) of 0.5% using Equation 3.6.

$$\frac{U\rho}{\rho} = \sqrt{\left(\frac{B\rho}{\rho}\right)^2 + \left(\frac{P\rho}{\rho}\right)^2} \quad (3.6)$$

The Arnold meter is considered the technique that best correlates with filling die cavities during compaction operations [1].

Tap density was measured by the method described in ASTM Standard B527 [74] and MPIF Standard 46 [66]. A graduated cylinder was filled with 100 g, as measured by the previously described Denver A-200DS, of powder and tapped 3000 times using a Quantachrome Dual Autotap. The resulting tapped volume, measured by cylinder graduations in cm^3 , and the 100 g mass were used with Equation 3.1 to compute the tap density. The measured volume included a bias uncertainty, as required by Standards, of $\pm 0.2 \text{ cm}^3$. Applying Equation 3.2, in this case, directly to Equation 3.1 yields Equation 3.7 to express the percent bias uncertainty in tap density.

$$\frac{B\rho}{\rho} = 100 \sqrt{\left(\frac{u_M}{M}\right)^2 + \left(\frac{u_V}{V}\right)^2} \quad (3.7)$$

Using the measured values of mass (M) and volume (V) with their corresponding uncertainties (u_M and u_V , respectively) in Equation 3.7, the tap density percent bias uncertainty was found to be 1%. The tapped volume measurement was repeated five times yielding a sample mean and standard deviation volume of 17.7 and 0.1 cm^3 ,

respectively. Since this time the 100 g mass was invariant, the volumetric sample statistics formed the basis of the precision uncertainty. Using Equation 3.5, the percent precision uncertainty to the same 90% confidence level was found to be 0.7%. Using Equation 3.6, the percent tap density uncertainty was found to be 1.2%.

The true (pycnometer) density was determined using an Micrometrics AccuPyc 1330, which operates based on the ideal gas law. Powder was placed in a test cell with a volume (V_{TC}) of 12.0564 cm³. Both this cell and another reference cell, of known volume (V_R in cm³), were pressurized with helium. The volume of the powder (V_P in cm³) is calculated using Equation 3.8:

$$V_P = \left(\frac{P_R}{P_{TC}} - 1 \right) (V_{TC} - V_R) \quad (3.8)$$

where P_R and P_{TC} are the pressures of the reference and tests cells, respectively. Equation 3.1 was then used to calculate the true density in g/cm³ using V_P and the mass of the powder in g. Calibration was performed by first measuring the empty cell to obtain a V_P of 0.0 ± 0.001 cm³. Next the volume measurement was performed on two calibrated spheres from AccuPyc with a combined mass and volume of 93.1495 g and 6.372 cm³, respectively. The AccuPyc 1330 was adjusted to the required bias uncertainty of less than $\pm 0.05\%$. Using this volumetric bias uncertainty and the previously specified mass bias uncertainty of 0.0004 g in Equation 3.7, the percent theoretical density bias uncertainty was found to be 0.05%. For the bronze measurements, 54.55 g of powder was used and the measurement was repeated 5 times until the sample standard deviation in the volume

measurement dropped below 0.001 cm^3 . Given the single measurement of powder mass, the volume standard deviation was used in Equation 3.5 to find a total precision uncertainty of 0.1% for the measurement. Combining the precision and bias uncertainty using Equation 3.6 the total percent theoretical density uncertainty was found to be 0.1%.

Surface area (SA) measurements were made using the Coulter SA 3100. This device measures BET surface area based on nitrogen adsorption. A sample of powder was placed in a preweighed glass tube, flushed with helium, and then outgassed at 300°C for a set number of minutes under high vacuum. The sample and a reference cell were then submerged in liquid nitrogen. Helium and nitrogen pressures to the cells were adjusted to eight different nitrogen partial pressures and the volume of the nitrogen adsorbed was measured for each. The partial pressure versus volume data were plotted and the SA 3100 software performed a fit to the data and gave its correlation coefficient. The surface area was determined by the slope and intercept of this fit. Calibration of this device is accomplished by measurements of an alumina standard from Coulter with a known SA of $310 \text{ m}^2/\text{g}$. The standard was outgassed at 300°C for 60 minutes. The SA 3100 was required to measure SA of the standard to a bias uncertainty of $4.5 \text{ m}^2/\text{g}$. Calibration prior to bronze measurements for this research yielded a bias uncertainty of $2.2 \text{ m}^2/\text{g}$ or 0.7%. Per the guidelines in the Coulter manual, bronze SA measurements were performed on a 3.6 g sample that was outgassed at 300°C for 25 minutes. The correlation coefficient for the curve used to calculate SA was greater than 0.999. The precision of this fit leaves the bias uncertainty as the dominant source of measurement error.

A qualitative measure of particle shape was obtained using a Topcon ABT-32 scanning electron microscope (SEM). The SEM permitted far greater viewing magnification than optical equipment. As shown in SEM image of Figure 3.1, the as received bronze powder shapes were nodular spheroids. A summary of all other powder characteristics measured is presented in Table 3.2. The SEM was also used to obtain images of the fracture surfaces of selected TRBs after they had been tested at room temperature. Such images were used to qualitatively evaluate the degree of interparticle bonding.

3.1.4 Test Apparatus Development

All TRS measurements were obtained using a thermal tester shown in Figure 3.2. This tester, designed by the author, was developed and fabricated entirely at the P/M Lab and has become informally known as the Flaming Tensile Tester (FTT).

3.1.4.1 Configuration

The FTT supported transverse rupture bars (TRBs) on two horizontal cylindrical supports in a sealed retort. A section view of the test region is shown in Figure 3.3. The retort was constructed from Inconel 601 in four parts; cap, two support rods and chamber. The cap had a 28.6 mm ID on center hole to accept the 25.4 mm OD load ram and was sealed to the chamber via stainless steel bolts. The support rods (6.35 mm OD per MPIF Standard 41 [66]) rested in semi-cylindrical grooves in the base of the chamber and could be replaced if damaged. The sealed retort permitted the incorporation of any desired

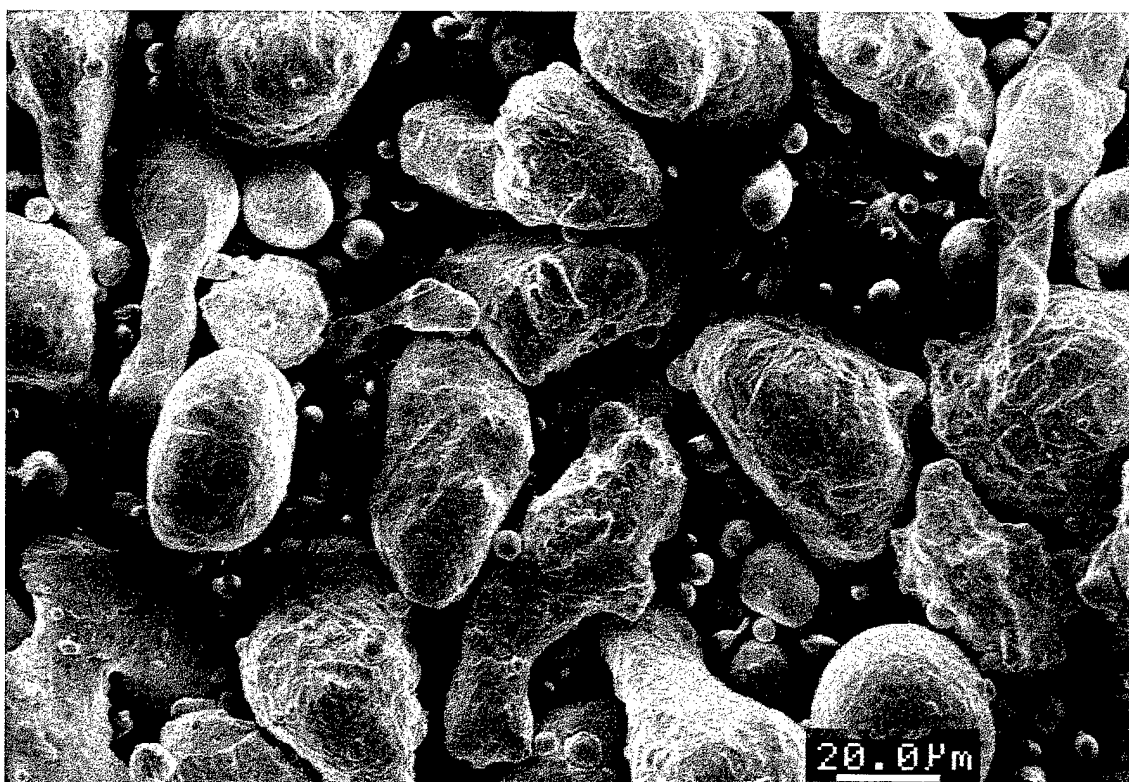


Figure 3.1: A scanning electron microscope image of the loose B-409 bronze powder.

Table 3.2: Particle characterization summary for United States Bronze Powders B-409 grade prealloyed powder.

Horiba LA-910 Particle Size Distributions	
D ₁₀ , μm	12
D ₅₀ , μm	26
D ₉₀ , μm	49
BET Measurements	
Surface Area, m^2/g	0.1
Density Measurements	
Apparent, g/cm^3	4.9
Tap, g/cm^3	5.7
Pycnometer, g/cm^3	8.91

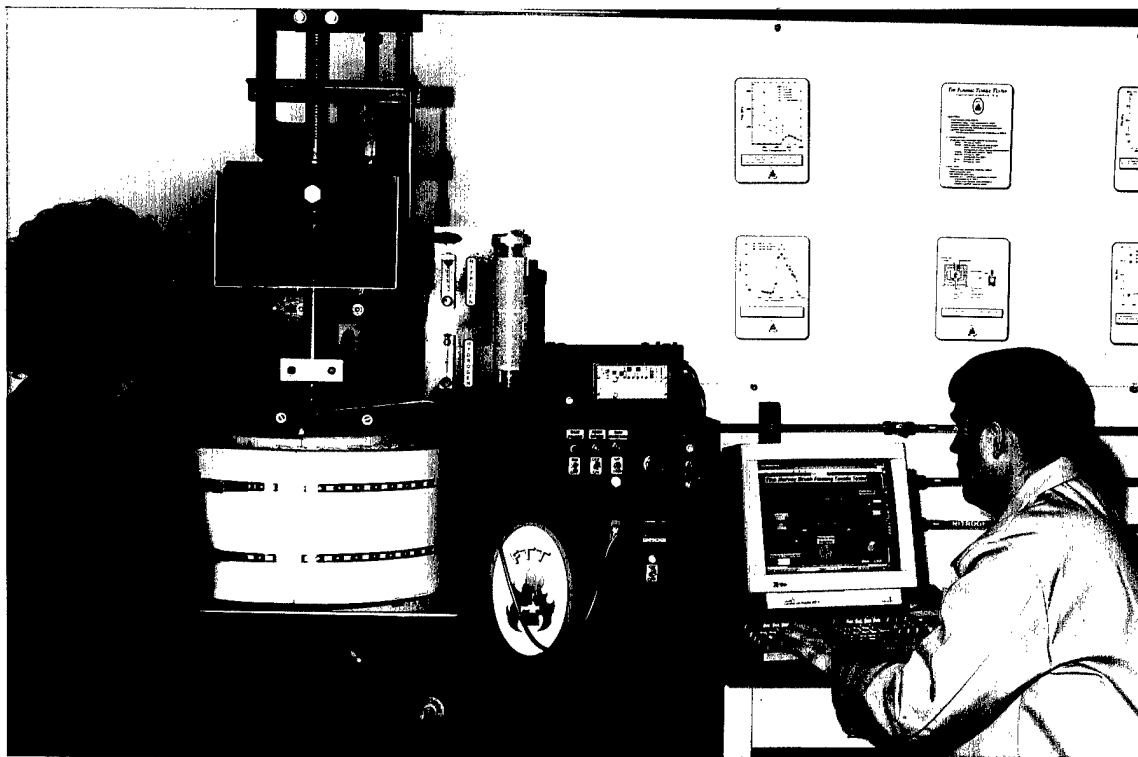


Figure 3.2: Kimberly Comstock and the author operating FTT with its PC based data acquisition system (photo courtesy of J. Thomas).

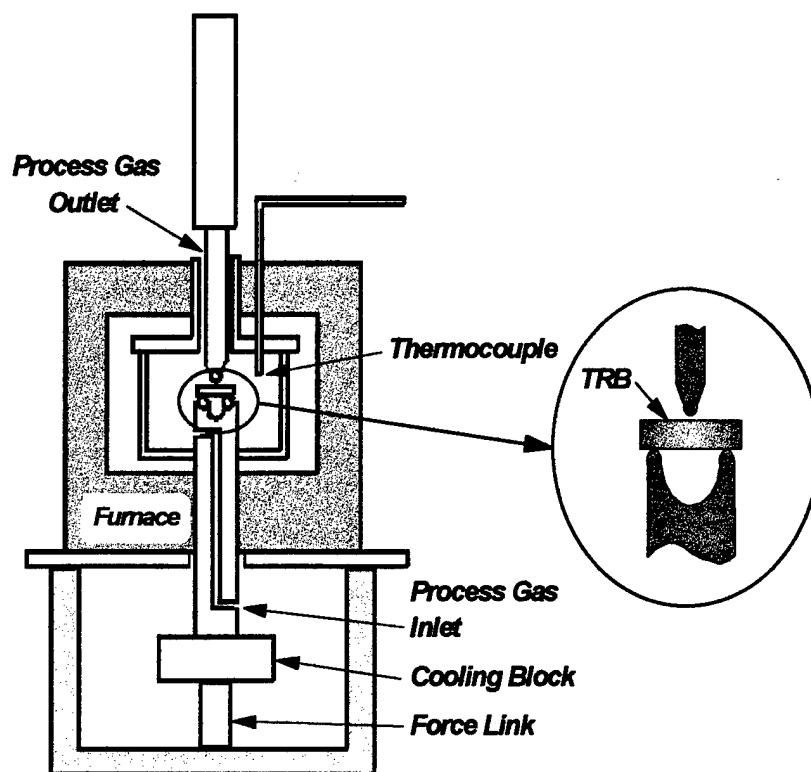


Figure 3.3: Section view of the FTT test region with close up of transverse rupture strength test 2-point supports and mid-span load ram.

process gas or combination of process gases throughout the test thermal profile. Gas was plumbed through the bottom of the chamber under the test section and exhausted through the annular clearance between the retort cap and the load ram. The load ram was machined from Inconel 601 and also included a replaceable 6.35 mm OD cylindrical rod at the bottom tip that acted as the center support. The load ram was aligned with corresponding machined scribes on the cap and ram shaft such that the axes of all three supports were parallel to within a machining tolerance of 0.5° . The displacement of the load ram and the center support is monitored via a Schaevitz GPD-121-500 linear variable displacement transducer (LVDT) and matched signal conditioner. The signal conditioner outputs a ± 20.0 V signal that is proportional to the displacement of ± 12.7 mm. Omega FL4200 series acrylic valved rotameters provided flow control of process gases. The retort is heated with two Thermacraft VFR-180-7-6 semi cylindrical resistance ribbon heating elements. Thermal control was accomplished by an Omega CN76122-PV Controller using a Nanmac Corp. K-type A8C-71-12-CT thermocouple for input. The controller permitted programming of one heating ramp with heating time and final temperature and one isothermal soak time. Additional segments could be added to any experiment by reprogramming after the initial segments were complete. At the desired test condition, the load ram was lowered at selectable constant speed to the specimen mid-span. Loading continued until the specimen ruptured. The entire retort and two-point support was supported by a Kistler Instrument Corporation type 9332A Quartz Force Link which in turn was supported by a rigid base. The force link sensed the change in axial force and output a proportional change in inductance measured in pC.

Specifically, proportionality to force measured in N was 4.04 pC/N. The inductance signal was conditioned by a Kistler type 58855A Control Monitor into a ± 10.0 V signal. The force link was provided with a NIST traceable calibrated bias uncertainty of $\pm 0.5\%$. The conditioned signals of the force link and LVDT were then recorded using LabVIEW software at 1000 Hz via National Instruments model AT-MIO-16E-10 Multifunction I/O board. This acquisition package permits a load and displacement versus time record of the entire force application event.

3.1.4.2 Operating Parameters

The FTT retort can sinter compacts in any atmosphere with thermal profiles up to 1100°C at heating rates up to 50°C/min. The maximum obtainable temperature versus time profile of the test section is shown in Figure 3.4. The atmosphere control can mix up to two different process gases with ratios controlled by calibrated flow meters.

3.1.4.3 Calibration

Prior to initial tests, the force system was checked with static weights of 50, 100, and 500 N. In all cases, the force system measurements were within the NIST documented $\pm 0.5\%$ bias uncertainty. The LVDT comes calibrated with a bias uncertainty of $\pm 0.25\%$. The calibration was checked five times using a Mitutoyo 12.7 mm gauge block and found repeatable to 0.001 mm and accurate to within less than 0.15%. The thermocouple was supplied with NIST documentation and the remainder of the temperature control system was calibrated using a NIST documented Nanmac calibration

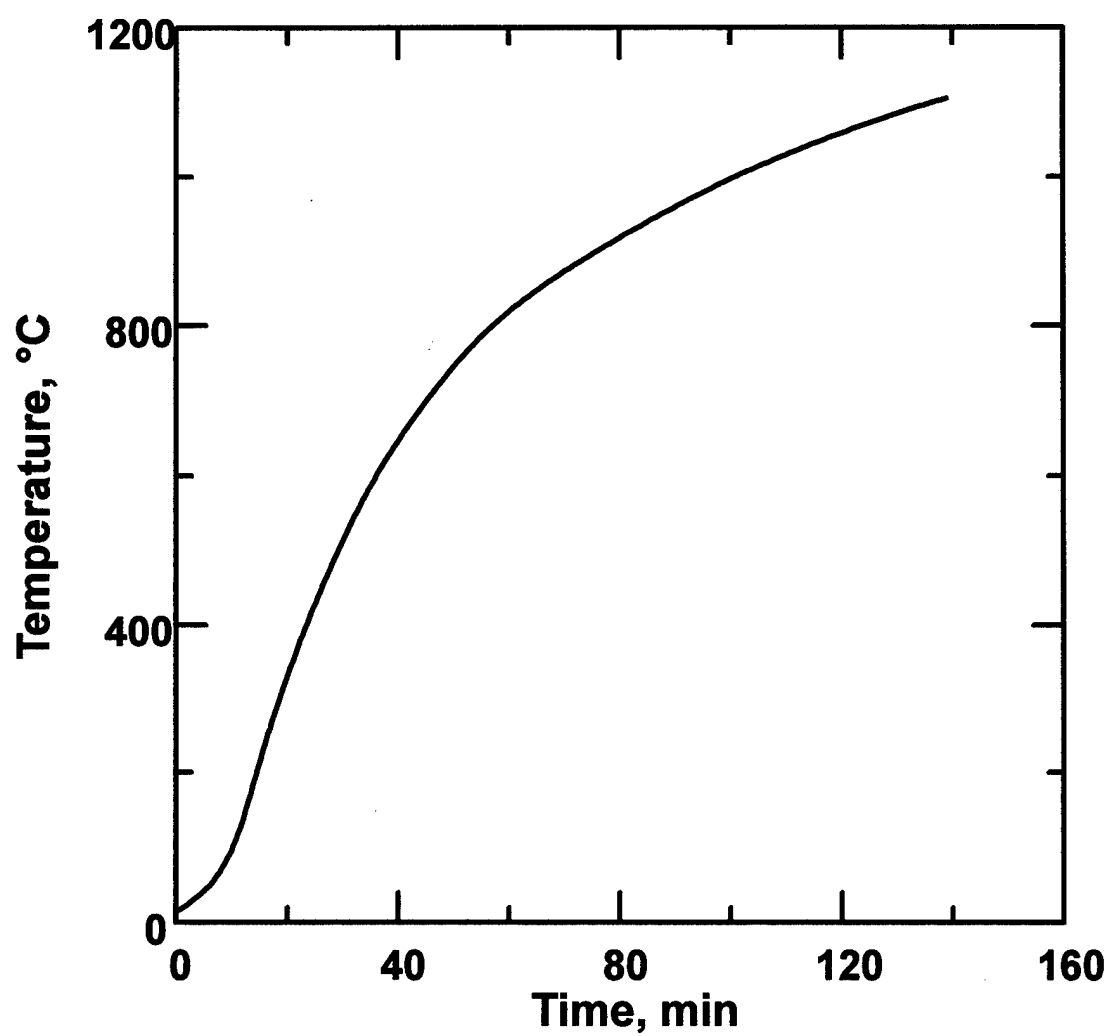


Figure 3.4: Time versus temperature of the FTT test section when operated at maximum heating rate.

unit from 0 to 1200°C. The system agreed with the calibration unit to $\pm 1^\circ\text{C}$ throughout the measurement range. For a final measure of the quality of the total test and measurement system, as well as a means of tracking its continued health, one of the test conditions was repeated throughout the test schedule. Specifically, this was the constant ramp to 600°C test temperature. In four repeats of this condition, the TRS precision uncertainty (90% confidence level) was 1.4%. The specific calculation of this uncertainty is addressed in section 3.1.6.

3.1.5 Compaction and Test Specimen Fabrication

Rectangular TRBs were die compacted per the standard [17] in a Gasbarre Products 60 ton uniaxial hydraulic research press. The projected dimensions of the TRB die was 31.7 mm by 12.7 mm for a projected area of 402.6 mm². Compaction pressure was determined by measuring the maximum load applied to the sample during compaction and dividing it by the sample's projected area, as shown in Equation 3.9;

$$P_c = \frac{F}{A} \quad (3.9)$$

where P_c was the compaction pressure in MPa, F was the maximum load in N, and A was the 402.6 mm² projected area. The powder was pressed to 550 MPa with a resulting fractional pycnometer density of approximately 0.86. Zinc stearate die wall spray was the only lubricant used. Pressure was sufficient to press test specimens to thicknesses of 6.35 \pm 0.13 mm as required by the Standard [66].

3.1.6 Test Procedures

Prior to loading in the tester, all TRB specimens were measured using calipers with a resolution of 0.005 mm and an accuracy of ± 0.0003 mm. Caliper accuracy was verified within the limits of available resolution using a Mitutoyo 12.7 mm gauge block. Each specimen was also weighed using the electronic balance described in Section 3.1.3. These measurements were used to verify the fractional green density using Equation 3.10;

$$f_G = \frac{m}{t w l \rho_T} \quad (3.10)$$

where m is the mass in g; t , w , and l are the specimen thickness, width and length, respectively in cm, and ρ_T is the powder's pycnometer density of 8.91 g/cm³ as measured in Section 3.1.3. Percent bias uncertainty was found for fractional density (B_f/f) by applying Equation 3.2 to the measured values of Equation 3.10 as shown in Equation 3.11;

$$\frac{B_f}{f} = 100 \sqrt{\left(\frac{u_m}{m}\right)^2 + \left(\frac{u_t}{t}\right)^2 + \left(\frac{u_w}{w}\right)^2 + \left(\frac{u_l}{l}\right)^2 + \left(\frac{u_{\rho}}{\rho_T}\right)^2} \quad (3.11)$$

where the bias uncertainties of m , t , w , and l were as described in previous sections for the electronic balance and the calipers. The theoretical density bias uncertainty (u_{ρ}/ρ) was 0.05%, as determined in Section 3.1.3. Using nominal values of 19.7 g, 6.35 mm, 12.7 mm, and 31.8 mm for the TRB mass and dimensions (m , t , w , and l , respectively), the resulting percent bias uncertainty for fraction density was 0.05%. As is evident by this

result, the fractional density bias uncertainty is dominated by that of the theoretical density. This is also the case for the measurement precision uncertainty. Given the level of precision used, the single direct measurement of mass and dimension carry essentially no precision uncertainty [75]. Therefore, from the result for the pycnometer density from Section 3.1.3, the percent precision uncertainty for fractional density becomes 0.1%. Combining bias and precision uncertainty as in Equation 3.6, the total fractional density uncertainty is 0.1%. The test TRB was then centered on the two supports and the retort sealed. Prior to performing any tests at temperature, the green strength of the compacted TRB was measured using the FTT at room temperature with the retort cover removed. This measurement was repeated five times and resulted in an average value of 10 MPa. Details of the TRS calculation (and the uncertainty associated with it) follow later in this section.

All *in situ* FTT tests were performed on TRBs sintered in 100% hydrogen. The first set of results were from TRS measurements at various test temperatures up to 854°C after a constant 10°C/min heating rate to that temperature. In order to explore the effect of sintering kinetics on strength, select measurements were repeated with variations to the pre-test sintering cycle. The first of these variations was simply to change the heating rate to a constant 5°C/min. Further variations included the incorporation of an isothermal hold (of up to 60 minutes) at or below the test temperature with 5, 10, or 20°C/min thermal transitions. To aid in isolation of the thermal softening behavior, measurements were performed on specimens that were sintered at a 10°C/min heating rate to preselected peak temperatures between 400 and 800°C and then cooled to lower test temperatures. These

strength data provided key insights in the development of the thermal softening portion of the *in situ* strength evolution model.

The mid-span load was applied by the FTT at a constant rate of 1 mm/s for all tests. For the span dimensions used, this resulted in a TRB bottom fiber strain rate of 0.3%/s after 1 mm of load ram travel. The peak load (P) was recorded in N and σ_{TRS} in MPa was calculated using Equation 3.12 [66];

$$\sigma_{\text{TRS}} = \frac{3 P L}{2 w t^2} \quad (3.12)$$

where L was the 2-point support span length of 25.4 mm, and w and t were the width and thickness of each specimen in mm. The elastic assumptions that are used to derive this equation require that deflection not exceed 0.25 mm (approximately 4%) [1]. Industry test practice, however, routinely ignores this requirement. This is because industry uses TRS as a comparative measure of the success in a P/M process. In fact, sintered TRBs of the most common P/M material, ferrous alloys, will exhibit deflections in excess of 2 mm. As would be expected, the higher the strength in a given TRB the greater the deflection will be prior to fracture. Since the goal of this research was to determine a comparative measure of strength evolution for sintering bronze compacts, Equation 3.12 (with its elastic assumptions intact) was used to calculate strength for all data. Similarly, the effect of strain rate was not used in the strength calculations. The rigid frame of the FTT permitted an identical constant load rate and therefore identical TRB bottom fiber strain versus time profile to be used for all measurements. Therefore, although specimens that

significantly deflected at high temperature could have experienced strain hardening, such a factor would be the same for all measurements. Since the effect would scale roughly proportionally to strength, adding this level of detail to the strength calculation would not improve knowledge of the strength evolution.

Just as with fractional density bias uncertainty, the bias uncertainty for caliper measurements was insignificant (less than 0.005%). The percent TRS bias uncertainty was therefore that of the force link or 0.5%. Also similar to the determination for fractional density, due to the single measurement nature of the dimensions in Equation 3.12, the precision uncertainty for TRS was dominated by the force link. Since measurement of TRS required a destructive test, estimation of TRS sample standard deviation was required. The dominance of the one measured value (force) in the TRS bias uncertainty calculation, made the estimation technique outlined by Kline and McClintock [75] appropriate. The technique takes the sample statistics of the four repeated measurements of TRS for the same condition discussed in Section 3.1.4 to estimate the single measurement statistics. The four tests yielded a sample mean and standard deviation of 102.6 MPa and 1.2 MPa. Using Equation 3.5, this resulted in a precision uncertainty in TRS of 1.4% (90% confidence level). Finally, combining bias and precision uncertainties as in Equation 3.6, the total percent TRS uncertainty was 1.5%.

3.2 Strength Due to Sintering

Another feature of the FTT was additional support area inside the retort, but out of the load path. This allowed for the sintering of additional “baseline” TRB specimens to

the same degree as the test specimen but subsequently cooled to room temperature. As shown by Figure 3.5, this additional support area can accommodate at least two of these baseline specimens. These specimens were also prepared as described in Section 3.1.5 and sintered at various thermal cycles. The cycles included ramps of either 5, 10, or 20°C/min, isothermal holds up to 60 minutes, and peak temperatures up to 854°C. The baselines were measured and tested for transverse rupture strength as described in Section 3.1.6. Measurements used in Equations 3.10 and 3.12 were made after cooling back to room temperature to account for any dimensional dilation due to sintering. These baseline measurements provide a correlation to determine overall degree of sinter strengthening during the test. Measurement uncertainty was identical to that determined in Section 3.1.6.

3.3 Thermal Softening

The thermal softening behavior for a wrought material was approximated by measurements made on TRBs sintered to high density. These specimens were first prepared as described in Section 3.1.5 and then sintered in the FTT at 840°C for 1 hour (10°C/min heating rate). This resulted in enough dimensional shrinkage to be refit into the TRB die. The specimens were then compacted a second time to a pressure of 550 MPa which resulted in a fractional density of 0.95 (as calculated by Equation 3.10). Finally, the specimens were sintered a second time using the same cycle described above. The density fraction after this final sintering cycle was 0.96. The FTT was then used to perform TRS measurements at various temperatures up to 857°C. In all cases the TRBs were heated to

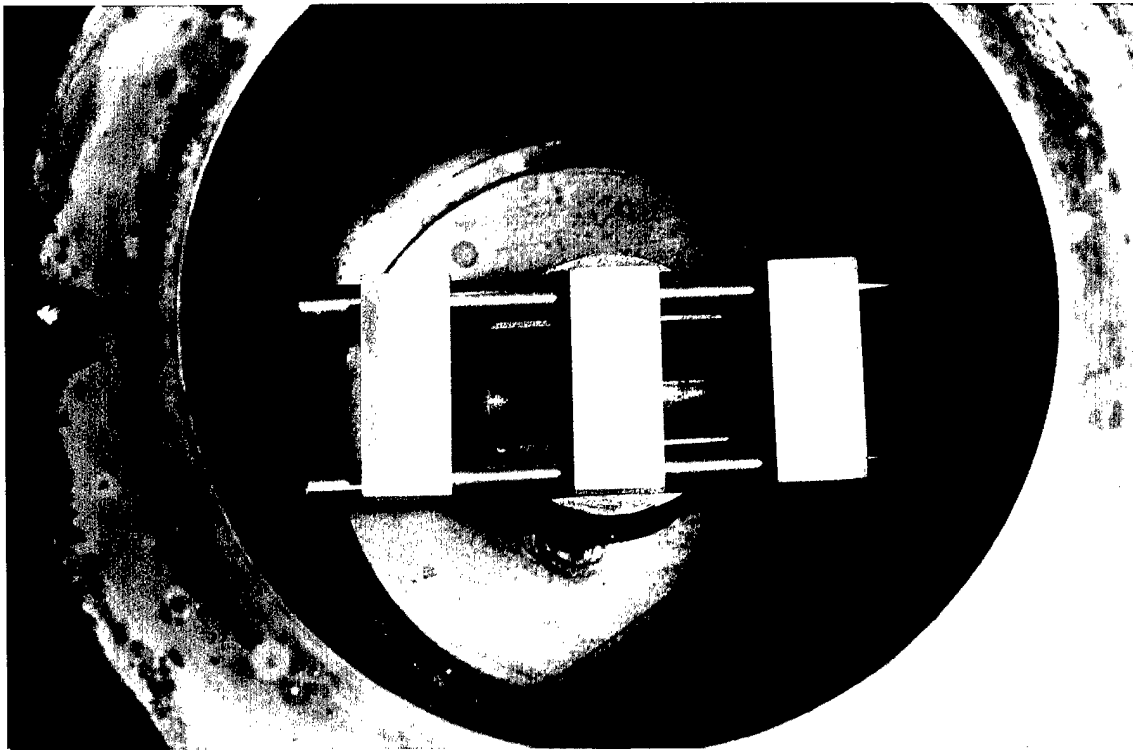


Figure 3.5: Photograph of FTT test chamber interior with retort cap removed. Two point support provides additional support space on either side of the central *in situ* test location (photo courtesy of J. Thomas).

the test temperature at 10°C/min in hydrogen. Two test temperatures were repeated, approximately 500 and 600°C, with 30 minutes holds at the test temperature prior to performing the test. These were intended to establish the influence of time on thermal softening. Equation 3.12 was used to calculate the transverse rupture strength.

3.4 Dilatometric Analysis

A dilatometric analysis was performed using an Anter Laboratories Unitherm™ Model 1161 vertical dilatometer. This provided *in situ* dilation behavior monitoring of the bronze compacts to aid in the understanding of sintering densification mechanisms. As shown by Figure 3.6, the dilatometer consisted of a specimen holder within a furnace tube. A portion of a TRB compact was placed in the specimen holder between two alumina discs. The discs eliminated the possibility of contamination of the apparatus and adhesion to the specimen holder or dilation probe. The discs also distribute the small load of the displacement probe over the entire sample. The alumina dilation probe rested lightly on the top of the sample disc assembly. A steel bar, acting as a counterweight, was connected to the probe assembly and adjusted till the probe force to the sample (distributed by the alumina disc) was 0.3 ± 0.1 N. Thus, a small expansion or contraction in the specimen produced probe motion. This motion was registered as a height change on a fiber optic grating sensor. The sensor sent information to a computer, which simultaneously recorded temperature and dilation once every minute.

Dilatometer calibration was accomplished with a single crystal sapphire rod used to determine correction values for the alumina dilation probe and the sample holding tube.

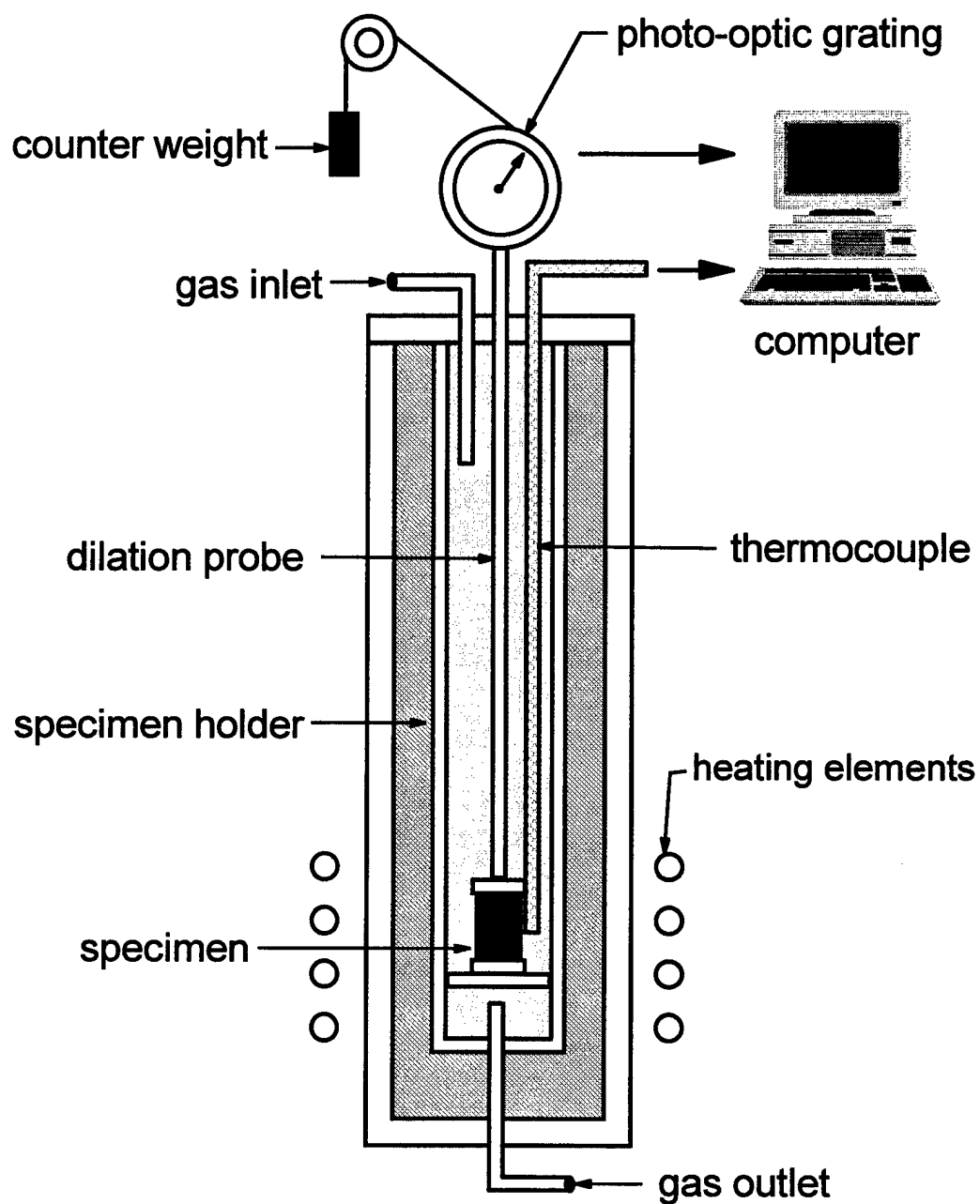


Figure 3.6: Schematic illustration of the Anter Laboratories Unitherm™ Model 1161 vertical dilatometer.

This was accomplished by five cycles of heating the dilatometer to 1500°C followed by subsequent cooling to room temperature. Data analysis using 4th order polynomials was done to obtain the correction coefficients from each of the five cycles. These coefficients were then averaged to produce the correction parameters. Having included the correction parameters in the dilatometer software, these effects were eliminated from the sample response output data. The standard error of the estimate (precision error) provided by the calibrated correction coefficients was 2 μm , while the accuracy (bias error) of the displacement measuring system was also 2 μm . Both errors were summed in the root mean square fashion of Equation 3.6 to determine the total dilation measurement uncertainty to be 3 μm . Temperature calibration was based on the measurement of an iron sample during the α to γ transformation at 910°C. During this calibration run the dilatometer detected this transformation to within 3°C.

The dilatometer can run in any hydrogen-nitrogen process gas mixture, controlled by flow meters similar to those described for the FTT. The heating can be controlled with up to 16 different segments, each including heating rate, soak temperature, and soak time. For this investigation the bronze compacts were tested in 100% hydrogen at 10°C/min in both the press direction and transverse direction. Both the resulting *in situ* shrinkages were used to estimate the *in situ* fractional density using Equation 3.13;

$$f_s = \frac{\rho_G / \rho_T}{\left(1 - (\Delta L / L)_A\right) \left(1 - (\Delta L / L)_T\right)^2} \quad (3.13)$$

where ρ_G is the green density in g/cm^3 , ρ_T is the theoretical density as defined previously and $(\Delta L/L)_A$ and $(\Delta L/L)_T$ are the linear shrinkage for the press direction and the transverse direction, respectively.

3.5 Differential Thermal Analysis

The melting characteristics of the bronze alloy chosen were determined by differential thermal analysis (DTA) using the TA Instruments SDT 2960 DTA shown in Figure 3.7. The unit was first calibrated using pure unalloyed metals, such as silver and nickel, to determine the offset temperature to within 2°C . The sample and a reference material were placed in adjacent sample cup holders. Alumina was used as a reference since it is thermally stable over the temperature range. A temperature difference between the sample and the reference therefore, indicates a change of phase.

In the case of melting, the temperature difference between the sample and the reference manifests itself as an endothermic peak in the DTA plot of temperature difference versus temperature. The solidus and liquidus points of transitions were determined from changes in slope of this plot. The point where the slope of the curve starts to deviate from the baseline is considered to be the solidus temperature (T_S). The temperature where the point of maximum deviation from the baseline occurs is considered to be the liquidus (T_L) [77].

The DTA runs were performed by heating to 1100°C at $5^\circ\text{C}/\text{min}$ in 100% argon, followed by cool down to room temperature. The cycle was then repeated to determine any difference between the powder characteristics and that of the homogenous alloy.

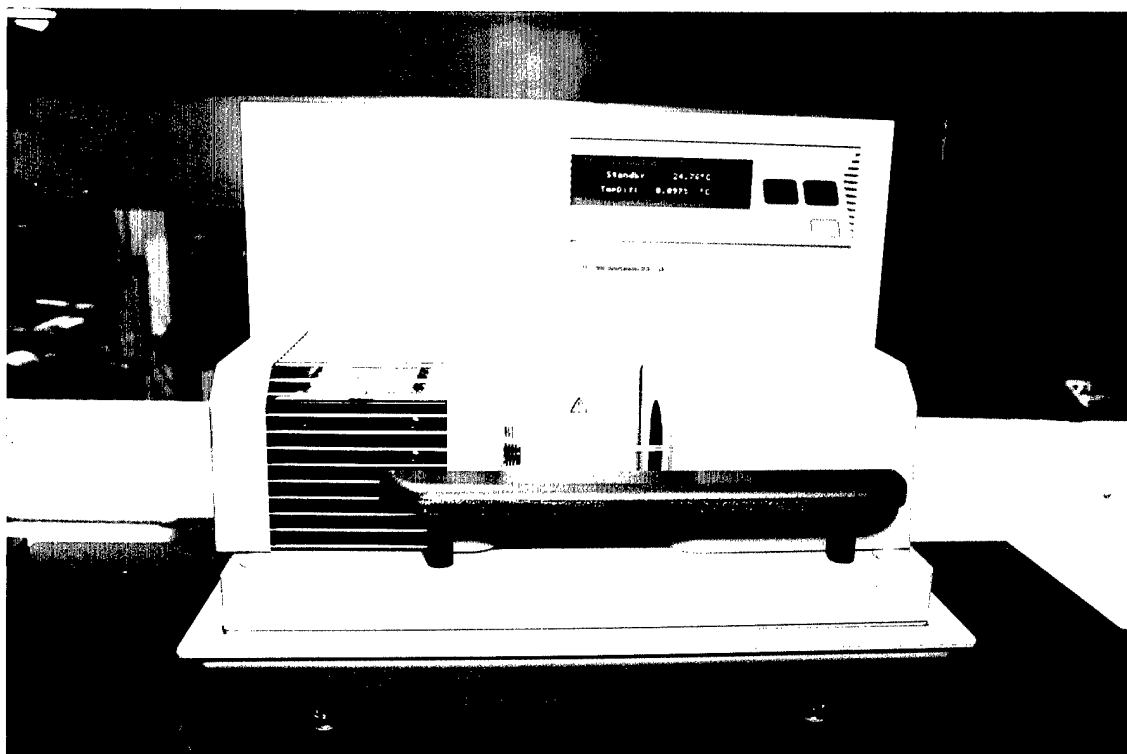


Figure 3.7: TA Instruments SDT 2960 used for differential thermal analysis.

3.6 Quenching

Samples were quenched in water from various temperatures using a CM vertical tube furnace. A schematic of this furnace is shown in Figure 3.8. The furnace had MoSi_2 heating elements and was controlled by a multi-segment Honeywell Universal Digital Controller. Calibration was accomplished by inserting a NIST traceable C-type thermocouple to determine the exact location of the hot zone and the deviation from the furnace's control thermocouple. A 75 mm hot zone was identified which had a deviation of less than 2°C . As an extra measure of temperature certainty, the calibration thermocouple was left in the hot zone next to the samples during quenching heats. Cut portions of pressed TRB specimens, produced as described in Section 3.1.5, were suspended in the hot zone using stainless steel wire. They were then sintered at $10^\circ\text{C}/\text{min}$ in 100% hydrogen. At the quenching temperature, the wire was cut and the sample allowed to fall into the water bath under the tube. The cooling rate was estimated to be $10^3^\circ\text{C}/\text{s}$. Quenches were accomplished from various temperatures to freeze the microstructure at that particular level of sintering.

3.7 Metallography

The quenched specimens were mounted for metallographic analysis. Specimens were first smoothed on one side with 120 grit sandpaper. The specimens were then mounted in epoxy. Epoxy mounts were made by mixing Norcast #2795 epoxy resin and hardener at a 10:1 wt. ratio. The specimen was placed in a tin cup with the smooth side

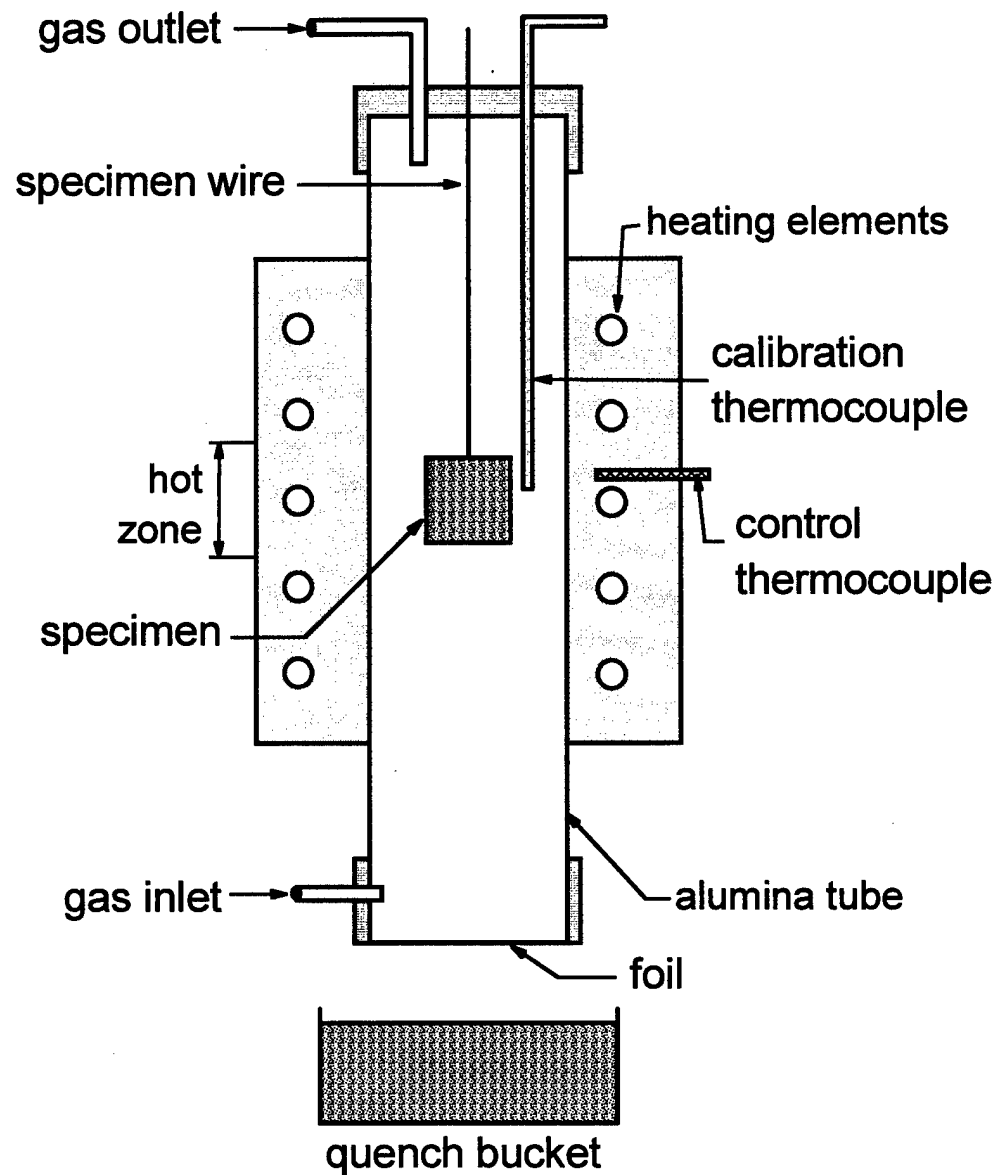


Figure 3.8: Schematic illustration of a CM vertical tube furnace used for quenching.

down and the cup filled with the epoxy mixture. The cup was then placed in a vacuum chamber to fill any pores. Finally, the mounts were allowed to stand for 6 hours to cure.

After removing the tin cup the mounted specimens were first ground using 120 grit silicon carbide grinding papers. A thin layer of epoxy was then applied to the ground surface and the specimens was again placed in a vacuum chamber. This gave a final chance to fill any surface pores, thus providing additional rigidity to the mount. The sample was then ground with 120, 320, 600, 800 and 1200 grit silicon carbide grinding papers. Following this process, the specimens were polished on Texmet with a 0.3 μm alumina aqueous slurry and final polished on microcloth with the same 0.3 μm alumina slurry. The specimens were etched using a solution of 2 wt.% potassium dichromate ($\text{K}_2\text{Cr}_2\text{O}_7$) in distilled water (the time varied from 3 to 5 seconds).

3.8 Microstructural Analysis: Grain Size Measurement

Mounted and etched specimens (as described in Section 3.7) were quantitatively analyzed to determine grain size by stereology methods. Stereology allows for three dimensional estimation using two dimensional measurements of microstructural features [78-80]. It began with a series of optical photographs of the feature taken at a known magnification (1500X). Detail was enhanced in these photographs with a DIC (Differential Interference Control) filter. The grain size measurement technique used in this research required both the line intercept and point counting methods. The technique was based on the linear intercept method with a correction made to account for the volume fraction porosity provided by the point count method.

Point counting used a transparent uniform orthogonal grid of intersecting lines. This grid is overlaid on the photograph and the number of intersection points that fall within grains are counted. If the intersection point falls on the boundary of a grain and a pore it is counted as $\frac{1}{2}$ point. The total *in grain* point count (P_G) was used with the total number of line intersection points in the photo (P_T) in Equation 3.14 to determine volume fraction of grains (V_G) in each photograph.

$$V_G = \frac{P_G}{P_T} \quad (3.14)$$

Line intercept is a technique where the intercepts of a desired feature with a line are counted over a specified length. A transparency with several randomly drawn lines were placed on each photo and the intercepts counted for each line. The number of intercepts between two adjacent grains (P_{GG}) and between a grain and a pore (P_{GP}) along a given line were counted. Both counts were then divided by the actual length of the line across the photograph to determine intercepts per unit length using Equations 3.15 and 3.16;

$$p_{GG} = \frac{P_{GG}}{L} \quad (3.15)$$

$$p_{GP} = \frac{P_{GP}}{L} \quad (3.16)$$

where L is the scaled line length in μm and p_{GG} and p_{GP} are the intercept counts per unit length in μm^{-1} . The mean grain intercept length, λ_G in μm , was then calculated using Equation 3.17.

$$\lambda_G = \frac{V_G}{2 p_{GG} + p_{GP}} \quad (3.17)$$

A minimum of fifty grains were counted by line intercept. The large sample size allowed the measurement uncertainty to be determined by the normal distribution [76]. The resulting approximation to the population grain size (μ) within a 90% confidence interval is given by Equation 3.18;

$$\mu = \bar{x} \pm 1.645 \frac{S_x}{\sqrt{n}} \quad (3.18)$$

where \bar{x} is the grain size sample mean in μm , S_x is the grain size sample variance in μm , and n is the number grains measured (sample size). Based on the result of this uncertainty calculation, the sample size could be adjusted to approach a desired level of uncertainty.

3.9 Microstructural Analysis: X-Ray Diffraction

X-ray diffraction (XRD) was performed to determine phases in the microstructure at various stages of sintering. The purpose was to detect phase changes, if any, over the temperature range where sinter strengthening occurred. The phase diagram [82] for this alloy predicted a continuous α -Cu phase from 340°C through the solidus. Below this temperature the phase diagram predicts a two phased α -Cu and ϵ -bronze microstructure. Since an extremely slow cooling rate, from above the transition temperature, is required

to decompose the α -Cu phase, Dowson [26] observes that the two phased microstructure is rarely the case in powder. Therefore, X-ray diffraction was used to make phase change determinations. Furthermore, comparison between the measured patterns and cataloged patterns from the *Powder Diffraction File (PDF)* [83] were used to determine the phase present at various stages of sintering.

Measurements were accomplished using a Rigaku Geigerflux XRD. The device used radiation from a K_{α} Cu (0.15 nm) target tube and a graphite monochromatometer to help separate x-rays prior to the detector. Selected quenched samples, as described in Section 3.5, were prepared using 120 and 320 grit silicon carbide grinding paper to create one smooth side. Additionally, as received powder was mounted in epoxy and polished in the same manner. The scan speed was $4^{\circ}/\text{min}$ and the intensity readings were recorded by the data acquisition system 0.02° intervals. After the scan of each sample was complete, the data acquisition system provided an output of intensity versus diffraction angle normalized to the maximum intensity.

3.10 Hardness Measurements

Hardness measurements were performed using a Leco M-400-H microhardness tester in conjunction with an Akashi VL-101 video line micrometer. Measurements were made of the as-received powder as well as the sintered and the quenched specimens described in Section 3.6 (water quenched from 400, 500, and 600°C after heating at $10^{\circ}\text{C}/\text{min}$ in hydrogen). The purpose of these measurements was to identify the presence of annealing in the powder particles in response to the thermal environment.

The hardness tester used a 25 g load to force an inverted pyramid-shaped indenter into the test specimen. The size of this indentation was then measured in both planar directions with the video line micrometer. This dimension was then converted to a hardness (HV scale) measurement. Hardness measurements were repeated at least 30 times on each specimen to permit the use of the normal distribution to approximate the population hardness for each condition. As with the grain size measurements (described in Section 3.8), the number of measurements, along with the sample mean and standard deviation were used in Equation 3.18 to calculate the precision uncertainty (90% confidence interval) associated with this approximation. In all cases, the indentation was made at the center of a particle to avoid the effect of porosity on the measurement.

The factory calibration of the combined hardness measurement system was verified prior to all tests. This called for five measurements of a standard block (Leco serial # 946014) to fall within 718 ± 2 KHN using a 300 g load. Three separate verifications fell within the required range. When compared to the precision uncertainty, the bias error associated with this range of accuracy represented an insignificant contribution to the total measurement uncertainty. Therefore, the total measurement uncertainty was simply the precision uncertainty represented by Equation 3.18.

Chapter 4

Experimental Results

The experimental results are presented in four main sections. The first section presents the results of the *in situ* strength measurements during sintering. The next presents the sinter strengthening measurements taken at room temperature. The third section focuses on three other sintering outcomes, densification, grain growth and inter particle bonding. The last section presents an evaluation of four bulk material characteristics in response to thermal processing; melting, phase change, thermal softening and hardness.

4.1 *In situ* Strength Evolution

As discussed in Section 3.1.1, the specific *in situ* property selected for this research was transverse rupture strength (TRS). The evolution of TRS was precisely determined for the sintering of bronze compacts using the FTT described in Section 3.1.4. The experimental determination of *in situ* TRS fell into three main categories based on the type of pretest sintering profile. The profile categories include constant heating rate to the test temperature, isothermal holds, and constant heating with subsequent cooling to the test temperature. All raw data are presented in tabular form in Appendix A. These tables include density fraction, sintering profile and TRS.

4.1.1 Constant Heating Rate Sintering

A constant heating rate of $10^{\circ}\text{C}/\text{min}$ to the test temperature was used for the first set of FTT measurements. The raw data from these experiments are presented in Table A-1. The sintering profile in this table includes heating rate and test temperature. Figure 4.1 presents these data by a plot of TRS as a function of test temperature. The TRS decays from the room temperature green strength of 10 MPa through 400°C where a minimum strength of 5 MPa is recorded. This is followed by a dramatic increase in TRS between 450°C and 600°C where the peak strength of 100 MPa is measured. The peak is followed by a continuous decay of strength through the highest test temperature of 854°C .

Selected test temperatures were repeated using a constant heating rate to the test temperature of $5^{\circ}\text{C}/\text{min}$. These data investigated the impact of heating rate and sintering kinetics variation on strengthening. These raw data are also included in Table A-1 and the TRS versus test temperature plot is presented in Figure 4.2. In this figure a trace of the $10^{\circ}\text{C}/\text{min}$ data from Figure 4.1 is also shown as a reference. These data exhibit the same strengthening trend as the higher ($10^{\circ}\text{C}/\text{min}$) heating rate FTT tests with the exception of significant strengthening beginning at a 50°C lower onset temperature of 400°C . After 600°C the TRS versus test temperature curve rejoins that of the higher heating rate.

4.1.2 Isothermal Sintering

To further investigate variations of sintering kinetics on strengthening, several FTT tests were performed that included isothermal holds in their pretest sintering profiles. Isothermal segments were both at the test temperature and at intermediate points during

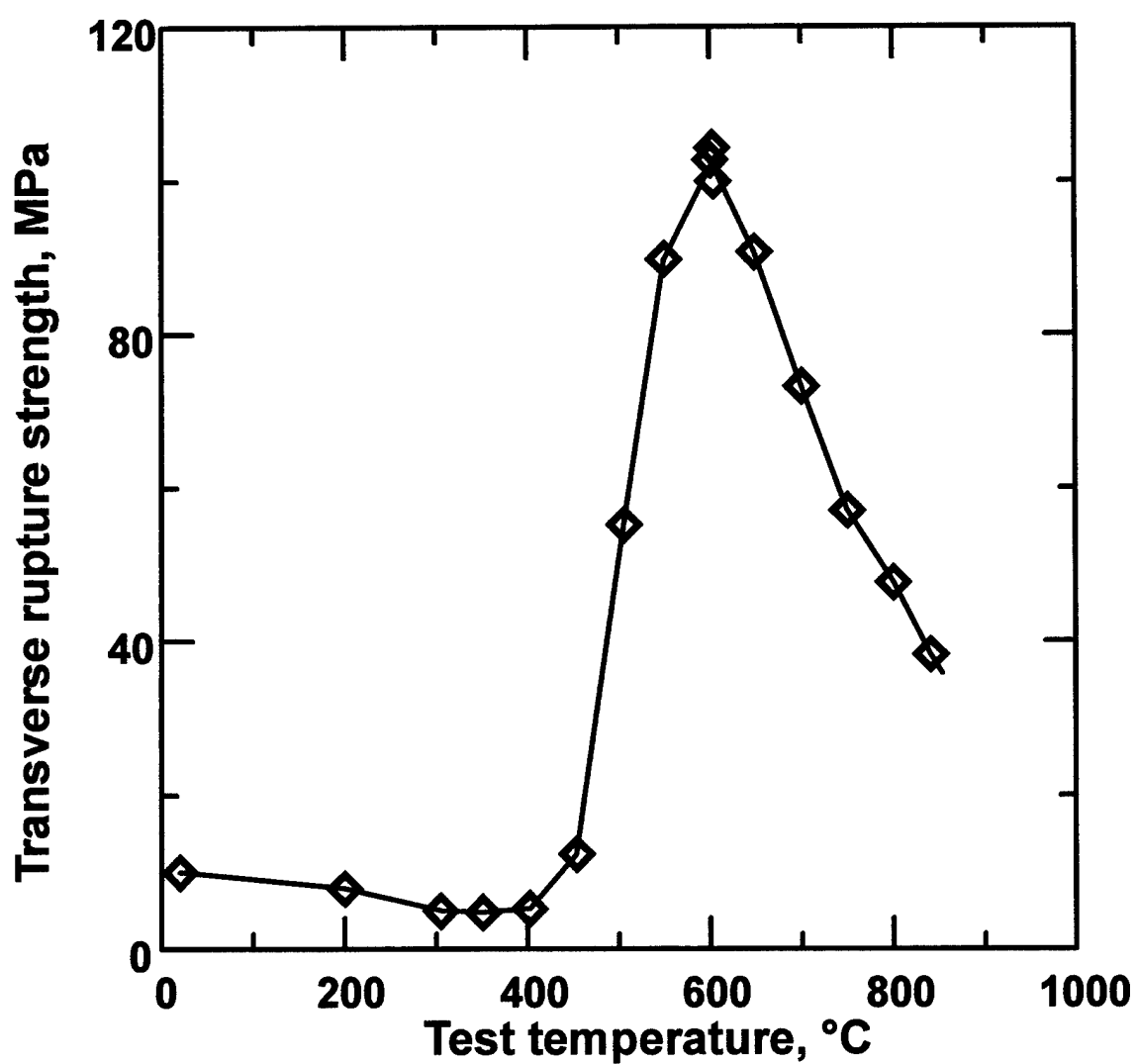


Figure 4.1: *In situ* transverse rupture strength versus test temperature for prealloyed 90Cu-10wt.%Sn bronze compacts sintered at 10°C/min in hydrogen. Compact fractional green density was 0.86.

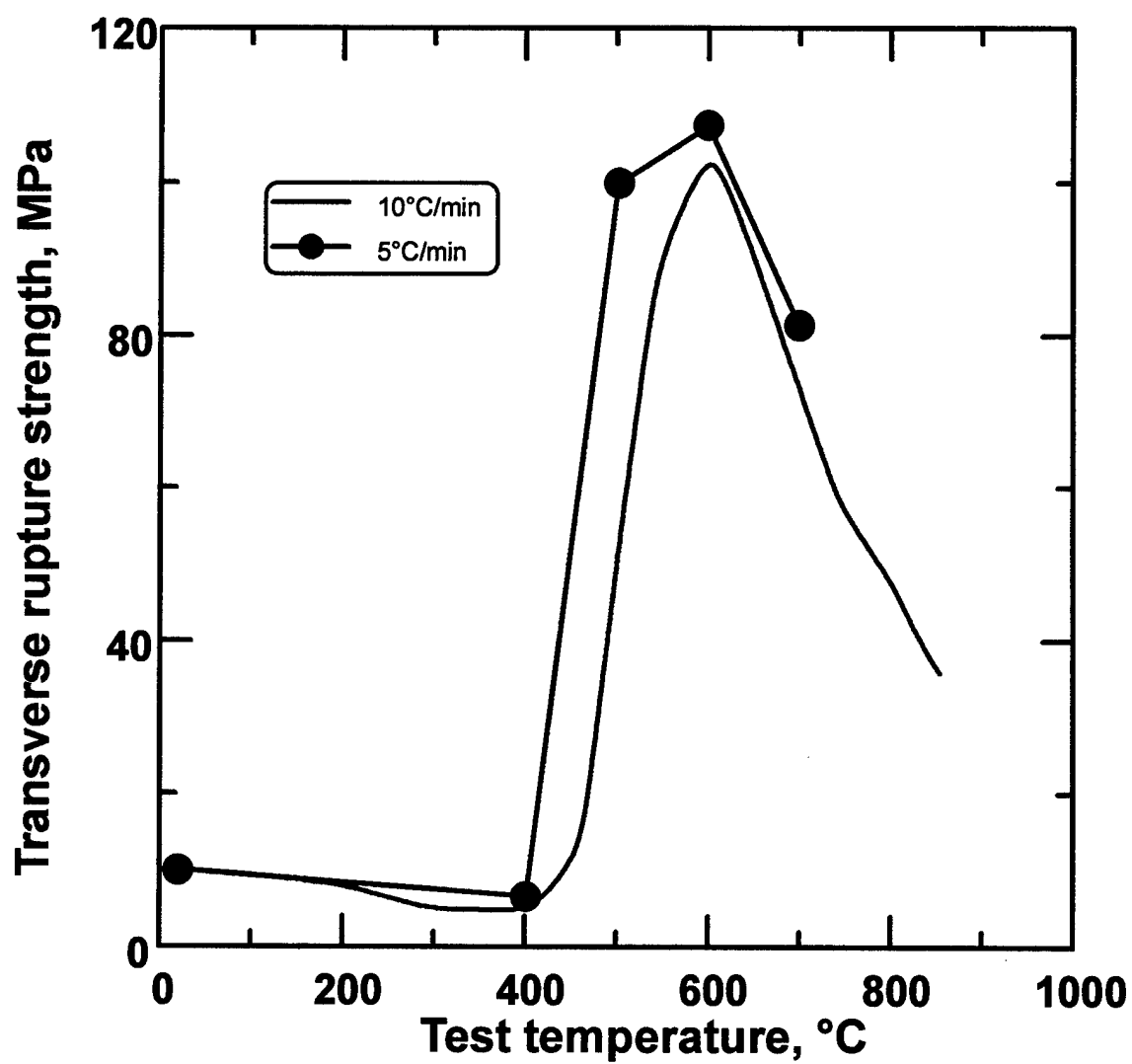


Figure 4.2: *In situ* transverse rupture strength versus test temperature for prealloyed 90Cu-10wt.%Sn bronze compacts sintered at 5°C/min in hydrogen. Trace of 10°C/min data from Figure 4.1 included as a reference. Compact fractional green density was 0.86.

the heating cycle. All tests in this section were performed in hydrogen with $10^{\circ}\text{C}/\text{min}$ thermal transitions. These raw data are presented in Appendix A, Table A-2. The sintering profile parameters for each of these tests includes heating rate, hold temperature, hold time, and test temperature. Figure 4.3 shows the plot of TRS versus test temperature from FTT tests in which the pretest sintering profiles included 10 or 20 minute holds at the test temperature. Also shown in this figure is a trace of the $10^{\circ}\text{C}/\text{min}$ data with no hold from Figure 4.1 as a reference. These data again repeat the same strength evolution trend as the earlier result (no hold) with longer holds resulting in progressively lower onset temperatures for significant strengthening. These temperatures are 400°C and 350°C for 10 and 20 minute holds, respectively. Strengthening between 350°C and 600°C resulted in higher strength at a given temperature for longer hold times. After 600°C all strength curves again become coincident.

Two final test were performed which included a 20 minute hold at 400°C followed by continued heating to higher test temperatures. These data are also included in Table A-2 and shown in Figure 4.4 as plots of TRS versus test temperature. Traces of the no hold data of Figure 4.1 along with the 20 min hold at the test temperature data of Figure 4.3 are included as reference. As shown in this figure, this hold results in higher net strength at 500°C but has no impact at the higher (600°C) test temperature.

4.1.3 Thermal Softening Behavior

The final sets of FTT experiments were designed to extract the thermal softening behavior of the sintered bronze. Specimens were sintered to peak temperatures between

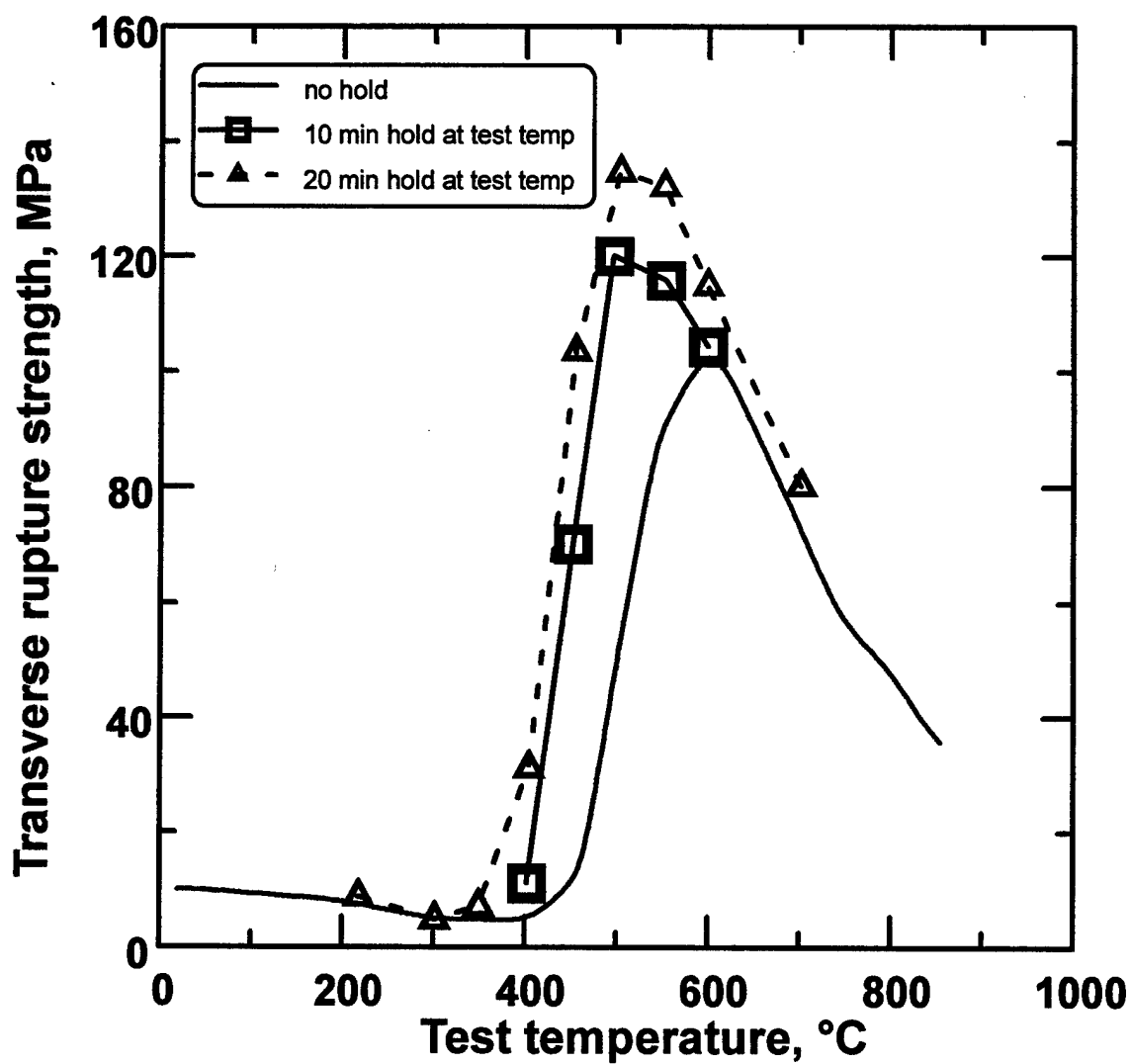


Figure 4.3: *In situ* transverse rupture strength versus test temperature for prealloyed 90Cu-10wt.%Sn bronze compacts sintered at 10°C/min in hydrogen with isothermal holds at the test temperature of either 10 or 20 min. Trace of no hold data from Figure 4.1 included as a reference. Compact fractional green density was 0.86.

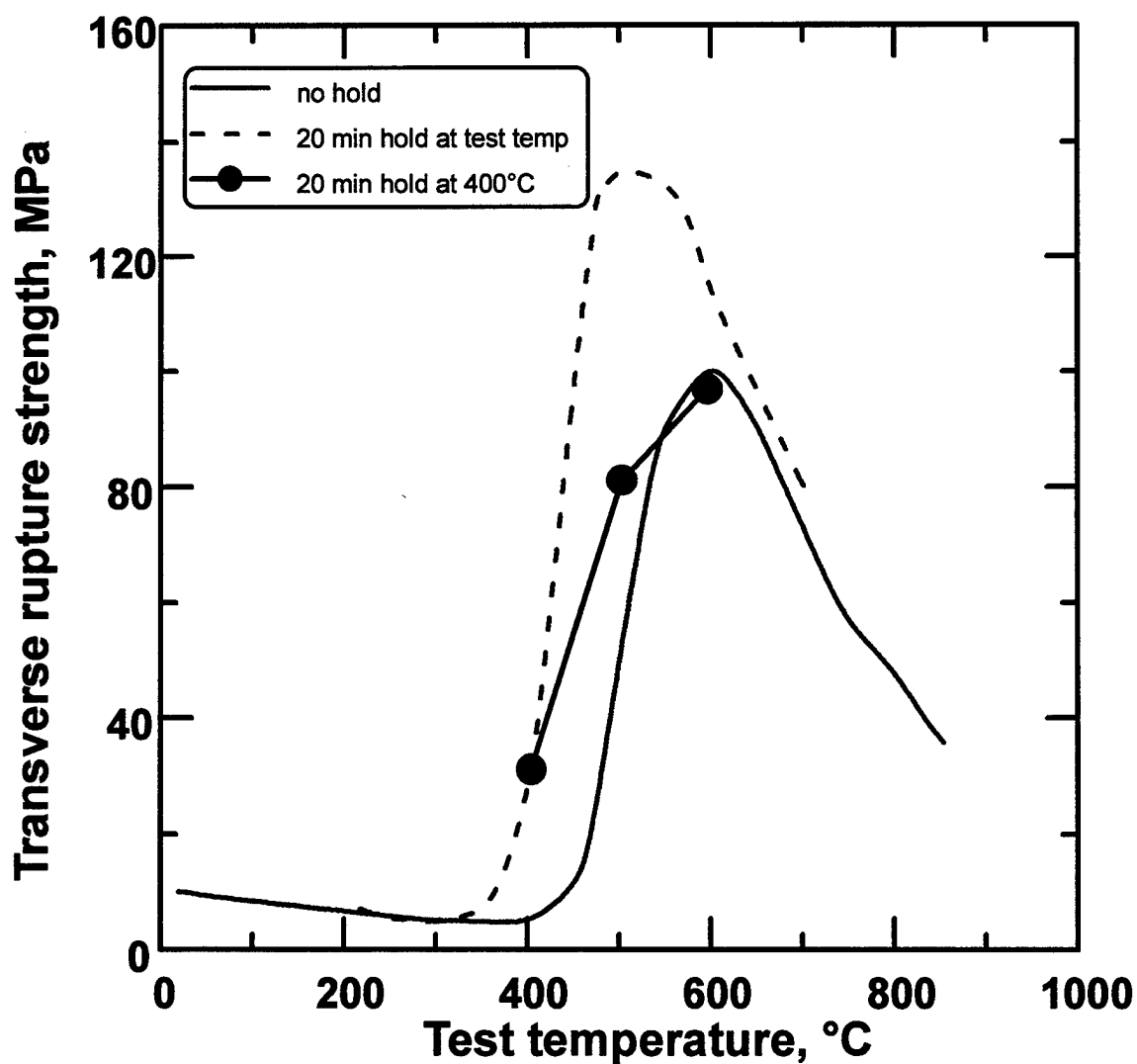


Figure 4.4: *In situ* transverse rupture strength versus test temperature for prealloyed 90Cu-10wt.%Sn bronze compacts sintered at 10°C/min in hydrogen with an isothermal hold at 400°C for 20 min. Trace of no hold data from Figure 4.1 and 20 min hold at the test temperature data of Figure 4.3 included as a reference. Compact fractional green density was 0.86.

400°C and 800°C and subsequently cooled to lower test temperatures. The resulting data are shown in Appendix A, Table A-3. The sintering profile in this table includes heating rate, peak temperature, cooling rate, and test temperature. These data are depicted in Figure 4.5 and have been plotted by TRS versus test temperature. The data are separated into series identified with each specimen's peak sintering temperature. Along with these data, the data of Figure 4.1 (no cool) is included as a reference. Note, the final point of each series is the strength after cooling to room temperature. Each series shows the same relative curve shape. This observation is more evident in Figure 4.6 when the data are normalized to their room temperature strength. From this representation, it is obvious that thermal softening profiles from sintering temperatures of 600°C or above are self-similar.

4.2 Compact Sintered Strength

The baseline samples sintered as described in Section 3.2 were measured using the FTT at room temperature. As discussed in that section, these results provide a correlation of overall degree of sintering with respect to strengthening. The complete set of data from these measurements are contained in the tables of Appendix B. These tables include post sinter density fraction, sintering profile, and TRS.

4.2.1 Constant Rate Sintering

The results from baselines sintered at 5, 10, and 20°C/min are presented in Table B-1 and shown graphically in Figure 4.7 by a plot of maximum sinter temperature versus

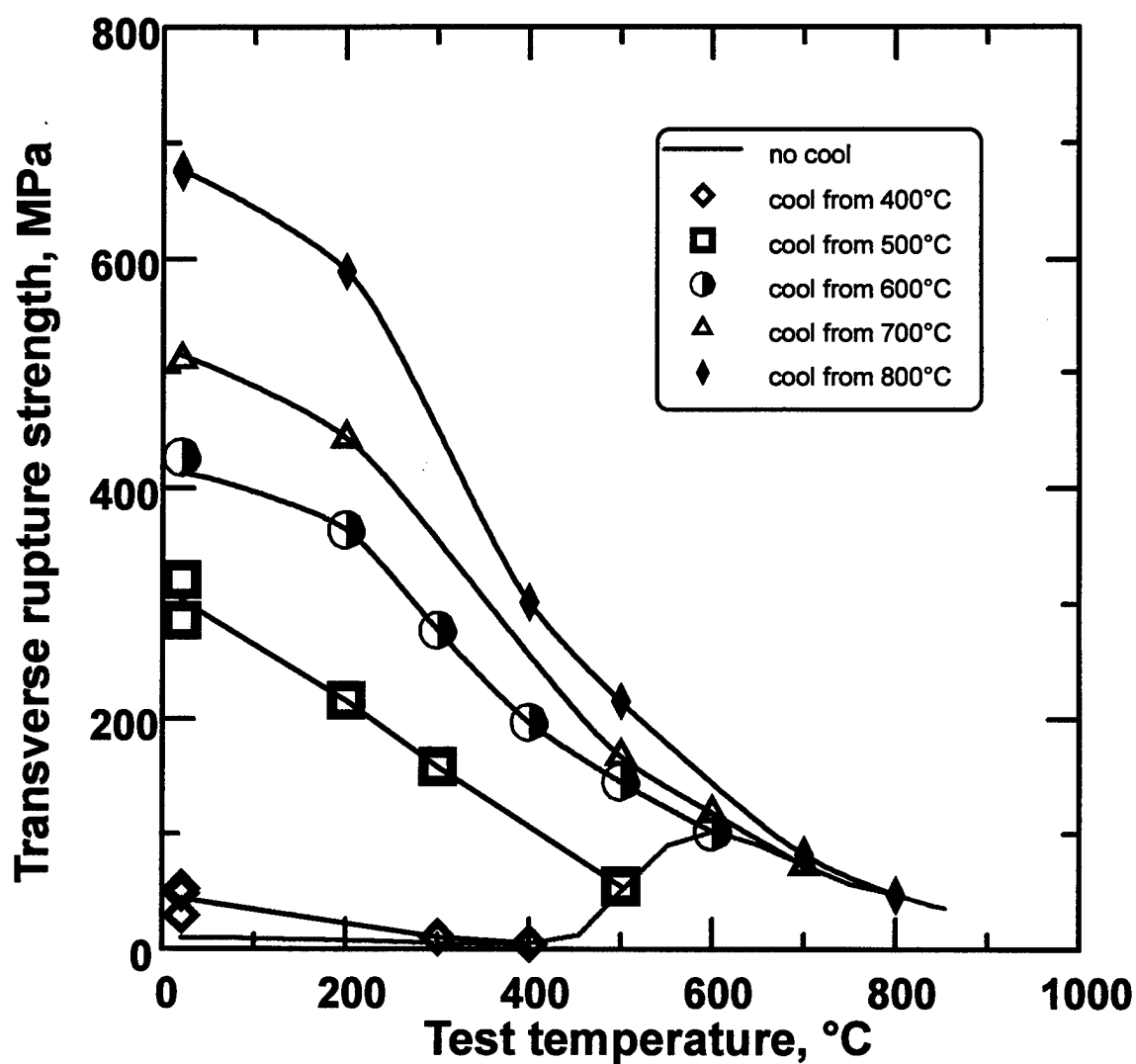


Figure 4.5: *In situ* transverse rupture strength versus test temperature for prealloyed 90Cu-10wt.%Sn bronze compacts sintered in hydrogen at 10°C/min to the peak temperature, indicated by series legend, followed by cool to the test temperature. Trace of no cool data from Figure 4.1 included as a reference. Compact fractional green density was 0.86.

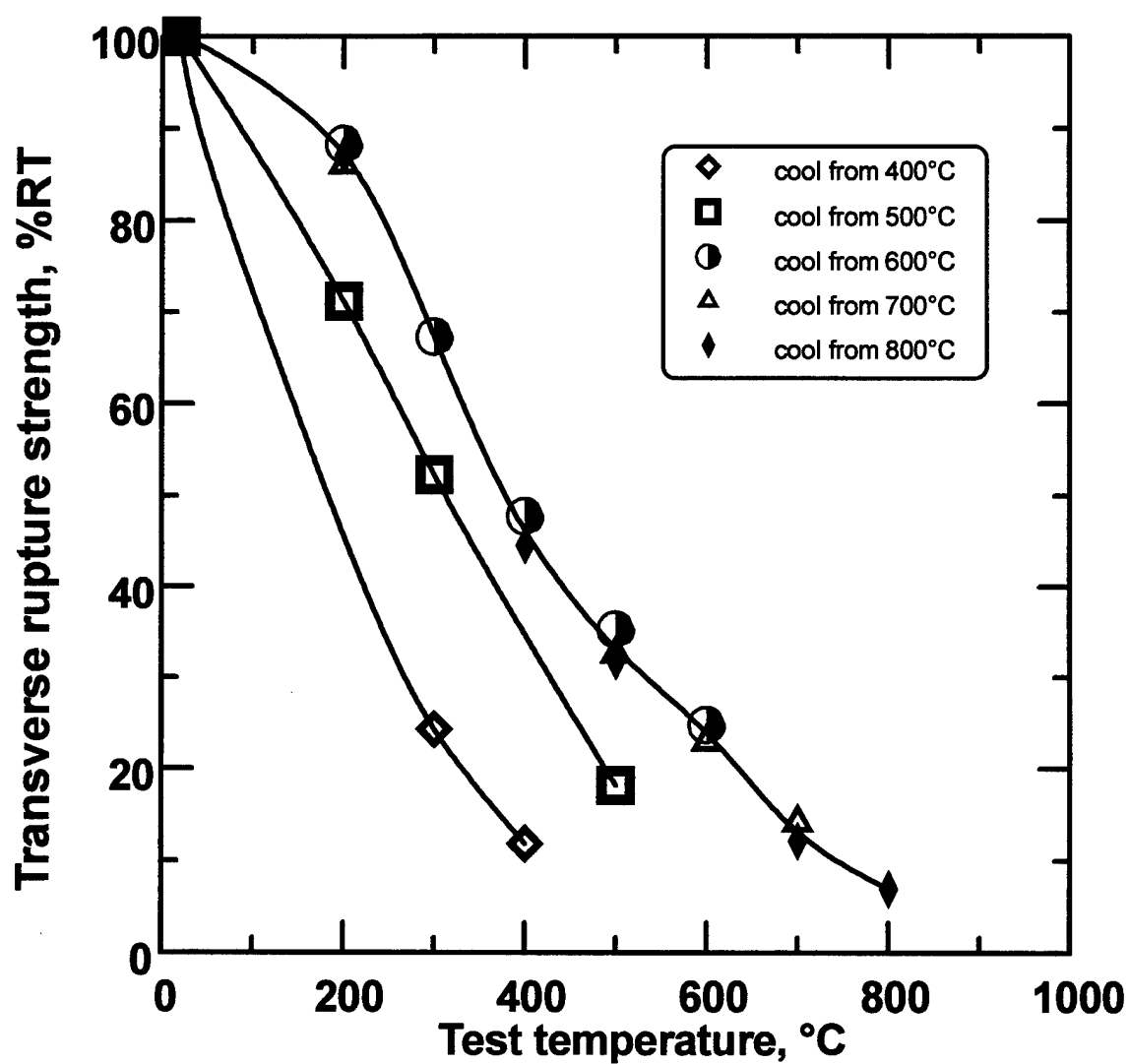


Figure 4.6: *In situ* transverse rupture strength normalized to room temperature strength versus test temperatures for prealloyed 90Cu-10wt.%Sn bronze compacts sintered in hydrogen at 10°C/min to the peak temperature, indicated by series legend, followed by cool to the test temperature. Compact fractional green density was 0.86.

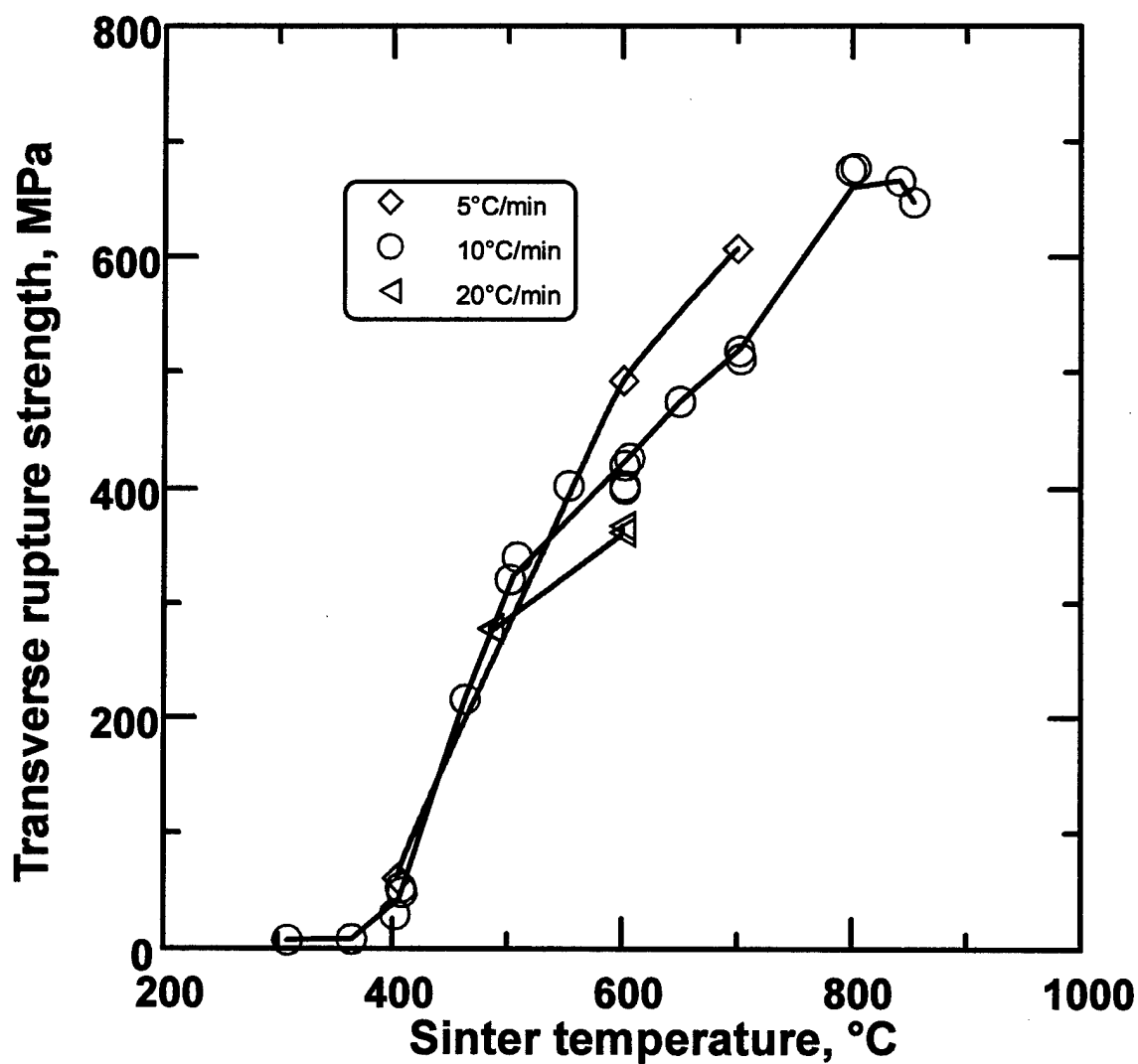


Figure 4.7: Room temperature transverse rupture strength versus maximum sinter temperature for prealloyed 90Cu-10wt.%Sn bronze compacts sintered in hydrogen at constant heating rates of 5, 10, or 20°C/min. Compact fractional green density was 0.86.

TRS. The sintering profile in the table includes heating rate, peak temperature and cooling rate. As shown by the graph, a steady increase in sintered strength is observed from specimens sintered to 400°C and above. Furthermore, above approximately 500°C, lower heating rates resulted in higher strengths for a given maximum sinter temperature.

4.2.2 Sintering with Isothermal Holds

A further evaluation of sintering strengthening was performed on specimens sintered to various temperatures with a variety of isothermal holds. These data are presented in Appendix B, Table B-2. The sintering profile in this table includes heating rate, hold temperature, hold time, peak temperature and cooling rate. These data are also depicted in Figures 4.8 through 4.11 where, for clarity, they are grouped by isothermal hold times and heating rates. Figure 4.8 shows the data from specimens sintered at 10°C/min with isothermal holds of either 10 or 20 minutes at the peak sinter temperature. Also included in this figure is the no hold data for the same 10°C/min heating rate from Figure 4.7 as a reference. These data show slightly higher strength for a given maximum sinter temperature as compared to the no hold data. It is also evident that specimens will begin to strengthen at a 50°C lower temperature (350°C) when held at that temperature for at least 20 minutes. Between 400°C and 600°C there is no discernible difference between 10 and 20 minute holds.

A longer 60 minute hold time was investigated at 5 and 20°C/min heating rates. Figure 4.9 shows the TRS versus maximum sinter temperature result for specimens sintered at 5°C/min. A trace of the no hold data for the same heating rate from Figure 4.7

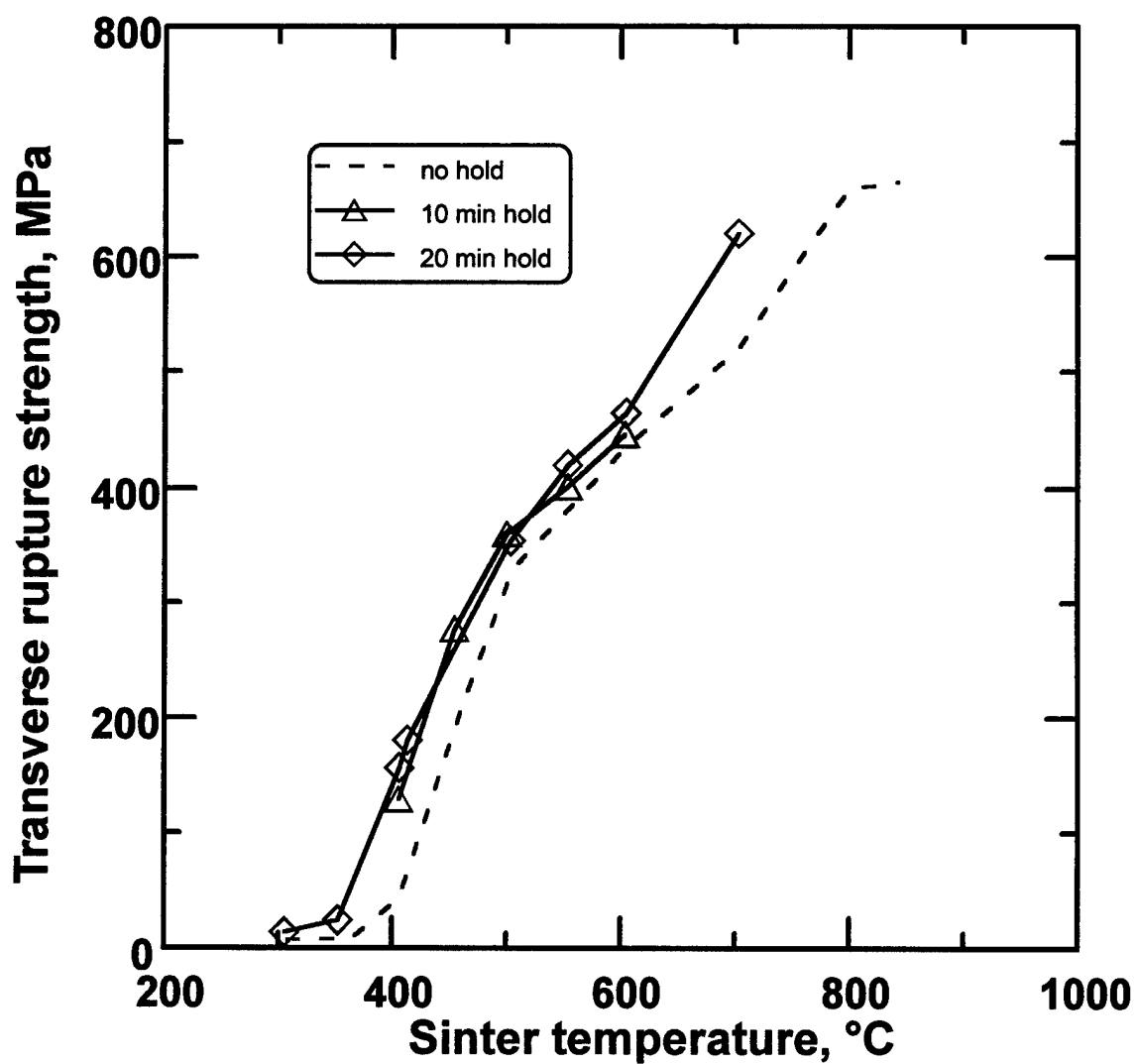


Figure 4.8: Room temperature transverse rupture strength versus maximum sinter temperature for prealloyed 90Cu-10wt.%Sn bronze compacts sintered at 10°C/min with isothermal holds of either 10 or 20 min at the maximum temperature. Atmosphere was pure hydrogen and compact fractional green density was 0.86.

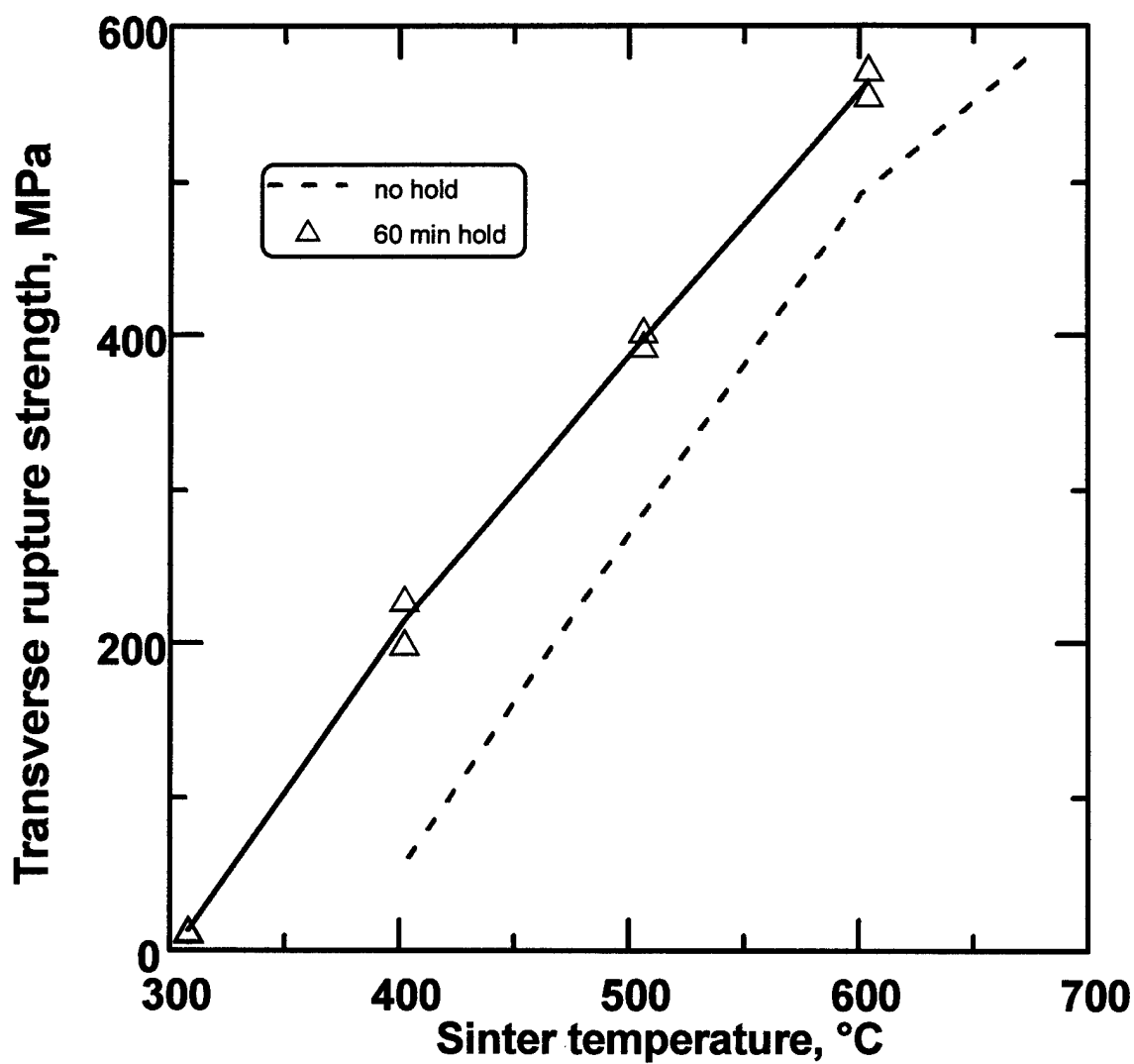


Figure 4.9: Room temperature transverse rupture strength versus maximum sinter temperature for prealloyed 90Cu-10wt.%Sn bronze compacts sintered at 5°C/min with an isothermal hold of 60 min at the maximum temperature. No hold data for same 5°C/min heating rate from Figure 4.7 included as a reference. Atmosphere was pure hydrogen and compact fractional green density was 0.86.

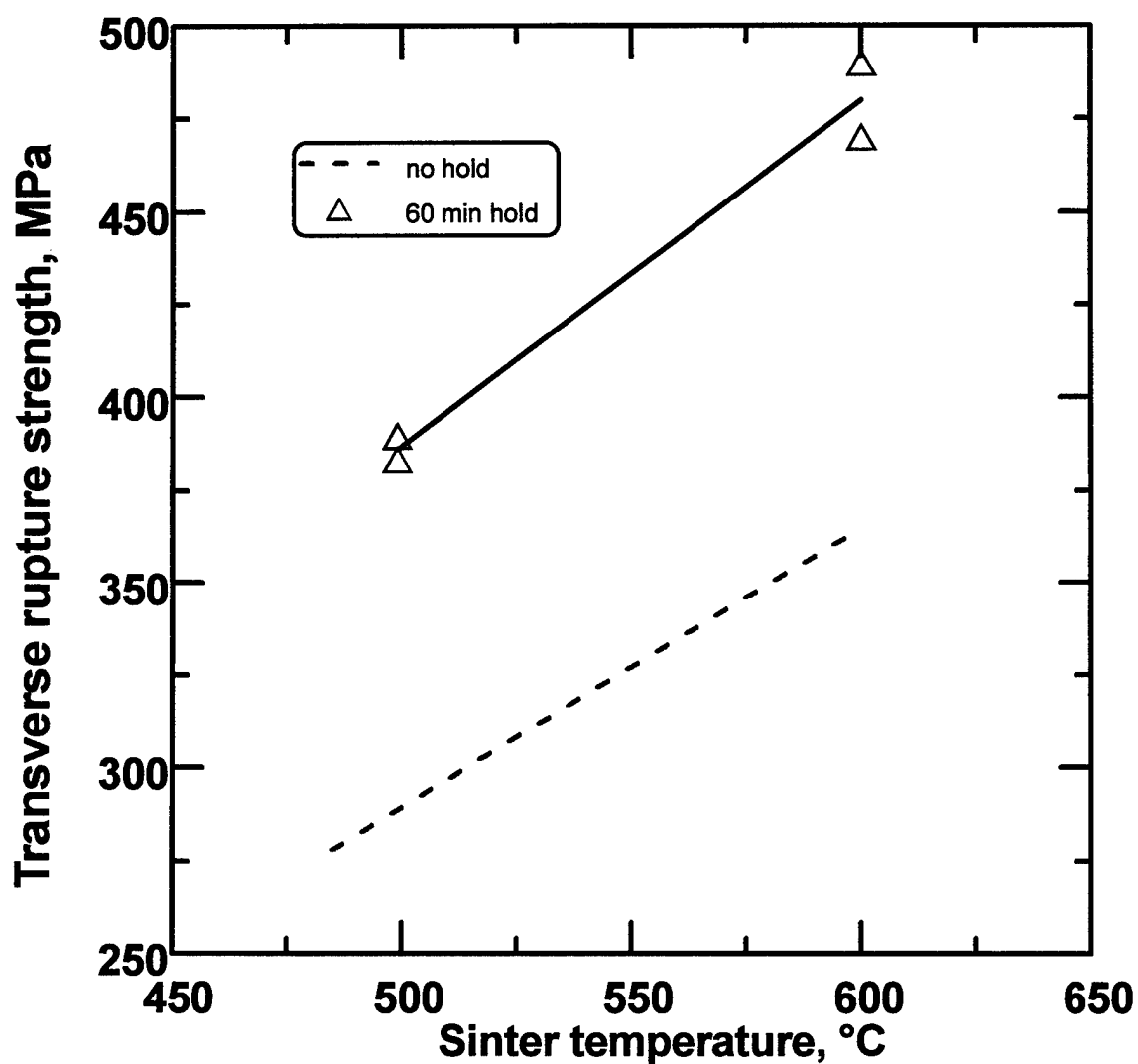


Figure 4.10: Room temperature transverse rupture strength versus maximum sinter temperature for prealloyed 90Cu-10wt.%Sn bronze compacts sintered at 20°C/min with an isothermal hold of 60 min at the maximum temperature. No hold data for same 20°C/min heating rate from Figure 4.7 included as a reference. Atmosphere was pure hydrogen and compact fractional green density was 0.86.

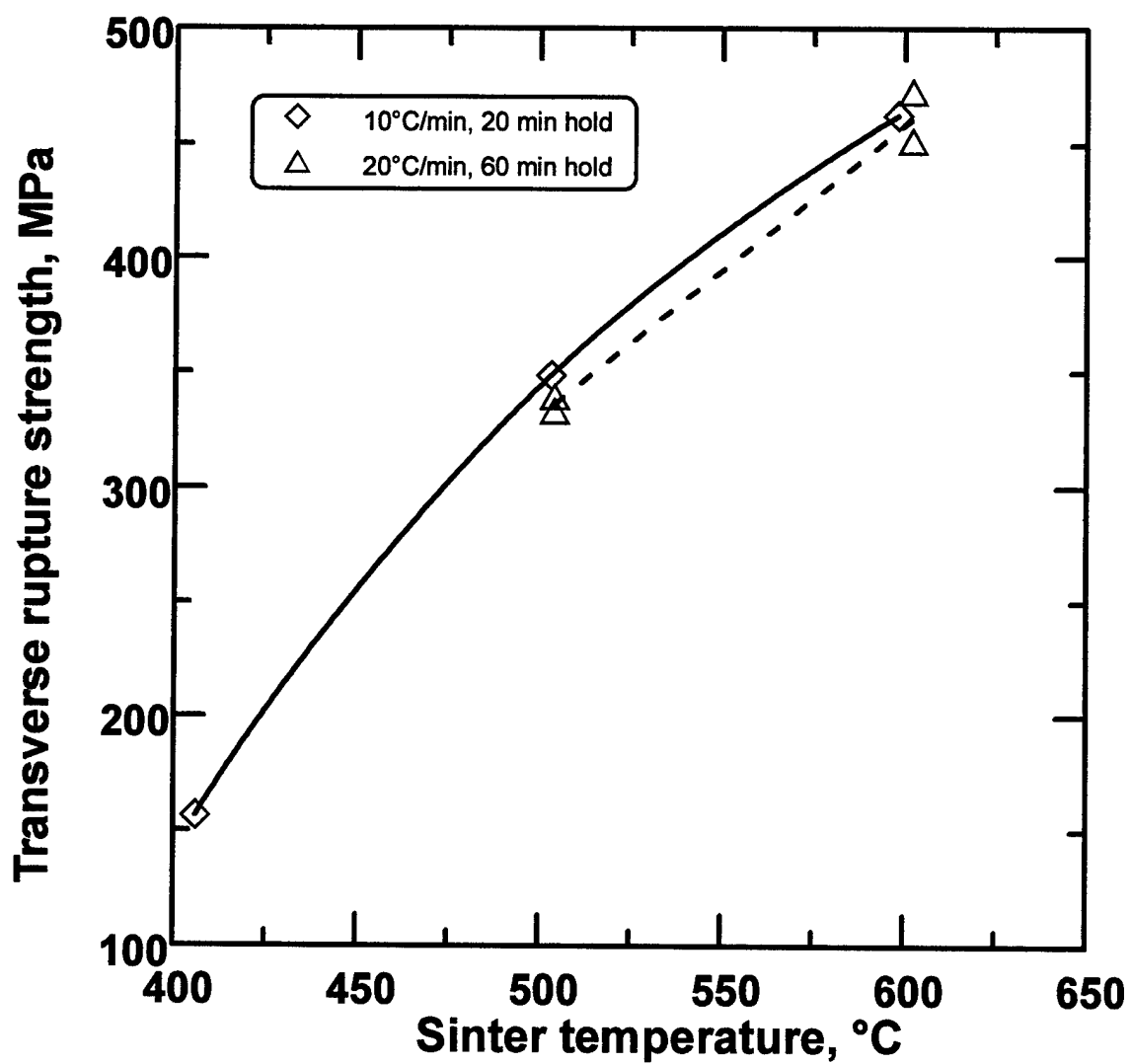


Figure 4.11: Room temperature transverse rupture strength versus maximum sinter temperature for prealloyed 90Cu-10wt.%Sn bronze compacts sintered at either 5°C/min or 10°C/min with isothermal holds of 20 or 60 minutes at 400°C. Atmosphere was pure hydrogen and compact fractional green density was 0.86.

is also included as a reference. The 60 min hold results in 50 to 100 MPa higher strength at a given sinter temperature than the no hold counterparts. Figure 4.10 shows a similar plot for specimens sintered with 20°C/min heating rates. Again the corresponding no hold data from Figure 4.7 has been included for reference. The 60 min isothermal hold results in approximately 100 MPa higher strength for a given sinter temperature.

Similar to the *in situ* result presented in Figure 4.4, specimens were also sintered with isothermal holds at 400°C and subsequently sintered to higher peak sinter temperatures before cooling. One set was sintered using 10°C/min heating rates and a 20 minute hold while the other set used 20°C/min heating rates and a 60 minute hold. As is evident from the TRS versus temperature result, shown in Figure 4.11, there is little difference between either condition.

4.3 Additional Sintering Outcomes

Further measurements were made of the bronze compacts to evaluate other sintering responses that account for strengthening. These are densification, grain growth, and neck growth. Experimental measurement of densification and grain growth were discussed in Section 3.4 and 3.8, respectively. A qualitative observation of neck growth was made using the fracture surface scanning electron microscope images described in Section 3.1.3.

4.3.1 Densification

Sinter shrinkage was measured by the dilatometric technique discussed in Section 3.4. Bronze transverse rupture bar compacts, prepared as described in Section 3.1.5 to a fractional green density of 0.86, were sintered in the dilatometer at 10°C/min to 800°C in pure hydrogen. Two separate runs were performed, one in the press direction, the other in the transverse direction. The results from these runs are both shown in Figure 4.12 as plots of percent shrinkage versus sinter temperature. As is evident by these plots, there is very little dimensional change throughout the sintering range. The press direction swells by 0.25% until approximately 400°C where it begins to shrink continuously for the remainder of the run. Ultimately, this dimension shrinks by the same percentage (0.25%) from the original value. The axial direction on the other hand, swells continuously until nearly 600°C where it reaches a maximum dimensional change of 0.6%. Above 600°C, this dimension also begins to shrink at approximately the same rate as the press direction. The final shrinkage is still approximately 0.2% larger than the original value. As discussed in Section 2.3, the initial swelling of the pressed dimension is consistent with the observations of Lenel *et al.* [40-42].

These shrinkage values do not represent significant sintering densification, as is common with press and sinter P/M components [1,2]. This observation is more evident when the data of Figure 4.12 are translated into fractional density using Equation 3.13. The plot of *in situ* fractional density versus sintering temperature is shown in Figure 4.13. The fractional density variation is less than 0.005 throughout the sintering range and the final sintered density is nearly the same as the green density.

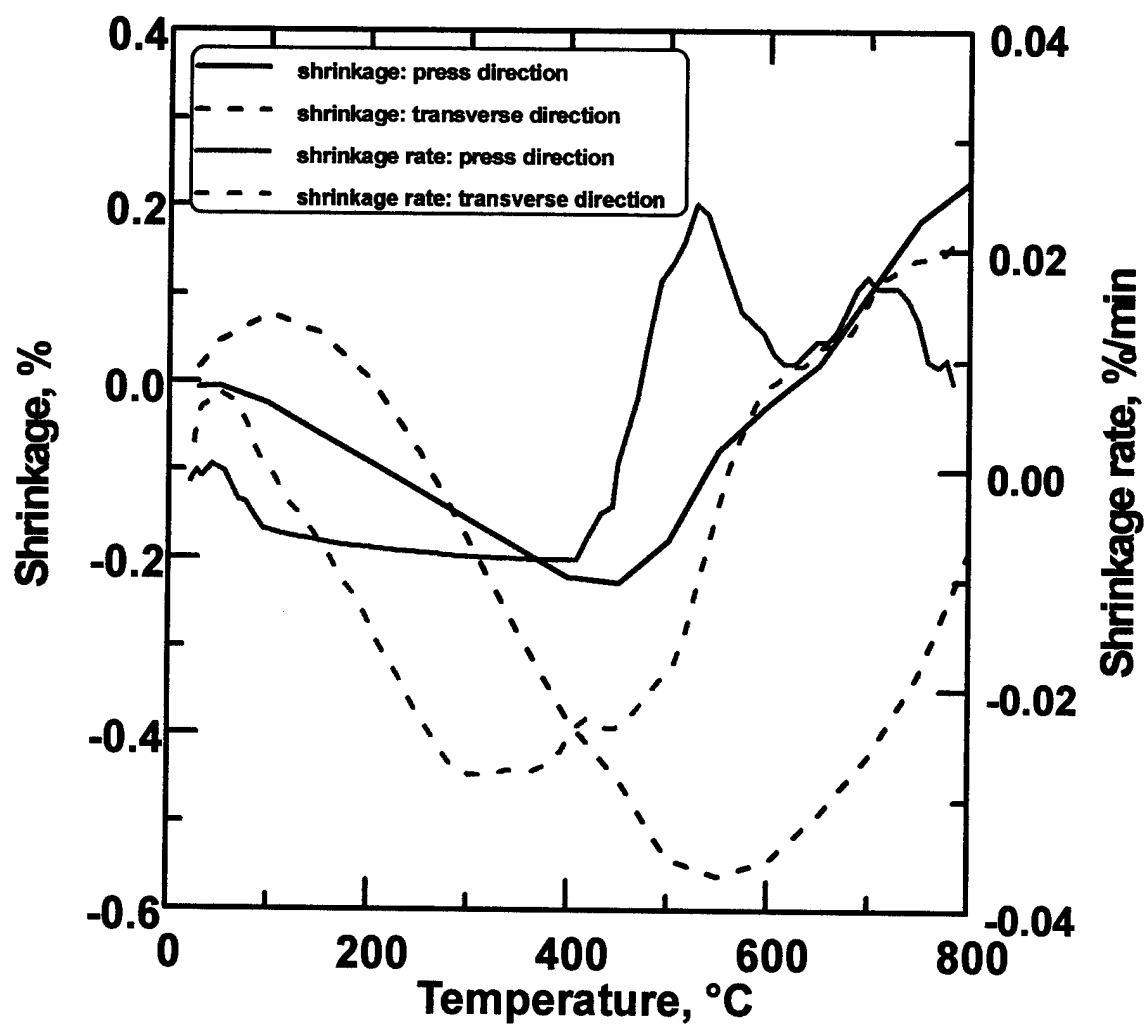


Figure 4.12: Dilatometric plot of shrinkage and shrinkage rate in transverse and press directions versus temperature for prealloyed 90Cu-10wt.%Sn bronze compact sintered at 10°C/min in hydrogen.

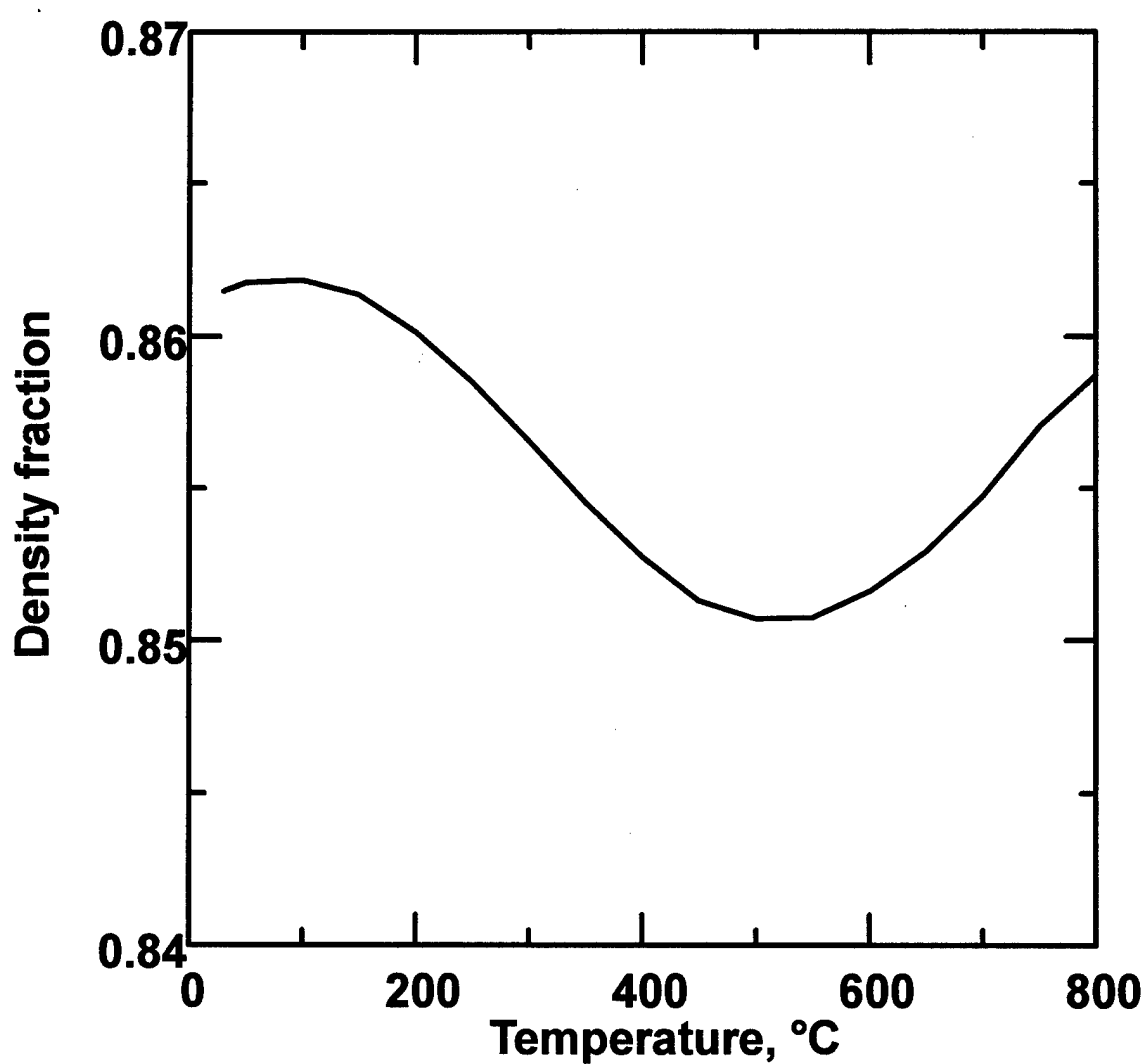


Figure 4.13: Dilatometric plot fractional density versus temperature for prealloyed 90Cu-10wt.%Sn bronze compact sintered at 10°C/min in hydrogen. Little densification is observed throughout the range.

4.3.2 Grain Growth

Grain size measurements were performed on sintered bronze compacts that were water quenched from 400°C, 500°C, and 600°C, as described in Section 3.6. These temperatures correspond to the range of significant strengthening observed in Figure 4.1. Since grain size affects strength [1,2], quenched specimens over this range were selected to determine the existence of grain growth. Compacts were mounted and polished according to procedures described in Section 3.7. The combination of point and line intercept methods described in Section 3.8 were used to statistically determine a characteristic grain size for each of the quenched samples. Typical optical micrographs from each temperature used in the procedures are shown in Figures 4.14 through 4.16. A characteristic grain size versus temperature is shown in Figure 4.17. As is evident from this figure, significant grain growth is observed through 600°C.

4.3.3 Neck Growth

Scanning electron microscope images of various transverse rupture bar fracture surfaces are shown in Figures 4.18 through 4.22. These fractures were formed during room temperature TRS tests of bronze specimens which had been sintered at 10°C/min in hydrogen to various peak temperature from 400°C to 800°C. A characteristic sintered neck size between particles was identified by regions of ductile fracture dimples on the particle surfaces. Such observations indicated the progression of neck size which is one of the dominant sources of sintered strength.

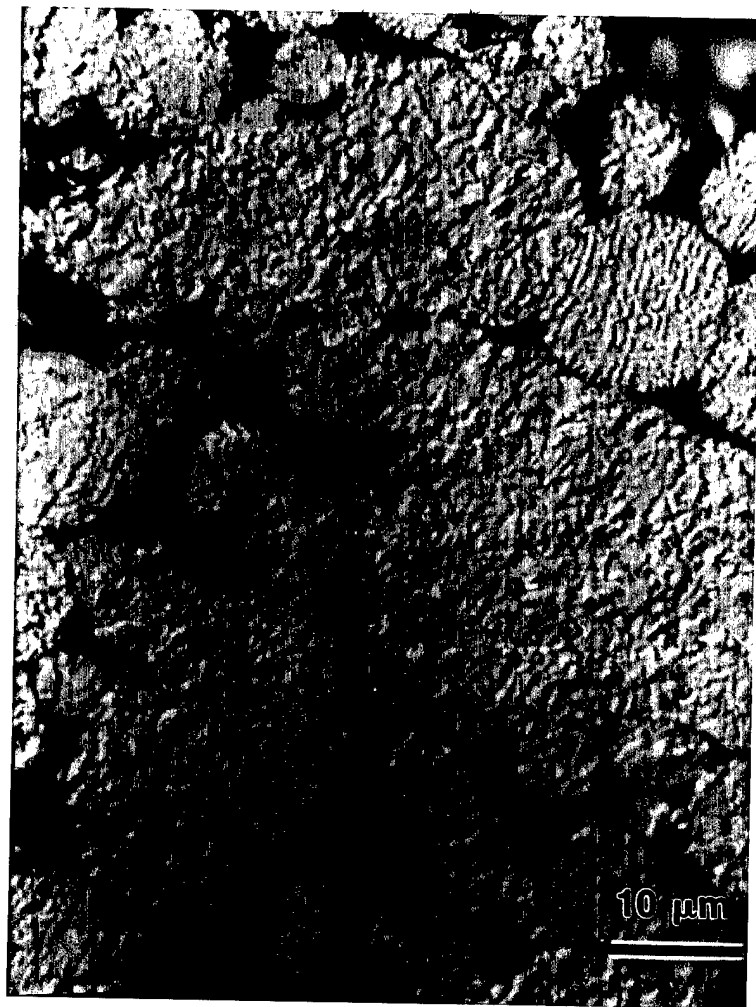


Figure 4.14: Optical micrograph of prealloyed 90Cu-10wt.%Sn bronze compact sintered to 400°C at 10°C/min in hydrogen and water quenched to room temperature at approximately 10³°C/s.



Figure 4.15: Optical micrograph of prealloyed 90Cu-10wt.%Sn bronze compact sintered to 500°C at 10°C/min in hydrogen and water quenched to room temperature at approximately 10^3 °C/s.

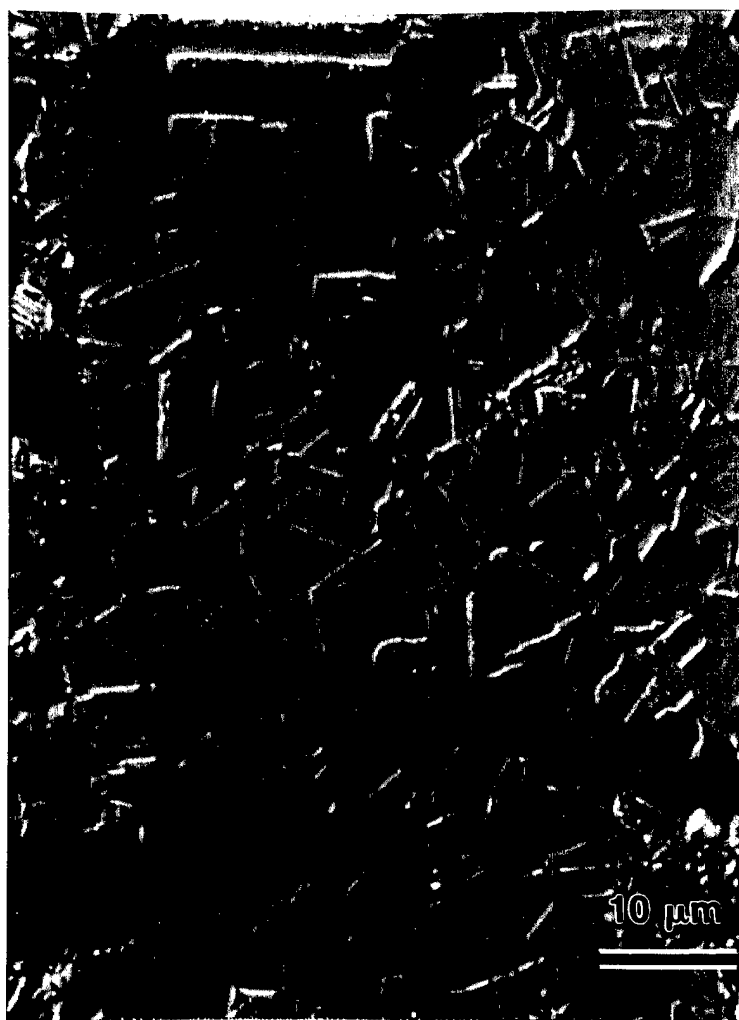


Figure 4.16: Optical micrograph of prealloyed 90Cu-10wt.%Sn bronze compact sintered to 600°C at 10°C/min in hydrogen and water quenched to room temperature at approximately 10³°C/s.

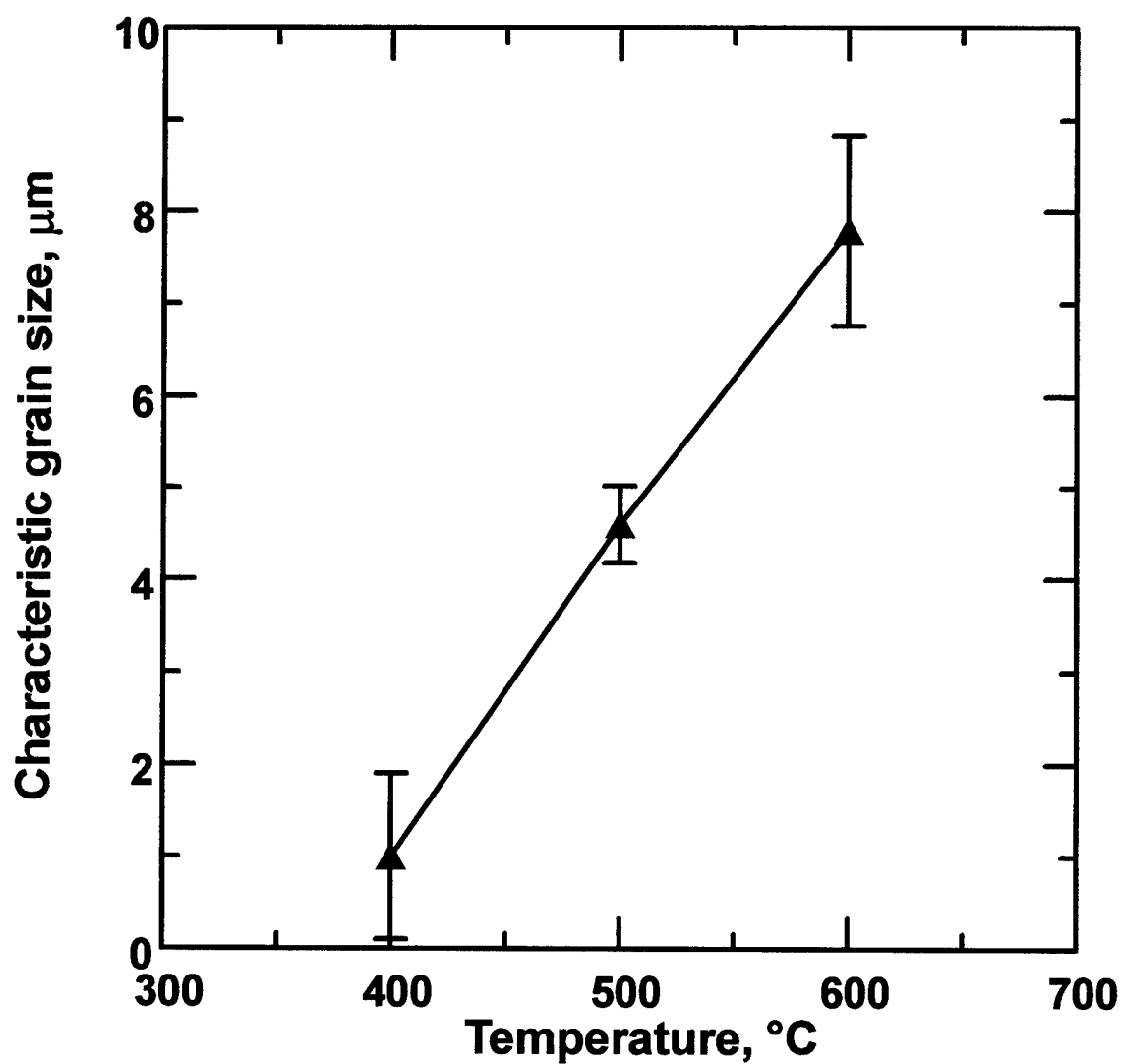


Figure 4.17: Characteristic grain size versus temperature for prealloyed 90Cu-10wt.%Sn bronze compact sintered at 10°C/min in hydrogen. Error bars represent the measurement uncertainty (90% confidence interval).



Figure 4.18: Fracture surface scanning electron microscope image of transverse rupture bar fabricated from prealloyed 90Cu-10wt.%Sn bronze powder and tested at room temperature after sintering at 10°C/min in hydrogen to 400°C. Almost no interparticle bonding was indicated at this degree of sintering. Compact fractional green density was 0.86.

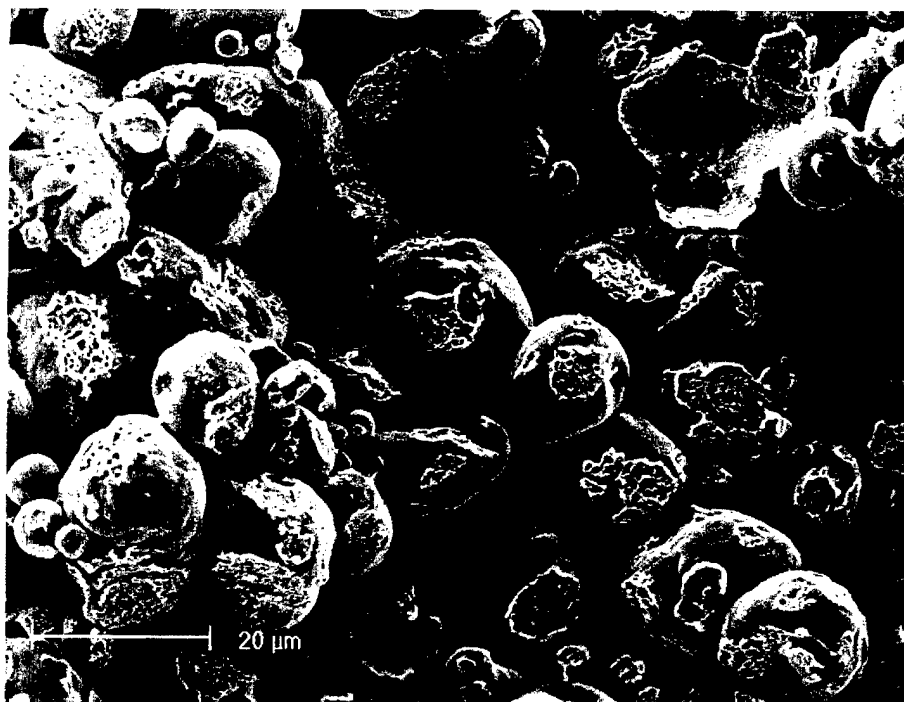


Figure 4.19: Fracture surface scanning electron microscope image of transverse rupture bar fabricated from prealloyed 90Cu-10wt.%Sn bronze powder and tested at room temperature after sintering at 10°C/min in hydrogen to 500°C. Interparticle bonds were less than $\frac{1}{4}$ hemispherical area at this degree of sintering. Compact fractional green density was 0.86.



Figure 4.20: Fracture surface scanning electron microscope image of transverse rupture bar fabricated from prealloyed 90Cu-10wt.%Sn bronze powder and tested at room temperature after sintering at 10°C/min in hydrogen to 600°C. Interparticle bonds were between $\frac{1}{4}$ and $\frac{1}{2}$ hemispherical area at this degree of sintering. Compact fractional green density was 0.86.

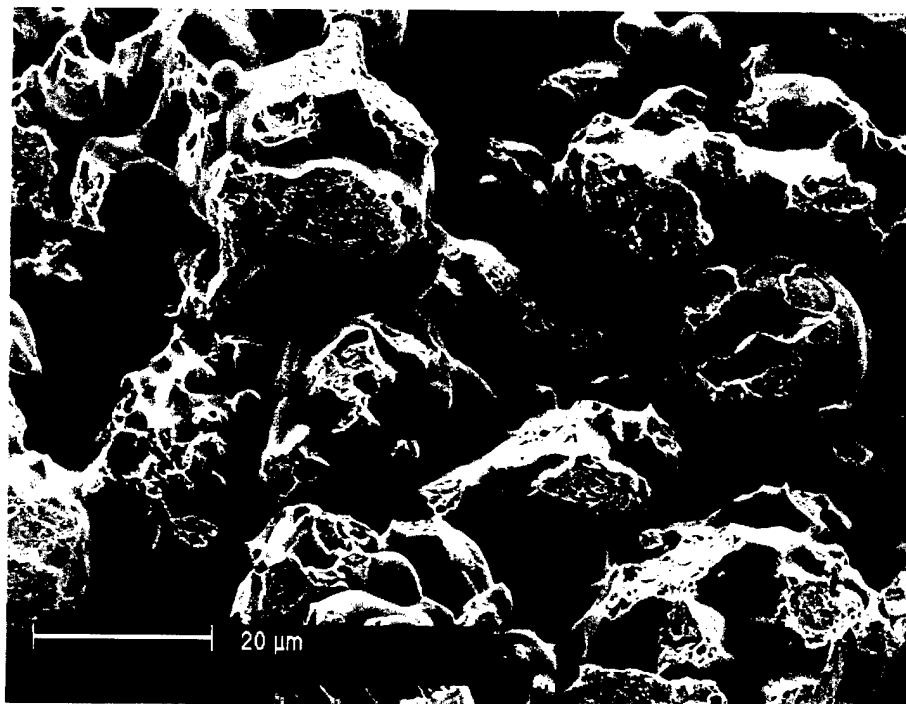


Figure 4.21: Fracture surface scanning electron microscope image of transverse rupture bar fabricated from prealloyed 90Cu-10wt.%Sn bronze powder and tested at room temperature after sintering at 10°C/min in hydrogen to 700°C. Interparticle bonds were greater than $\frac{1}{2}$ hemispherical area at this degree of sintering. Compact fractional green density was 0.86.

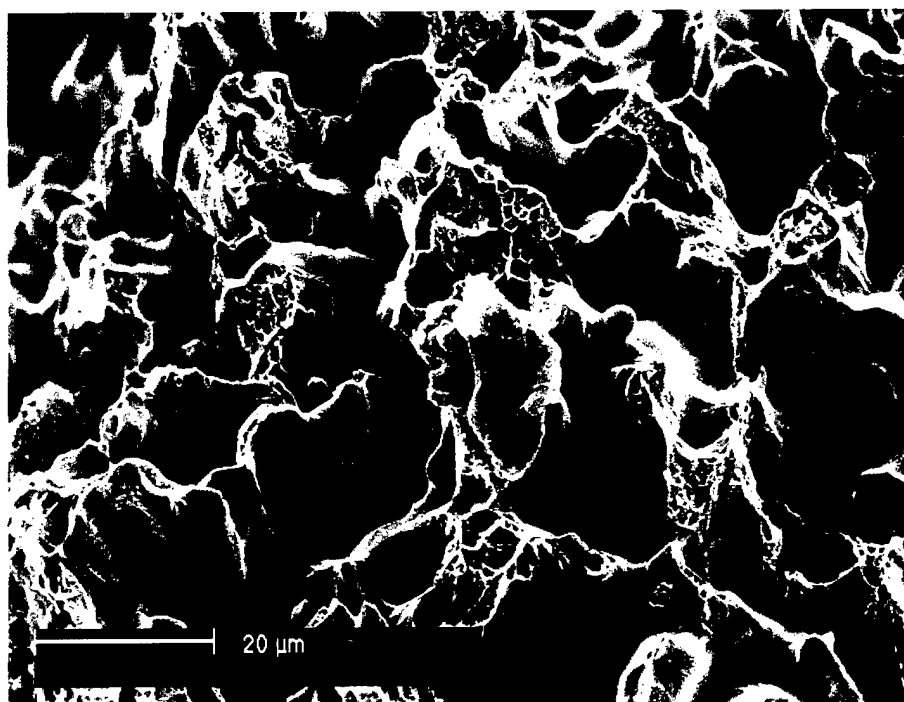


Figure 4.22: Fracture surface scanning electron microscope image of transverse rupture bar fabricated from prealloyed 90Cu-10wt.%Sn bronze powder and tested at room temperature after sintering at 10°C/min in hydrogen to 800°C. Significant fracture surface tearing due to high degree of interparticle bonding was evident at this degree of sintering. Compact fractional green density was 0.86.

Almost no contact area was evident in the specimen sintered to 400°C (Figure 4.18). The sintered neck size increased to approximately 20% hemispherical particle area in the sample sintered to 500°C (Figure 4.19) and to more than 50% in the sample sintered to 700°C (Figure 4.21). As shown in Figure 4.22 (sintered to 800°C), ultimately the interparticle bond area increases to the point that the fracture results in a high degree of fracture surface tearing and transparticle fracture. The high degree of deformation associated with such tearing precluded any assessment of the interparticle contact area at this degree of sintering.

4.4 Bulk Material Characteristics

Strength is strongly influenced by the mechanisms of sintering that lead to interparticle bonds. Once bonded, the overall strength of the compact in turn depends on the strength of the particles themselves. This is the strength of the bulk material and would parallel that of a homogenous fully dense bronze alloy. A complete evaluation of the strength evolution during sintering must therefore include the characteristics of the bulk material in response to the thermal environment.

4.4.1 Melting

The temperature corresponding to the formation of the first liquid in an alloy is referred to as the solidus while the temperature where the full transformation to liquid is complete is referred to as the liquidus. Formation of a liquid phase in the compact would have a direct impact on the strength. The phase diagram for 90Cu-10wt.%Sn bronze alloy

predicts solidus and liquidus temperatures of 861°C and 1015°C, respectively [82]. These melting transition points were verified for the as received bronze powder using differential thermal analysis (DTA) as described in Section 3.4. As discussed in that section, the test was performed twice to account for any difference between the powder and the homogenous material. This DTA plot for the range where temperature deviation occurs is shown in Figure 4.23. Solidus and liquidus temperatures of the powder are determined to be 851°C and 1016°C, respectively, from the first cycle and 862°C and 1016°C, respectively, from the second cycle. Different values of solidus temperature are obtained because the powder was fabricated by gas atomization where solidification is a non-equilibrium event. This type of cooling results in a depressed solidus temperature. During the second cycle the solidified melt is well homogenized and does not exhibit a depressed solidus temperature. Both the solidus and liquidus from the second cycle are in good agreement with the phase diagram values of 861°C and 1015°C. This result helps verify the alloy composition of the powder. Furthermore, within the range of measurements in this research, it can be concluded that the formation of a liquid in the powder will not be a factor in compact strength.

4.4.2 Phase Evaluation

The low temperature phase diagram, as discussed in Section 3.9, predicts a transition from a two phased microstructure to a single α -Cu phase at 340°C for 90Cu-10wt.%Sn bronze. Dowson [26] observes that a two phased microstructure is rarely the case in powder due to the extremely slow cooling rate, from above the transition

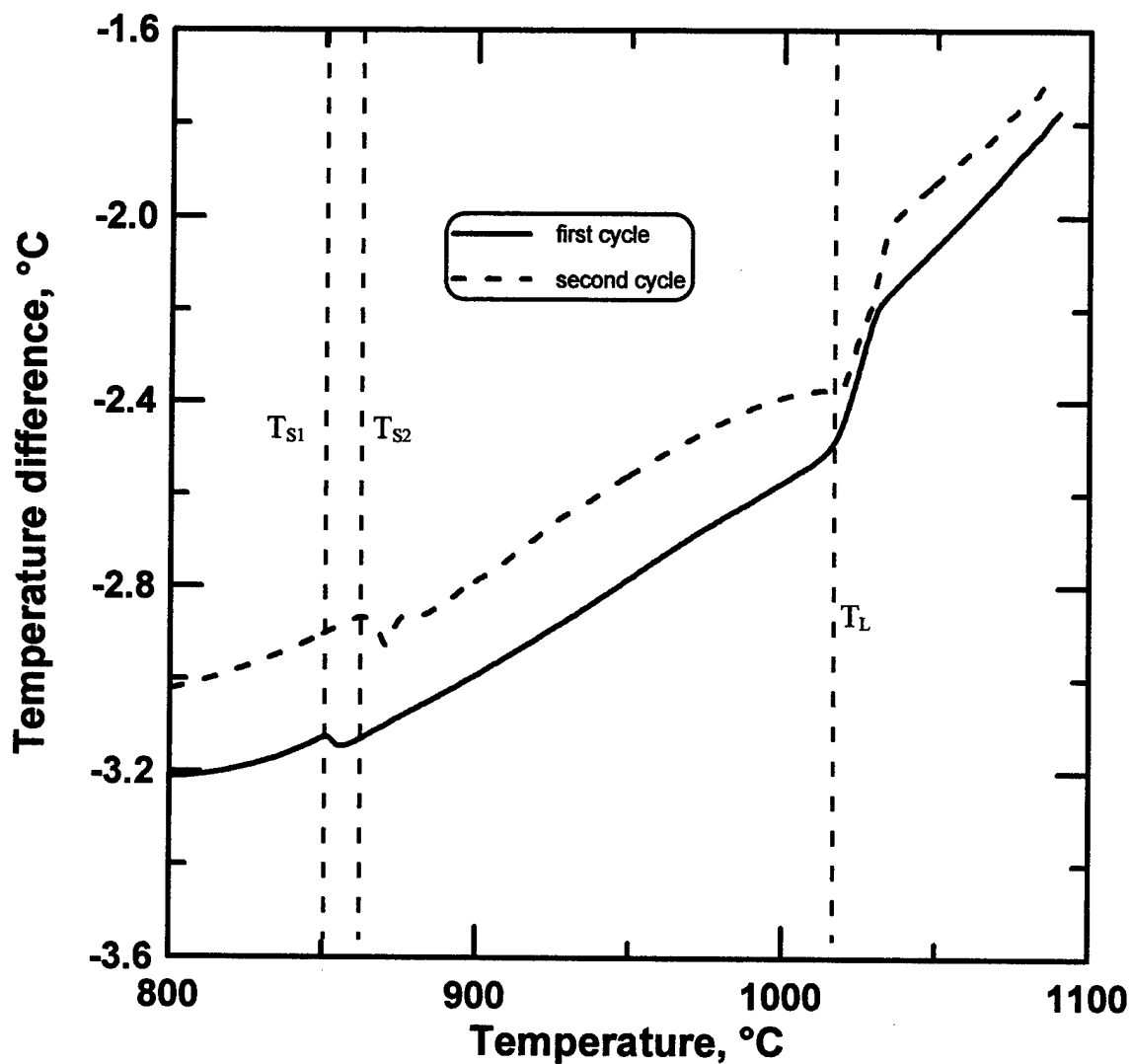


Figure 4.23: Differential thermal analysis (DTA) plot of temperature difference versus temperature showing two continuous cycles for prealloyed 90Cu-10wt.%Sn bronze. Cycle profiles consisted of 5°C/min heating to 1100°C, cooling to room temperature, followed by a reheat to 1100°C at the same rate. Argon atmosphere used throughout. The solidus temperature from the first and second cycles are indicated by T_{S1} and T_{S2} , respectively. The liquidus temperature from both cycles is indicated by T_L .

temperature, required to decompose the α -Cu phase. A slow cooling rate is far from reality in industrial practice and certainly in atomized powder production. X-ray diffraction measurements were made to determine if any phase changes occur in the sintering compacts which could impact the mechanical properties. The technique described in Section 3.9 was used to obtain these measurements. Diffraction patterns of the as received powder as well as sintered compacts, quenched from maximum sintering temperatures of 400°C, 500°C and 600°C, are shown in Figures 4.24, 4.25, 4.26, and 4.27, respectively. Also included in these figures are the peaks for α -Cu as well as the unique peaks of ϵ -bronze adapted from the cataloged data found in the *Powder Diffraction File (PDF)* [83]. The as-received powder pattern in Figure 4.24 shows peaks aligned with all α -Cu reference peaks. The only possible peak aligned with an ϵ -bronze reference is an approximately 0.1 relative intensity pattern at a 2 Theta of 77°. This is the highest intensity peak that is unique to the *PDF* pattern of ϵ -bronze. The same observations can be made for the specimen quenched from 400°C shown by Figure 4.25. Samples quenched from 500°C and 600°C, shown in Figures 4.26 and 4.27, respectively, show only the α -Cu peaks. A further observation in these figures is in the shape of the diffraction peaks. The lower temperature specimens show a smearing of all but the strongest peak. The patterns of both the specimens quenched from above 400°C show sharp, well defined peaks.

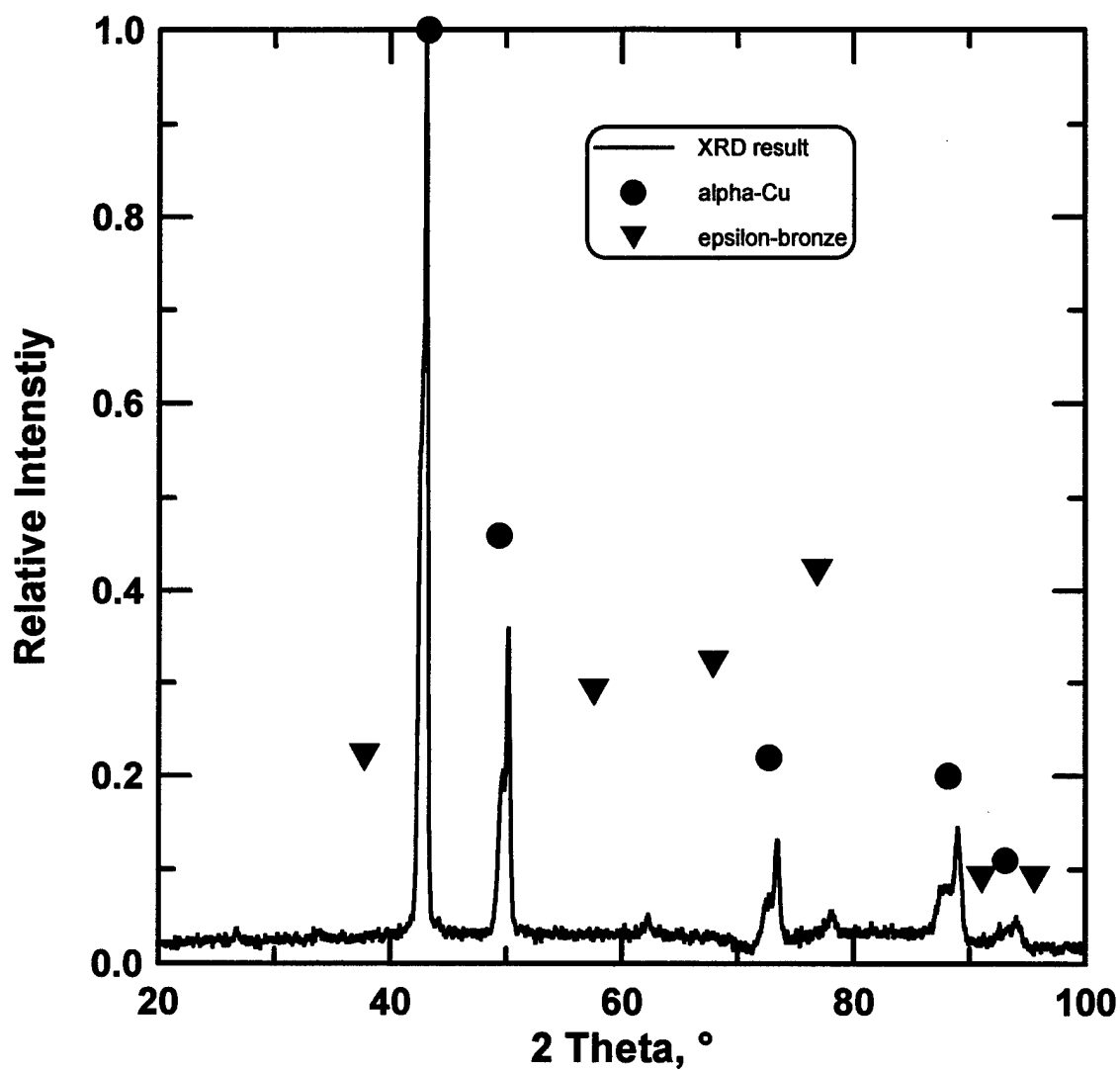


Figure 4.24: X-ray diffraction pattern of as-received prealloyed 90Cu-10wt.%Sn powder. Peaks of cataloged pattern [83] for α -Cu as well as the unique significant peaks for ϵ -bronze are included as a reference. Intensity normalized to maximum value.

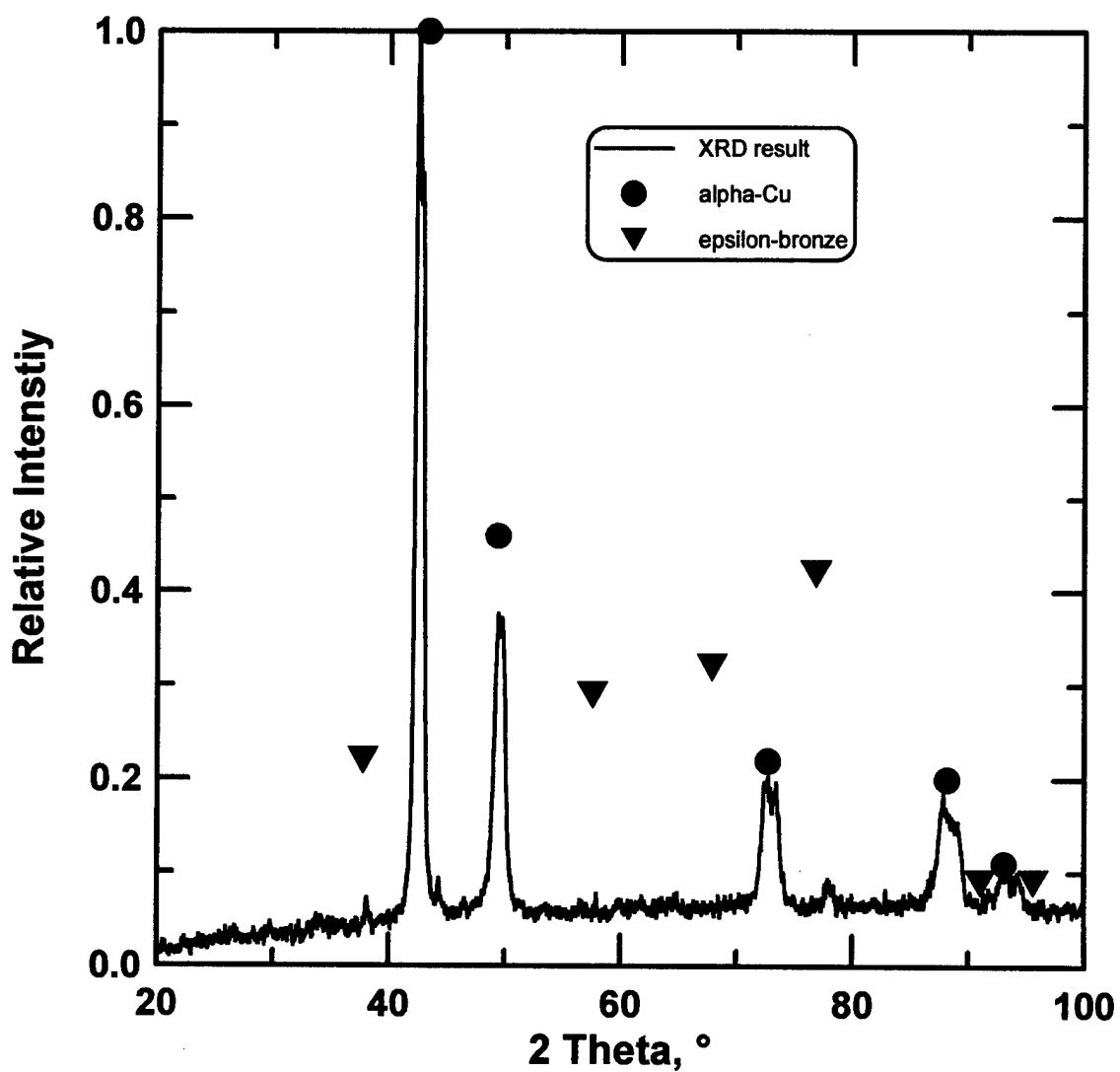


Figure 4.25: X-ray diffraction pattern of prealloyed 90Cu-10wt.%Sn compact water quenched from 400°C after sintering at 10°C/min in hydrogen. Cataloged patterns, depicted by significant peaks, for α -Cu as well as the unique significant peaks for ϵ -bronze are included as a reference. Intensity normalized to maximum value.

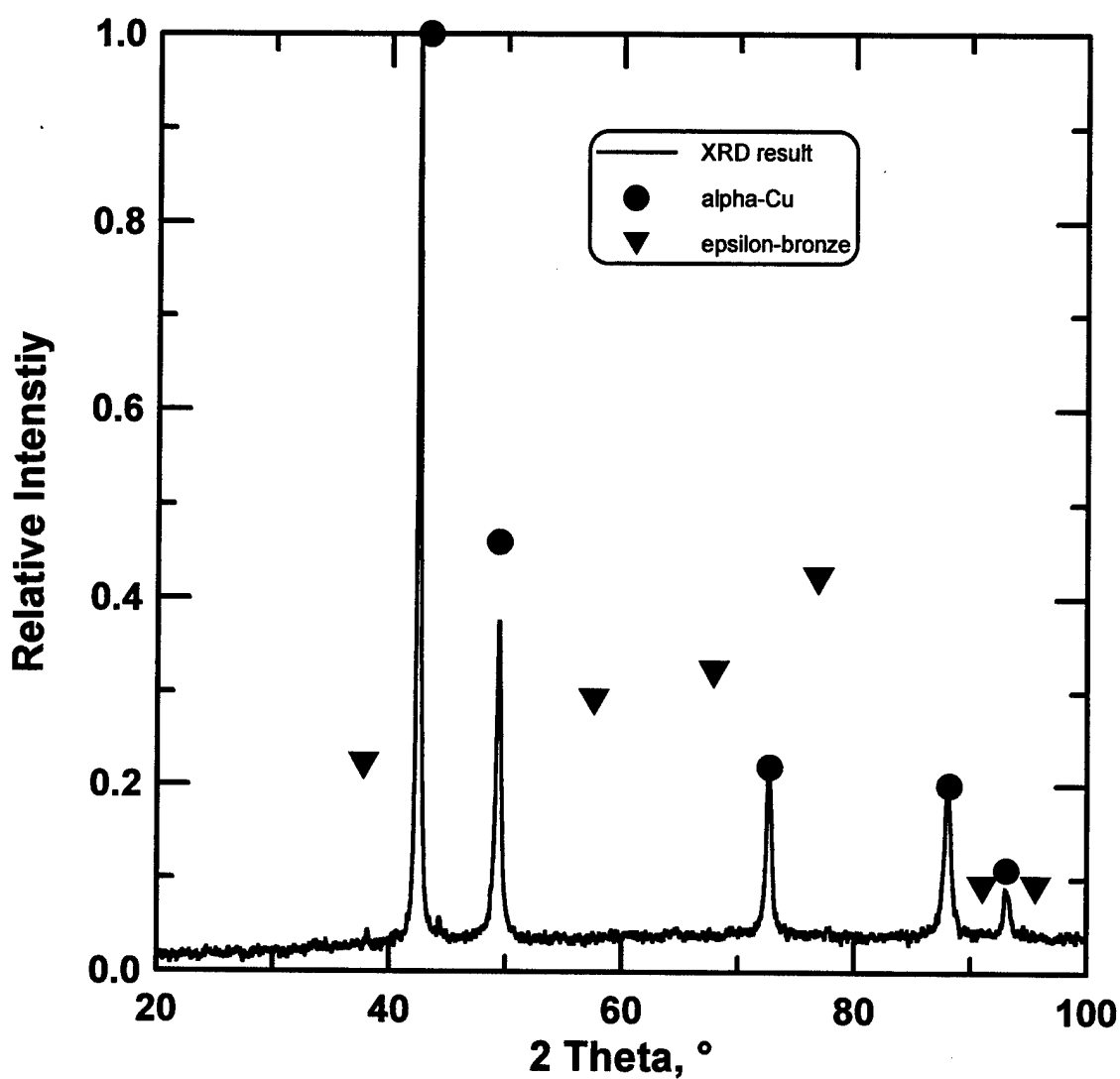


Figure 4.26: X-ray diffraction pattern of prealloyed 90Cu-10wt.%Sn compact water quenched from 500°C after sintering at 10°C/min in hydrogen. Cataloged patterns, depicted by significant peaks, for α -Cu as well as the unique significant peaks for ϵ -bronze are included as a reference. Intensity normalized to maximum value.

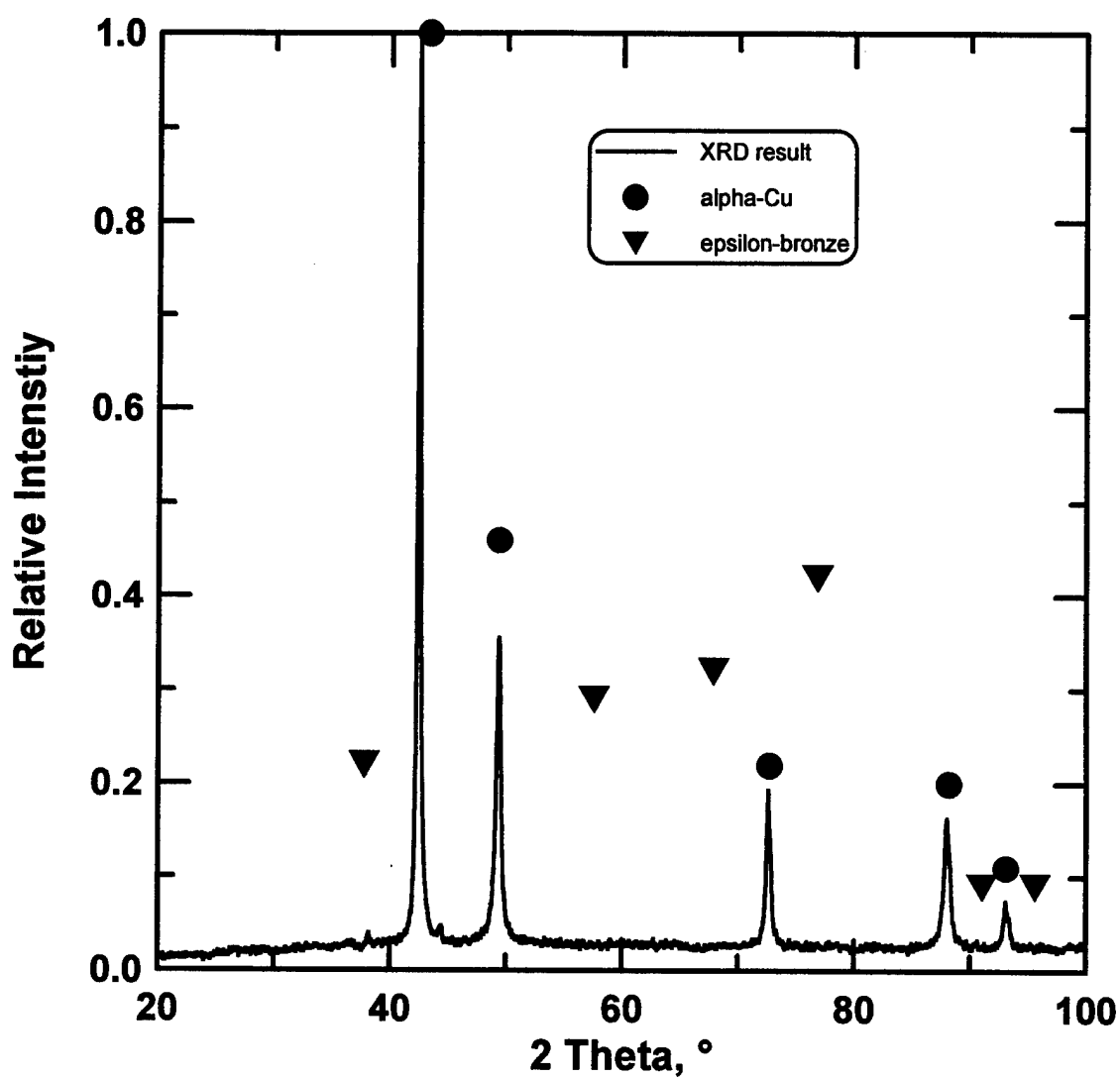


Figure 4.27: X-ray diffraction pattern of prealloyed 90Cu-10wt.%Sn compact water quenched from 600°C after sintering at 10°C/min in hydrogen. Cataloged patterns, depicted by significant peaks, for α -Cu as well as the unique significant peaks for ϵ -bronze are included as a reference. Intensity normalized to maximum value.

4.4.3 Thermal Softening

Transverse rupture strength measurements were performed on TRB specimens that had been sintered to high density. As described in Section 3.3, these measurements were made in the FTT at temperatures up to 857°C on TRBs with a density fraction of 0.96. All measurements were from TRBs heated to the test temperature at 10°C/min in hydrogen. The load measurement from the FTT was used in Equation 3.12 to calculate the transverse rupture strength at each test temperature. These results are presented in Appendix C, Table C-1, and graphically shown as TRS versus test temperature in Figure 4.28. This approximation of the thermal softening behavior of wrought bronze shows a loss of strength of over 75% by 600°C and a 93% loss by 850°C. A further observation is the comparison between the test temperatures repeated with isothermal holds. Both the repeated points at 500°C (test C4 and C5) and 700°C (test C7 and C8) show no difference in TRS with or without a pre-test hold.

4.4.4 Hardness

Microhardness measurements were performed according to the experimental method of Section 3.10 on the as-received powder as well as specimens which were water quenched from 400°C, 500°C, and 600°C. Quenching from these temperatures was performed after sintering at 10°C/min in hydrogen according to procedures specified in Section 3.6. Prior to hardness measurements, all specimens were mounted and polished according to procedures detailed in Section 3.7. Figure 4.29 shows that the hardness

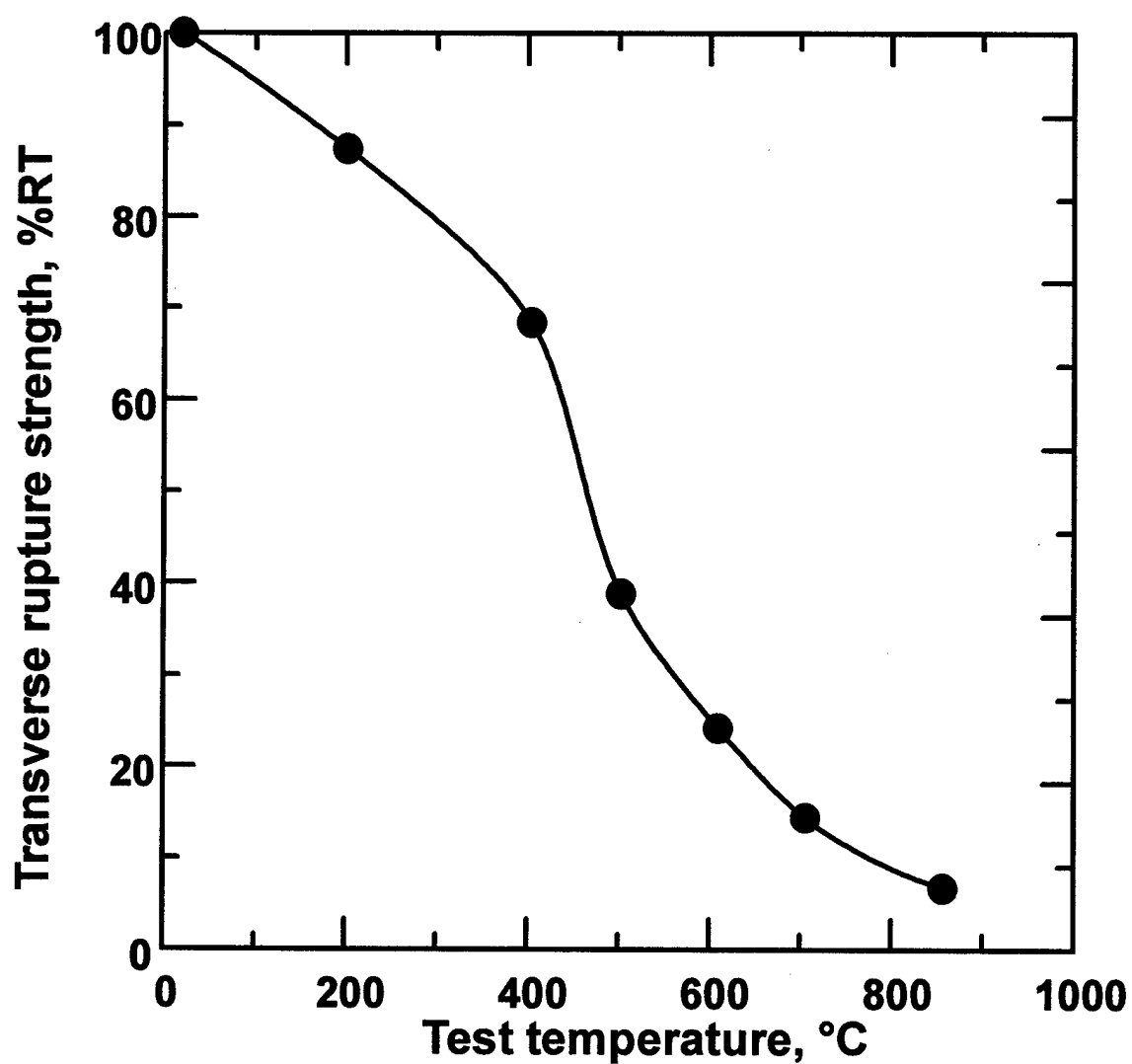


Figure 4.28: Transverse rupture strength normalized to room temperature strength versus test temperature for high density prealloyed 90Cu-10wt.%Sn compacts. Heating to test temperature was 10°C/min in hydrogen and compact fractional density was 0.96.

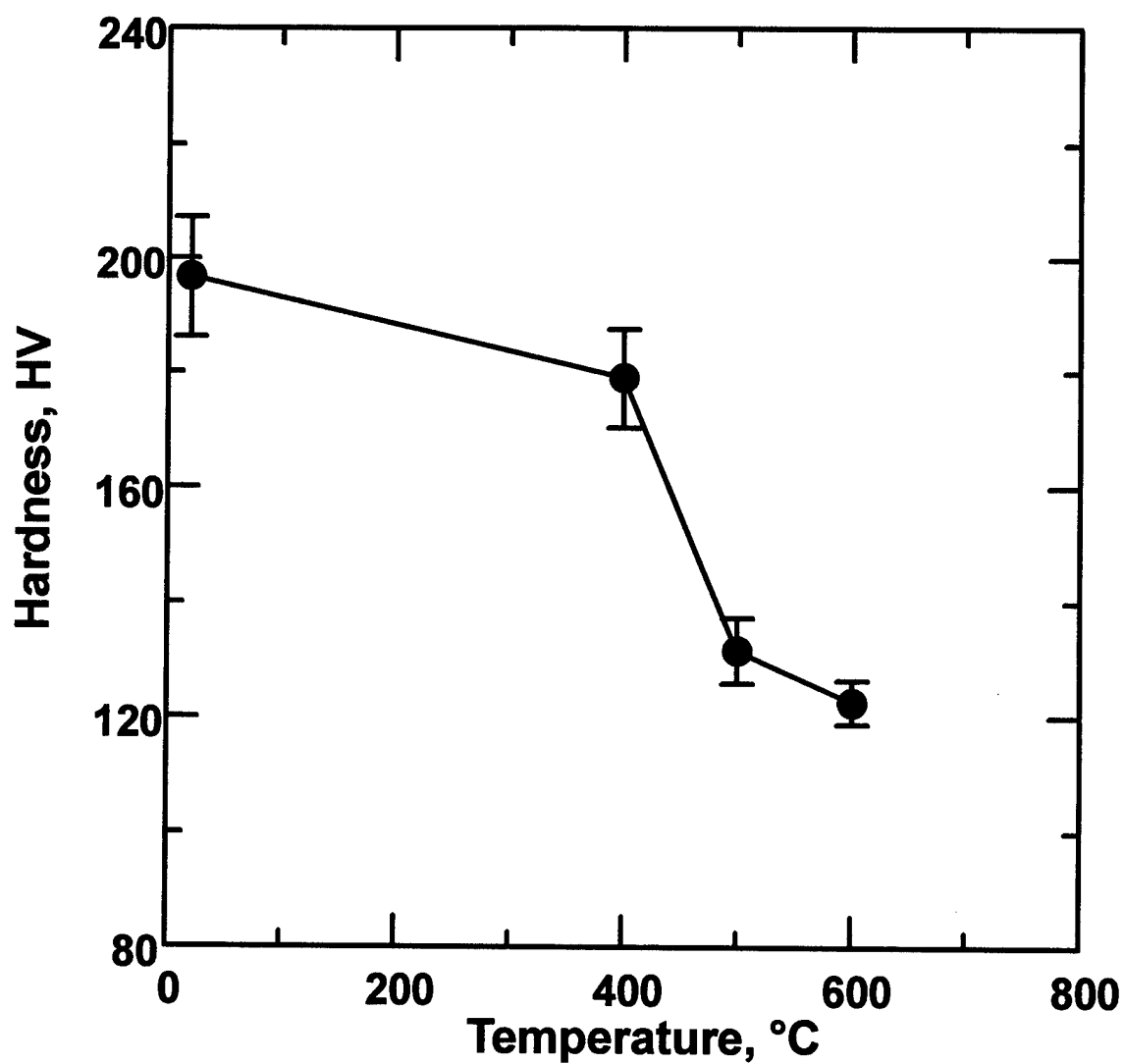


Figure 4.29: Microhardness versus temperature of as-received prealloyed 90Cu-10wt.%Sn bronze powder compacts water quenched after sintering at 10°C/min in hydrogen to 400°C, 500°C and 600°C. Error bars represent the measurement uncertainty (90% confidence interval). Fractional green density was 0.86.

decreases with progressively higher temperatures. Approximately half the hardness is lost from room temperature to 600°C with the most significant change occurring near 400°C.

Chapter 5

Modeling

The following chapter details the model development and its subsequent implementation for thermal cycle design. The development sections will present the specifics of each portion of the model and define the critical experimental data required to determine the key constants. The implementation section will detail the programming and operation of the resulting model into personal computer (PC) based software.

5.1 Model Development

Using insights gained from the experimental results, the development of a predictive model for *in situ* strength evolution followed the concept outlined in Section 2.5. These results, as presented in Chapter 4, were used both as a guide to determine the dominant mechanisms of *in situ* strength evolution and as inputs to determine the model parameters associated with those mechanisms.

5.1.1 Green Strength

Green strength is the strength that results from the initial shaping step for a powder component. It is the handling strength of the component prior to sintering. In powder injection molding, the green strength is influenced by the addition of a binder phase that is largely removed prior to sintering. For compacted parts, common to press and sinter

components and measured in this research, the green strength is the direct result of mechanical cold working during the compaction step. As discussed previously in Section 2.5.1, the measured green strength is often a key measure of success for the compaction step.

Also discussed in that section was that several attempts have been made to model green strength as a function of the various process parameters associated with this compaction step [5-8,53,84]. Table 5.1 presents several examples of these models. Model parameters in this table include powder apparent density, compacted density, compaction pressure, particle shape, as well as other empirical constants. It is not the intent of this research to determine the validity of these models, or to formulate a new model applicable to compacted bronze test specimens. Therefore, the measured value of green strength (σ_G), as determined in Section 3.1.6, is used as the initial strength input of the *in situ* strength evolution model.

5.1.2 Annealing

As discussed in the previous section, green strength is a direct result of cold working the powder during the compaction step. Since strength due to cold working is lost to recrystallization during thermal processing [47,63], so too is a portion of the green strength lost during sintering. The Arrhenius temperature dependence for annealing suggested by Reed-Hill and Abbaschian [47] is modeled by reducing the green strength

Table 5.1: Strength of compacted particles as a function of compaction parameters.

Strength (σ)	Reference
$\sigma = A (f-f_0) / (1-f_0)$	5
$\sigma = A [(f-f_0) / (1-f_0)]^2$	5,8,53
$\sigma = A (1-f)^{2/3}$	5
$\sigma = A \exp(B(f-1))$	5,84
$\sigma = A \sigma_0 f^M$	8
$\sigma = \sigma_1 P^M$	6
A,B,M = empirically determined constants	
f, f_0 = compacted and apparent fractional density	
σ_0 = wrought strength	
σ_1 = green strength at 1 MPa compaction pressure	
P = compaction pressure in MPa	

(σ_G) by the portion of strength lost during the recrystallization phase of annealing . This type of model is represented by Equation 5.1;

$$\sigma_R = \sigma_G \left[1 - A \exp\left(\frac{Q_R}{RT}\right) \right] \quad (5.1)$$

where A is an empirically determined constant, σ_G is the green strength at room temperature in MPa, Q_R is the empirically determined activation energy of recrystallization in kJ/mol, R is the gas constant ($8.314 \cdot 10^{-3}$ kJ/mol-K), and T is the absolute temperature in K. This annealing model depends only on the temperature. For simple sintering cycles which consist solely of a single constant heating rate to temperature, this form is easily implemented. Such an annealing model was successfully used in the earlier work [85] for constant 10°C/min heating of bronze compacts. The obvious limitation is the requirement that the empirical constants be derived from experimental results of the same heating rate to be modeled. Additionally, since annealing is a diffusion controlled process that is *both* time and temperature dependent, this model will not accurately represent the effects of isothermal annealing.

A review of the results obtained with the nonisothermal kinetic models [50,51,52] discussed in Section 2.5.2 failed to disclose any with a clear advantage over the others. All require a rather extensive set of experimental results to determine the relevant constants with any degree of certainty. Beretka [86] performed an extensive analytical comparison of 11 different kinetic models as applied to solid-state reactions between powders. In this work he fit diffusion reactions of seven different powder systems which

he experimentally measured as well as the published tabulated data from three additional systems. He concluded that when fitting to 100% of the reaction, the three dimensional diffusion equation first proposed by Jander [87] is clearly superior.

This model, also recommended for reactive P/M processes by German [2], is represented by Equation 5.2;

$$1 - (1 - \beta)^{1/3} = \Gamma t^{1/2} \quad (5.2)$$

where β is the fraction transformed, Γ is a rate constant in units of inverse root time, and t is time. The rate constant is a thermally activated term which follows an Arrhenius type law as shown in Equation 5.3;

$$\Gamma = \Gamma_0 \exp\left(-\frac{Q_R}{RT}\right) \quad (5.3)$$

where Γ_0 is the frequency factor in units of inverse root time, Q_R , R , and T are as defined for Equation 5.1. Since any sintering cycle has a dependency of temperature upon time,

$$T = T(t) \quad (5.4)$$

substitution Equation 5.4 and 5.3 into 5.2 results in an expression for the fraction transformed dependent on time alone which is valid to the point of full (100%) transformation. This expression is then differentiated with respect to time and integrated

from the beginning of the sintering cycle to the point of prediction. Finally, representing the fraction of the room temperature green strength (σ_G in MPa) lost during complete recrystallization by R_f , the evolution of the green strength during sintering as reduced by recrystallization is represented by Equation 5.5;

$$\sigma_R = \sigma_G (1 - R_f \beta) \quad (5.5)$$

where σ_R is the remaining green strength in MPa and β is the fraction transformed.

The critical experimental results for this portion of the model are the *in situ* strength measurements that are made prior to sinter strengthening. These data include measurements presented in Appendix A, Tables A-1 and A-2 and Figures 4.1 through 4.3 for *in situ* strength below approximately 450°C. The constants R_f , Γ_0 , and Q_R , of Equation 5.3 and 5.5 are determined by empirical fits of these data and σ_G in MPa is the measured green strength discussed in Section 5.1.1. This model was used successfully with similar data for W-20vol.%Cu (with an admixed Co sintering activator) in an earlier work [88]. With only four measurements in the presinter strengthening temperature range, the model predictions correlated to experimental results to a coefficient of greater than 0.98.

5.1.3 Sinter Strength

The most significant strengthening of any P/M component is by far that which is directly due to sintering. Many of the outcomes of sintering have direct impact on

strength. In fact, the measured room temperature strength of a sintered component is customarily referred to as the strength due to sintering. Indeed, it is this post-sinter strength that is the most frequently used metric to judge the success or failure of a sintering cycle.

5.1.3.1 Contributions of Sintering Outcomes

The growth of interparticle necks and therefore the area of the bond between powder particles is the most evident indication of initial stage sintering. Later stages of sintering are often indicated by decreases in porosity. Many models exist [53,54] which relate neck size or porosity to the strength of a compact. Of the many empirical models cataloged by Haynes [53,89-92] which account for the porosity effect on strength (σ), most take on forms similar to Equations 5.6 and 5.7;

$$\sigma = \sigma_0 (1 - \varepsilon)^N \quad (5.6)$$

$$\sigma = \sigma_0 \exp(-A\varepsilon) \quad (5.7)$$

where σ_0 is the wrought material strength, ε is the fractional porosity, and A and N are empirical constants. Haynes concluded, however, that with the exception of a few specialized cases, these models are inadequate because they fail to account for any factor but total porosity content.

Starting with the initial green strength of a compact as it begins sintering, Moon and Choi [7] concluded there was a direct strength dependence upon particle contact area. Their investigation centered around spherical copper but they also demonstrated the relationship held for published results of irregular shaped copper and spherical lead powder compacts. The direct dependence of contact area to strength was extended into initial stages of sintering by Nyce and Shafer [54] when researching spherical copper. They studied 115 and 48 μm copper powder compacts sintered to 850 and 950°C in hydrogen for various times. From the results they concluded that independent of powder size, transverse rupture strength (σ_T) followed a relationship similar to Equation 5.8;

$$\sigma_T = A \sigma_o \left(\frac{X}{D} \right)^2 \quad (5.8)$$

where A is an empirical constant, σ_o is the wrought strength, and X/D is the neck size ratio (interparticle neck diameter divided by particle diameter). Sintering conditions of time and temperature, while not directly expressed in Equation 5.8, have a direct impact to the sintering outcome of neck growth. Such a progression of neck size and therefore interparticle contact area is clearly evident in Figures 4.19 through 4.23. Sintering at constant 10°C/min in hydrogen to temperatures from 400°C to 800°C results in an evolution of interparticle contact area from negligible to well in excess of 50%.

semi-spherical area

Another outcome common to the later stages of sintering is grain growth. Research [55-58] has shown that all measures of strength in crystalline materials is directly

proportional to the inverse root of the grain size. This relation, customarily referred to as the Hall-Petch [55,56] relation after the first investigators in this area, is represented by Equation 5.9;

$$\sigma \sim \frac{1}{\sqrt{G}} \quad (5.9)$$

where σ is the strength and G is the grain size. The earlier work for bronze [85] modified Equation 5.8 with Equation 5.9 as well as a factor to include porosity evolution during sintering to define a model for sinter strengthening (σ_s). The resulting model had the form shown by Equation 5.10;

$$\sigma_s = \frac{A(1-\varepsilon)}{\sqrt{G}} \left(\frac{X}{D} \right)^2 \quad (5.10)$$

where A , ε , X/D , and G are as defined in Equations 5.7 through 5.9. This model required a considerable body of data to correlate the strength with the various sintering outcomes. Neck ratio and grain size in particular required a significant number of quenching studies to capture microstructural information at different stages of sintering.

Alternatively, several models exist to predict such sintering outcomes. German and Lathrop [93] modeled single mechanism sintering of spherical powders. Ashby followed a systematic approach to modeling material systems [94] and devised sintering maps [95]. These maps indicated the dominant mechanisms of sintering versus sintering parameters such as time, temperature and densification. Johnson [96] developed a

computer simulation of W-Cu composites which accounted for all stages of sintering and included both solid state and liquid phase sintering mechanisms.

All of these models require experimental determination of constants by correlation with experimental data. By additional approximations and adjustment of empirical values, each model can be fine tuned to precisely predict a particular sintering outcome. This is given that a data set matching the material and sintering conditions desired for the prediction is available to the investigator. Whereas strength is influenced by a multitude of sintering outcomes, a corresponding multitude of models (with their associated approximations and empirical adjustments) must be combined with one another. Since strength itself can be viewed as a sintering outcome, it makes sense that it be modeled directly based on the influence of sintering process parameters.

5.1.3.2 Master Sintering Curve

The master sintering curve (MSC) as proposed by Su and Johnson [59,60] lumps all thermally activated, time dependent influences on a particular sintering outcome into a single master parameter. This parameter (θ) has units of s/K and is found by integrating in time (t in s) from the beginning of the process to the prediction point as shown by Equation 5.11.

$$\theta = \int_0^t \frac{1}{T} \exp\left(-\frac{Q_s}{RT}\right) dt \quad (5.11)$$

In this expression R , T have the same definition as previously stated for Equation 5.1 and Q_s is the equivalent activation energy of sintering in units of kJ/mol. This equivalent activation energy is the only adjustable parameter in the relation and is intended to include the temperature dependence for all mechanisms present during a particular sintering cycle. This parameter is adjusted until the a plot of the sintering response (sinter strength in this case) versus the sinter parameter, independent of sintering path, fall on to the same master curve. The technique requires calculation of a set of MSC parameters (that represent the sintering path of each of the response data) and selection of an appropriate equation to correlate the sintering response to that set of parameters. The process is repeated with different values for Q_s and by graphical or numerical methods each result is compared. The Q_s used for the model is that which causes the response versus sinter parameter plot to best fit a single master curve. Degree of correlation between the response versus sinter parameter data and the single curve is judged by correlation coefficient, standard error or whatever statistic is deemed appropriate. Once the equivalent activation energy value is chosen, the expression of the single curve defines the correlation between θ and the sinter strength response (σ_s) as represented by Equation 5.12.

$$\sigma_s = \sigma_s(\theta) \quad (5.12)$$

As stated previously, the MSC technique is similar to that used by Shercliff and Ashby [52] for describing the annealing of aluminum alloys. Flynn [97] observed that many such thermally activated reactive kinetic processes have been modeled by similar

versions of what he referred to as the "Temperature Integral." Cited examples of the integral varied by the number and form of the empirical parameters used to describe the response. Flynn concluded that precise determination of these constants to provide the best correlation with data has been the greatest barrier to these methods. Reliance on sophisticated computational methods and technique of the investigator made success of one method over another difficult to repeat from one study to another. However, he further concluded that this type of modeling method has far greater utility now than in years past. The reason is not improved computational methods, but the availability of advanced computers that permit rapid testing and fit of data to a wide variety of complex kinetic models.

The MSC was the approach used for modeling the contributions to strength due to sintering. Sinter strengthening response data used were the baseline measurements described in Section 3.2. These data were presented in the tables of Appendix B and shown graphically in Figures 4.7 through 4.11. Included with the TRS response data in Appendix B are descriptions of the sintering cycles. Since the response correlated to the MSC parameter includes all contributions from sintering, Equation 5.11 must be evaluated through the entire sintering cycle. This includes; all heating ramps, isothermal holds, if any, and cooling to room temperature. Depending on the value ultimately chosen for the equivalent activation energy (Q_s), the contribution at lower temperatures is far less dominant than at peak temperatures of a given cycle. For best precision, however, this distinction cannot be made while performing the Q_s determination.

5.1.4 Thermal Softening

As discussed previously, available thermal softening data is typically far below sintering temperatures. *Smithells Metals Reference Book* [62] lists thermal softening data for wrought 0.5% phosphor bronze up to 500°C. The limited scope of published data requires an independent model for this research to adequately account for this effect. The Arrhenius model suggested by Dieter [63] and employed in the previous work [85] was dependent on temperature and an empirical thermal softening activation energy. This simplified model is valid for uniform strain rate and as shown by Equation 5.13, has no time dependency.

$$f_T = A \exp\left(\frac{Q_T}{RT}\right) \quad (5.13)$$

In this equation f_T is remaining room temperature strength fraction due to thermal softening, R and T have the same meaning as Equation 5.1, A and Q_T are empirical constants. As with other Arrhenius relations, Q_T is the activation energy in kJ/mol associated with the reaction. When applied to two different grades of bronze compacts [85], the model achieved correlation coefficients of greater than 0.99. Also in this work, the thermal softening model constants were determined using *in situ* strength data such as that shown in Figure 4.1. These data could also be used to derive other types of phenomenological models of the thermal softening strength fraction. Such correlation of temperature to strength fraction would be similar to that discussed in the previous section for MSC parameter and room temperature sinter strength.

The assertion made by the model represented in Equation 5.13, that temperature is the dominant factor in thermal softening, is supported by the results presented in Section 4.4.3. When comparing thermal softening measurements of high density bronze compacts, time had no observable impact on the strength fraction at a given temperature. Therefore other phenomenological temperature dependent models were considered using the available data. The first of these was based on the measurements derived from the FTT cooling tests presented in Section 4.1.3. As seen in Figure 4.5, all strength measurements from cooling tests follow the same curve shape between the peak temperature and room temperature. When normalized to room temperature strength, as depicted in Figure 4.6, curves derived from measurements that had peak temperatures of 600°C and above are self similar. Therefore another model considered was that which describes the normalized cooling curve derived from FTT cooling tests. A limitation of these data is that some degree of sintering continues during the initial portion of cooling. Models derived from these data would therefore not completely isolate the thermal softening effect.

The final model considered was derived directly from measurements of strength at temperature for high density bronze compacts. These data, presented in Section 4.4.3 and shown in Figure 4.29, effectively extend the temperature range of the published data [62]. They are also more precise representations of the subject material because they are from a densified compact of the same powder. As discussed earlier, these data also support the conclusion that temperature is a far more dominant factor than time in thermal softening. Each phenomenological model of strength fraction due to thermal softening was evaluated for precision of predicted results as well as availability of critical data. Regardless of the

path ultimately chosen, the strength fraction (f_T) as function of temperature (T in K), due to thermal softening, has the form of Equation 5.14.

$$f_T = f_T(T) \quad (5.14)$$

This fraction reduces the sinter strength calculated by Equation 5.12. It should be noted that given the substitution of the thermal profile, as denoted by Equation 5.4, this model can also be modeled as a pure time dependency. When summed with Equation 5.5, the final form of the evolution model to predict *in situ* strength (σ_{SE} in MPa) is represented by Equation 5.15.

$$\sigma_{SE} = \sigma_G (1 - R_f \beta) + f_T \sigma_s \quad (5.15)$$

As with the strength measurements discussed in Section 3.1.5, the effect of strain rate was not included in the *in situ* strength evolution model. Specimens that significantly deflect at high temperature can experience strain hardening. Since pre-fracture deformation increases with increasing compact strength, such a factor would scale roughly proportionally to strength. Although modeling this phenomena might improve prediction of absolute values of strength, it would not improve the prediction of strength evolution.

5.2 Model Implementation

The *in situ* strength evolution model was programmed into Lotus 1-2-3 release 5 for Windows spreadsheet software and carried out on a Gateway 2000 486/33E personal computer. The spreadsheet format offered ease of development and operation because of the direct graphical interface. Once the model constants are programmed, the only input is the time and temperature profile of the desired sintering cycle. The output is the *in situ* strength as tabulated and graphed by time or temperature. The program sequence is depicted in flowchart form in Figure D-1 of Appendix D. Separate sheets are devoted to the input sintering profile, each of the primary sub models discussed in Section 5.1, and the output. Examples of these sheets are also shown in the figures of Appendix D. These examples are based on model constants discussed in Chapter 6.

5.2.1 Process Profile Sheet

The thermal description of the sintering cycle is input via segments, each segment defined by its end time and thermal transition (ramp) rate. The process profile sheet initializes at room temperature. Each row increments on time by the time step input (Δt). The columns of the row then set segment flags (flag = 1 if true) based on the segment end time. The non zero flags then allow the appropriate ramp rate combined with the time step to increment the temperature column. Therefore each row begins with the instantaneous time and ends with the applicable temperature. An example of the first twenty rows and a sample graphical output of this sheet is depicted in Figure D-2. The

process indicated by the graph shows a 10°C/min heat to 400°C, a 20 min hold, continued 10°C/min heating to the peak temperature of 800°C, and a final 10 min hold.

5.2.2 Annealing Sheet

The integration of Equation 5.2 was accomplished numerically on this sheet. This technique integrates by summing incremental time slices of the function. The total fraction transformed by annealing of the i^{th} increment is based on Equation 5.16;

$$\beta_i = \beta_{i-1} + \frac{d\beta_i}{dt} \Delta t \quad (5.16)$$

where β_{i-1} is the fraction from the preceding increment, $d\beta_i/dt$ is the differential increment of the i^{th} segment and Δt is the same time step defined in Section 5.2.1. To determine the differential increment both sides of Equation 5.2 were differentiated with respect to time with the result shown by Equation 5.17.

$$\frac{1}{3} (1 - \beta)^{-2/3} \frac{d\beta}{dt} = \frac{1}{2} \Gamma t^{-1/2} \quad (5.17)$$

Rearranging this equation resulted in Equation 5.18.

$$\frac{d\beta}{dt} = \frac{3}{2} \Gamma \frac{(1 - \beta)^{2/3}}{t^{1/2}} \quad (5.18)$$

To remove the time dependency, the original expression was solved for root time to yield Equation 5.19.

$$t^{1/2} = \frac{1 - (1 - \beta)^{1/3}}{\Gamma} \quad (5.19)$$

Substitution of this expression back into Equation 5.18 yielded the expression for the differential of the i^{th} increment shown by Equation 5.20.

$$\frac{d\beta_i}{dt} = \frac{3}{2} \Gamma^2 \frac{(1 - \beta_{i-1})^{2/3}}{1 - (1 - \beta_{i-1})^{1/3}} \quad (5.20)$$

The rows of this sheet are also incremented on the time step defined in Section 5.2.1 and each included the time and temperature. The further columns of each row calculate the rate constant using Equation 5.3, the differential increment using Equation 5.20 and the fraction transformed using Equation 5.16. An example of the first twenty rows, cell formulas and a sample graphical output of this sheet is depicted in Figure D-3. The output corresponds the process profile in Figure D-2.

5.2.3 MSC Parameter Sheet

The integration of Equation 5.11 follows the same format used for annealing. Again the rows are incremented in time by Δt and each includes the time, temperature, the

MSC increment and summed MSC parameter . The increment of the MSC parameter (θ) for the i^{th} time increment is found by Equation 5.21;

$$\frac{d\theta_i}{dt} = \frac{1}{T_i} \exp \left(-\frac{Q_s}{RT_i} \right) \quad (5.21)$$

where T_i is the temperature of the i^{th} increment in K. Each increment is numerically summed by Equation 5.22 to find the summed MSC parameter of the i^{th} time increment;

$$\theta_i = \theta_{i-1} + \frac{d\theta_i}{dt} \Delta t \quad (5.22)$$

where θ_{i-1} is the summed MSC parameter from the previous row. An example of the first twenty rows, cell formulas and a sample graphical output of this sheet is depicted in Figure D-4. The output corresponds the process profile in Figure D-2.

5.2.4 *In situ* Transverse Rupture Strength Sheet

The final output is assembled on the *in situ* TRS sheet. Unlike all previous sheets, where numerical integration on time was performed, this sheet assembles the results of the previous calculations. Therefore, the output is generated based on any desired time increment. The example shown in Figure D-5 is based on an increment of one minute. Columns of each row include; the corresponding temperature, the fraction transformed by annealing from Equation 5.16, the green strength evolution in MPa as reduced by annealing from Equation 5.5, the summed MSC parameter from Equation 5.22, the sinter

strength from Equation 5.12, the thermal softening strength fraction from 5.14 and the *in situ* TRS in MPa from Equation 5.15. The example in Figure D-5 is of the first twenty rows, cell formulas and a sample graphical output. The output corresponds to the process profile in Figure D-2.

Chapter 6

Discussion

The following chapter is presented in three main sub sections. The first discusses the application of the *in situ* strength evolution model to the subject prealloyed 90Cu-10wt.%Sn bronze powder compact. Strength data obtained at room temperature as well as during sintering were used to determine the model constants. These data were presented in Chapter 4. The determinations of the model constants and implementation of that model followed the approach described in Chapter 5. The *in situ* strength measurements were made possible by the Flaming Tensile Tester (FTT) which was developed specifically for this research and described in Section 3.1.4. Discussions in the next main sub section are that of additional material characteristics as they evolved during sintering. These additional characteristics, while they were either deemed not significant to the evolution of strength in bronze or otherwise not specifically included in the model, are included for completeness. The final sub section presents an overview of the model's application to other powder compacts and to sintering cycle design. The additional powders include a variety of systems for which the critical FTT data, required by the model, were obtained in the P/M Lab. Using the model to map *in situ* strength evolution, sintering cycles are designed where environmental stresses are matched with sufficient strength to minimize distortion and otherwise improve dimensional tolerances.

6.1 *In Situ* Strength Evolution of Bronze

The first step to applying the *in situ* strength evolution model to any new powder system is to determine the model parameters. These parameters were defined using the method described in Section 5.1 with the bronze data presented in Chapter 4.

6.1.1 Annealing of Green Strength

A portion of the 10 MPa (measurement presented in Section 3.1.6) green strength for the bronze compacts was lost to annealing. As described by Equation 5.5, annealing was modeled by multiplying the fraction of strength lost during complete recrystallization (R_f) by the transformation fraction (β) and in turn subtracting from the room temperature green strength. Computing the transformation fraction requires determination of the frequency factor (Γ_o) and the activation energy of recrystallization (Q_R). This assumes the material undergoes plastic deformation during die compaction or other presinter forming process step. Therefore this portion of the model would not be appropriate with brittle or hard materials such as ceramics. PIM components use a binder phase to provide green strength rather than particle to particle contact deformation. Strength evolution of PIM components might therefore replace the annealing model with one that describes *in situ* strength during debinding. The critical data used was the FTT measurements obtained from constant 10°C/min sintering for temperatures prior to sinter strengthening. Specifically, these data were the green strength and test numbers A1 through A4 (constant heating to various test temperatures up to 402°C). Once modeled, data from other low temperature thermal profiles were used for validation. These were tests A26 and A27

which consisted of 10°C/min to test temperatures of 218 and 305°C, respectively, followed by pretest holds of 20 minutes. These data are considered appropriate since, prior to the onset of sinter strengthening, annealing dominates *in situ* strength evolution.

The minimum strength measured in these data was 4.8 MPa at 351°C which was a decrease of just over half of the room temperature green strength. The total fraction of green strength lost during complete recrystallization, R_f , was therefore chosen as 0.5. This magnitude of strength loss was supported by a similar degree of hardness reduction over the same temperature range (shown in Figure 4.29). The remaining constants of the annealing model were the parameters of the transformation fraction computation (β) from Equation 5.2. Specifically, these parameters were those of the thermally activated rate constant defined by Equation 5.3. This relation, repeated by Equation 6.1,

$$\Gamma = \Gamma_o \exp\left(-\frac{Q_R}{RT}\right) \quad (6.1)$$

follows the form first put forth by Arrhenius [98] and is common to nearly all thermally dependent reaction models [97]. The key model parameters in this case are the frequency factor (Γ_o in units of inverse root time) which controls the magnitude of thermal activation and the activation energy (Q_R in units of kJ/mol) which governs the rate of reaction.

The spreadsheet software was employed to develop these parameters (Γ_o and Q_R) using process profile and annealing sheets similar to those described in Sections 5.2.1 and 5.2.2, respectively. Numerical integration of this reaction equation required the transformation fraction to be initialized, thus preventing a division by zero in Equation

5.20. At the same time this value must be set sufficiently small so as not to adversely impact the magnitude of the outcome. Therefore, $\beta(t=0)$ was chosen as 0.0001. It should be noted that similar initialization was used in the sintering neck growth models of Swinkels and Ashby [95,99]. Using the results from test A1, the reaction rate (Q_R) was chosen such that the onset of transformation was below this datum's 200°C test temperature. The frequency factor (Γ_0) was then adjusted to model a transformation fraction indicated by the data from tests A1 through A4. The spreadsheet approach permitted efficient input of iterations and evaluation of the impact upon the results. The combination that provided the highest correlation with data and the lowest standard error is summarized (along with the other previously discussed parameters) in Table 6.1. The values for Γ_0 , Q_R and $\beta(t=0)$ were used in the annealing sheet described in Section 5.2.2 and shown in Figure D-3. The value for R_f was used in the *in situ* TRS sheet described in Section 5.2.4 and shown in Figure D-5. Using these parameters the model also predicted the results of test A26 and A27 within 0.5 MPa which is within the accuracy of the measurement. The model is also consistent with Cahn's [48] result for bronze which concluded recrystallization would be complete between 400 and 500°C. Actual correlation coefficient or standard error is not presented here since this model is only a portion of the mechanisms responsible for *in situ* strength evolution represented by the data.

Relative statistical comparisons were used to evaluate the computational technique as per the cautions of Flynn [97]. Since numerical integration precision is affected by the size of the integration step, an evaluation of the time step (Δt) used for the final model was

Table 6.1: Summary of *in situ* strength evolution model parameters.

Annealing Model Parameters	
Fraction Recrystallized, R_f	0.5
Frequency Factor, Γ_0	$7 \text{ s}^{-1/2}$
Activation Energy, Q_R	25 kJ/mol
Transformation Initial Condition, $\beta(t=0)$	0.0001
Sinter Strength Model	
MSC Equivalent Activation Energy	130 kJ/mol
MSC - Sinter Strength Correlation (Polynomial Coefficients)	
a	390 ln MPa
b	75.25 ln MPa
c	5.32 ln MPa
d	0.16625 ln MPa
e	$1.941 \cdot 10^{-3} \text{ ln MPa}$
Thermal Softening Model (Polynomial Coefficients)	
A	1.05
B	720 K
C	138 K

appropriate. The annealing model prediction for tests A1 through A4 as well as A26 and A27 were compared with the data. This comparison is depicted in Figure 6.1 which graphically shows correlation coefficient and standard error as a function of Δt . As shown by this figure, based on minimum standard error and maximum correlation coefficient, a Δt between 6 and 30 s produces the best result.

6.1.2 Sinter Strengthening

As outlined in Section 5.1.3.2, the sinter strengthening model followed the Master Sintering Curve (MSC) approach of Johnson and Su [59,60,100]. The basic assumption of Johnson's MSC approach is that sintering is dominated by a single mechanism over the range to be modeled. Application of the Ashby sintering model [101] to this powder compact shows net density change in agreement with that observed here (under 1%) and indicates dominance by grain boundary diffusion over the entire range of experiments. Similar "Temperature Integral" techniques were employed by Shercliff and Ashby [52] for the annealing of aluminum. Flynn [97] thoroughly demonstrated its validity for thermally activated processes. The MSC model used here considered the room temperature strength (shown in Figures 4.7 through 4.11 and tabulated in Appendix B) as the sintering response. The sinter strengthening portion of the *in situ* strength evolution model therefore only requires the determination of the MSC equivalent energy (Q_s) and a correlation equation between the MSC parameter (θ) and the strength response.

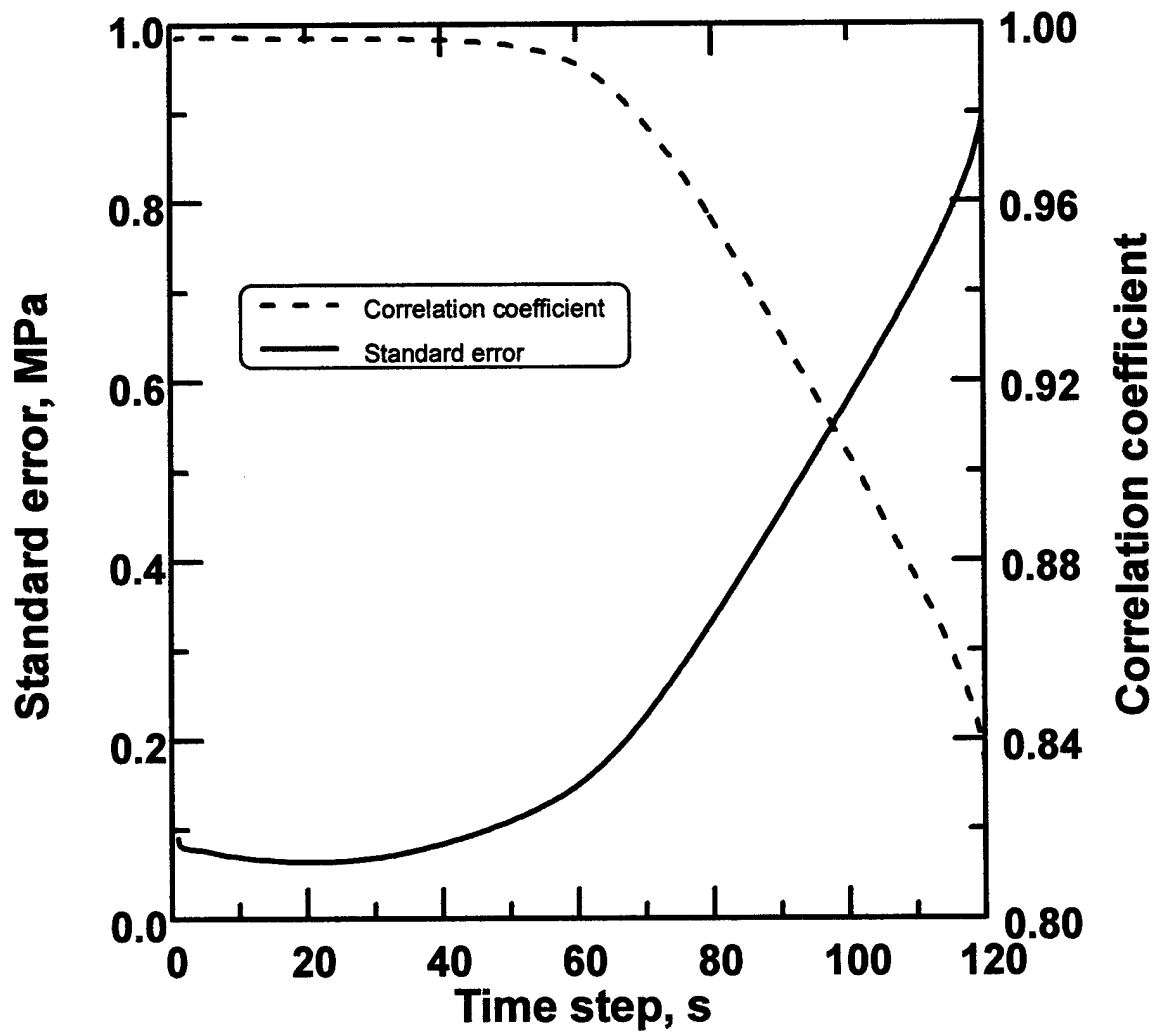


Figure 6.1: Evaluation of time step (Δt) for annealing model. Based on correlation coefficient and standard error, the best prediction of data occurs for time steps between 6 and 30 s.

6.1.2.1 MSC Equivalent Energy

The MSC equivalent energy (Q_s) in units of kJ/mol is the single adjustable constant in the calculation of the MSC parameter (θ) for a given sintering (time and temperature) profile [100]. The MSC parameter is calculated by Equation 6.2 (repeated from Equation 5.11) for the sintering profile of test numbers B1 through B58.

$$\theta = \int_0^t \frac{1}{T} \exp\left(-\frac{Q_s}{RT}\right) dt \quad (6.2)$$

An MSC parameter sheet similar to that described in Section 5.2.3 was used to evaluate this integral from each datum's sintering profile. As suggested by Johnson and Su [100], the natural log of θ was plotted against the corresponding strength response. The resulting plot was then evaluated for the convergence along a single curve. This process was repeated with different values for Q_s until the best convergence was found.

The spreadsheet tool made possible easy changes to Q_s while providing immediate graphical results. A step size (Δt) was chosen for these calculations which was the smallest time increment indicated (for best results) from the annealing model. A small increment was desirable to provide smooth resolution of thermal transitions in the process profile. Both visual evaluation of the graph and a simple linear regression correlation coefficient provided a rough estimate of convergence. Figures 6.2 and 6.3 show examples of how such estimates were made. A Q_s of 10 kJ/mol is represented by Figure 6.2. Without consulting any fit statistics, it is clear that this choice results in little convergence. Similarly, at the other extreme, a Q_s of 1000 kJ/mol is represented by

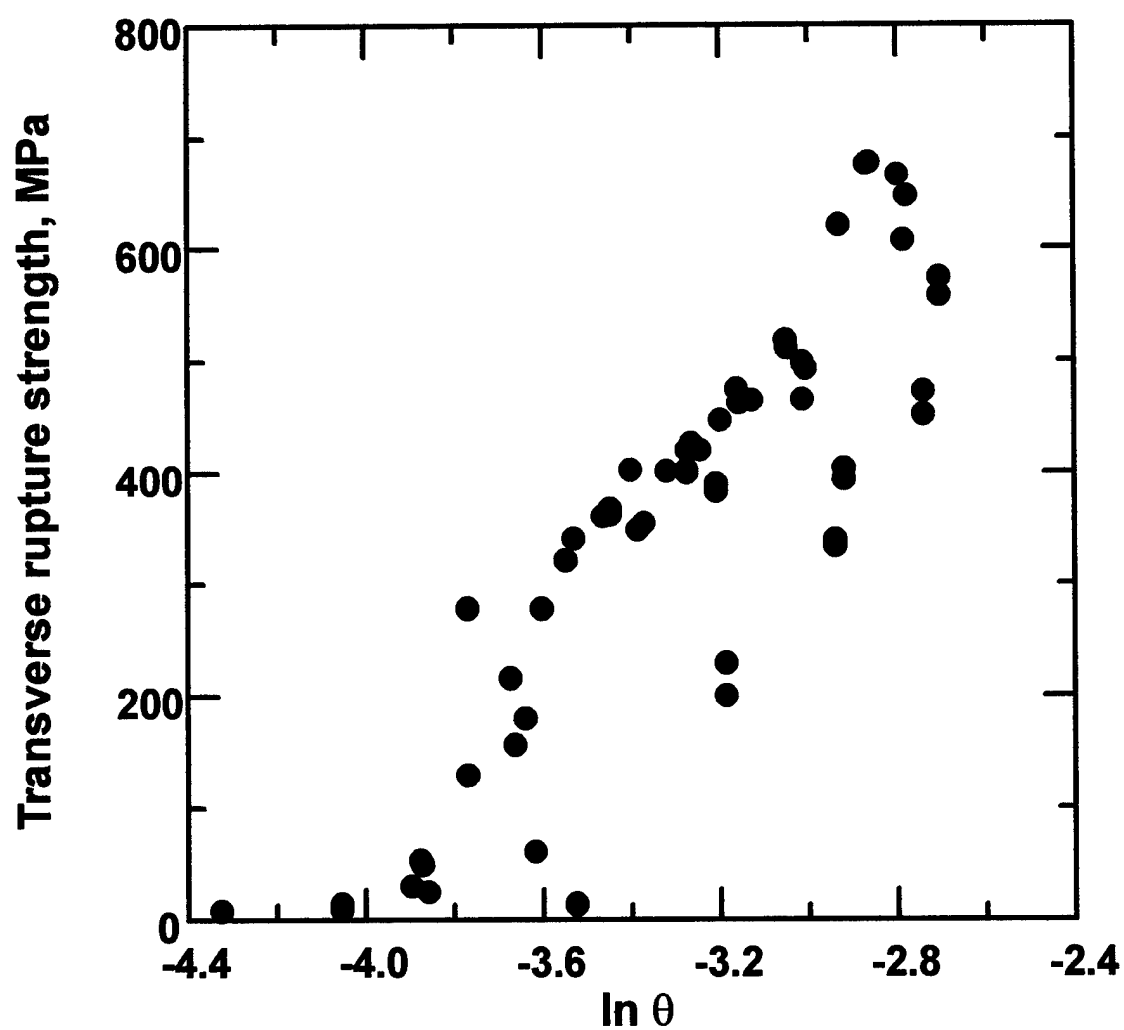


Figure 6.2: Natural log of MSC parameter ($\ln \theta$) versus measured room temperature transverse rupture strength for $Q_s = 10$ kJ/mol. This choice of MSC parameter produces poor correlation between calculated MSC parameter and strength data. Linear correlation coefficient is 0.74.

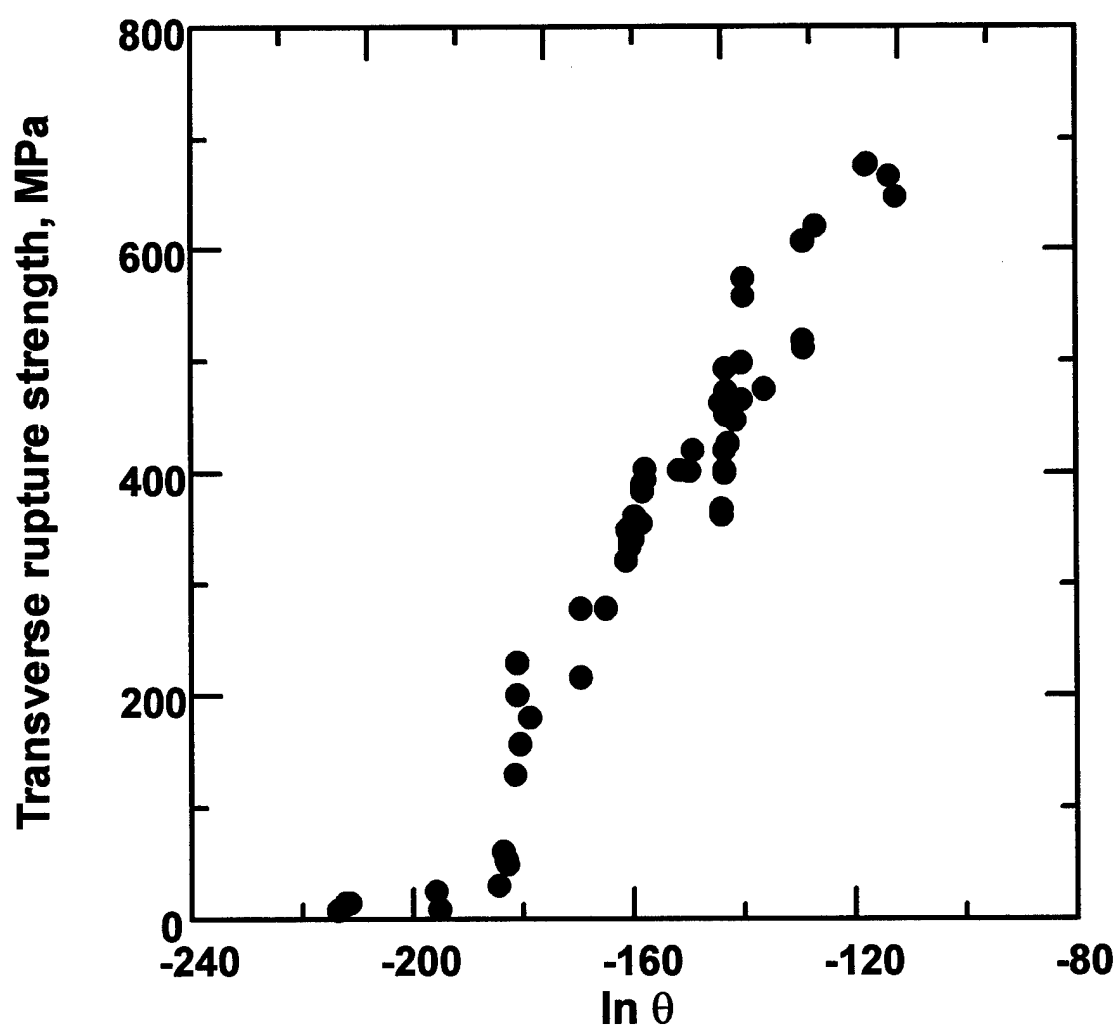


Figure 6.3: Natural log of MSC parameter ($\ln \theta$) versus measured room temperature transverse rupture strength for $Q_s = 1000$ kJ/mol. This choice of MSC parameter produces poor correlation between calculated MSC parameter and strength data. Linear correlation coefficient is 0.93.

Figure 6.3. In this case the linear correlation coefficient is 0.93. This process was continued and Q_s versus linear correlation coefficient was plotted as shown in Figure 6.4. This plot indicated the mostly likely range of Q_s was between 85 and 145 kJ/mol for which the linear correlation coefficients were in excess of 0.96. Since the data correlations are obviously not linear, the exact determination of Q_s required selection of an equation that provided a more precise fit. The specific equation is discussed in more detail in the next sub section. Once chosen, correlation coefficient and standard error fit statistics permitted the selection of the best value for Q_s . Figure 6.5 indicates the result of these comparisons. As is clearly evident by this plot the best choice for Q_s was 130 kJ/mol. This value was used in the MSC parameter sheet described in Section 5.2.3 and shown in Figure D-4.

The Q_s of 130 kJ/mol chosen for bronze compares to 400 kJ/mol in the previous work [88] for W-Cu-Co. That result was derived from a much smaller data set which was dominated by constant rate sintering. One would not expect identical values due to the two powder's different sintering kinetics and mass transport mechanisms which lead to strengthening. Still both Q_s are the same order of magnitude. Additionally, as advised by Johnson and Su [100], a far more accurate determination of Q_s will result if the data are from a wide variety of heating rates and isothermal holds. According to this guidance and given the varied set of thermal profiles represented in the data set (Appendix B), the Q_s value determined here for bronze is more precise.

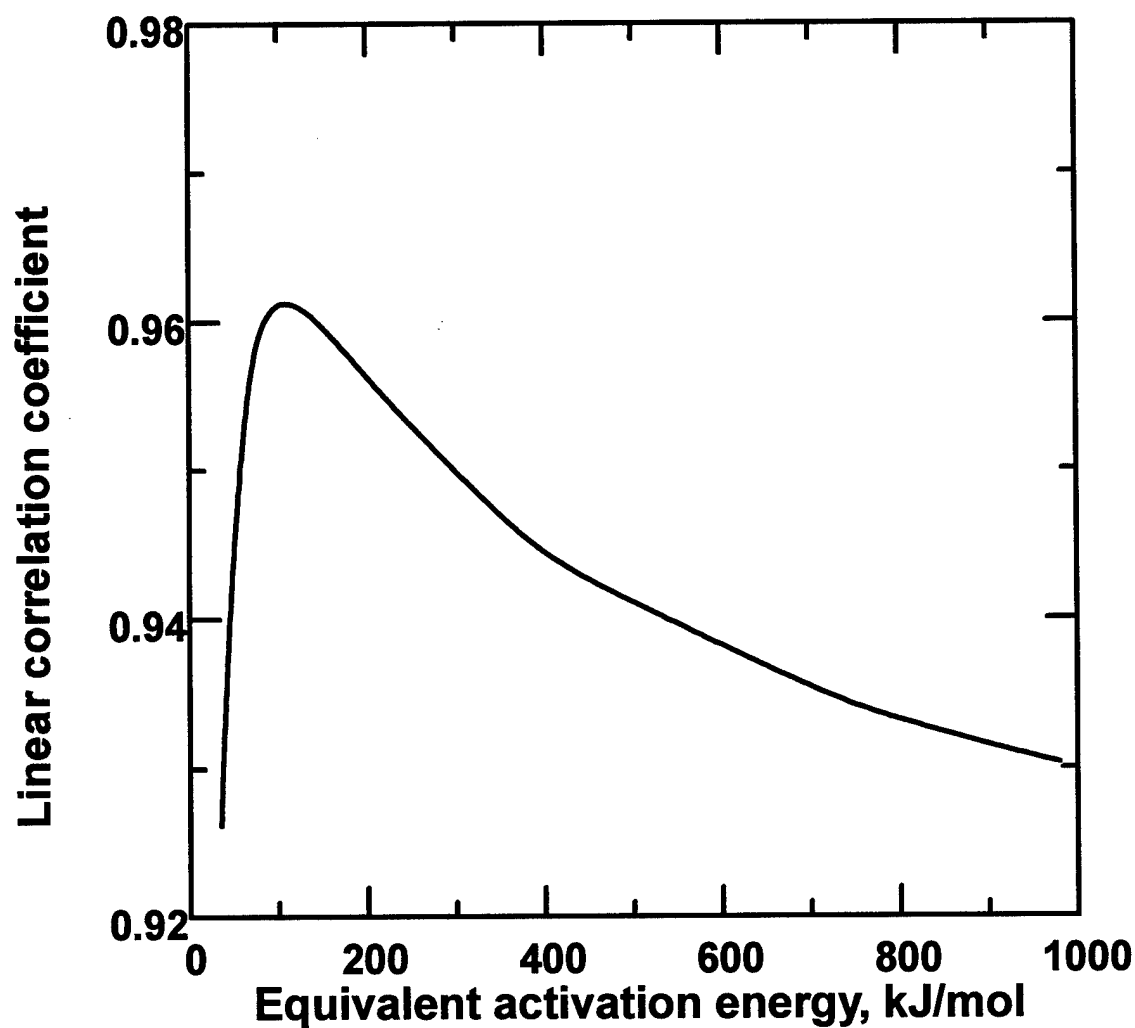


Figure 6.4: Linear correlation coefficient versus equivalent activation energy (Q_s) for correlation of MSC parameter (θ), as calculated by Equation 6.2, with all room temperature strength measurements specified in Appendix B.

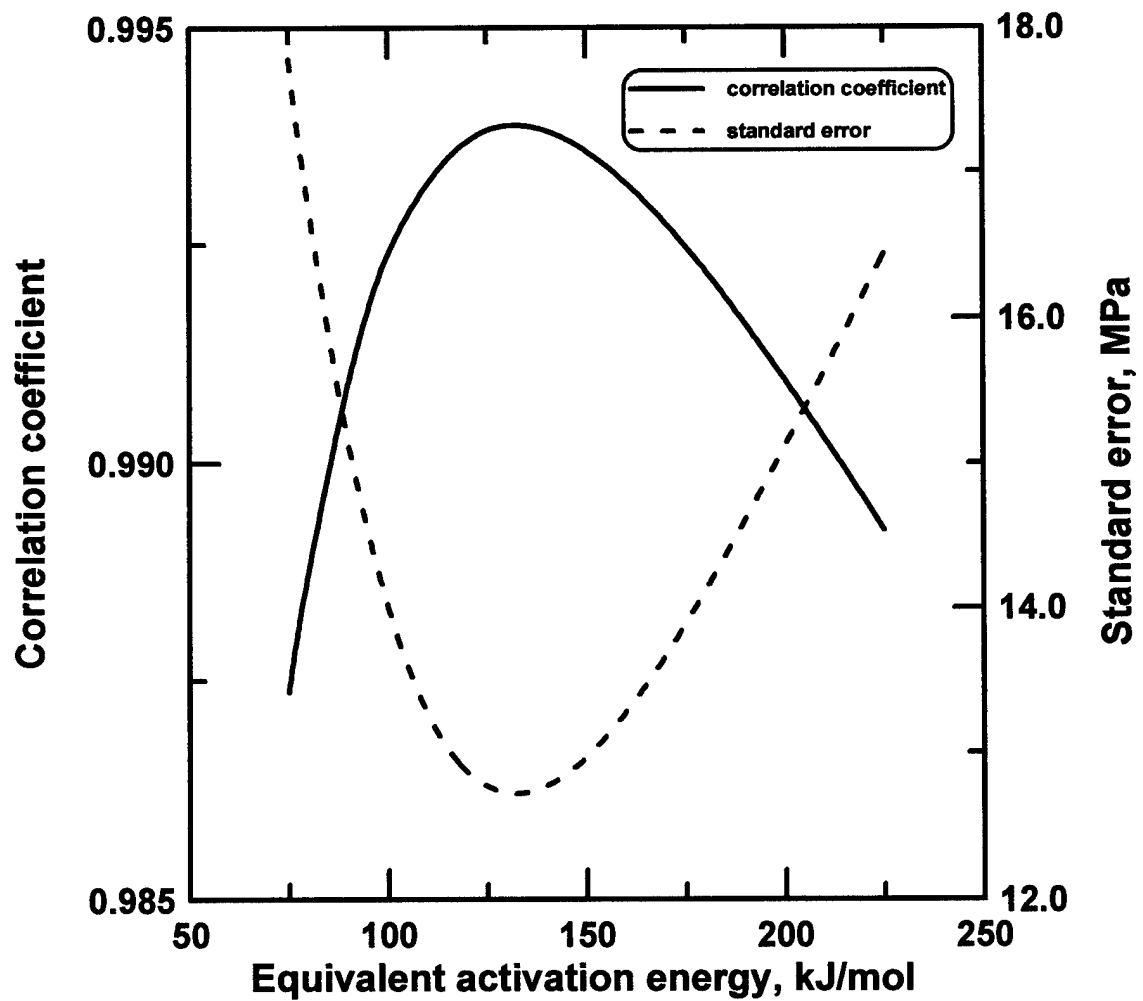


Figure 6.5: Correlation coefficient and standard error versus equivalent activation energy (Q_s) for correlation of MSC parameter (θ), as calculated by Equation 6.2, with all room temperature strength measurements specified in Appendix B.

6.1.2.2 MSC - Sinter Strength Correlation

The final portion of the sinter strengthening model was to define the equation that correlates the MSC parameter (θ) to sinter strength response as represented by Equation 5.12. This step was identical to that used by Johnson and Su [59,60,100] to correlate densification to MSC parameter (θ) for alumina and TiO_2 as well as by Shoales *et al.* in a previous work [88] to correlate sintering strength to MSC parameter for W-Cu-Co. As in the later work, Jandel Scientific's Table Curve™ 2D software was used to aid this process. This software attempts to fit over eight thousand equations to any set of two-dimensional data. The software reports results based on a user selectable variety of fit statistics. Since the goal of the fit for this model was to accurately represent the data across the entire range of measurement, the standard error and correlation coefficient were the statistics chosen. This software also permits graphical review of all potential fits which allowed evaluation of the function's continuity over the range.

As described in the previous section, $\ln \theta$ versus strength data sets, computed by Equation 6.2 for Q_s values from 75 to 225 kJ/mol, were fit by the software. In all cases, the equation with the lowest standard error was an exponential of a fourth order polynomial shown by Equation 6.3;

$$\sigma_s = \exp[-(a + bx + cx^2 + dx^3 + ex^4)] \quad (6.3)$$

where a , b , c , d and e are the polynomial constants in units of $\ln \text{MPa}$, σ_s is the sinter strength in MPa, and x is the natural log of the MSC parameter minus 1 ($\ln \theta - 1$). For the

Q_s of 130 kJ/mol determined in Section 6.1.2.1 the standard error (as shown in Figure 6.5) was less than 13 MPa for this equation. This equation not only provided significantly higher precision than the other choices but was also more representative to the physical phenomena of strengthening. For example, when ranked by standard error, the next best fit was 75% worse. The next 25 equations were discontinuous at the extrema of the $\ln \theta$ range. The previous work [88] used a sigmoidal fit for sinter strengthening of W-Cu-Co. Although this equation is somewhat simpler (one less coefficient), using the same correlation equation for these data resulted in more than a 400% increase in standard error.

The polynomial coefficients along with the MSC equivalent energy discussed in the previous section are included in Table 6.1. Equation 6.3, along with the polynomial coefficients, therefore becomes the correlation equation represented by Equation 5.12. Equation 6.3 along with its coefficients are used in the *in situ* TRS sheet as described in Section 5.2.4 and shown in Figure D-5. The correlation coefficient between Equation 6.3 and the data of Appendix B, shown graphically in Figure 6.6, is greater than 0.99.

The chosen time step (Δt) was evaluated by comparing the standard error of sinter strength predictions between various values of Δt and the 6 s. value used in Section 6.1.2.1. Although a smaller time step causes some increased computational load, it also provides increased resolution of thermal transitions in the process profile. Figure 6.7 graphically shows the impact of varying the time step in the sinter strength model. As is clearly evident from this plot, there is no additional error resulting from choosing time

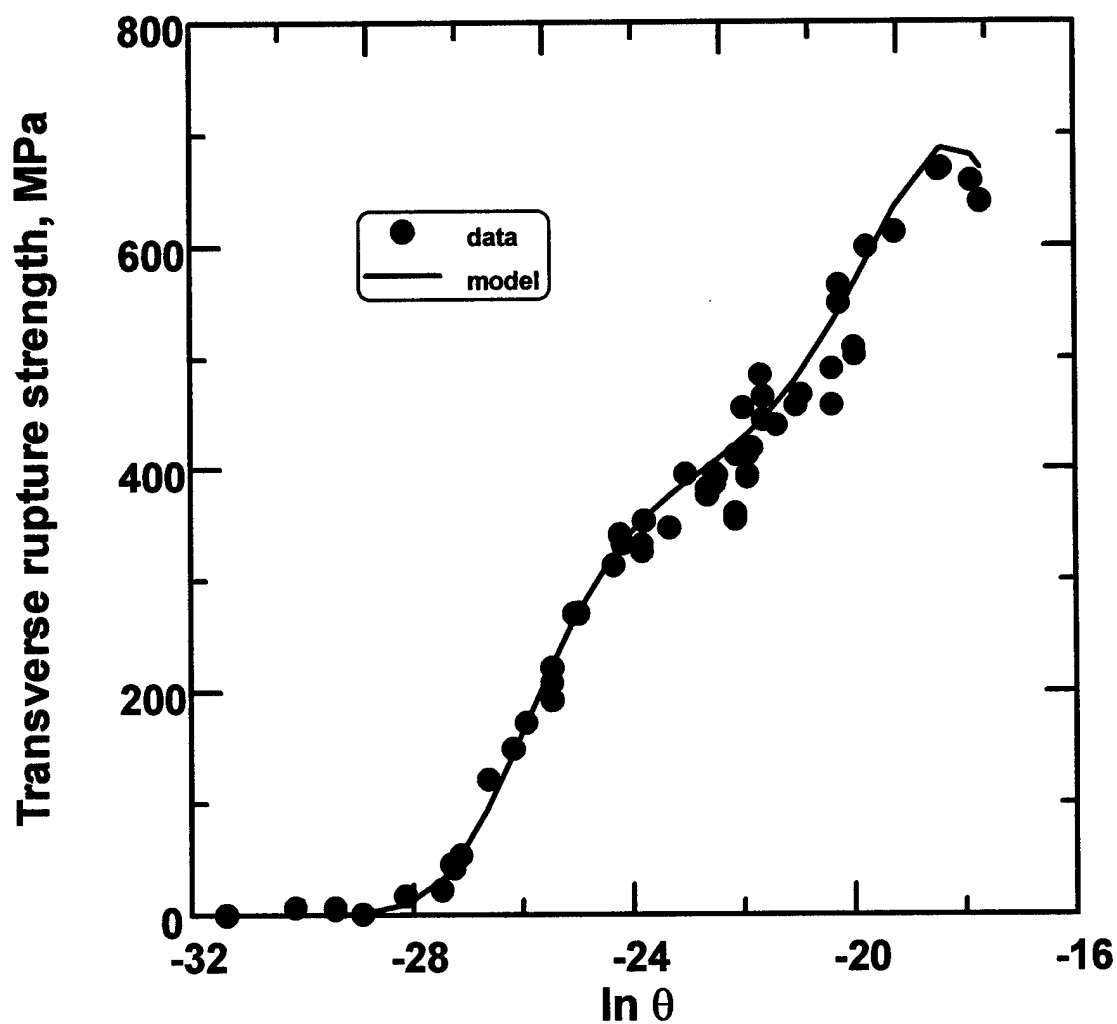


Figure 6.6: Natural log of MSC parameter ($\ln \theta$) versus measured room temperature transverse rupture strength for $Q_s = 130$ kJ/mol. Correlation coefficient is greater than 0.99.

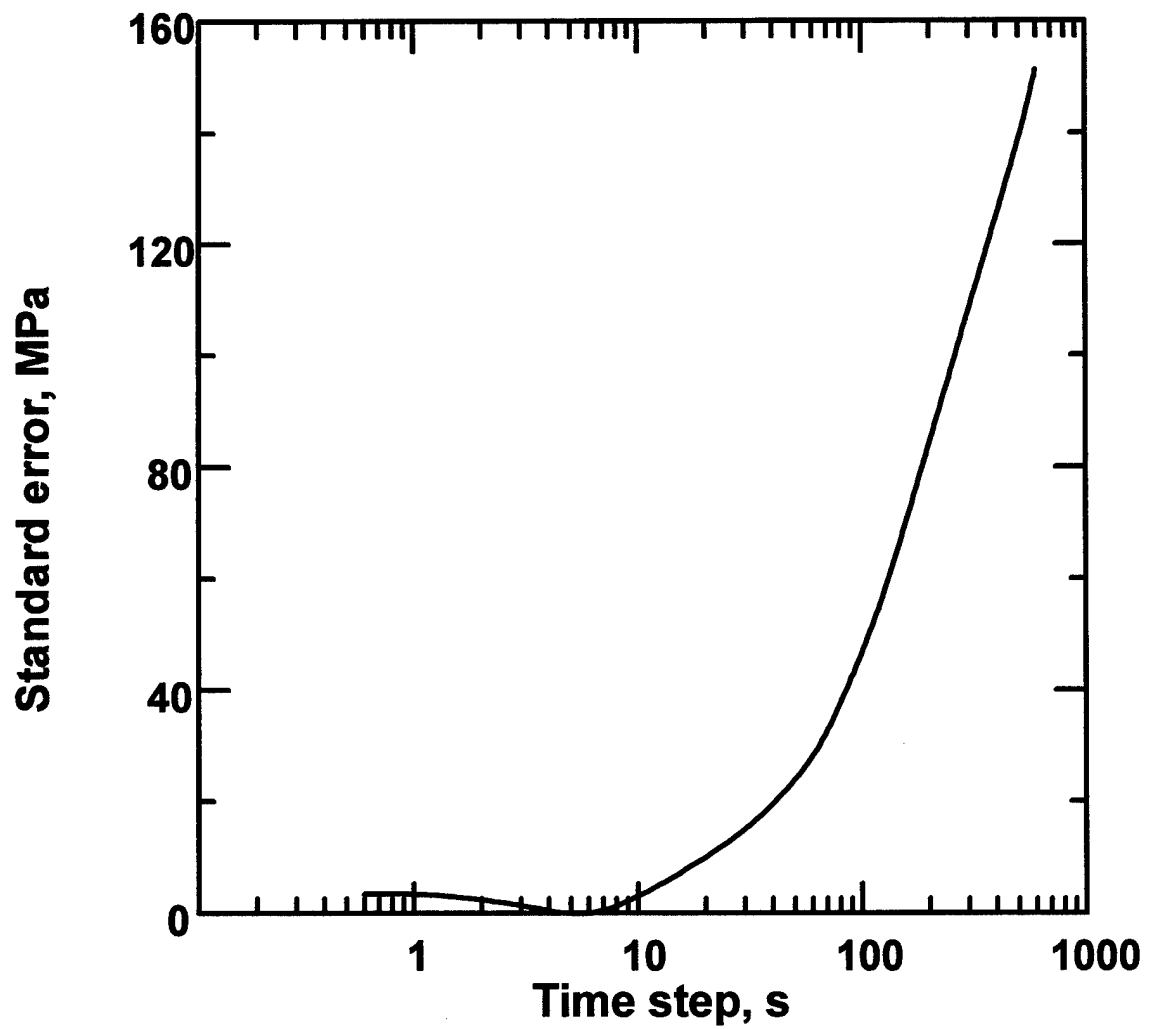


Figure 6.7: Effect of time step (Δt) on sintering strength model. Standard error of model prediction between various time steps and that of $\Delta t = 6$ s versus time step.

steps between 4 to 7 s. Since the best result for the annealing model was obtained using a Δt between 6 and 30 s, 6 s was the Δt chosen for the *in situ* strength evolution model.

A further representation of the sinter strengthening model is depicted by Figure 6.8. In this figure, the room temperature sinter strength (found by combining Equations 6.2 and 6.3) as a function of both heating rate and time is shown as a surface plot as well as a contour plot. Figure 6.9 shows similar graphs of the sinter strength gained during isothermal sintering as a function of time and temperature. This depiction disregards the contribution to strength during any thermal transitions between temperatures. Such contributions are, however, available from Figure 6.8. The implications of such plots as an aid to sintering cycle design will be discussed in Section 6.3.

6.1.3 Thermal Softening

Two sources of thermal softening data were evaluated to produce the thermal softening model discussed in Section 5.1.4 and represented by Equation 5.14. These are the FTT cooling tests (shown in Table A-3) and the direct TRS measurement of dense 90Cu-10wt.%Sn bronze compacts taken at temperatures from room temperature through 857°C (shown in Table C-1). These data for dense bronze also demonstrated the temperature dominance of thermal softening indicated by Equation 5.14. Thermal softening measurements of dense 90Cu-10wt.%Sn bronze compacts taken at approximately 500 and 700°C were unchanged, whether taken after 0 or 30 min pretest holds at the test temperature. Temperature dominance is further demonstrated by the FTT measurements. Recall that Figures 4.1 through 4.4 represented FTT data from various

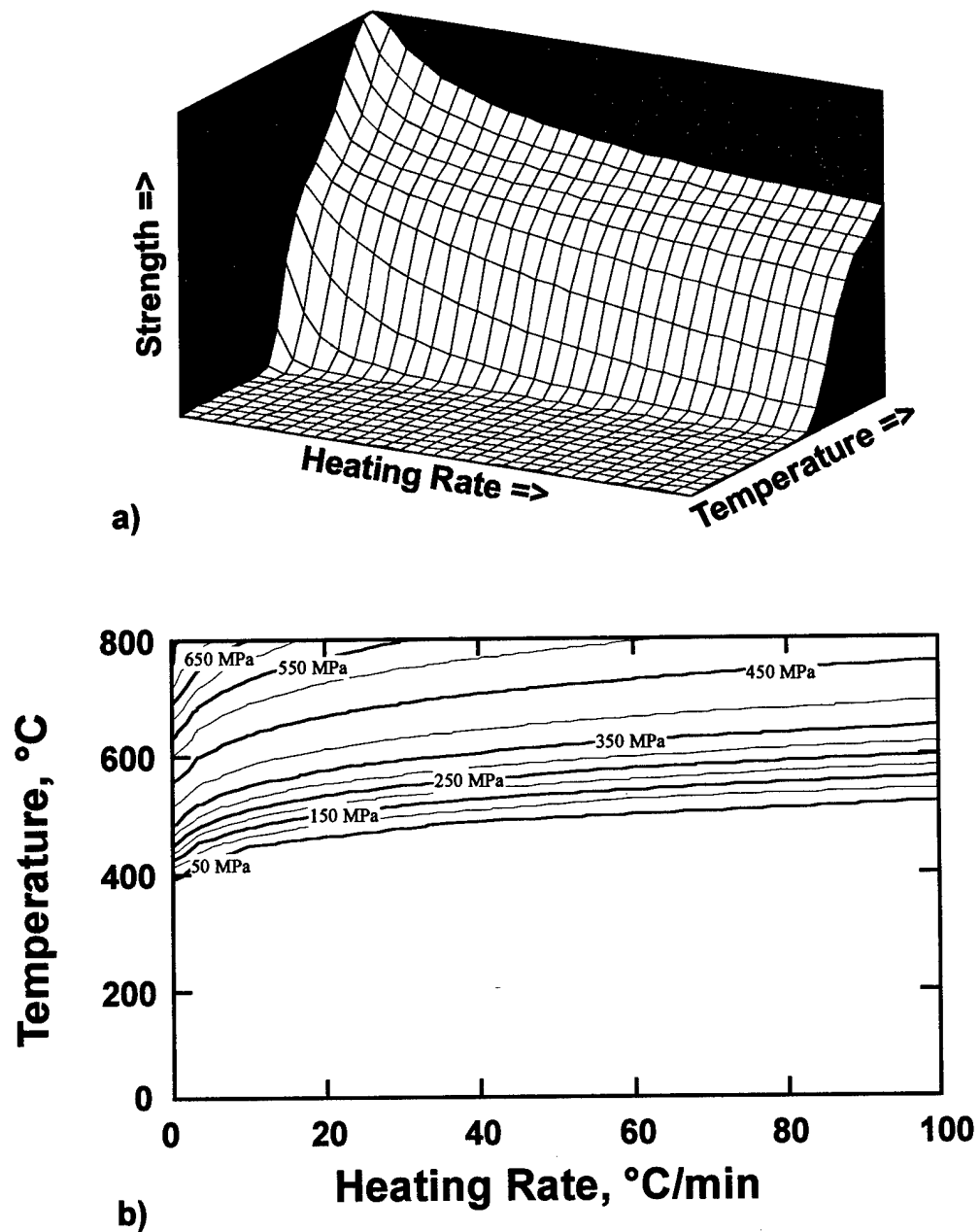


Figure 6.8: Room temperature transverse rupture strength, as determined by the sinter strengthening model, for constant rate sintering versus heating rate and temperature. Shown as a) surface plot with increasing heating rate from left to right and increasing temperature from front to back; and as b) contours of strength in MPa.

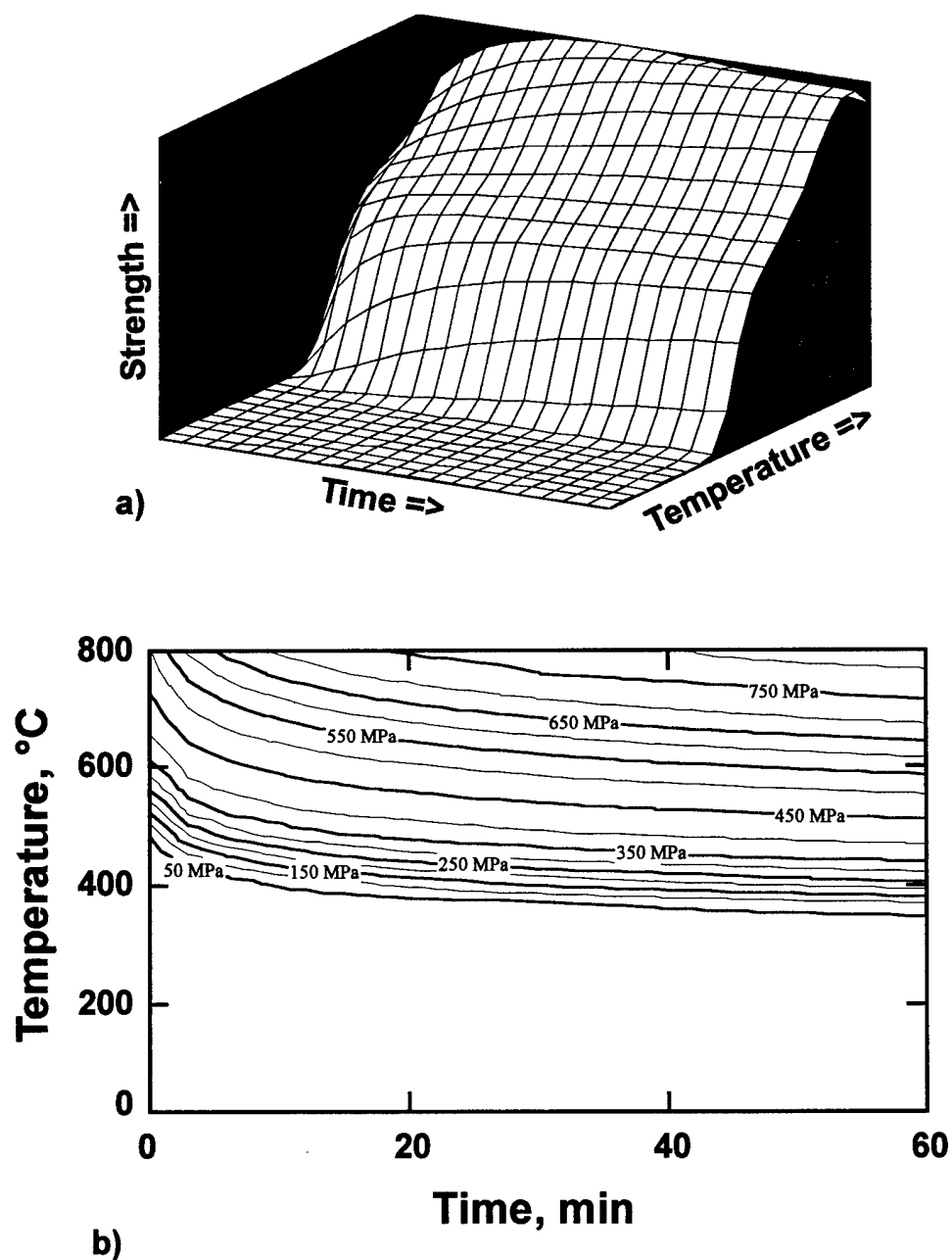


Figure 6.9: Room temperature transverse rupture strength, as determined by the sinter strengthening model, for isothermal sintering versus time and temperature. Shown as a) surface plot with increasing time from left to right and increasing temperature from front to back; and as b) contours of strength in MPa.

sintering paths. Figure 4.1 was the result from constant $10^{\circ}\text{C}/\text{min}$ heating rate to the test temperatures. Figure 4.2, on the other hand, showed the result of constant $5^{\circ}\text{C}/\text{min}$ heating rate to the test temperatures. Figure 4.3 depicted measurements taken after a 10 or 20 min hold at the test temperature ($10^{\circ}\text{C}/\text{min}$ heating). Finally, the effect of a 20 minute hold at 400°C followed by continued $10^{\circ}\text{C}/\text{min}$ heating to higher test temperatures was shown in Figure 4.4. As shown by all figures, regardless of the thermal path taken, once the peak strength temperature was reached, all results followed identical thermal softening curves (with respect to temperature). This also agrees with the fact that the available thermal softening data [61,62] is only tabulated by temperature. Therefore, the available data were used to determine the thermal softening character based solely on test temperature.

Table Curve™ 2D software, as described in Section 6.1.2.2, was used to find a suitable fit to the data. The models produced by these fits were evaluated by the quality of the prediction when combined with the total *in situ* strength evolution model shown by Equation 5.15. As in Section 6.1.2.2, prediction quality was determined by correlation coefficient and standard error. In this case correlation was with the $10^{\circ}\text{C}/\text{min}$ constant rate sintering FTT data presented in Section 4.1.1 and shown in Figure 4.1. Additional requirements for the function was that it be continuous across the temperature range as well as at the extrema. Finally, as guided by Reed-Hill and Abbaschian [47], Dieter [63] and Cahn [48], a smooth continuous, decaying transition between data was required. Equation 5.14 represents a strength fraction (f_T) as function of temperature (T) in K.

Thus, the normalized (to room temperature strength) TRS data paired with temperature in K were used as inputs to the software.

The thermal softening character extracted from the FTT cooling tests was presented in Section 4.4.3. When the data of cooling tests from temperature of 600°C and higher are normalized to the room temperature TRS, the *in situ* TRS versus temperature curves are self similar (shown by the top curve of Figure 4.6). A fit of these data, specifically test numbers A45 through A55, was used to determine an initial thermal softening model. Equation 6.4 represents the model with the lowest standard error (0.021) and highest correlation coefficient (0.997) that met the previously stated requirements for continuity and transition.

$$f_T = \frac{1.03}{1 + \left(\frac{T}{660}\right)^{4.8}} \quad (6.4)$$

As with Equation 5.14, f_T is the strength fraction and T is the temperature in K. Table Curve™ 2D refers to this equation as a logistic dose response and it is identical to that used in the previous work for bronze [85] to model neck growth. Incorporating this into Equation 5.15 and plotting the resulting prediction (of TRS versus test temperature) with the data of Figure 4.1 yields Figure 6.10. Evident in this figure is the over prediction of thermal softening until approximately 700°C when the model begins to under predict the data. The correlation coefficient is less than 0.96 and the average deviation of the prediction is greater than 15%. A possible explanation for this discrepancy is the fact that additional sintering potential exists below the peak temperature. This means the compacts

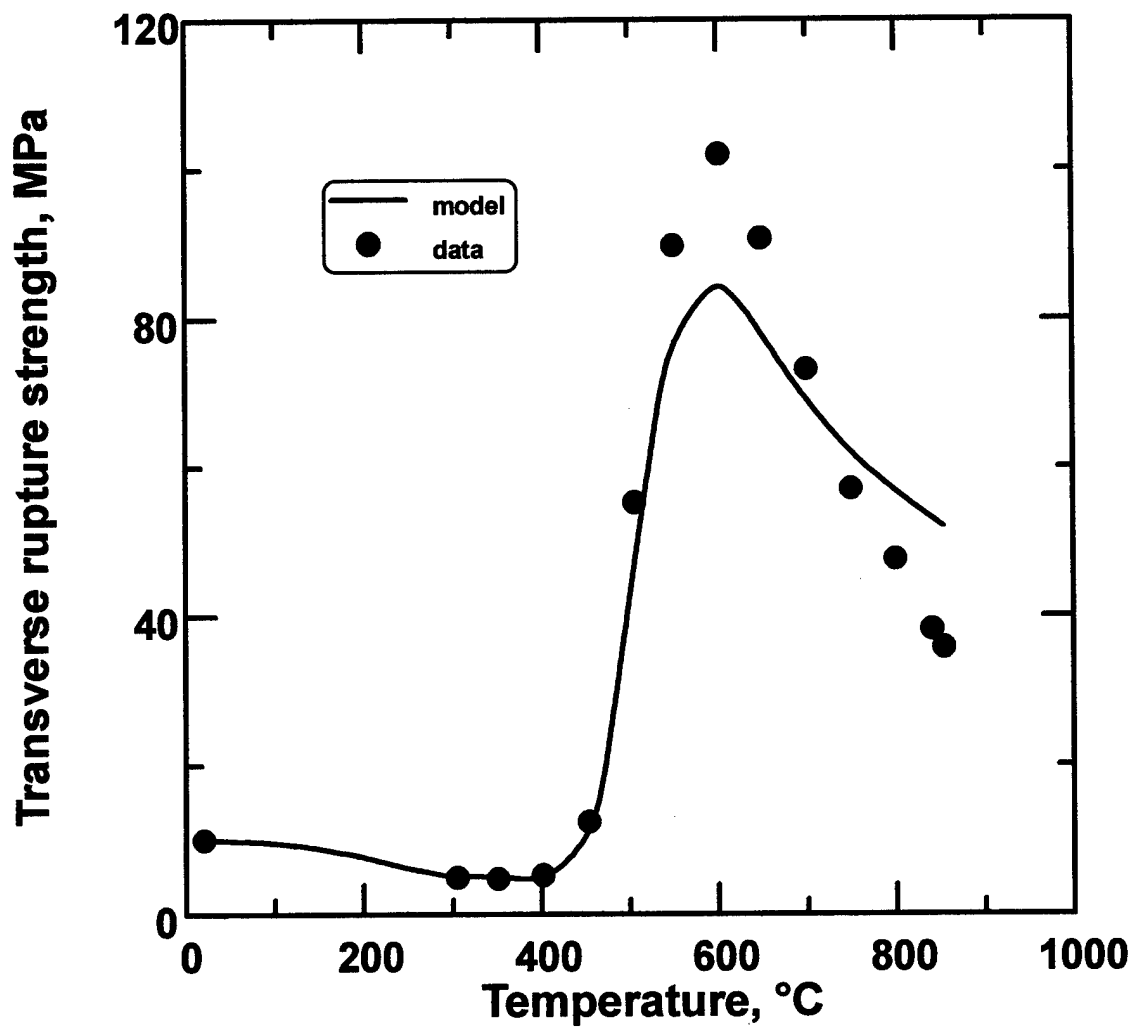


Figure 6.10: Prediction of *in situ* strength evolution using FTT cooling data to derive thermal softening. When compared to data, prediction correlation coefficient is less than 0.96 and average deviation is greater than 15%.

continue to sinter as they are cooled to test temperature. The result is that measurements taken after cooling from peak temperatures, as described in Section 3.1.6, include additional sinter strengthening and thus do not truly isolate thermal softening.

Another approach was to obtain direct measurements of thermal softening behavior from TRS measurements at temperatures up to 857°C of dense 90Cu-10wt.%Sn compacts. This essentially extends the tabulated data found in *Smithells Metals Reference Book* [62] of phosphor bronze for temperatures up to 500°C. The *Smithells* data is not only for a different alloy but also falls far short of the temperature range required by this model. The thermal softening data from the dense compacts (Appendix C) were normalized and imported into Table Curve™ 2D as with the previous set. The fit that produced the lowest standard error and highest correlation coefficient in this case was the sigmoidal equation shown by Equation 6.5;

$$f_T = \frac{A}{1 + \exp\left(\frac{T-B}{C}\right)} \quad (6.5)$$

where A, B, and C are the equation coefficients with values of 1.05, 720 K, and 138 K, respectively, and f_T and T are the strength fraction due to thermal softening and the temperature in K, respectively, as defined for Equations 5.14 and 6.4. This form is identical to that used in a previous work [88] to correlate the MSC parameter to the sinter strength of W-Cu-Co. The coefficients (A, B and C) are included in Table 6.1 and were used in the *in situ* TRS sheet described in Section 5.2.4 and shown in Figure D-5. Incorporating Equation 6.5 into Equation 5.15 and plotting the resulting prediction (of

TRS versus test temperature) with the data of Figure 4.1 yields Figure 6.11. In this case the model agrees with the data to a correlation coefficient in excess of 0.99. The standard error of the fit is less than 3%. This error compares very well with the FTT measurement uncertainty of just under 2% (Section 3.1.6).

The fidelity of the model was further evaluated by comparing predictions with the data from the cooling tests. Model process profile input was defined to match the that of the data in Table A-3. Note the heating rate in all profiles in this table was 10°C/min. Thus, appropriate portions of the data in Figure 4.1 could be combined with cooling data to compare the entire *in situ* strength prediction output. Examples of such comparisons are shown in Figures 6.12 and 6.13 for cooling from 600 and 700°C, respectively. The correlation coefficient for both is again in excess of 0.99. The average deviation across the entire range between model prediction and data is 5 and 3% for the cooling data from 600 and 700°C, respectively. The deviation of the data with prediction along the actual cooling curve is somewhat greater than other portions of the sintering profile. This is to be expected since (as observed in Section 6.1.3) there is additional sintering strengthening during the initial stages of cooling. Since sintering kinetics (and therefore strengthening) is strongly influenced by the time and temperature profile, model precision requires the exact cooling profile. For the model results presented here, the average cooling rate (rather than the precise instantaneous time versus temperature profile), was used for the process profile input. Using this greatly simplified input produces excellent results without adding undue data processing complexity. These average cooling rate inputs were as presented in Table A-3

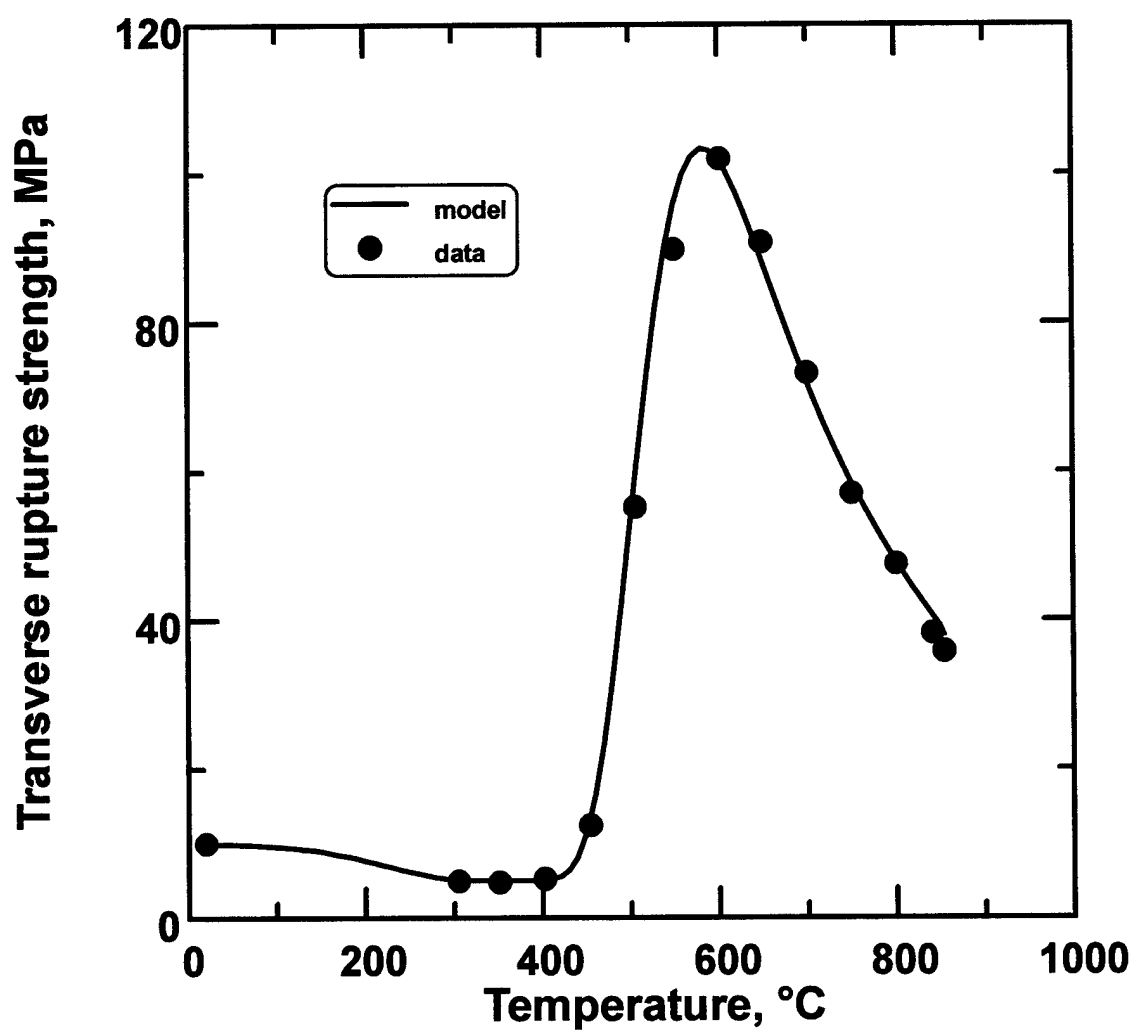


Figure 6.11: Prediction of *in situ* strength evolution using thermal softening data from dense 90Cu-10wt.%Sn bronze compacts to derive thermal softening portion of the model. When compared to data, prediction correlation coefficient is greater than 0.99 and average deviation is less than 3%.

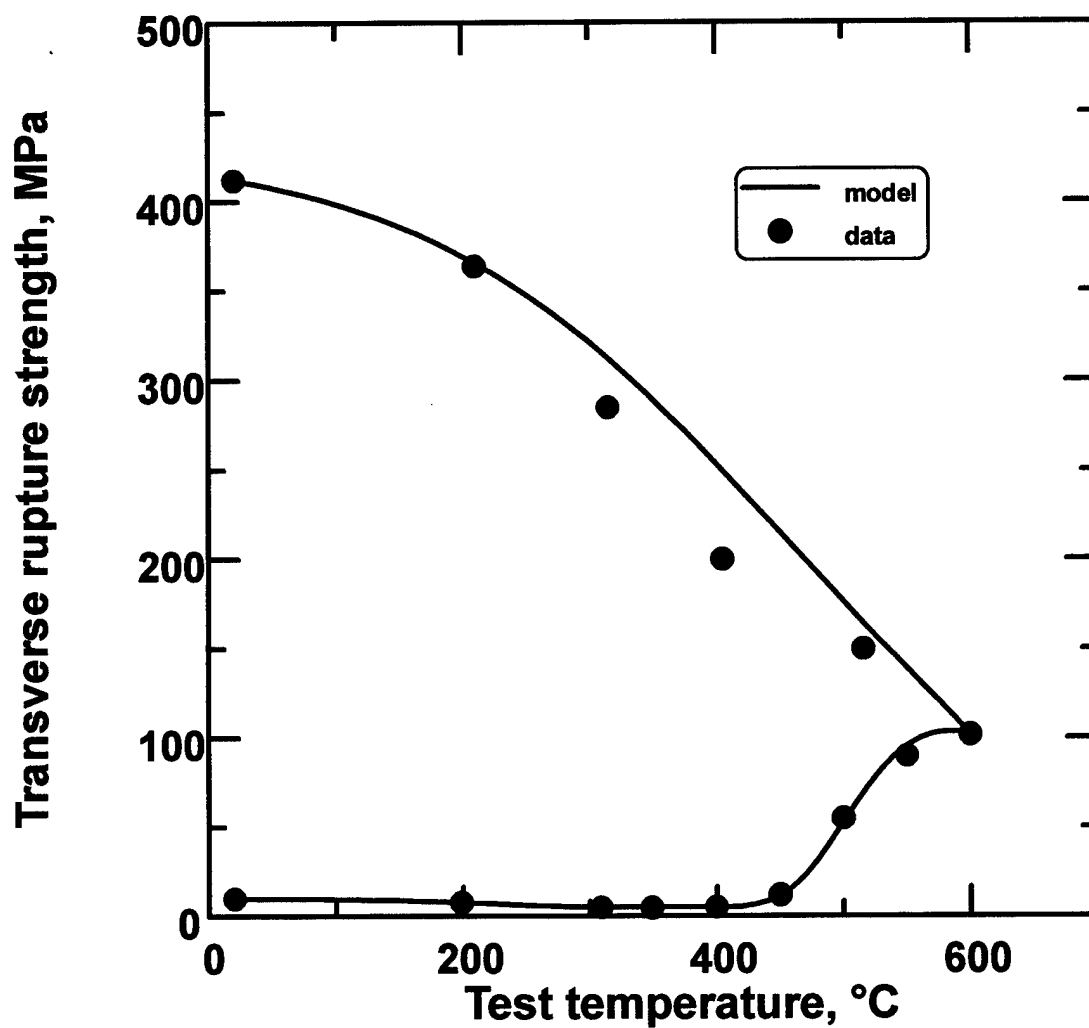


Figure 6.12: Comparison between *in situ* strength evolution model and data plotted by transverse rupture strength versus test temperature. Data for B-409 grade bronze derived from constant 10°C/min to test temperatures up through 600°C followed by subsequent cooling to lower test temperatures. When compared to data, prediction correlation coefficient is greater than 0.99 and average deviation 5%.

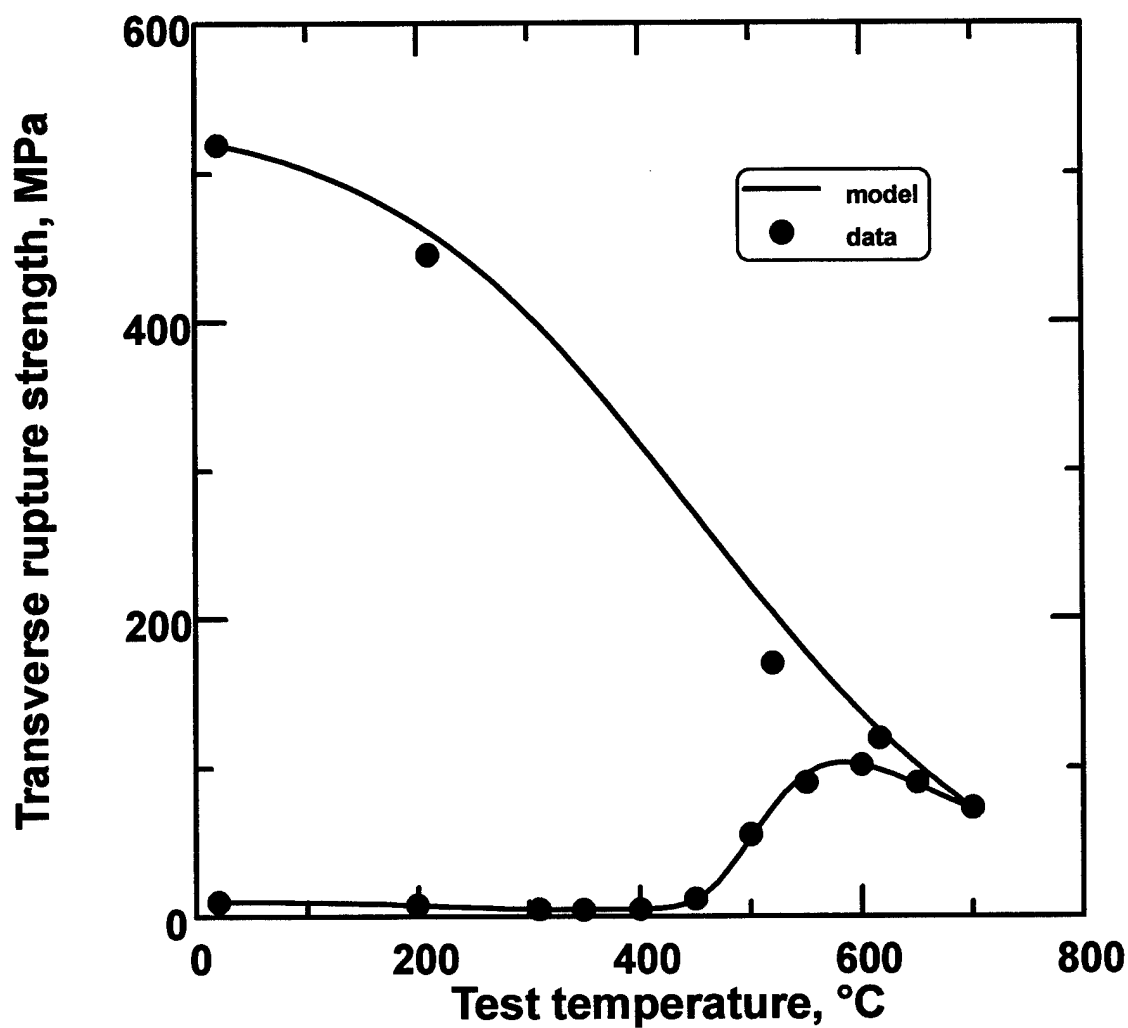


Figure 6.13: Comparison between *in situ* strength evolution model and data plotted by transverse rupture strength versus test temperature. Data for B-409 grade bronze derived from constant 10°C/min to test temperatures up through 700°C followed by subsequent cooling to lower test temperatures. When compared to data, prediction correlation coefficient is greater than 0.99 and average deviation 3%.

The errors shown in Figures 6.11 through 6.13 represents model predictions using the constants determined in the preceding sections. If necessary, higher resolution of selected temperature regions would be possible by “fine tuning” model parameters. The current *in situ* strength evolution model, as described by Chapter 5 with the parameters of Table 6.1, is more than adequate for the thermal design of this thesis.

6.2 Additional Sintering Outcomes

This section discusses additional results that were not directly included in the *in situ* strength evolution of bronze model. Some were evaluated and determined to be of no influence to the development of strength in prealloyed 90Cu-10wt.%Sn bronze compacts. In other cases, they have been incorporated indirectly into portions of the model.

6.2.1 Phase Evaluation

Change of phase can have significant impact on many alloy properties. This is particularly true when transition to the new phase includes a change to a different crystal structure. An example is the α (BCC) to γ (FCC) transition of Fe at 910°C. The transition to a close packed crystal structure would likely cause an influence on strength. Such transitions are temperature dependent and predictable given the alloy composition and appropriate phase diagram. It would therefore be possible to model such an influence as a temperature dependent factor such as that used for thermal softening.

The phase diagram [82] for 90Cu-10wt.%Sn bronze predicts transition from two phased α -Cu and ϵ -bronze to single phase α -Cu at 340°C. Dowson [26], however,

observes that the two phased structure is rarely the case due to the extraordinarily slow cooling rate required to decompose the α -Cu phase. The rapid cooling required for atomized powder production [1] makes this even less likely. The X-ray diffraction results to evaluate the change of phase in bronze were presented in Section 4.4.2 and shown in Figures 4.24 through 4.27. The location and magnitude of the significant peaks from the *Powder Diffraction File* [83] are included for both phases. All results indicated an overwhelming dominance of α -Cu. Thus, phase transition was not considered to be a factor in the *in situ* strength evolution of bronze. A final observation of the XRD results is with regards to the smearing of the peaks described in Section 4.4.2 for the room temperature and the 400°C quenches. This is an expected result due to the slight segregation of the alloy during powder production cooling. The small amount of two-phased material (ϵ -bronze and α -Cu) discussed previously would form with slight variations in composition as the melt cooled to progressively lower temperatures. Such composition variation would cause a shift in the lattice constant and therefore the diffraction pattern. The result is low intensity patterns slightly offset from the primary pattern. These shifts are not observed in the specimens quenched from above 400°C because they have had time at sufficient temperature to fully transform to α -Cu.

6.2.2 Melt Characteristics

The formation of a liquid phase in a sintering compact has been shown to have significant influence on its ability to hold shape [9,11,12,14]. German [14] concluded the yield strength of a sintering powder compact with a liquid phase varies with the liquid

fraction. The loss of yield strength due to liquid fraction is the major factor leading compact slumping under the influence of gravity. Controlled experiments to visually measure slumping relative to sintering conditions were performed by Lal, Shoales and German [12] on bronze and Upadhyaya and German [11] on various W, Fe and Mo alloys. Lal, Shoales and German observed distortion in bronze began above approximately 880°C. FTT measurements made above this temperature recorded a corresponding rapid decrease in strength. Upadhyaya and German concluded there was a critical maximum liquid fraction below which a compact would have sufficient strength to resist slumping. This liquid fraction is influenced by the intersolubility between alloy components as well as time and temperature profiles. A model to incorporate liquid fraction would require the exact correlation of liquid fraction to strength for a given alloy such as the model used for recrystallization fraction. The time and temperature dependence of liquid fraction could be treated by modeling the appropriate heat transport events which cause melt formation.

The evaluation of liquid fraction in 90Cu-10wt.%Sn prealloyed bronze was presented in Section 4.4.1 and shown in Figure 4.23. The formation of first liquid (solidus) occurs at 851°C when the powder is initially heated from room temperature at 5°C/min. The phase diagram [82] gives a solidus temperature of 861°C for this alloy. The discrepancy is due to the powder fabrication technique. The rapid solidification during atomization is a non-equilibrium event and results in a depressed solidus temperature. This is also evident in the X-ray diffraction results, discussed in Section 6.2.1, by the segregation events which lead to peak smearing. When the melted powder was cooled to solid and reheated, during the second cycle shown in Figure 4.23, the solidus is in

agreement with the phase diagram. In either case, the solidus temperature is sufficiently high to conclude that liquid fraction did not influence the strength within the temperature range of this research. This conclusion is further supported by the observations of Lal, Shoales and German [12] for 90Cu-10wt.%Sn prealloyed bronze. They concluded there was no influence of liquid formation upon strength of this bronze alloy through 880°C. Therefore, liquid fraction was not considered to be a factor in the current *in situ* strength evolution model.

6.3 Model Application

This last section discusses the application of the *in situ* strength evolution model. The first application is to model two other powder compacts. The model is then used to design thermal cycles to meet hypothetical strength evolution requirements.

6.3.1 Other Powder Compacts

Given the proper data set, the *in situ* strength evolution model can be applied to other powder compacts. The method of parameter determination follows the same method outlined in Section 6.1. This section presents the results of using such methods for a larger size increment of the same bronze alloy as well as for a W alloy. The raw data for these two powder systems are contained in Appendix E. The tables of this appendix also contain sets of raw data from FTT measurements of a variety of additional powder systems. Measurements of the additional systems include *in situ* strength evolution during

sintering as well as debinding. Also included with each set of data is a brief description of the powder system.

6.3.1.1 Strength Evolution in B-406 Grade Bronze

In a previous work [85], a limited set of constant sintering rate (10°C/min) FTT data was gathered for United States Bronze Powders, Inc. B-406 grade 90Cu-10wt.%Sn prealloyed bronze compacts. These data were gathered in the identical manner used to gather the data presented in Figure 4.1. In addition, ten additional baseline TRBs were included in FTT tests up to 800°C. Just as with the B-409 in this research, these were tested at room temperature to determine the sinter strengthening contribution. The B-406 grade represents a larger sieve fraction of the same bronze alloy used for B-409. Median size is 40 μm as determined by Horiba LA-910. Additional powder description, compaction details, and raw data is contained in Table E-1.

Since the same alloy was cold worked the same degree, neither the annealing model nor the thermal softening models were altered. The lowest strength reached during FTT testing was 4 MPa at 400°C, however, so the value for R_f was changed from 0.5 to 0.4. The room temperature TRS from the baseline TRBs were used to determine the correlation between MSC parameter and strength. No attempt was made to recalculate the MSC equivalent energy (Q_s) since all baseline measurements were derived from the same type of sintering profile (constant 10°C/min heating to the peak temperature). This was reasonable since the larger powder size of the same alloy would change the sintering rate without necessarily changing the dominant sintering mechanisms. Thus the sinter

strengthening model changed only by the equation used to represent Equation 5.12. In this case, a sigmoidal correlation to data was used as shown by Equation 6.6;

$$\sigma_s = \frac{380}{1 + \exp\left(\frac{-\ln \theta - 25}{0.75}\right)} \quad (6.6)$$

where σ_s and θ are as defined for Equation 6.4. When this expression for Equation 5.12 along with the new value for R_f was used, the model prediction compared to the data was as shown in Figure 6.14. The correlation coefficient is again in excess of 0.99 and the average deviation over the range of sinter strengthening is 8%. Higher fidelity would be possible with a larger set of baseline measurements that included varied ramp rates and isothermal holds.

6.3.1.2 Strength Evolution in W-Cu-Co

In the previous work by Shoales *et al.* [88], the model was applied to W-20vol.%Cu with 0.35wt.% admixed Co. The tungsten was Teledyne C-3 and the copper was AcuPowder 635. The preweighed mixture was blended in a turbula mixer for 30 minutes. It was then ball-milled in heptane for 24 hours using a ball to powder ratio of 6 to 1 (by weight). The milling balls were hardened 440C stainless steel with a diameter of 4.76 mm (3/16 in). After milling, the powder was separated from the milling media and air dried at 60°C. Size analysis by laser scattering using a Sympatec Helos, compaction details, and raw data are recorded in Table E-2.

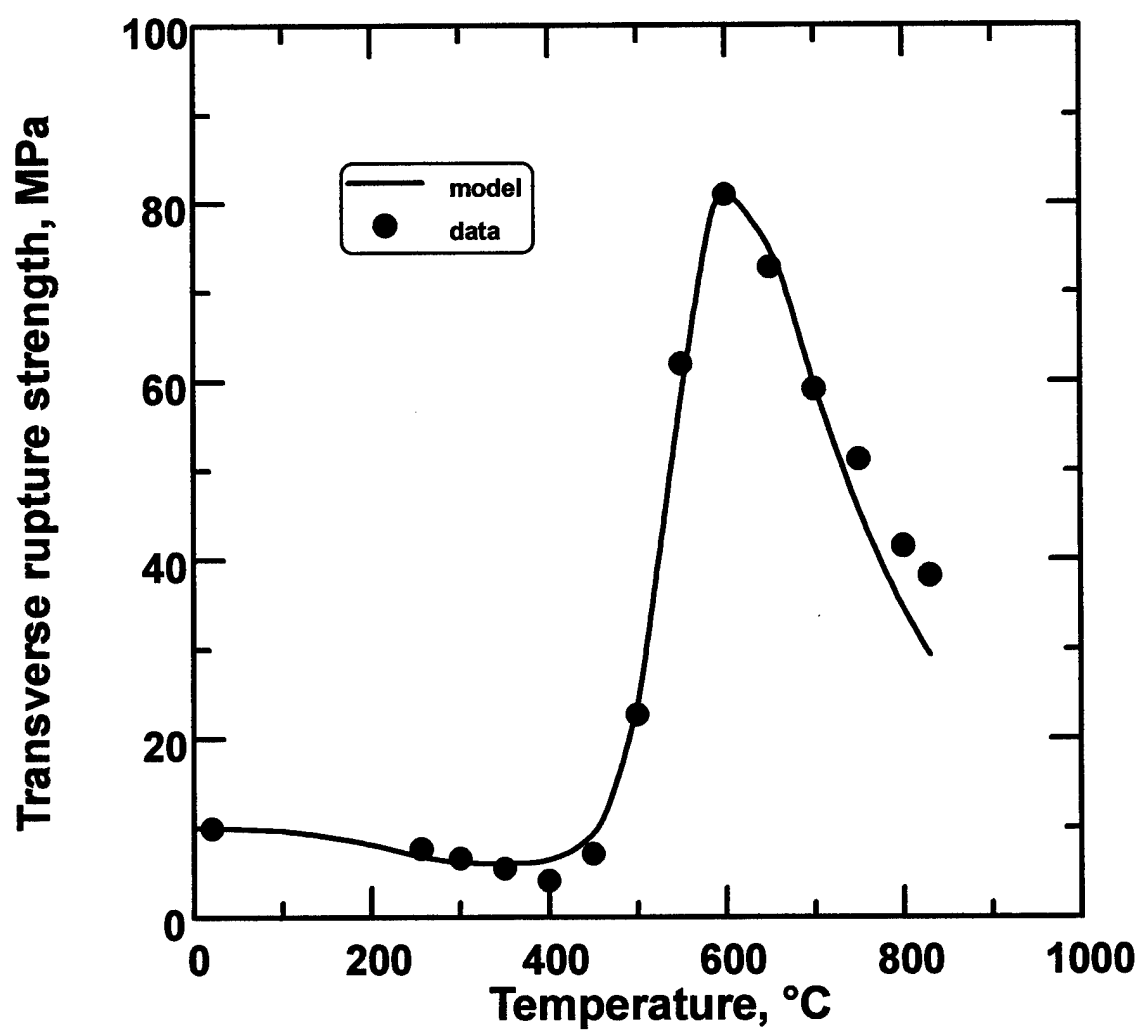


Figure 6.14: Comparison of *in situ* strength evolution model prediction and data for United States Bronze, Inc. grade B-406 prealloyed 90Cu-10wt.%Sn bronze compacts. When compared to the data, prediction correlation coefficient is greater than 0.99 and average deviation in the sinter strengthening region is 8%.

Model parameters were determined from nine constant heating rate FTT tests and two additional cooling tests (as described in Section 3.1.6). The constant heating tests were performed after sintering at 10°C/min to test temperatures up to 1105°C. The two cooling tests were performed at 500 and 700°C after cooling from the peak sintering temperature of 900°C (also 10°C/min heating rate). Additionally, room temperature TRS measurements were performed on TRBs sintered to various temperatures up to 1105°C. As with the B-406 application, parameter determinations followed the procedures outlined in Section 6.1. The green strength (σ_G) was 6 MPa. The fraction of green strength remaining after recrystallization (R_f) was 0.3. Values of 5 s^{-1/2} and 30 kJ/mol for Γ_O and Q_R , respectively, provided the best annealing model. The MSC equivalent activation energy (Q_R) was determined to be 400 kJ/mol. This value of Q_R resulted in a fit of MSC parameter (θ) to the room temperature strength (σ_s) best described by Equation 6.7.

$$\sigma_s = \frac{100}{1 + \exp\left(\frac{-\ln \theta - 46}{1.15}\right)} \quad (6.7)$$

Note, this is the same form used in the previous application for B-406 bronze. Finally, using the cooling tests as a guide, the thermal softening strength fraction (f_T) as a function of temperature in (°C) was best described by Equation 6.8.

$$f_T = \frac{1}{1 + 3(10)^{-6}T^2} \quad (6.8)$$

The performance of this model is shown in Figure 6.15. Similar to Figures 6.12 and 6.13, this figure depicts both the constant rate data as well as the cooling test data. The cooling curve is shown as strength versus test temperature starting at the peak temperature of 900°C and terminating with the room temperature test. With the limited data the fit still correlates to an acceptable 0.989 and the average deviation in the sinter strengthening region is 7%. Again, higher fidelity would be possible with a larger set of baseline measurements that included varied ramp rates and isothermal holds. Also, as observed with the B-409 bronze, true thermal softening data (Figure 4.29) would provide a better thermal softening model.

6.3.2 Thermal Cycle Design

The model described here could also be used to design thermal cycles that meet specific *in situ* strength requirements. Predictions of strength evolution would form the vital portion of a larger sintering design package. Such a package would include the parameters relating to the heat transport within the furnace as well as within the component. This package would also include corresponding models to describe the dominant sources of stress during the sintering cycle. The model developed here would then allow key comparison between sintering stress and component strength. Feedback between the various modules of the entire package would then ensure that the thermal cycle was designed such that the necessary levels of strength were available to resist distortion and cracks.

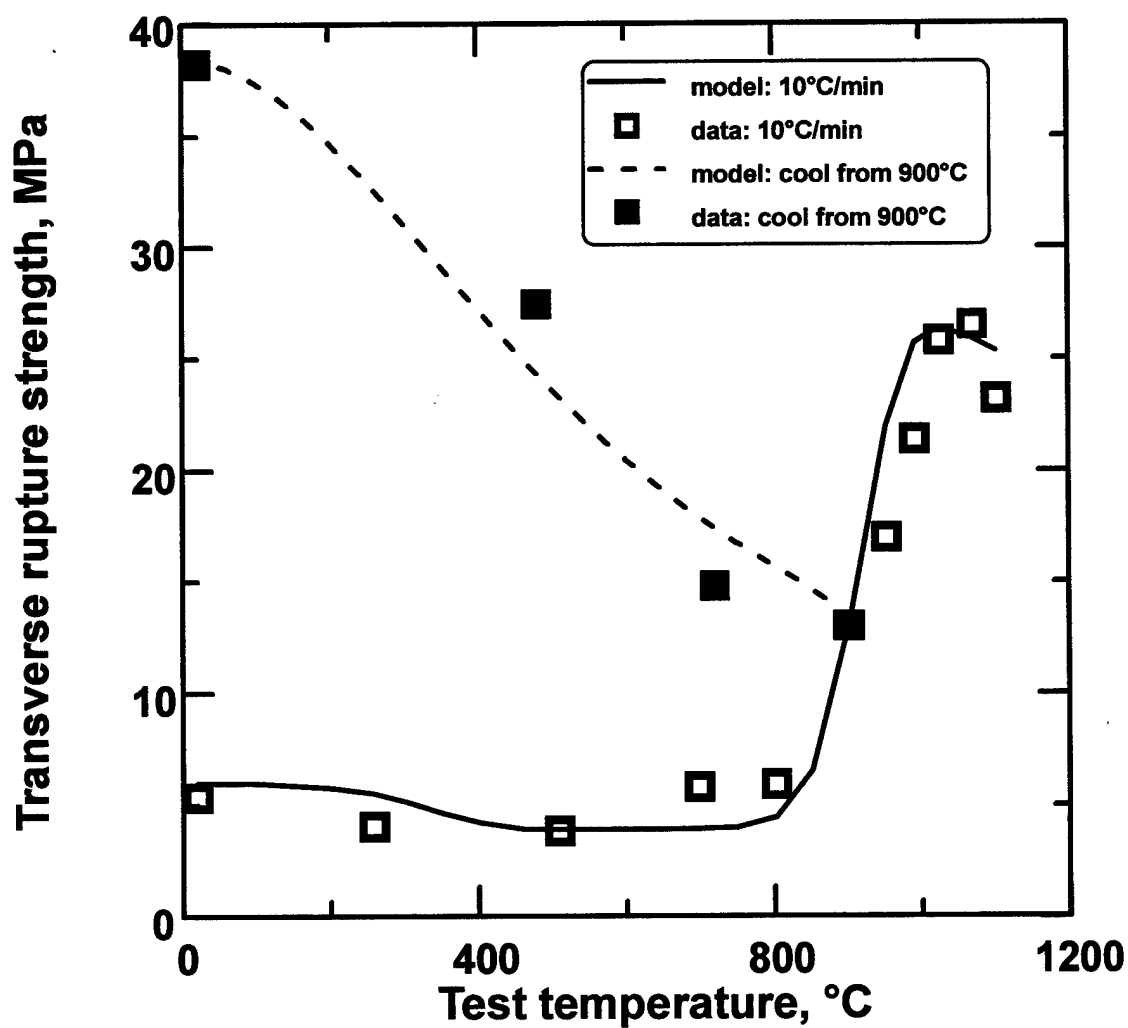


Figure 6.15: Comparison of *in situ* strength evolution model prediction and data for W-Cu-Co compacts. Comparison with data from constant 10°C/min heating rate to test temperature and to tests cooled from 900°C. When compared to the data, prediction correlation coefficient is greater than 0.98 and average deviation in the sinter strengthening region is 7%.

Since all the modules of the aforementioned design package are not yet in place, the following hypothetical strength requirement will illustrate the model's application. This requirement was imposed upon a component compacted to a green strength of 10 MPa from the B-409 bronze. Recall that the observations by Yoel, Miller and Olson [17-19] as well as Mizuno, Kawasaki and Watanabe [20-23] agreed that the majority of distortion occurs during the ramp to temperature. Lenel *et al.* [40-42] concluded the peak residual stress in sintering copper was highest at approximately 400°C. Heat transport is also poor at this early stage compared to a sintered structure due to the weak presinter particle bonds [102]. Poor heat transport at low temperature is further worsened by lack of significant radiant heating. Therefore, the assumption was made that due to heat transport through our component's geometry, deformation begins between 400 and 500°C. Such conclusions could have been drawn from video imaging observations. They could have also been made from models of sintering stress or differential thermal strain response. The hypothetical strength requirement was to regain the compact strength lost to recrystallization prior to heating above 400°C. An additional requirement was to not create an unduly long cycle time. The thermal profile designed to meet these requirements is shown in Figure 6.16 as a plot of strength and temperature versus time. This profile uses a rather high heating rate (50°C/min) to 400°C to minimize the time spent to reach a temperature where sinter strengthening can begin. A 6 min hold at this temperature returns the compact to its original green strength of 10 MPa. The heating then continues at a slower 10°C/min to minimize heat transport lag (and therefore stress) within the component. It should be noted that this cycle is actually 24 min quicker to the end of the

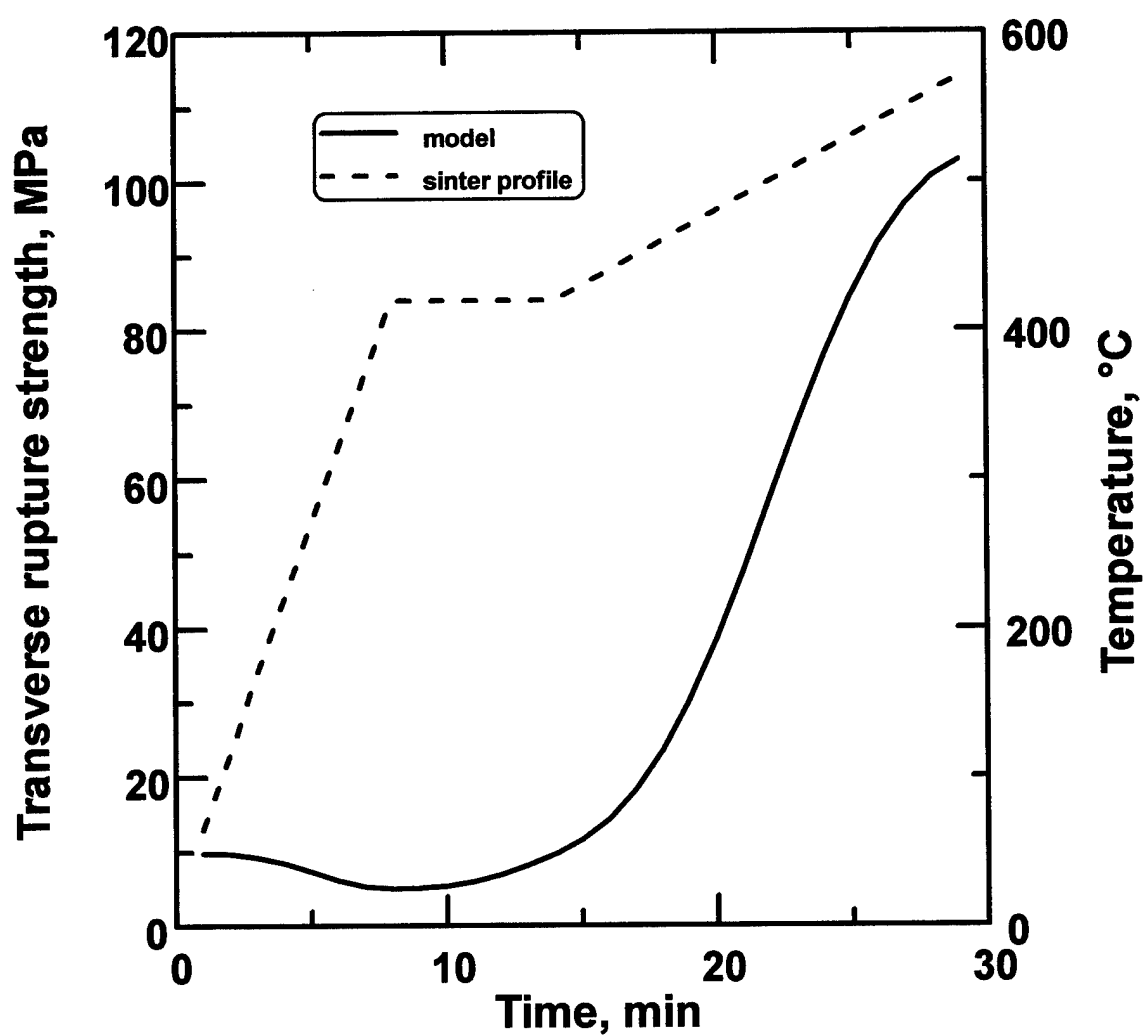


Figure 6.16: Predicted transverse rupture strength versus time for 50°C/min to 400°C followed by a 6 min hold and continued heating at 10°C/min. Also shown is the plot of temperature versus time as a reference.

400°C hold than for constant 10°C/min to the same temperature. Note also that, at this heating rate, the compact has strengthened four-fold over the green state prior to 500°C.

If more strength was required prior to heating above 400°C, the hold time could be increased as appropriate. Prior observations by De Jonghe *et al.* [103-105] have focused on low temperature, long term holds (for example 200 h at 800°C for alumina) to induce strength prior to sintering for microstructural control. As shown by the contour map of isothermal sinter strengthening in Figure 6.9, longer holds at low temperature do increase strength and reduce susceptibility to component damage during sintering. To illustrate, Figure 6.17 shows the model prediction for heating to 400°C and holding for 20 minutes prior to continued heating. In this simulation, the model predicts more than double the strength at the end of the hold as compared to the 6 min case. Note that despite the hold, the peak strength at 600°C is still near the no hold value of 100 MPa found in Figure 6.11. This result agrees with the FTT measurements reported in Section 4.1.2 and shown in Figure 4.4. Note also that the heating in the current simulation is 10°C/min throughout. This change from the previous case (50°C/min to 400°C) permits further model performance validation by comparison with a wide variety of data. Shown in Figure 6.17 are data (labeled with their test number) from Figures 4.1, 4.3 and 4.4 which match the sinter profile. Despite the variety of test types from which these data were extracted, the average deviation is under 5%.

More complex strength evolution requirements could be easily addressed by contour plots such as those shown in Figures 6.8 and 6.9. As a final demonstration, a similar contour map was plotted for the entire *in situ* strength evolution model (Equation

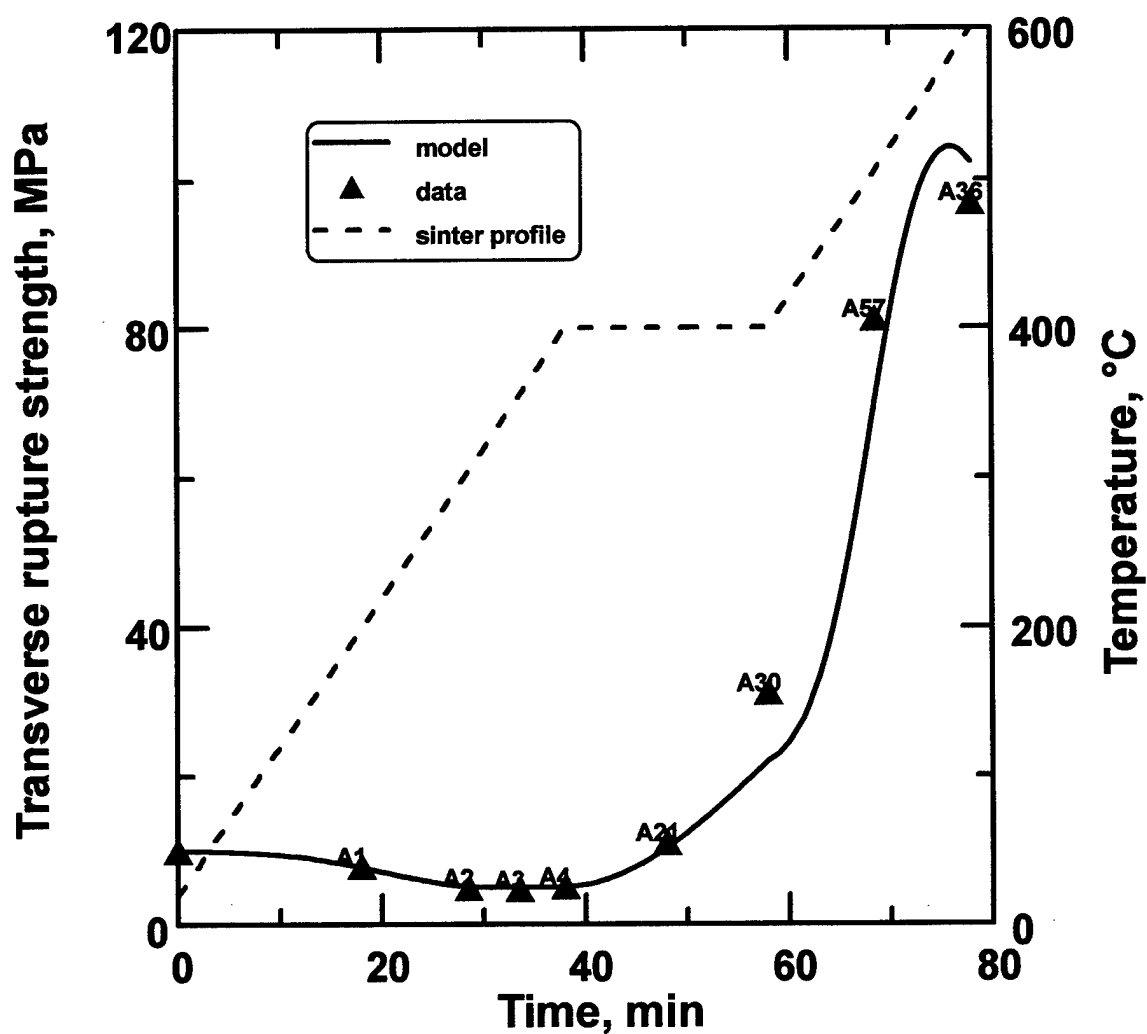


Figure 6.17: Predicted transverse rupture strength versus time for 10°C/min to 400°C followed by a 20 min hold and continued heating at 10°C/min to 600°C. Also shown for comparison are the FTT data from Appendix A which match this sinter profile. The average deviation between the data and the model is under 5%. The plot of temperature versus time is given as a reference.

5.15) in an earlier work [106]. This map, shown by Figure 6.18, plots strength contours which were calculated for instantaneous heating and therefore reflect the sintering value of isothermal holds. The effect of realistic heating rate, $10^{\circ}\text{C}/\text{min}$, is indicated by the curvature of the vertical axis at times of 0, 20, and 40 min. This displacement represents the additional work of sintering during the heating period. From these contours it is obvious that the strength of the compact is most sensitive to temperature. This plot also indicates that hold times more than approximately 20 min have a much less dramatic impact on sinter strengthening. Plots such as these provide easy visual design information as to the impact of the various time-temperature combinations on the evolution of strength. As also observed in the previous work, such strength modeling is best used when paired with finite elements tools which estimate thermal [107] as well as other environmental stresses [38,39,42]. The major industrial impact of such a combination will be in the design of thermal cycles where all sources of stress are countered with a sufficient level of compact strength. Thus, distortion, cracks, and other factors which degrade the final component dimensional precision are eliminated.

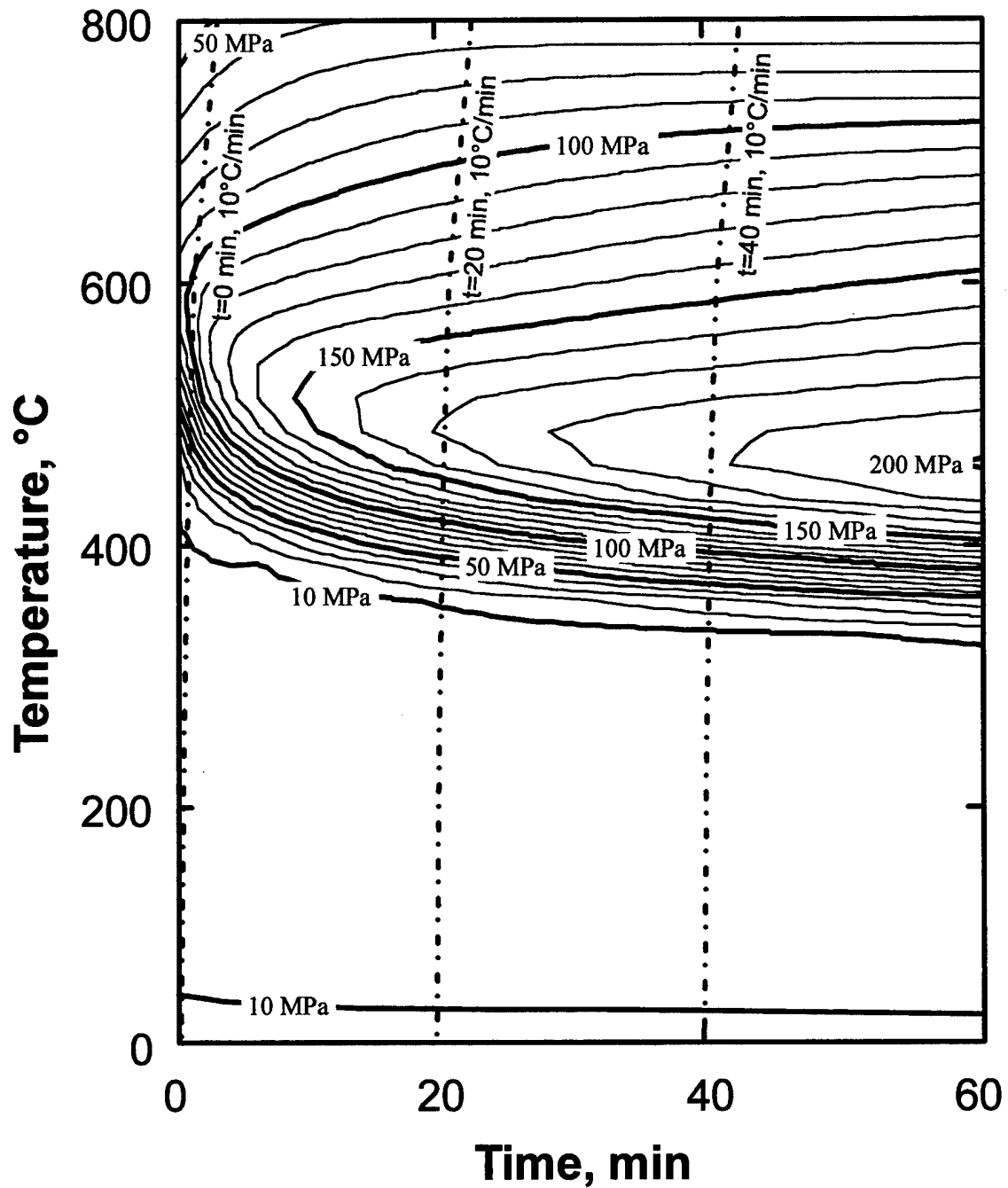


Figure 6.18: A contour map of *in situ* strength evolution versus time and temperature for instantaneous heating. To account for a realistic heating rate of $10^{\circ}\text{C}/\text{min}$ to temperature, the time axes (vertical) are curved to show the equivalent work of sintering during heating [106].

Chapter 7

Conclusions

This research was initiated by a basic need to understand the evolution of strength in sintering P/M components. The significance of this work has been threefold. First was the development of a new category of test apparatus to make *in situ* strength measurements of P/M systems during sintering. Second was the successful measurement of strength in bronze compacts throughout the range of sintering. And finally, the thesis has developed an *in situ* strength evolution model as a practical aid to thermal parameter design.

The Flaming Tensile Tester combines the most common P/M mechanical test (transverse rupture strength) with a batch sintering furnace. Its design allows test specimens to remain undisturbed prior to performing the test, thus preventing the test from influencing the measurement. The measurement carries an uncertainty of less than 2%. Such precision is sufficient to detect strength evolution during annealing recrystallization in compacted components as well as debinding in powder injection molded components. A personal computer based data acquisition system permits economical recording and post processing of load and temperature versus time measurements. It can sinter with any combination of heating ramps and isothermal holds to more than 1100°C. The test supports are sealed in a retort throughout the test which allows the inclusion of any process gas into the sintering cycle. Thermal control is

measured at the test specimen which permits excellent correlation of the test condition to the results.

Precise experimental determination of the *in situ* strength evolution in bronze during sintering were the first data of their kind. For the first time it is known that the low strength green parts actually lose strength as they begin to heat during sintering. The bronze compacts measured in this research lost between 50 and 60% of their initial 10 MPa green strength by approximately 400°C. Measurements of W-Cu-Co pressed to 6 MPa (0.50 fractional theoretical density) showed a similar loss of approximately 30%. This initial degradation of strength was due to the recrystallization of cold worked strength gained during compaction. Sinter strengthening accounted for the most significant contribution to *in situ* strength evolution. Depending on the heating rate, the bronze measurements found more than a ten-fold increase in *in situ* strength between 400 and 600°C. The rate of evolution over this range and the exact temperature of peak strength also depended on the presence of isothermal holds during the heating ramp. Sinter strengthening competes with thermal softening to give a complicated strength evolution curve that, at higher temperatures, hides the progressive increase in sintered strength typically reported at room temperature. Regardless of the path taken, the strength evolution after reaching the temperature of peak strength was governed by temperature dependent thermal softening. Thermal softening in bronze accounted for more than a 60% *in situ* strength loss between 600 and 800°C.

The *in situ* strength evolution model provides the missing piece to understanding the physical response of a sintering compact to the thermal environment. By itself, this

model can be used to create maps of strength response with respect to time, temperature and heating rate. Such a response can in turn be correlated with known sintering stress to ensure the compact has sufficient strength to resist distortion. A hypothetical thermal cycle design doubled strength at 400°C (over the 10°C/min constant heating baseline) while decreasing the corresponding sintering time by over 60%. The model developed by this thesis for bronze compacts is not without certain limitations. The loss of strength due to recrystallization represented by the annealing model is not to be expected when modeling hard or brittle materials such as ceramics. This is of course due to the lack of significant plastic deformation of these materials during the compaction step. Similarly, PIM components, which owe their green strength to the addition of a binder phase rather than plastic deformation, would also lack an annealing response in their strength evolution. Thermal debinding would, however, lead to a somewhat analogous contribution to strength evolution as the removal of binder usually results in a corresponding loss of green strength. The model is also generalized with respect to phase transformation. The subject prealloyed bronze exhibits no significant change of phase throughout the investigated range of sintering. Elemental mixes of copper and tin and systems such as Fe-Cu-C would undergo strength evolution due in part to the transition from one alloy phase to another as they are thermally processed.

The model presented here is an essential component to the larger total sintering design package. Such a total package would determine heat transport within a sintering component along with the thermal strain and corresponding stress due to thermal differentials. It would also account for additional sources of stress such as those due to

shaping inhomogeneities. As a P/M component design tool, the larger model would be useless, however, without inclusion of the compact's strength evolution response.

Feedback between the stress models and this *in situ* strength evolution model could create thermal cycles which ensured the necessary strength was available to resist distortion and cracks. Such concepts represent a new view of sintering based on cycles designed for strength evolution rather than densification or other properties.

References

1. R.M. German, *Powder Metallurgy Science*, 2nd edition, Metal Powder Industries Federation, Princeton, NJ, 1994.
2. R.M. German, *Sintering Theory and Practice*, John Wiley & Sons, Inc., New York, NY, 1996.
3. S. Bradbury (ed.), *Powder Metallurgy Equipment Manual*, 3rd edition, Metal Powder Industries Federation, Princeton, NJ, 1986.
4. R.M. German, *Powder Injection Molding*, Metal Powder Industries Federation, Princeton, NJ, 1990.
5. R.M. German, *Particle Packing Characteristics*, Metal Powder Industries Federation, Princeton, NJ, 1989.
6. E. Klar and W.M. Shafer, "On Green Strength and Compressibility in Metal Powder Compaction," *Modern Development in Powder Metallurgy*, H.H. Hausner and P.V. Taubenblat (eds.), vol. 9, Metal Powder Industries Federation and American Powder Metallurgy Institute, Princeton, NJ, 1976, pp. 91-113.
7. I.H. Moon and J. S. Choi, "Dependence of Green Strength on Contact Area Between Powder Particles for Spherical Copper Powder Compacts," *Powder Metallurgy*, vol. 28, 1985, pp. 21-26.
8. R.M. German, "Strength Dependence on Porosity for P/M Compacts," *The International Journal of Powder Metallurgy & Powder Technology*, vol. 13, no. 4, 1977, pp. 259-271.
9. R.M. German, *Liquid Phase Sintering*, Plenum Press, New York, NY, 1985.
10. F. Vollertsen and M. Geiger, "Precision of P/M Parts - a System Property," *Powder Metallurgy International*, vol. 22, no. 3, 1990, pp. 15-20.
11. A. Upadhyaya and R.M. German, "Control of Distortion During Liquid Phase Sintering," *Proceedings of the 14th International Plansee Seminar*, G. Kneringer, P. Rodhammer and P. Wilhartitz (eds.), Plansee Metalwerk, Reutte, Austria, vol. 2, 1997, pp. 68-85.

12. A. Lal, G.A. Shoales and R.M. German, "Thermal Characterization to Study the Sintering of Bronze Powders," *Twenty-Fourth International Thermal Conductivity Conference / Twelfth International Thermal Expansion Symposium*, Pittsburgh, PA, 1997.
13. F.V. Lenel, H.H. Hausner, O.V. Roman and G.S. Ansell, "The Influence of Gravity in Sintering," *The Transactions of the Metallurgical Society of AIME*, vol. 227, 1963, pp. 640-644.
14. R.M. German, "Supersolidus Liquid-Phase Sintering of Prealloyed Powders," *Metallurgical and Materials Transactions A*, vol. 28A, 1997, pp. 1553-1567.
15. W.J. Tseng and P.D. Funkenbusch, "Sintering of Inhomogeneous ZnO Powders," *Physical Chemistry of Powder Metals Production and Processing*, W.M. Small (ed.), The Minerals, Metals and Materials Society, Warrendale, PA, 1989, pp. 371-385.
16. R.M. German, K.F. Hens, and S.T. Paul Lin, "Key Issues in Powder Injection Molding," *American Ceramic Society Bulletin*, 1991, vol. 70, no. 8, pp. 1294-1302.
17. D.W. Yoel, C.W. Miller, and R.K. Olson, "Quantitative Imaging of MIM Debinding and Sintering," *Advances in Powder Metallurgy & Particulate Materials - 1995*, Metal Powder Industries Federation, Princeton, NJ, 1995, pp. 4.19-4.29.
18. D.W. Yoel, C.W. Miller, and R.K. Olson, "Image Acquisition and Analysis During Sintering: A Method of Monitoring and Controlling P/M Part Characteristics," *Advances in Powder Metallurgy & Particulate Materials - 1994*, Metal Powder Industries Federation, Princeton, NJ, 1994, vol. 4, pp. 85-94.
19. D.W. Yoel, C.W. Miller, and R.K. Olson, "Direct Imaging During MIM Sintering," presentation to *The 1995 International Powder Injection Molding Symposium*, 20 July 1995, State College, PA.
20. Y. Mizuno, A. Kawasaki and R. Watanabe, "In Situ Measurements of Sintering Shrinkage in Powder Compacts by Digital Image Correlation Method," *Powder Metallurgy*, 1995, vol. 38, no. 3, pp. 191-195.
21. Y. Mizuno, A. Kawasaki and R. Watanabe, "Nonuniform Sintering Shrinkage of Stainless Steel Powder Compacts Prepared by Metal Injection Molding," *Journal Japan Institute of Metals*, 1996, vol. 6, no. 1, pp. 106-112.

22. Y. Mizuno, A. Kawasaki and R. Watanabe, "In situ Measurement of Nonuniform Sintering Shrinkage of Complex-shaped Powder Compacts," *Journal Japan Institute of Metals*, 1994, vol. 58, no. 10, pp. 1184-1190.
23. Y. Mizuno, A. Kawasaki and R. Watanabe, "Measurement of Nonuniform Sintering Shrinkage of Functionally Gradient Material by Digital Image Processing," *Metallurgical and Materials Transactions B*, 1995, vol. 26B, pp. 75-79.
24. F. Vollertsen and M. Geiger, "Precision of P/M Parts - a System Property," *Powder Metallurgy International*, vol. 22, no. 3, 1990, pp. 15-20.
25. G.F. Bocchini, "Influence of Process Parameters on Precision of P/M Parts," *Powder Metallurgy*, vol. 28, no. 3, 1985, pp. 155-165.
26. G. Dowson, "The Sintering of Bronze," *Metal Powder Report*, vol. 39, 1984, pp. 71-73.
27. R.M. German, "Supersolidus Liquid-Phase Sintering of Prealloyed Powders," *Metallurgical and Materials Transactions A*, vol. 28A, 1997, pp. 1553-1567.
28. Y. Liu, R. Tandon and R.M. German, "Modeling of Supersolidus Liquid Phase Sintering: I. Capillary Force," *Metallurgical and Materials Transactions A*, vol. 26A, 1995, pp. 2415-2422.
29. Y. Liu, R. Tandon and R.M. German, "Modeling of Supersolidus Liquid Phase Sintering: II. Densification," *Metallurgical and Materials Transactions A*, vol. 26A, 1995, pp. 2423-2430.
30. Y. Liu, R. Tandon and R.M. German, "Advanced Sintering Technology for Prealloyed Powders," *Advances in Powder Metallurgy and Particulate Materials - 1995*, vol. 1, Metal Powder Industries Federation, Princeton, NJ, 1995, pp. 4.175-4.184.
31. K. Breitzkreutz and K. Haedecke, "Determination of Activation Energies of Shrinkage Processes During Sintering - Part 2: Application to Technical Powders," *Powder Metallurgy International*, vol. 14, 1982, pp. 213-216.
32. K. Breitzkreutz and K. Haedecke, "Die Aktivierungsenergien der Schrumpfung beim Sintern einiger technischer Metallpulver," *Z. Metallkunde*, vol. 74, 1983, pp. 402-405.
33. P.Z. Cai, G.L. Messing and D.L. Green, "Determination of Mechanical Response of Sintering Compacts by Cyclic Loading Dilatometry," *Journal of American Ceramic Society*, vol. 80, no. 2, 1997, p 445-452.

34. A.L. Dawson, M. Dubois, S. Pellitier and J.F. Bussiere, "Non-destructive Evaluation of Iron P/M Compacts During Sintering," *Advances in Powder Metallurgy & Particulate Materials - 1997*, Metal Powder Industries Federation, Princeton, NJ, pp. 16.87-16.98.
35. J. Krautkramer and H. Krautkramer, *Ultrasonic Testing of Materials*, 3rd edition, Springer Verlag, Berlin, Germany, 1983.
36. E.H. Aigeltinger, "Relating Microstructure to Sintering Force," *The International Journal of Powder Metallurgy and Materials Technology*, vol. 11, no. 3, 1975, pp. 195-203.
37. R.A. Gregg and F.N. Rhines, "Surface Tension and the Sintering Force in Copper," *Metallurgical Transactions*, vol. 4, 1973, pp. 1365-1374.
38. W.J. Tseng and P.D. Funkenbusch, "Sintering of Inhomogeneous ZnO Powders," *Physical Chemistry of Powder Metals Production and Processing*, W.M. Small (ed.), The Minerals, Metals and Materials Society, Warrendale, PA, 1989, pp. 371-385.
39. R.M. German, "Prediction of Sintered Density for Bimodal Powder Mixtures," *Metallurgical Transactions A*, vol. 23A, 1992, pp. 1455-1465.
40. F.V. Lenel, H.H. Hausner, E. Hayashi and G.S. Ansell, "Some Observations on the Shrinkage Behavior of Copper Compacts and Loose Powder Aggregates," *Powder Metallurgy*, no. 8, 1961, pp. 25-36.
41. F.V. Lenel, H.H. Hausner, I.A. El Shanshoury, J.G. Early and G.S. Ansell, "The Driving Force for Shrinkage in Copper Powder Compacts During the Early Stages of Sintering," *Powder Metallurgy*, no. 10, 1962, pp. 190-198.
42. F.V. Lenel, H.H. Hausner, O.V. Roman and G.S. Ansell, "The Influence of Gravity in Sintering," *The Transactions of the Metallurgical Society of AIME*, vol. 227, 1963, pp. 640-644.
43. W.D. Callister, Jr., *Materials Science and Engineering*, John Wiley and sons, Inc., New York, NY, 1985.
44. F.P. Beer and E.R. Johnston, Jr., *Statics and Mechanics of Materials*, McGraw Hill, Inc., New York, NY, 1992.
45. L. P. Martin and M. Rosen, "Analysis of Ultrasonic Velocity Measurements on Sintering Zinc Oxide," *Ultrasonics*, 1997, vol. 35, pp. 65-73.

46. E. Klar and W.M. Shafer, "On the Nature of Green Strength," *International Journal of Powder Metallurgy*, vol. 5, no. 2, 1969, pp. 5-10.
47. R.E. Reed-Hill and R. Abbaschian, *Physical Metallurgy Principals*, 3rd edition, PWS-Kent Publishing Co., Boston, MA, 1991, pp. 230-233.
48. R.W. Cahn (ed.), *Physical Metallurgy*, North-Holland Publishing Co., Amsterdam, 1965, pp. 926-936.
49. J.A. Belk, M.R. Edwards, W.J. Farrell and B.K. Mullah, "Deformation Behavior of Tungsten-Copper Composites," *Powder Metallurgy*, vol. 36, no. 9, 1993, pp. 293-296.
50. S.K. Nath, S. Ray, V.N.S. Mathur and M.L. Kapoor, "Non-isothermal Austenitisation Kinetics and Theoretical Determination of Intercritical Annealing Time for Dual-phase Steels," *ISIJ International*, vol. 34, no. 2, 1994, pp. 191-197.
51. N. Wang, Z. Wang, K.T. Aust and U. Erb, "Isokinetic Analysis of Nanocrystalline Nickel Electrodeposits Upon Annealing," *Acta Metallurgica*, vol. 45, no. 4, 1997, pp. 1655-1669.
52. H.R. Shercliff and M.F. Ashby, "Modeling Thermal Processing of Aluminium Alloys," *Material Science and Technology*, vol. 7, 1991, pp. 85-88.
53. R. Haynes, *The Mechanical Behaviour of Sintered Metals*, Freund Publishing House, London, England, 1981.
54. A.C. Nyce and W.M. Shaffer, "The Relationship of B.E.T. Surface Area to the Sintering Behavior of Spherical Copper Particles," *International Journal of Powder Metallurgy*, vol. 8, no. 4, 1972, pp. 171-180.
55. E.O. Hall, "The Deformation and Ageing of Mild Steel: III Discussion of Results," *Proceedings of the Physical Society B*, vol. 64, 1951, pp. 747-753.
56. N.J. Petch, "The Cleavage Strength of Polycrystals," *Journal of the Iron and Steel Institute*, vol. 173, 1953, pp. 25-28.
57. R. Armstrong, I. Codd, R.M. Douthwaite and Petch, "The Plastic Deformation of Polycrystalline Aggregates," *The Philosophical Magazine*, vol. 7, ser. 8, 1962, pp. 45-58.
58. N. Hansen and B. Ralph, "The Strain and Grain Size Dependence of the Flow Stress of Copper," *Acta Metallurgica*, vol. 30, no. 4, 1982, pp. 411-417.

59. H. Su and D.L. Johnson , "Master Sintering Curve: A Practical Approach to Sintering," *Journal of the American Ceramic Society*, 1996, vol. 79, no. 12, pp. 3211-3217.
60. H. Su and D.L. Johnson, "A Practical Approach to Sintering," *American Ceramic Society Bulletin*, 1997, vol. 76, no. 2, pp. 72-76.
61. MIL-HDBK-5F, *Metallic Materials and Elements for Aerospace Vehicle Structures*, U.S. Air Force Wright Materials Lab, Wright-Patterson AFB, OH, 1994.
62. E.A. Brandes (ed.), *Smithells Metals Reference Book*, 7th edition, Butterworth-Heinemann Ltd., Oxford, U.K., 1992.
63. G.E. Dieter, *Mechanical Metallurgy*, third edition, McGraw-Hill, New York, NY, 1986, pp. 275-279.
64. H.E. Boyer and T.L. Gall (eds.), *Metals Handbook*, American Society for Metals, Metals Park, OH, 1985, pp. 3.12.
65. B.D. Tapley (ed.), *Eshbach's Handbook of Engineering Fundamentals*, 4th edition, John Wiley and Sons, New York, NY, 1990
66. *Standard Test Methods for Metal Powder and Powder Metallurgy Products*, Metal Powder Industries Federation, Princeton, NJ, 1997.
67. M.P. Thomas and A. Rosen, "The Validity of Transverse Rupture Strength for WC-Co Hard Materials," *Journal of Material Science Letters*, Vol. 14, 1995, pp. 1512-1514.
68. F.R. Vandeput and N. Mastrantonis, "A Comparison of the Strength of WC-Co Measured by Ring and Transverse Rupture Strength Specimens," *Materials Science and Engineering*, Vol. A105/106, 1968, pp. 423-428.
69. R.L. Rolf and J.D. Weyand, "Structural Design of Brittle Materials," *American Ceramic Society Bulletin*, vol. 64, no. 10, 1985, pp. 1360-1363.
70. V.B. Phadke, "Relationship Between Transverse Rupture Strength and Hardness of P/M Fe-Cu Alloys," *The International Journal of Powder Metallurgy and Powder Technology*, vol. 17, no.1, 1981, pp. 37-43.
71. R. Talmage, "A New Look at Hardness-Strength Relationship in Sintered Metals," *Progress in Powder Metallurgy*, Metal Powder Industries Federation, New York, NY, vol. 17, 1961, pp. 168-175.

72. P.F. Lindskog and G.F. Bocchini, "Development of High Strength P/M Precision Components in Europe," *The International Journal of Powder Metallurgy and Powder Technology*, vol. 15, 1979, pp. 199-230.
73. R.H.T. Dixon and A. Clayton, *Powder Metallurgy for Engineers*, Machinery Publishing Co. Ltd., Sussex, England, 1971, pp. 65.
74. *ASTM Metric Practices Guide*, American Society for Testing and Materials, Philadelphia, PA, 1986.
75. S.J. Kline and F.A. McClintock, "Describing Uncertainties in Single-Sample Experiments," *Mechanical Engineering*, vol. 75, 1953, pp. 3-8.
76. T.G. Beckwith, R.D. Marangoni and J.H. Lienhard V, *Mechanical Measurements*, fifth edition, Addison-Wesley Publishing Co., Reading, MA, 1993, pp. 64-76.
77. R.F. Spreyer, *Thermal Analysis of Materials*, Marcel Dekker, Inc., New York, NY, 1994.
78. E.E. Underwood, *Quantitative Stereology*, Addison-Wesley Publishing Co., Inc., Reading, MA, 1986.
79. R.T. DeHoff and F.N. Rhines, *Quantitative Microscopy*, McGraw-Hill Inc., New York, NY, 1968.
80. G.F. Vander Voort, "Grain size Measurement," *Practical Applications of Quantitative Metallography*, ASTM STP 839, J.L. McCall and J.H. Steele, Jr. (eds.), American Society for Testing and Materials, Philadelphia, PA, 1984, pp. 85-131.
81. J. Mandel, *The Statistical Analysis of Experimental Data*, Dover Publications, Inc., New York, NY, 1964, pp. 34-38.
82. T.B. Massalski (ed.), *Binary Alloy Phase Diagrams*, 2nd edition, American society of Metals, Metals Park, OH, pp. 1481-1483.
83. *Powder Diffraction File*, 3rd edition, Joint Committee on Powder Diffraction Standards, Swarthmore, PA, 1974.
84. G.F. Bocchini, "Influences of Porosity on the Characteristics of Sintered Metals," *Metal Powder Report*, vol. 41, 1986, pp. 829-832.

85. G.A. Shoales and R.M. German, "In situ Strength Evolution of the Sintering of Bronze Powders," *Metallurgical and Materials Transactions A*, vol. 29, no. 4, 1998, pp. 1257-1263.
86. J. Beretka, "Kinetic Analysis of Solid-State Reactions Between Powdered Reactants," *Journal of the American Ceramic Society*, vol. 67, no. 9, 1984, pp. 615-620.
87. W. Jander, "Reactions in the Solid State at High Temperatures," *Zeitschrift fur Anorganische und Allgemeine Chemie*, vol. 163, 1927, pp. 1-30.
88. G.A. Shoales, A. Griffo, A.L. Cardamone, K.K. Comstock and R.M. German, "In Situ Strength Evolution of W-20Cu P/M Compacts," *1997 International Conference on Tungsten, Refractory Metals and Alloys*, Orlando, FL, Metal Powder Industries Federation, Princeton, NJ, 1997, pp. 407-414.
89. R. Haynes and J. T. Egediege, "Effect of Porosity and Sintering Conditions on Elastic Constants of Sintered Irons," *Powder Metallurgy*, vol. 32, no. 1, 1989, pp. 47-52.
90. R. Haynes, "Effects of Porosity on the Tensile Strengths of Sintered Irons," *Metal Powder Report*, vol. 46, no. 2, 1991, pp. 49-51.
91. R. Haynes, "A Study of the Effect of Porosity Content on the Ductility of Sintered Metals," *Powder Metallurgy*, vol. 20, no. 1, 1977, pp. 17-20.
92. R. Haynes, "Effect of Porosity Content on the Tensile Strength of Porous Materials," *Powder Metallurgy*, vol. 14, no. 27, 1971, pp. 64-71.
93. R.M. German and J.F. Lathrop, "Simulation of Spherical Powder Sintering by Surface Diffusion," *Journal of Material Science*, vol. 13, 1978, pp. 921-929.
94. M.F. Ashby, "Physical Modeling of Material Systems," *Material Science and Technology*, vol. 8, 1992, pp. 102-111.
95. M.F. Ashby, "A First Report on Sintering Diagrams," *Acta Metallurgica*, vol. 22, 1974, pp. 275-289.
96. J.L. Johnson, "Densification, Microstructural Evolution, and Thermal Properties of Liquid Phase Sintered Composites," *Ph.D. Thesis*, The Pennsylvania State University, 1994.

97. J.H. Flynn, "The 'Temperature Integral' - Its Use and Abuse," *Thermochimica Acta*, vol. 300, 1997, pp. 83-92.
98. S. Arrhenius, "Über die Reaktionsgeschwindigkeit bei der Inversion von Rohrzucker durch Säuren," *Zeitschrift Physik Chemie*, vol. 4, 1889, pp. 226-248.
99. F.B. Swinkels and M.F. Ashby, "A Second Report on Sintering Diagrams," *Acta Metallurgica*, vol. 29, 1981, pp. 259-281.
100. D.L. Johnson and H. Su, "The Master Sintering Curve," *Advances in Powder Metallurgy & Particulate Materials - 1997*, Metal Powder Industries Federation, Princeton, N.J., vol. 2, 1997, pp. 14.115-14.121.
101. M.F. Ashby, *HIP 6.0*, Department of Engineering, Cambridge, England, 1990.
102. J.C.Y. Koh and A. Fortini, "Prediction of Thermal Conductivity and Electrical Resistivity of Porous Metallic Materials," *International Journal of Heat and Mass Transfer*, vol. 16, 1973, pp. 2013-2022.
103. M.Y. Chu, L.C. De Johghe, M.K.F. Lin and F.J.T. Lin, "Precoarsening to Improve Microstructure and Sintering of Powder Compacts," *Journal of the American Ceramic Society*, vol. 74, 1991, pp. 2902-2911.
104. F.J.T. Lin and L.C. De Johghe, "Initial Coarsening and Microstructural Evolution of Fast-Fired and MgO-Doped Al_2O_3 ," *Journal of the American Ceramic Society*, vol. 80, 1997, pp. 2891-2896.
105. F.J.T. Lin and L.C. De Johghe, "Microstructure Refinement of Sintered Alumina by a Two-Step Sintering Technique," *Journal of the American Ceramic Society*, vol. 80, 1997, pp. 2269-2277.
106. G.A. Shoales and R.M. German, "Combined Time and Temperature Effects on Strength Evolution Using Integral Work of Sintering Concepts," *Metallurgical and Materials Transactions A* (pending approval).
107. B. Dorri, V. Kadambi, F.W. Staub and D.R. Lynch, "Thermal Stress Analysis of Sintering Using a Moving Grid," *International Journal of Numerical Methods in Engineering*, vol. 24, 1987, pp. 47-57.

Appendix A. Raw FTT Data of B-409 Grade Bronze

Table A-1: Raw FTT data presented in Section 4.1.1. *In situ* transverse rupture strength measurements from prealloyed 90Cu-10wt.%Sn bronze compacts sintered at constant heating rate to test temperature in hydrogen.

Test Number	Density Fraction	Sinter Profile		TRS, MPa
		HR	Test T	
A1	0.86	10	200	7.9
A2	0.86	10	305	5.0
A3	0.86	10	351	4.8
A4	0.86	10	402	5.2
A5	0.86	10	454	12.4
A6	0.86	10	506	55.2
A7	0.86	10	550	89.8
A8	0.86	10	601	102.8
A9	0.86	10	603	104.3
A10	0.86	10	604	100.0
A11	0.86	10	649	90.8
A12	0.86	10	700	73.3
A13	0.86	10	750	57.1
A14	0.86	10	800	47.7
A15	0.85	10	841	38.2
A16	0.86	10	854	35.8
A17	0.86	5	401	6.5
A18	0.86	5	502	99.9
A19	0.86	5	600	107.5
A20	0.86	5	700	81.3
HR = heating rate in °C/min				
Test T = FTT Test Temperature in °C				

Test Number	Density Fraction	Sinter Profile				TRS, MPa
		HR	Hold t	Hold T	Test T	
A21	0.86	10	10	405	402	11.1
A22	0.87	10	10	453.5	452	70.2
A23	0.87	10	10	500	496	120.1
A24	0.86	10	10	553	553	115.8
A25	0.86	10	10	603	599	104.3
A26	0.88	10	20	218	218	8.8
A27	0.86	10	20	305	301	4.9
A28	0.87	10	20	352	349	7.1
A29	0.86	10	20	413	396	46.9
A30	0.86	10	20	402	404	31.2
A31	0.87	10	20	454	455	103.5
A32	0.86	10	20	503	503	134.8
A33	0.86	10	20	552.5	552	132.3
A34	0.87	10	20	604	599	115.0
A35	0.86	10	20	702.5	701	80.2
A36	0.86	10	20	419	596	96.9
A37	0.86	10	20	408.5	503	81.2
HR = heating rate in °C/min Hold t = Hold time in min						
Hold T, Test T = Hold Temperature, FTT Test Temperature in °C						

Test Number	Density Fraction	Sinter Profile				TRS, MPa
		HR	Peak T	CR	Test T	
A38	0.86	10	402	-6	120	12.3
A39	0.86	10	400	-6	200	10.5
A40	0.86	10	400	-6	300	10.7
A41	0.86	10	504	-6	120	221.2
A42	0.86	10	500	-6	200	216.1
A43	0.86	10	500	-6	300	158.6
A44	0.86	10	500	-6	400	132.7
A45	0.86	10	600	-7	200	364.0
A46	0.86	10	600	-7	300	277.4
A47	0.86	10	600	-7	400	197.0
A48	0.86	10	600	-7	500	145.3
A49	0.86	10	700	-8	200	442.8
A50	0.85	10	700	-8	500	167.7
A51	0.86	10	700	-8	600	118.5
A52	0.86	10	800	-8	200	589.0
A53	0.86	10	800	-8	400	301.9
A54	0.86	10	800	-8	500	215.5
A55	0.87	10	800	-8	700	82.6
HR, CR = heating rate, cooling rate in °C/min						
Peak T, Test T = Peak Temperature, FTT Test Temperature in °C						

Appendix B. Sinter Strength of B-409 Grade Bronze

Table B-1: Raw data presented in Section 4.2.1. Room temperature transverse rupture strength measurements from prealloyed 90Cu-10wt.%Sn bronze compacts sintered in hydrogen. Sintering profiles included constant heating to a peak sintering temperature followed by cooling to room temperature.

Test Number	Density Fraction	Sinter Profile			TRS, MPa
		HR	Peak T	CR	
B1	0.86	5	404	-7	60.9
B2	0.87	5	601	-7	492.7
B3	0.87	5	700	-7	607.0
B4	0.86	10	308	-7	7.9
B5	0.86	10	364	-7	8.7
B6	0.86	10	402	-7	30.1
B7	0.86	10	407	-8	53.1
B8	0.86	10	408	-7	49.1
B9	0.86	10	463	-7	215.9
B10	0.86	10	502	-7	321.1
B11	0.86	10	508	-7	340.5
B12	0.86	10	553	-7	402.6
B13	0.87	10	602	-8	420.2
B14	0.86	10	602	-7	399.8
B15	0.86	10	602	-8	402.3
B16	0.87	10	606	-7	426.3
B17	0.87	10	650	-7	474.9
B18	0.87	10	702	-7	518.0
B19	0.87	10	703	-7	511.1
B20	0.88	10	799	-7	675.8
B21	0.88	10	803	-7	677.4
B22	0.87	10	842	-7	666.0
B23	0.86	10	854	-7	647.5
B24	0.86	20	485	-5	277.5
B25	0.87	20	485	-5	278.3
B26	0.87	20	600	-4	367.6
B27	0.86	20	600	-4	362.2
HR, CR = Heating Rate, Cooling Rate in °C/min					
Peak T = Peak Sinter Temperature in °C					

[illegible]

Appendix C. Thermal Softening of Dense B-409 Grade Bronze

Table C-1: Raw data presented in Section 4.4.3. Transverse rupture strength measurements performed at various temperatures on prealloyed 90Cu-10wt.%Sn bronze compacts that had been sintered 0.96 density fraction.

Test Number	Test Temperature, °C	Hold Time, min	TRS, MPa
C1	20	0	877
C2	201	0	767
C3	404	0	599
C4	503	0	340
C5	504	30	341
C6	610	0	212
C7	705	30	125
C8	706	0	126
C9	857	0	59

Appendix D. *In situ* Strength Evolution Model - Program Description

Figure D-1: *In situ* strength evolution model flow chart. Ovals indicate input and output blocks, rectangles indicate program sheets as shown in the specified figures and hexagons represent derivation of model parameters from data similar to that in referenced figures.

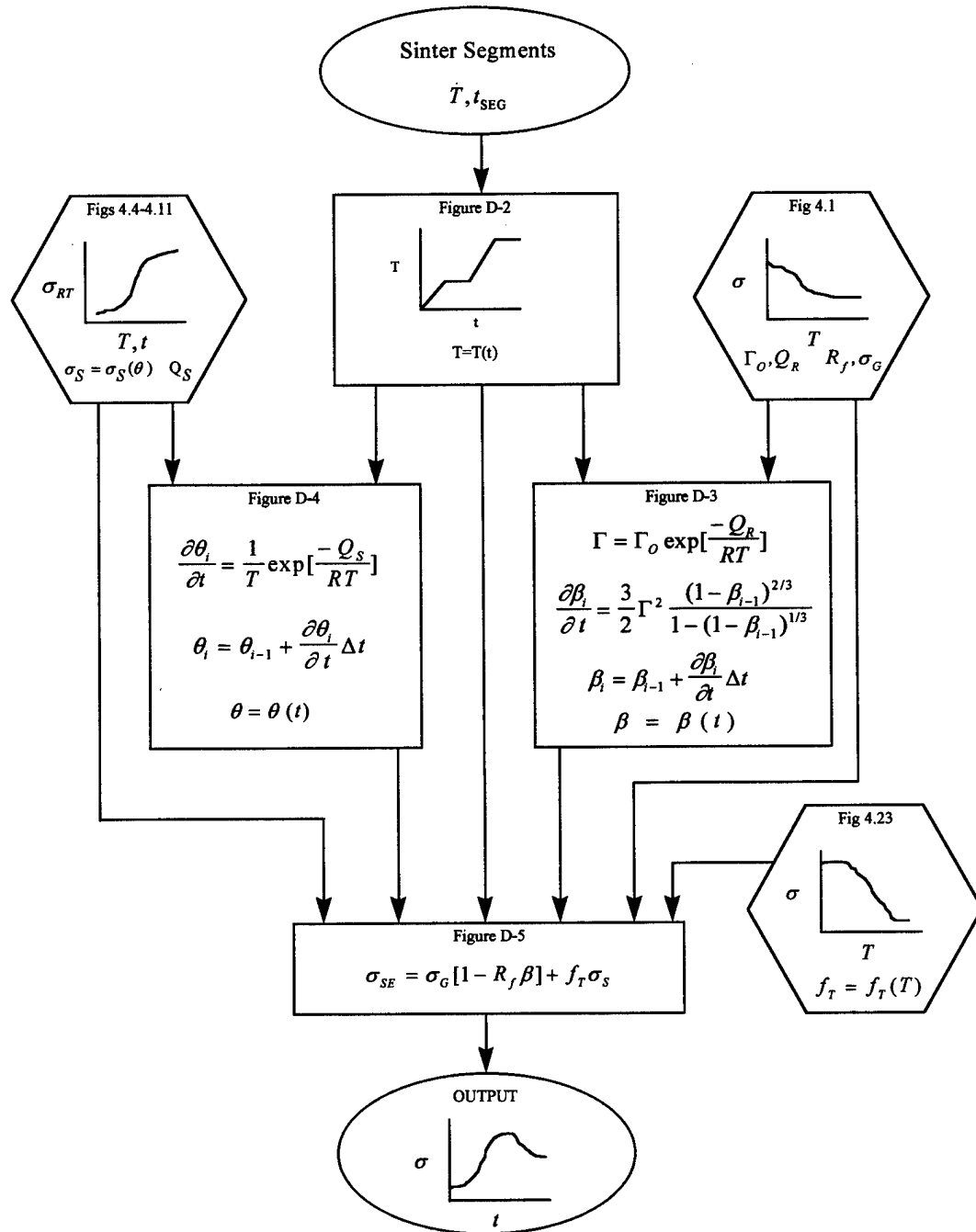


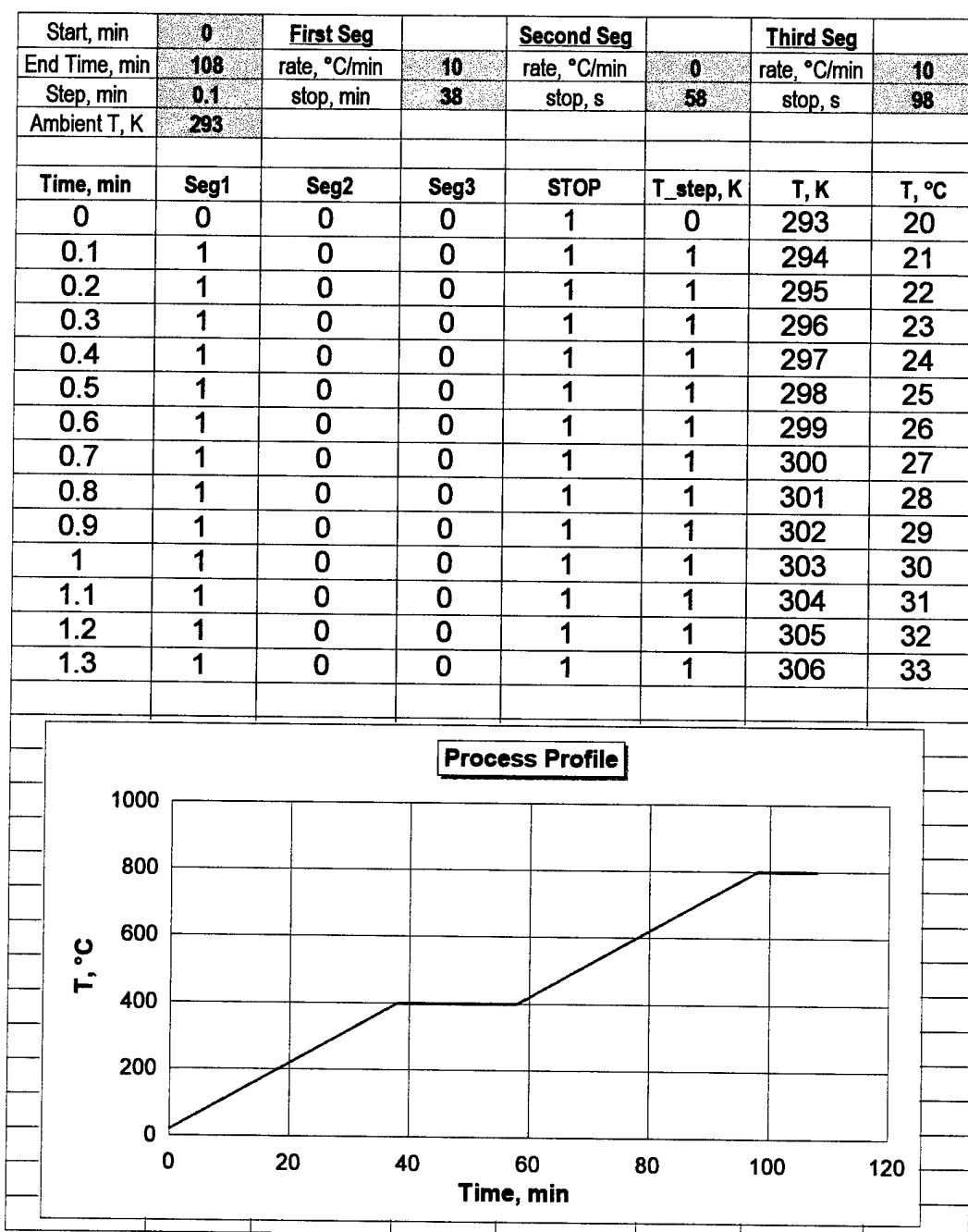
Figure D-2: Sample process profile sheet for the *in situ* strength evolution model.

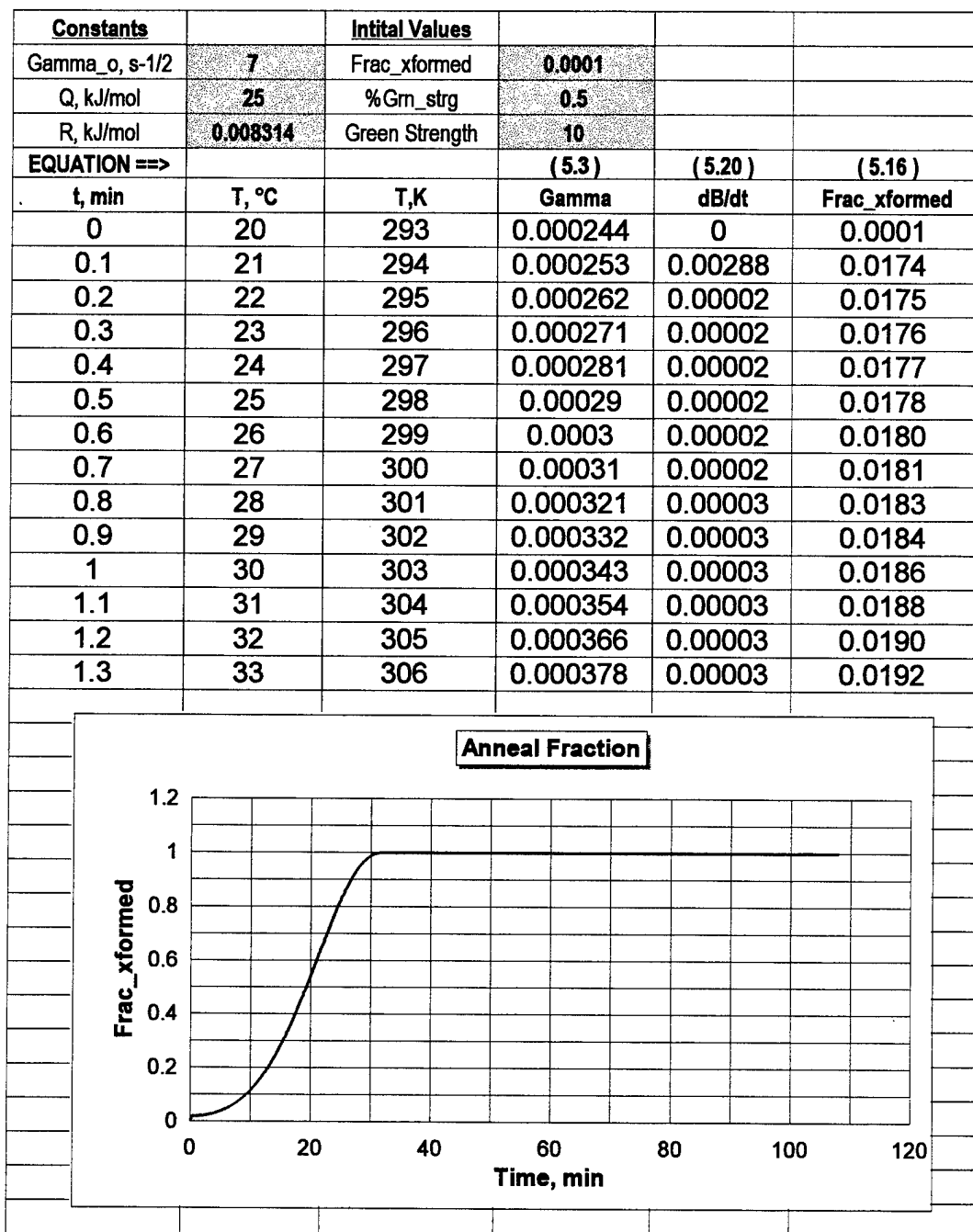
Figure D-3: Sample annealing sheet for the *in situ* strength evolution model.

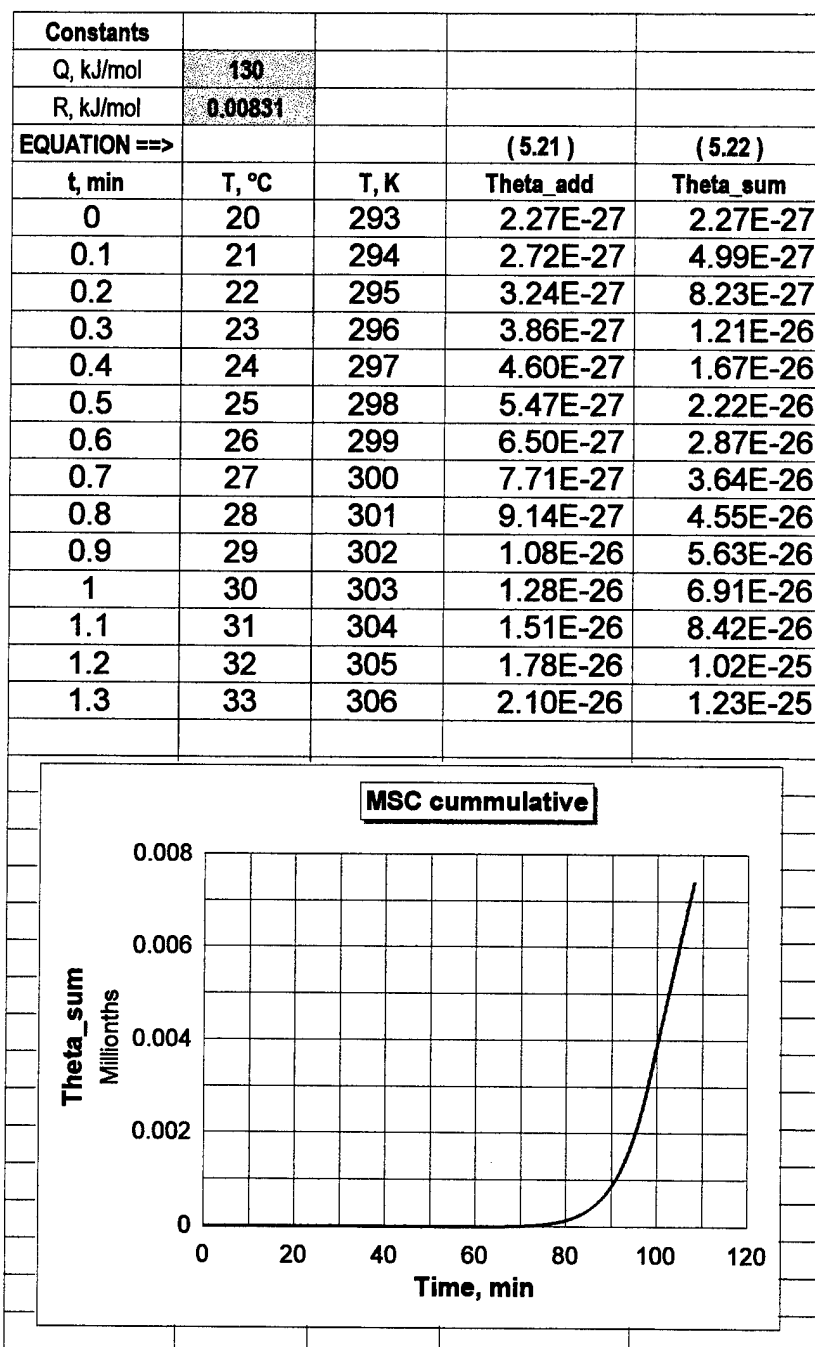
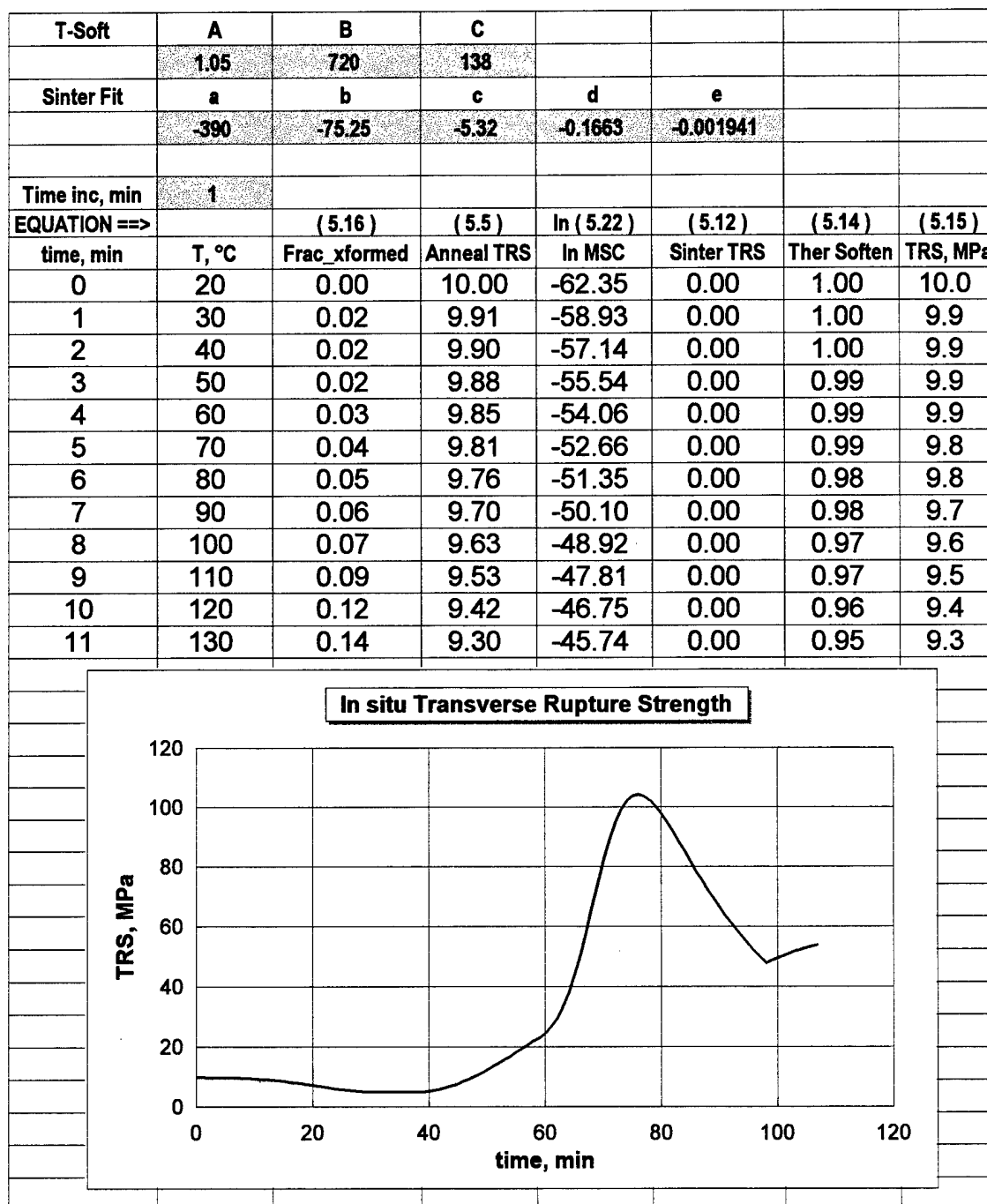
Figure D-4: Sample MSC parameter sheet for the *in situ* strength evolution model.

Figure D-5: Sample *in situ* transverse rupture strength sheet for the *in situ* strength evolution model.



Appendix E: Raw FTT Data from Additional Powders

Table E-1: Raw data for FTT measurements of bronze compacts sintered in hydrogen.

Powder Chararacteristics		Bronze			
Vendor		United States Bronze Powders			
Grade		B-406			
D ₅₀ , μm		40			
Pycnometer Density, g/cm ³		8.91			
Apparent Density, g/cm ³		4.7			
Compaction Pressure, MPa		550			
Strength Data					
Density Fraction	Sinter Profile				TRS, MPa
	HR	Peak T	Test T	CR	
0.86	--	--	20	--	10.5
0.86	10	--	256	--	7.7
0.86	10	--	300	--	6.7
0.86	10	--	350	--	5.5
0.86	10	--	400	--	4.1
0.86	10	--	450	--	7.1
0.86	10	--	500	--	22.7
0.86	10	--	550	--	62.0
0.86	10	--	600	--	81.0
0.86	10	--	650	--	72.8
0.86	10	--	700	--	59.2
0.86	10	--	750	--	51.3
0.86	10	--	800	--	41.5
0.86	10	--	830	--	38.2
0.86	10	256	20	5	10.8
0.86	10	300	20	5	10.2
0.86	10	350	20	6	12.0
0.86	10	400	20	6	36.5
0.86	10	550	20	6	333.8
0.86	10	600	20	7	396.1
0.86	10	650	20	7	428.0
0.86	10	700	20	7	504.4
0.86	10	700	20	7	501.8
0.86	10	750	20	8	489.9
0.86	10	800	20	8	580.9
HR, CR = Heating Rate, Cooling Rate in °C/min					
Peak T, Test T = Peak Sinter and Test Temperature in °C					

Table E-2: Raw data for FTT measurements of W-10wt.%Cu (with 0.35wt.% admixed Co) compacts sintered in hydrogen.

Powder Chararacteristics		W	Cu	Co	
Vendor		Teledyne	ACuPowder	Westiam	
Grade		C-3	635	ultrafine	
D ₅₀ , μm		1.3	12.5	--	
Theoretical Density, g/cm ³		19.35	8.92	--	
Apparent Density, g/cm ³		1.94	3.39	--	
Compaction Pressure, MPa		154			
Strength Data					
Density Fraction	Sinter Profile				TRS, MPa
	HR	Peak T	Test T	CR	
0.54	--	--	20	--	5.8
0.53	10	--	258	--	4.1
0.54	10	--	509	--	4.0
0.54	10	--	698	--	6.4
0.53	10	--	802	--	5.7
0.53	10	--	902	--	13.0
0.52	10	--	952	--	15.2
0.54	10	--	991	--	23.9
0.53	10	--	1024	--	25.3
0.53	10	--	1069	--	24.6
0.53	10	--	1101	--	23.1
0.54	10	901	699	8	14.8
0.52	10	902	500	6	27.4
0.54	10	902	20	7	37.0
0.56	10	271	20	5	6.3
0.54	10	511	20	6	16.9
0.55	10	698	20	7	20.4
0.54	10	803	20	7	15.5
0.54	10	902	20	7	38.2
0.59	10	991	20	7	75.5
0.53	10	1055	20	7	81.3
0.58	10	1101	20	8	89.1
HR, CR = Heating Rate, Cooling Rate in °C/min					
Peak T, Test T = Peak Sinter and Test Temperature in °C					

Table E-3: Raw data for FTT measurements of W compacts sintered in hydrogen.

Powder Chararacteristics		W			
Vendor		Teledyne			
Grade		C-3			
D ₅₀ , μm		1.3			
Theoretical Density, g/cm ³		19.35			
Apparent Density, g/cm ³		1.94			
Compaction Pressure, MPa		154			
Strength Data					
Density Fraction	Sinter Profile				TRS, MPa
	HR	Peak T	Test T	CR	
0.51	--	--	20	--	6.1
0.51	10	--	403	--	6.7
0.51	10	--	501	--	6.0
0.50	10	--	800	--	4.1
0.50	10	--	900	--	2.5
0.51	10	--	1032	--	20.3
0.50	10	--	1050	--	21.6
0.51	10	--	1101	--	43.4
0.51	10	902	700	8	11.4
0.50	10	917	500	6	14.0
0.51	10	917	20	7	20.5
0.51	10	901	20	--	23.0
HR, CR = Heating Rate, Cooling Rate in °C/min					
Peak T, Test T = Peak Sinter and Test Temperature in °C					

Table E-4: Raw data for FTT measurements of Ni_3Al (with 0.04wt.% admixed B) compacts sintered in a 90% argon - 10% hydrogen mix.

Powder Chararacteristics		Ni ₃ Al			
Vendor		XForm			
Designation		121			
D ₅₀ , μm		21.2			
Pycnometer Density, g/cm ³		7.39			
Apparent Density, g/cm ³		2.35			
Compaction Pressure, MPa		580			
Strength Data					
Density Fraction	Sinter Profile				TRS, MPa
	HR	Peak T	Test T	CR	
0.69	--	--	20	--	13.0
0.69	--	--	20	--	15.3
0.69	10	--	401	--	13.5
0.69	10	--	503	--	14.8
0.69	10	--	604	--	17.0
0.69	10	--	704	--	17.3
0.70	10	--	800	--	22.6
0.68	10	--	900	--	25.5
0.69	10	--	1000	--	70.0
0.68	10	1000	793	8	72.8
0.70	10	1000	598	8	121.7
0.67	10	400	20	6	13.6
0.68	10	503	20	6	13.5
0.68	10	606	20	7	14.1
0.67	10	704	20	7	19.1
0.67	10	801	20	7	34.0
0.67	10	900	20	7	44.4
0.68	10	1000	20	8	169.7
0.68	10	1000	20	8	171.5
0.68	5	400	20	5	14.2
0.68	5	503	20	6	14.9
0.67	5	701	20	7	24.8
HR, CR = Heating Rate, Cooling Rate in °C/min					
Peak T, Test T = Peak Sinter and Test Temperature in °C					

Table E-5: Raw data for FTT measurements of FC0208 (with Cu155) compacts sintered in a 80% nitrogen - 20% hydrogen mix.

Powder Chararacteristics		Fe	Cu	C	
Vendor		Quebec Metal Powders	United States Bronze Powders	SW Graphite	
Grade		Fe-A88	Cu155-A8	1651	
D ₅₀ , μm		107.1	40.7	--	
Theoretical Density, g/cm ³		7.9	8.92	--	
Apparent Density, g/cm ³		3.1	3.0	--	
Compaction Pressure, MPa		550			
Strength Data					
Density Fraction	Sinter Profile				TRS, MPa
	HR	Peak T	Test T	CR	
0.92	--	--	20	--	12.1
0.92	10	--	300	--	10.1
0.92	10	--	300	--	10.5
0.92	10	--	500	--	13.4
0.92	10	--	500	--	13.6
0.92	10	--	700	--	10.2
0.92	10	--	700	--	14.3
0.92	10	--	800	--	13.9
0.92	10	--	940	--	39.1
0.92	10	--	940	--	39.3
0.92	10	--	1090	--	56.8
0.92	5	--	701	--	21.4
0.92	5	--	941	--	47.3
0.92	5	--	1101	--	55.9
HR, CR = Heating Rate, Cooling Rate in °C/min					
Peak T, Test T = Peak Sinter and Test Temperature in °C					

Powder Characteristics			Fe		Cu		C
Vendor			Quebec Metal Powders		United States Bronze Powders		SW Graphite
Grade			Fe-A88		Cu278-A8		1651
D ₅₀ , μm			107.1		26.1		--
Theoretical Density, g/cm ³			7.9		8.92		--
Apparent Density, g/cm ³			3.1		3.0		--
Compaction Pressure, MPa			550				
Strength Data							
Density Fraction	Sinter Profile						TRS, MPa
	HR	Peak T	Test T	Hold T	Hold t	CR	
0.92	--	--	20	--	--	--	12.3
0.92	10	--	300	--	--	--	10.7
0.92	10	--	300	--	--	--	11.4
0.92	10	--	500	--	--	--	12.9
0.92	10	--	500	--	--	--	13.1
0.92	10	--	501	500	20	--	13.9
0.92	10	--	503	500	20	--	11.5
0.92	10	--	700	500	20	--	13.2
0.92	10	--	700	500	20	--	13.5
0.92	10	--	940	500	20	--	54.2
0.92	10	--	937	500	20	--	76.6
0.92	5	--	701	--	--	--	17.7
0.92	5	--	941	--	--	--	73.2
HR, CR = Heating Rate, Cooling Rate in °C/min							
Peak T, Test T, Hold T = Peak Sinter, Test, and Hold Temperature in °C							
Hold t = Hold time in min							

Vita

Gregory A. Shoales

Degrees:

B.S. Aeronautical Engineering, May 1979
Rensselaer Polytechnic Institute, Troy, NY

M.S. Aeronautical Engineering, August 1981
Rensselaer Polytechnic Institute, Troy, NY

Ph.D. Engineering Science and Mechanics
Pennsylvania State University, University Park, PA

Employment Record:

Aircraft Designer, May 1979 through August 1980
McDonnell Aircraft Company, St. Louis, MO

Research and Development Engineer, May 1981 through September 1983
Benet Weapons Lab, Watervliet, NY

Officer, U.S. Air Force, September 1983 through present
Development Engineer, Wright-Patterson AFB, OH
Flight Test Engineer, Edwards AFB, CA
Assistant Professor of Engineering Mechanics, U.S.A.F. Academy, CO

Recent Publications:

G.A. Shoales and R.M. German, "In situ Strength Evolution of the Sintering of Bronze Powders," *Metallurgical and Materials Transactions A*, vol. 29, no. 4, 1998, pp. 1257-1263.

G.A. Shoales and R.M. German, "Combined Time and Temperature Effects on Strength Evolution Using Integral Work of Sintering Concepts," *Metallurgical and Materials Transactions A* (pending approval).

G.A. Shoales, A. Griffo, A.L. Cardamone, K.K. Comstock and R.M. German, "In Situ Strength Evolution of W-20Cu P/M Compacts," 1997 *International Conference on Tungsten, Refractory Metals and Alloys*, Orlando, FL, Metal Powder Industries Federation, Princeton, NJ, 1997, pp. 407-414.

G.A. Shoales, A. Lal and R.M. German, "Thermal Characterization to Study the Sintering of Bronze Powders," *Twenty-Fourth International Thermal Conductivity Conference / Twelfth International Thermal Expansion Symposium*, Pittsburgh, PA, 1997.

G.A. Shoales, and S.V. Atre, "Strength Evolution During Thermal Debinding of PIM Components," *PIM 98 - The International Conference on Powder Injection Molding of Metals and Ceramics*, University Park, PA, 1998.

T.S. Shivashankar, G.A. Shoales, and S.V. Atre, "The Master Debinding Curve," *PIM 98 - The International Conference on Powder Injection Molding of Metals and Ceramics*, University Park, PA, 1998.

J.B. Henderson, G.A. Shoales, and L. Hagemann, "Evolution of Thermophysical Properties of a Bronze Powder During Sintering," *PIM 98 - The International Conference on Powder Injection Molding of Metals and Ceramics*, University Park, PA, 1998.

G.A. Shoales and R.M. German, "Strength Controlled Sintering of ZnO for Dimensional Precision," *The American Ceramic Society's 100th Annual Meeting*, Cincinnati, OH, The American Ceramic Society, Westerville, OH, 1998.

A. Lal, J. Liu, G.A. Shoales, and R.M. German, "Component Shape Retention in Supersolidus Liquid Phase Sintering of Prealloyed Powders," *PM²TEC '98 International Conference on Powder Metallurgy & Particulate Materials*, Las Vegas, NV, Metal Powder Industries Federation, Princeton, NJ, 1998.

E. Olevsky, G.A. Shoales, and R.M. German, "Temperature - Dependent Accumulated Strength Under Sintering," *PM²TEC '98 International Conference on Powder Metallurgy & Particulate Materials*, Las Vegas, NV, Metal Powder Industries Federation, Princeton, NJ, 1998.

A. Upadhyaya, G.A. Shoales, and R.M. German, "Effect of Transition Element Addition on Strength Evolution of W-Cu Composites," *PM²TEC '98 International Conference on Powder Metallurgy & Particulate Materials*, Las Vegas, NV, Metal Powder Industries Federation, Princeton, NJ, 1998.

Honors:

Inducted into Phi Kappa Phi Honor Society

Professional Organizations:

The Minerals, Metals and Material Society
ASM International
APMI International
American Society for Nondestructive Testing
American Society for Engineering Education
Air Force Association (life member)
Society of Flight Test Engineers